

University of Bath



**PHD**

**The influence of crystallisation on the mechanical and interfacial properties of active pharmaceutical ingredients**

Kubavat, Harshal

*Award date:*  
2011

*Awarding institution:*  
University of Bath

[Link to publication](#)

**General rights**

Copyright and moral rights for the publications made accessible in the public portal are retained by the authors and/or other copyright owners and it is a condition of accessing publications that users recognise and abide by the legal requirements associated with these rights.

- Users may download and print one copy of any publication from the public portal for the purpose of private study or research.
- You may not further distribute the material or use it for any profit-making activity or commercial gain
- You may freely distribute the URL identifying the publication in the public portal ?

**Take down policy**

If you believe that this document breaches copyright please contact us providing details, and we will remove access to the work immediately and investigate your claim.

# **The Influence of crystallisation on the mechanical and interfacial properties of active pharmaceutical ingredients**

**Harshal A. Kubavat**

A thesis submitted for the degree of Doctor of Philosophy

University of Bath

Department of Pharmacy and Pharmacology

June 2011

## **COPYRIGHT**

Attention is drawn to the fact that copyright of this thesis rests with its author.

This copy of the thesis has been supplied on condition that anyone who consults it is understood to recognize that its copyright rests with its author and that no quotation from the thesis and no information derived from it may be published without the prior written consent of the author.

This thesis may be made available for consultation within the University Library and may be photocopied or lent to other libraries for the purposes of consultation.

## Acknowledgements

To my supervisors Rob Price, Graham Ruecroft and post-doc/colleague Jag Shur, I am eternally indebted for your patience, enthusiasm, support and direction throughout the project. Additional members of Pharmaceutical Surface Science Research Group including Chonladda, Amandeep and Hanne are thanked alongside past and present members for all their advice and guidance during my time at Bath University.

I would also like to take the opportunity to thank the Prosonix team for their funding and allowing me to continue some of my research in their facilities alongside the active interest they have taken in my work. Furthermore, I want to acknowledge the EPSRC and the University of Bath for funding and support. Directly, these include Ursula from CEOS for all her help in training for scanning electron microscopy, Gabrielle from chemistry who performed the X-ray powder diffraction of my samples, Rod & Steve (workshop), Don (lab) and Ade (IT). Thanks are also given to Andy Smith at Sympatec/MT, Debbie at Malvern for offering a wonderful insight into modern particle imaging and also John (DMV-Fonterra) and Seamus (Oxford Lasers) for being great company.

To the friends in the Pharmacy department and others I would like to thank you all for your company and friendship, without it, these three years would not have been the same.

This PhD would not be possible without two key people swaying me into this field. They are Steve Brocchini at The School of Pharmacy, University of London who got me on this path and Denny Mählin who supervised me at Uppsala University.

Finally, I would like to thank the love and heartfelt support I have received from my family, especially my Mum, Dad and sister. Without your love and care, none of what follows in this thesis would be possible. Thank you.

**Abstract**

Crystallisation of organic molecules is a fundamental process routinely used for purification and isolation of active pharmaceutical ingredients (APIs). In the formulation of traditional dry powder inhaler (DPI) products, harvested primary crystalline APIs are secondarily processed and subsequently blended with excipients to form an ordered mixture. In DPI formulations containing drug particles and coarse carrier material, the delicate balance of cohesive and adhesive forces between the drug(s) and carrier enable delivery of respirable APIs to the targeted regions of the lungs. The destructive and relative uncontrolled nature of secondary-processing techniques such as milling, leads to the generation of respirable formulations of varying performance, resulting in varying clinical efficacy. The relationship between the primary crystallisation of APIs and the physical, chemical, mechanical properties of the primary crystals and the relationship to the secondary processing of these materials remain poorly understood. This body of work aimed to address the paucity of data within this area, within the context of DPI formulations.

A nanoindentation approach using atomic force microscopy (AFM) developed to determine the elastic modulus of crystalline pharmaceutical samples provided the Young's modulus of a range of pharmaceutical materials. Differences were observed indicating lactose monohydrate to have the highest stiffness (high Young's modulus) and formoterol fumerate dihydrate having the lowest of the materials tested (0.93 GPa). Utilising AFM cohesive-adhesive force measurements against a reference Highly Ordered Pyrolytic Graphite (HOPG) substrate, fluticasone propionate was seen to have the greatest cohesive tendency of 1.13 times greater to itself over HOPG. In contrast, budesonide had the most adhesive tendency towards HOPG, with a cohesive-adhesive balance (CAB) value of 0.65, indicating that the differences in DPI performance of these materials may be as a result of differences in their interfacial properties which could be influenced by prior processing history.

Crystallisation of fluticasone propionate (FP) was conducted using four different solvent/anti-solvent combinations to investigate the influence of different end-solvents on the Young's modulus of the resultant crystals, their micronisation



behaviour and *in vitro* performance in carrier based DPI formulations. The Young's modulus of FP crystals produced varied significantly and these differences were reflected in the number of passes required in the microniser to reduce the particle size of the primary crystals to less than 5  $\mu\text{m}$ . Furthermore, the resultant micronised materials were determined to have different cohesive-adhesive balance values, supporting differences in their respective DPI formulation performance attributes, both in binary formulation and in combination with a second drug, salmeterol xinafoate.

The impact of changes in crystal habit on the mechanical properties of budesonide crystals was investigated alongside the resultant effect on interactive forces of the micronised material and the performance in a DPI formulation. The Young's modulus determined by AFM nanoindentation on the {002} face of each habit confirmed a Young's modulus four times greater for one of the habits and supported the particle size data of the resultant micronised materials from each primary crystal samples. Cohesive-adhesive balance measurements of the micronised budesonide samples with respect to lactose monohydrate supported *in vitro* aerosolisation performance studies, whereby the fine particle dose and fine particle fraction of the emitted dose of the sample with lower adhesive tendency towards the lactose carrier particle was greater.

The relative mechanical and processing differences between anhydrous and monohydrate forms of ipratropium bromide (IB) was evaluated using supercritical fluid technology and temperature drop crystallisation techniques, respectively. The aerosolisation efficiency of these materials from DPI formulations determined the effect of crystal form on the functionality of the two samples. Repeated force-distance measurements revealed no significant differences between the anhydrous and monohydrate form of IB and revealed both forms to have an average elastic modulus of approximately 4 GPa. No differences were seen in the secondary processing of these materials relating the milling behaviour, interfacial properties or aerosolisation performance *in vitro*, demonstrating the suitability of supercritical fluid technology in producing an anhydrous form of ipratropium bromide for inclusion in a carrier-based DPI formulation.

Acknowledgements .....	i
Abstract .....	ii
Abbreviations .....	ix
List of Figures.....	xii
List of Tables.....	xvii
<b>Chapter 1: Introduction .....</b>	<b>1</b>
1.1 Respiratory Medicine .....	1
1.1.1 The Respiratory Tract .....	1
1.1.2 Asthma .....	3
1.1.3 Chronic Obstructive Pulmonary Disease (COPD).....	4
1.1.4 Differentiation Between Asthma and COPD .....	4
1.1.5 Inhaled Pharmacological Treatment of Asthma and COPD .....	5
1.2 Pulmonary Drug Delivery.....	7
1.2.1 Particle Deposition in the Lungs.....	7
1.2.2 Inertial Impaction .....	8
1.2.3 Sedimentation .....	9
1.2.4 Brownian Diffusion .....	9
1.2.5 Interception .....	9
1.2.6 Electrostatic Precipitation .....	10
1.3 Respiratory Drug Delivery Devices.....	10
1.3.1 Nebulisers .....	10
1.3.2 Pressurised Metered Dose Inhalers (pMDIs) .....	11
1.3.3 Dry Powder Inhalers (DPIs) .....	12
1.3.4 Summary of the Various Drug Delivery Options to the Lungs.....	15
1.4 Pharmaceutical Considerations in the Formulation of DPI Powders .....	15
1.4.1 Types of DPI formulations.....	18
1.4.2 Blending .....	19
1.4.3 Interparticulate Forces .....	20
1.4.4 Factors Influencing the Degree of Interparticulate Forces .....	25
1.4.5 The Impact of Particle Size Reduction on the Physico-Chemical Behaviour of APIs.....	29
1.5 Characterisation of Pharmaceutically Processed Materials .....	30
1.5.1 Crystallinity .....	31
1.5.2 Methods of Surface Energy Determination .....	33
1.5.3 Measuring particle removal efficiency .....	35
1.5.4 Single Particle Investigations of Interfacial Forces.....	35

1.6	Primary Crystallisation of APIs .....	39
1.6.1	Background Theory of Crystallisation .....	39
1.6.2	Effect of Solvents and Impurities on Crystallisation .....	44
1.6.3	The Mechanical Properties of Crystalline Materials .....	45
1.7	Methods of Measuring the Young's Modulus of Organic Materials .....	46
1.7.1	Flexure Testing (Beam Bending) .....	47
1.7.2	Compression Testing .....	47
1.7.3	Nanoindentation Measurements .....	48
1.8	Aim of Study .....	51
<b>Chapter 2: General Methods and Materials .....</b>		<b>53</b>
2.1	General Physicochemical Characterisation .....	53
2.1.1	Overview .....	53
2.1.2	Scanning Electron Microscopy .....	53
2.1.3	Particle Size Analysis .....	54
2.1.4	Differential Scanning Calorimetry .....	55
2.1.5	X-Ray Powder Diffraction .....	56
2.2	Atomic Force Microscopy .....	57
2.2.1	Overview .....	57
2.2.2	Topographical Surface Analysis .....	58
2.3	Force Interaction Microscopy .....	60
2.3.1	Overview .....	60
2.3.2	Colloidal Probe Microscopy .....	62
2.3.3	AFM Nanoindentation .....	63
2.4	<i>In vitro</i> Testing of Inhaled Drug products .....	67
2.4.1	Next Generation Impactor (NGI) Testing .....	68
<b>Chapter 3: Investigation of the Mechanical and Surface Interfacial Properties of Long-Acting <math>\beta</math>2 Agonists and Inhaled Corticosteroids .....</b>		<b>71</b>
3.1	INTRODUCTION .....	71
3.2	METHODS AND MATERIALS .....	76
3.2.1	Crystal Substrate Crystallisation .....	76
3.2.2	Topographical and Mechanical Analysis using Atomic Force Microscopy (AFM) .....	78
3.2.3	AFM Probe Tip Size Characterisation .....	78
3.2.4	Young's Modulus Determination .....	79
3.2.5	Cohesive-Adhesive Balance (CAB) Measurements .....	80

3.3 RESULTS AND DISCUSSION .....	82
3.3.1 Quantification of Spring Constant and Contact Radius of AFM probes ....	82
3.3.2 Determination of Young's Modulus of Crystalline Substrates .....	84
3.4 CONCLUSIONS .....	94
<b>Chapter 4: Investigation into the influence of primary crystallisation conditions on the mechanical properties and secondary processing behaviour of fluticasone propionate.....</b>	<b>95</b>
4.1 INTRODUCTION .....	95
4.2 MATERIALS AND METHODS.....	99
4.2.1 Materials.....	99
4.2.2 Methods .....	99
4.2.3 Micronisation of crystalline samples of fluticasone propionate by air-jet milling	102
4.2.4 Methodology of the cohesive-adhesive balance (CAB) approach to colloidal probe atomic force microscopy (AFM) .....	102
4.2.5 Atomic Force Microscopy – Colloidal Probe Force Measurements .....	103
4.2.6 Preparation of Powder Formulations.....	104
4.2.7 HPLC Analysis of Fluticasone Propionate and Salmeterol Xinafoate .....	105
4.2.8 Content Uniformity Measurements.....	105
4.2.9 <i>In vitro</i> Aerosolisation Studies .....	105
4.3 RESULTS AND DISCUSSION .....	107
4.3.1 Characterisation of the physicochemical properties of crystals of fluticasone propionate produced using different anti-solvents .....	107
4.3.2 Nanomechanical measurements of the Young's modulus of FP samples	110
4.3.3 Physicochemical and surface interfacial properties of secondary processed crystals of sample A and C .....	112
4.3.4 <i>In vitro</i> inhalation performance of binary and combination DPI formulations containing secondary processed FP from samples A and C .....	117
4.3.5 <i>In vitro</i> aerosolisation performance of binary DPI formulations containing micronised samples A and C .....	120
4.3.6 <i>In vitro</i> aerosolisation performance of combination DPI formulations of FP and SX containing micronised FP from samples A and C .....	121
4.4 CONCLUSIONS .....	125

---

<b>Chapter 5: Influence of primary crystallisation conditions on the mechanical and interfacial properties of micronised budesonide for dry powder inhalation .....</b>	<b>126</b>
5.1 INTRODUCTION .....	126
5.2 METHODS AND MATERIALS .....	131
5.2.1 Materials .....	131
5.2.2 Crystallisation of Budesonide .....	131
5.2.3 Particle Size Reduction .....	131
5.2.4 Physico-Chemical Characterisation .....	132
5.2.5 Cohesive-Adhesive Balance .....	134
5.2.6 HPLC Analysis of Budesonide .....	136
5.2.7 Preparation of DPI formulation .....	136
5.2.8 Content Uniformity .....	137
5.2.9 <i>In Vitro</i> Aerosol Deposition Studies .....	137
5.3 RESULTS AND DISCUSSION .....	139
5.3.1 Physicochemical Characterisation of Primary Budesonide Crystals .....	139
5.3.2 Mechanical measurements of the primary budesonide crystals .....	142
5.3.3 Effect of crystal habit and mechanical properties of primary budesonide crystals on secondary processing and DPI formulation performance .....	145
5.4 CONCLUSIONS .....	152
 <b>Chapter 6: The Influence of Crystal Form on the Primary Crystallisation and Secondary Processing of Ipratropium Bromide for Dry Powder Inhalation .....</b>	<b>153</b>
6.1 INTRODUCTION .....	153
6.2 MATERIALS AND METHODS .....	156
6.2.1 Determination of IB Solubility .....	156
6.2.2 Crystallisation of IB .....	157
6.2.3 Physicochemical Properties Analysis .....	159
6.2.4 Atomic Force Microscopy – Interactive Force Measurements .....	161
6.2.5 HPLC Analysis of Ipratropium Bromide .....	162
6.2.6 Preparation of carried-based DPI formulations .....	164
6.2.7 Content Uniformity .....	165
6.2.8 <i>In Vitro</i> Aerosol Deposition Studies .....	165
6.3 RESULTS AND DISCUSSION .....	166
6.3.1 Solubility of IB in Experimental Solvents .....	166
6.3.2 Physicochemical Characterisation of primary IB crystals .....	166

---

6.3.3	Nanomechanical Analysis of Monohydrate and Anhydrous IB crystals ..	170
6.3.4	Physicochemical Characterisation of secondary processed monohydrate and anhydrous IB .....	172
6.3.5	Investigation into the Interfacial properties of Micronised anhydrous and monohydrate IB using Cohesive-Adhesive Balance (CAB) Measurements.....	175
6.3.6	<i>In Vitro</i> Aerosolisation Performance of Carrier-Based DPI formulations.	177
6.4	CONCLUSIONS .....	180
<b>Chapter 7: General Conclusions and Further Work .....</b>		<b>181</b>
7.1	Introduction.....	181
7.2	Summary .....	182
7.3	General Conclusions .....	184
7.4	Future Work.....	185
<b>References .....</b>		<b>187</b>

## Abbreviations

$A$	Pre-exponential factor
$\text{\AA}$	Angstrom
$A_s$	Area produced by the separation of two surfaces
$a$	Polarisability
AFM	Atomic force microscope
API	Active pharmaceutical ingredient
BUD	Budesonide
BTS	British Thoracic Society
$C_{50}$	Cunningham slip correction factor for a particle of size $d_{50}$
CFC	chlorofluorocarbon
cm	Centimeter
COPD	Chronic obstructive pulmonary disease
$d$	Diameter
$d_{50}$	Aerodynamic diameter of particle collected with 50% efficiency
$d_p$	Distance between planes of the crystal
DPI	Dry powder inhaler
DSC	Differential scanning calorimetry
$E$	Young's modulus
$F$	Force
$F$	Vibrational frequency
$F_c$	Capillary force
$F_{VDW}$	van der Waals force
FFD	Formoterol fumarate dihydrate
FP	Fluticasone propionate
$g$	Acceleration due to gravity
H	Hardness
$H$	Hamaker constant
$h$	Planck's constant
HDAC	Histone deacetylase
HFA	Hydrofluoroalkane

---

HPLC	High performance liquid chromatography
IB	Ipratropium bromide
IGC	Inverse gas chromatography
ICS	Inhaled corticosteroid
IgE	Immunoglobulin E
$K_c$	Critical stress intensity factor
$k$	Spring constant
$k$	Boltzmann constant
$\text{kJ}$	Kilojoules
$\text{kV}$	Kilovolt
$\text{L}$	Litre
LABA	Long-acting $\beta_2$ agonist
LALLS	Low angle laser light scattering
$\text{m}$	Meters
$\text{mol}$	Moles
MMAD	Mass median aerodynamic diameter
MOC	Micro-orifice collector
$\text{N}$	Newtons
NCE	New chemical entity
NICE	National Institute for Health and Clinical Excellence
$n$	Order of reflection
$n_n$	Number of nozzles on NGI stage
$\text{nm}$	Nanometer
pMDI	Pressurised metered dose inhaler
$\text{pN}$	PicoNewton
PSD	Particle size distribution
$Q$	Total volumetric flow rate through an impactor stage
$R^*$	Contact radius
$R$ and $r$	Radius
RH	Relative humidity
RI	Refractive index
ROS	Reactive oxygen species
$S$	Solubility
$s$	Separation distance



---

SABA	Short-acting beta <sub>2</sub> agonist
SEM	Scanning electron microscopy
$Stk$	Stokes's number
SX	Salmeterol xinafoate
STM	Scanning tunnel microscope
TIO	Tiotropium bromide
$V$	Velocity
$V_m$	Molecular volume
$v$	Number of atoms per unit volume of particle
$W_{adh}$	Thermodynamic work of adhesion
$W_{coh}$	Thermodynamic work of cohesion
$W_{coh}$	Thermodynamic work of cohesion
XRPD	X-ray powder diffraction
$x$	Cantilever deflection
$\Delta G$	Gibbs free energy
$\Delta G_s$	Surface free energy
$\Delta G_v$	Volume free energy
$\Delta z$	Piezo displacement
$\theta$	Angle
$\delta$	Indentation depth
$\varepsilon$	Extensional deformation
$\rho_a$	Density of air
$\rho_{ae}$	Unit density
$\rho_p$	Particle density
$\eta$	Viscosity
$\mu m$	Micrometer
$\mu$	Air viscosity
$\nu$	Poisson ratio
$\gamma$	Free energy per unit surface area
	Surface tension
$\gamma_w$	Surface tension of water
$\lambda_{1,2}^d$	Constant of dispersion
$\sigma$	Tensile stress

## List of Figures

Figure 1.1 Structure of the lungs (Adapted from Griesenbach et al., 2004) .....	2
Figure 1.2 The deposition profile of inhaled particles as a function of airway generation (Reproduced from Patton and Byron, 2007).....	8
Figure 1.3 The three different types of unit dosing mechanisms employed in commonly used DPI devices; a – single unit-dose, b – multiple unit-dose, c – reservoir metered (Adapted from Daniher and Zhu, 2008).....	13
Figure 1.4 An overview of the various steps required in producing a formulated dry-powder inhalation device and the possible implications of each process....	17
Figure 1.5 A representative graphical description of a CAB-graph for a binary system (Adapted from Begat et al., 2004) .....	38
Figure 1.6 The surface structure of a growing crystal (Adapted from Myerson, 1993).....	43
Figure 1.7 A representational load versus displacement graph obtained from a single nanoindentation experiment (Reproduced from Taylor et al., 2004).....	49
Figure 1.8 A flow diagram illustrating the structure of this thesis in relation to the primary hypothesis.....	52
Figure 2.1 Scattering phenomena that occur when particles are illuminated with light (Reproduced from Keck and Mueller 2008) .....	55
Figure 2.2 A representative DSC trace showing the glass transition temperature ( $T_g$ ), recrystallisation exotherm temperature ( $T_c$ ) and enthalpy ( $\Delta H_c$ ), melting endotherm temperature ( $T_m$ ) and enthalpy ( $\Delta H_f$ ) and onset of degradation. Endothermic transitions are down (Reproduced from Class et al., 1999) .....	56
Figure 2.3 A schematic representation of an AFM (a) and a photograph of a multimode™ AFM (b).....	58
Figure 2.4 An illustration of different imaging modes with tip and deflection showing contact (a), non-contact (b) and tapping-mode (c) tip interactions with a substrate .....	60
Figure 2.5 A schematic force-distance curve obtained from AFM using a colloidal probe technique. Adapted from (Turner et al., 2007).....	61

Figure 2.6 A representative deflection versus cumulative z-step for a single nanoindentation experiment performed using AFM.....	65
Figure 2.7 A representative nanoindentation plot of loading force versus indentation obtained from an AFM experiment.....	67
Figure 2.8 Next Generation Impactor (NGI) (Adapted from <a href="http://www.mspcorp.com">http://www.mspcorp.com</a> ) .....	68
Figure 2.9 A schematic representation of particle impaction through a NGI nozzle (Adapted from <a href="http://www.copleyscientific.com">http://www.copleyscientific.com</a> ).....	69
Figure 3.1 Representative scanning electron micrograph images of the two different AFM cantilever probes used for nanoindentation in this study (A-B: Veeco TESP; C-D: Nanosensors R150-NCL) qualitatively indicating differences in probe tip-radius .....	83
Figure 3.2 Representative optical and AFM images of all samples prior to indentation (A) Lactose, (B) Salmeterol, (C) Budesonide, (D) Fluticasone, (E) Formoterol .....	85
Figure 3.3 AFM TM images of crystal surfaces after nanoindentation with the respective indenting probes (A: Lactose-TESP, B: FP-Nanosensors). The white squares indicate areas of loading and the arrows indicate initial point of probe contact which were unsuitable for Hertzian extrapolation.....	86
Figure 3.4 Individual loading forces plotted against the indentation depths of salmeterol and lactose monohydrate crystals using a Veeco-TESP AFM probe .....	87
Figure 3.5 Individual loading forces against the indentation depths of fluticasone, budesonide and formoterol crystals using a Nanosensor probe AFM probe.....	88
Figure 3.6 Young's modulus measurements of different pharmaceutical crystals determined by AFM nanoindentation.....	89
Figure 3.7 Cohesive-adhesive balance of the different inhaled APIs with respect to Highly Ordered Pyrolytic Graphite (HOPG) where the dashed line represents a CAB ratio of 1.0 .....	92
Figure 4.1 Representative SEM images and corresponding simulated morphologies of crystals of fluticasone propionate produced using different anti-solvents.....	108
Figure 4.2 Cumulative particle size distribution of crystals of fluticasone propionate produced using different anti-solvents. ....	109

Figure 4.3 X-ray powder diffractograms of the different samples of fluticasone propionate.....	110
Figure 4.4 The measured loading force against indentation depth <sup>(3/2)</sup> for each sample of crystalline fluticasone propionate. ....	111
Figure 4.5 Comparison of the force of cohesion, force of adhesion and CAB ratio of fluticasone propionate – lactose systems (FP-Lactose) and fluticasone propionate – salmeterol xinafoate systems (FP-SX) produced following re-pass air-jet milling of sample A crystals of fluticasone propionate over four cycles. ....	114
Figure 4.6 Comparison of the force of cohesion, force of adhesion and CAB ratio of fluticasone propionate – lactose systems (FP-Lactose) and fluticasone propionate – salmeterol xinafoate systems (FP-SX) produced following air-jet milling of sample C crystals of fluticasone propionate. ....	116
Figure 4.7 Representative HPLC calibration curve obtained for FP.....	118
Figure 4.8 A Representative HPLC trace for FP.....	118
Figure 4.9 <i>In vitro</i> stage-by-stage deposition of fluticasone propionate following aerosolisation of binary DPI formulations containing samples A and C of micronised fluticasone propionate. ....	121
Figure 4.10 <i>In vitro</i> stage-by-stage deposition of fluticasone propionate and salmeterol xinafoate following aerosolisation of combination DPI formulations containing micronised fluticasone propionate sample A.....	122
Figure 4.11 <i>In vitro</i> stage-by-stage deposition of fluticasone propionate and salmeterol xinafoate following aerosolisation of combination DPI formulations containing micronised fluticasone propionate sample C.....	123
Figure 5.1 Scanning electron micrographs and computer models of the crystal habits of Sample A (a,b) and Sample B (c, d) .....	140
Figure 5.2 Representative thermograms of budesonide samples A and B. ....	142
Figure 5.3 The X-ray powder diffraction profiles of the primary budesonide crystals of samples A and B. ....	142
Figure 5.4 Atomic force microscope images (3 x 3 µm) of Sample A before indentation (a), Sample A post indentation (b) and Sample B prior to indentation (c) and Sample B after indentation. The boxes (□) indicate areas where mechanical measurements were undertaken. The black arrows indicate the point of initial contact upon tip-substrate engagement, where high loading has resulted in plastic deformation. ....	143

Figure 5.5 Individual loading force against indentation <sup>3/2</sup> for the contact of a hemispherical probe on the {002} faces of a number of different crystals of samples A and B.....	145
Figure 5.6 The particle size distribution of the unmicronised (primary) and micronised (secondary) samples of budesonide. ....	146
Figure 5.7 CAB plots for micronised samples A and B of budesonide with respect to lactose.....	148
Figure 5.8 Representative HPLC calibration curve obtained for budesonide ..	149
Figure 5.9 A representative HPLC trace for budesonide .....	149
Figure 5.10 NGI stage-by-stage deposition profile of budesonide samples A and B .....	150
Figure 6.1 A schematic representation of the supercritical fluid extraction rig used to produce anhydrous IB.....	158
Figure 6.2 The determined solubility of IB in ethanol and H <sub>2</sub> O .....	166
Figure 6.3 Differential scanning calorimetry thermograms of two crystalline ipratropium bromide samples produced using a seeded aqueous and supercritical approach.....	167
Figure 6.4 The X-ray powder diffraction profiles for the primary crystals of ipratropium bromide anhydrous and monohydrate. ....	168
Figure 6.5 Scanning electron micrographs of the crystalline monohydrate (A-B) and anhydrous (C-D) forms of ipratropium bromide. ....	169
Figure 6.6 Representative force-indentation curves for both samples of IB investigated using AFM nanoindentation.....	171
Figure 6.7 Young's modulus measurements for three different crystals from each IB sample. ....	172
Figure 6.8 Scanning electron micrographs of the micronised monohydrate (A) and anhydrous. ....	173
Figure 6.9 Cumulative particle size distribution of the crystalline and micronised samples of anhydrous and monohydrate forms of ipratropium bromide.....	174
Figure 6.10 CAB plot of monohydrate IB with respect to lactose. (The dashed line represents where $F_{COH} = F_{ADH} = 1.0$ ) .....	176
Figure 6.11 CAB plot of anhydrous IB with respect to lactose (The dashed line represents where $F_{COH} = F_{ADH} = 1.0$ ).....	176
Figure 6.12 Representative HPLC calibration curve obtained for IB .....	177

---

Figure 6.13 A Representative HPLC trace for IB.....	178
Figure 6.14 Mean mass deposition profiles for monohydrate and anhydrous carrier-based DPI formulations. ....	179

**List of Tables**

Table 3.1 Crystalline substrates grown for AFM measurements .....	76
Table 3.2 Details of the crystallisation solvents and methods used in producing substrate crystals for analysis.....	78
Table 3.3 The two different AFM probes used in this study <sup>(a)</sup> measured by thermal tuning, <sup>(b)</sup> using the manufacturers quoted value).....	83
Table 3.4 Surface roughness measurements for all substrates using TM-AFM (R <sub>a</sub> , Mean roughness; R <sub>q</sub> , Root mean squared roughness) .....	84
Table 3.5 Measured Young's modulus values for each crystal substrate using AFM nanoindentation.....	89
Table 3.6 Calculated cohesive strength values of API samples interacted with HOPG using AFM colloidal probe microscopy. IGC reference values were provided from a previous study (Jones et al., 2008).....	91
Table 3.7 Summary of the physicochemical properties and CAB ratios of the micronised form of the different APIs.....	93
Table 4.1 Particle size distribution (PSD) and Young's modulus of crystals of fluticasone propionate using different solvents.....	109
Table 4.2 An overview of the number of milling cycles required to obtaine the defined particle size requirements and the final particle size distributions of the micronised fluticasone propionate. ....	113
Table 4.3 Comparison of the force of cohesion, force of adhesion and CAB ratio of fluticasone propionate – lactose systems (FP-Lactose) and fluticasone propionate – salmeterol xinafoate systems (FP-SX) produced following re-pass air-jet milling of sample A crystals of fluticasone propionate over four cycles. ....	114
Table 4.4 Comparison of the force of cohesion, force of adhesion and CAB ratio of fluticasone propionate – lactose systems (FP-Lactose) and fluticasone propionate – salmeterol xinafoate systems (FP-SX) produced following air-jet milling of sample C crystals of fluticasone propionate. ....	116
Table 4.5 <i>In vitro</i> formulation performance (emitted dose (ED), fine particle dose (FPD), fine particle fraction of the emitted dose (FPF <sub>ED</sub> ) and mass median aerodynamic diameter (MMAD) and geometric standard deviation (GSD)) from aerosolisation of binary DPI formulations of fluticasone propionate into the NGI (n = 3). ....	119

Table 4.6 <i>In vitro</i> formulation performance (emitted dose (ED), fine particle dose (FPD), fine particle fraction of the emitted dose (FPF <sub>ED</sub> ) and mass median aerodynamic diameter (MMAD) and geometric standard deviation (GSD)) from aerosolisation of combination DPI formulations containing micronised fluticasone propionate (FP) sample A and salmeterol xinafoate (SX) into the NGI (n = 3).....	119
Table 4.7 <i>In vitro</i> formulation performance (emitted dose (ED), fine particle dose (FPD), fine particle fraction of the emitted dose (FPF <sub>ED</sub> ) and mass median aerodynamic diameter (MMAD) and geometric standard deviation (GSD) from aerosolisation of combination DPI .....	119
Table 5.1 Particle size distribution of crystalline budesonide samples A and B. ....	140
Table 5.2 The Young's modulus values obtained on the {002} face of different crystals of samples A and B using AFM nanoindentation. At total of 8 nanoindentation measurements were undertaken on three different crystals of each sample (n=24).....	145
Table 5.3 Particle size distribution analysis of micronised budesonide samples A and B.....	147
Table 5.4 <i>In vitro</i> performance characteristics of the two samples of budesonide using NGI testing (FPF <sub>RD</sub> – fine particle fraction of the recovered dose, FPF <sub>ED</sub> – fine particle fraction of the emitted dose).....	151
Table 6.1 Binary pump settings for the gradient mixing of two different buffer compositions used in the detection of IB. ....	164
Table 6.2 Particle size distribution (PSD) of the crystalline samples obtained using laser diffraction (VMD – Volume median-mass diameter).....	170
Table 6.3 Particle size distribution of the micronised materials determined by laser diffraction (VMD – Volume median-mass diameter). ....	174
Table 6.4 <i>In vitro</i> aerosolisation properties of DPI formulations produced from the monohydrate and anhydrous crystal form of ipratropium bromide (ED: emitted dose, FPD: fine-particle dose, MMAD: mass median aerodynamic diameter, GSD: geometric standard diameter FPF <sub>ED</sub> : fine-particle fraction of the emitted dose).....	179



## **Chapter 1: Introduction**

### **1.1 Respiratory Medicine**

The delivery of medication to the lungs is seen as one approach in delivering therapeutic agents to the local airways and increasingly for systemic delivery. As a non-invasive drug delivery strategy, inhaling active pharmaceutical ingredients avoids the harsh conditions of the gastro-intestinal tract, first pass effects of the gastro or hepatic system and in many cases, limits systemic toxicity. The pharmaceutical engineering of formulations for this process is however, demanding. Variables arising from the production of active ingredients combined with the effects of processing and device performance lead to significant challenges in developing and manufacturing consistently high-quality products.

#### **1.1.1 The Respiratory Tract**

The human lungs are primarily responsible for the exchange of gases between the external environment and systemic circulation. They work together with the heart and blood to extract oxygen from inspired air and expel waste gases, principally carbon dioxide (Kumar, 2002). Given the limited space for this process to occur, the lungs have to provide a large surface area within which gaseous exchange can take place and ensure adequate defence mechanisms are in place. Prevention of damage from inspired particulate matter and infective agents is achieved by a combination of structural and immunological barriers to foreign material.

##### **1.1.1.1 Structure of the Respiratory System**

The upper respiratory zone encompasses the nose, nasal passages, mouth, pharynx, larynx, trachea and bronchi and is known as the conducting airways. The lower respiratory region is responsible for the exchange of gases and comprises of the bronchioles and alveoli (Griesenbach et al., 2004). These are all illustrated in Figure 1.1 below.

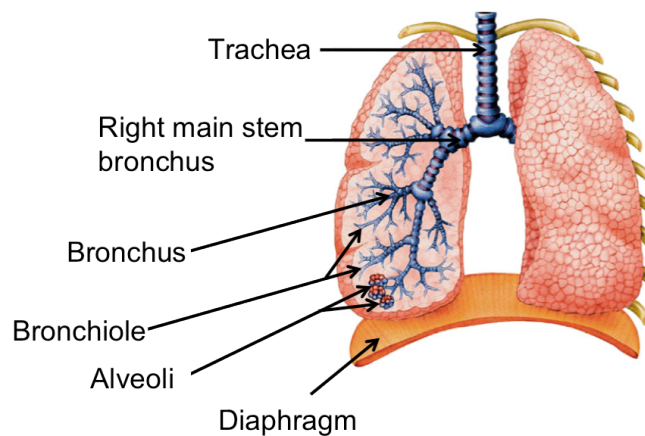


**Figure 1.1 Structure of the lungs (Adapted from Griesenbach et al., 2004)**

The trachea is 10-12 cm in length and divides into the left and right main bronchi, which in turn connects to shorter bronchi, bronchiole and alveoli through a series of approximately 25 bifurcating airways. Of the first seven divisions, the bronchi have walls consisting of cartilage and smooth muscle, epithelial lining including cilia and goblet cells and endocrine cells. The next 16-18 divisions contain bronchioles that have no cartilage, progressively thinner muscular layers with a single layer of ciliated cells and reduced goblet cells alongside Clara cells that produce a surfactant like liquid. Connected to the bronchioles are the alveoli, of which their total surface area is in the region of 40-80 m<sup>2</sup> consisting of an epithelial lining containing attenuated cytoplasm (Malcolmson and Embleton, 1998).

#### ***1.1.1.2 Defence Mechanisms of the Respiratory Tract***

The lungs receive around 10,000 L of air daily (Kumar, 2002) and have evolved to remove inhaled foreign particles including grass pollens, environmental particles, dander and prevent infection from invading bacteria, fungal spores and viruses. The continual branching and narrowing of the airways are responsible for filtering the inspired air and removal of particulate material by impaction against the respiratory tract. Mucous secretion enables the trapping of these materials while the beating cilia upon which this mucous rests, is continually moving this substance upwards towards the oropharynx where it is

swallowed (Hansel and Barnes, 2009). Within the nasal cavity, particles can be removed within 15 minutes due to faster ciliary movement and is responsible for the removal of 90% of particles greater than 10  $\mu\text{m}$  inspired from this section (Kumar, 2002). This is in contrast to the relatively slower acting cilia of the bronchi where clearance can take up to an hour and delays of several days if particles are deposited further down within the respiratory bronchioles (Byron and Patton, 1994).

### **1.1.2 Asthma**

Asthma is a common respiratory condition associated with broncho-constriction and airway inflammation for which an estimated 5.4 million people in the UK are receiving treatment (Murphy, 2010). In most instances, underlying pathophysiology of this disease is mediated in part, by immunoglobulin E (IgE) dependent mechanisms. These antibodies are produced in response to allergens such as pollen, dust mite or dander, inspired through the respiratory tract and cause sensitisation and produce allergen-specific IgE, increasing serum concentrations. Upon re-exposure, the binding of these triggers to IgE molecules results in the release of inflammatory mediators such as histamine, prostaglandins and leukotrienes from mast cells in a process known as degranulation (Tattersfield et al., 2002). These mediators cause the contraction of the smooth muscles of the airways and result in bronchospasm and patient wheezing, characteristic with the early (acute) phase of an asthma attack.

If left untreated at this stage, degranulation of mast cells result in the local infiltration of further inflammatory molecules including eosinophils, T-lymphocytes and additional mast cells. Release of cytokines by these lymphocytes recruit further pro-inflammatory cells while an increase of goblet cells produce mucus plugs that restrict airflow. This late phase response results in increased basal airway tone and airway responsiveness, causing hyper-responsiveness associated with airway obstruction and sputum production (Murphy, 2010). If this condition is uncontrolled or poorly treated, chronic inflammation of the airway produces permanent structural changes to the airways, termed airway remodelling. Changes include subepithelial fibrosis (basement membrane thickening), airway smooth muscle hypertrophy and

hyperplasia, angiogenesis and increased mucus secretory cells (goblet-cell hyperplasia and submucosal-gland hyperplasia) (Barnes, 2004a).

### **1.1.3 Chronic Obstructive Pulmonary Disease (COPD)**

For patients with COPD, airway restriction is usually progressive and not fully reversible. This umbrella term encompasses a range of different respiratory conditions with unique pathophysiology, including emphysema and chronic bronchitis, which in most cases is attributed to inhalation of noxious gases and particles (Ohri and Steiner, 2004).

In chronic bronchitis, mucus hyper-secretion, often characteristic of cigarette smoking, promotes the activation of macrophages that secrete inflammatory proteins and mediators that attract inflammatory cells. Destruction of the alveolar regions follows whilst reactive oxygen species (ROS) found in cigarette smoke, alongside nitric oxide and peroxynitrate cause damage to host cells suppressing immuno-response and further reinforce pro-inflammatory responses (Hansel and Barnes, 2009). This is also thought to contribute to the resistance of steroid therapy in COPD (Barnes, 2004b).

In addition to the progressive worsening of respiratory symptoms, COPD is associated with increased susceptibility to infections, disability and premature death (Murphy, 2010). Successful management of this disease is therefore, crucial in minimising and controlling the debilitating nature of this illness (Barnes, 2008).

### **1.1.4 Differentiation Between Asthma and COPD**

Though there are many overlapping physiological features shared between asthma and COPD, a different response to treatment requires correct diagnosis for appropriate pharmacological management of each disease. A marked difference between the inflammatory mediators and pathways responsible for each disease state (Barnes, 2004b) requires the delivery of medicament to specific areas of the respiratory tract. For asthma, inflammation is located to a greater extent in the large conducting airways, while in COPD inflammation is

observed in the peripheral regions of the lung and the smaller conducting airways.

### **1.1.5 Inhaled Pharmacological Treatment of Asthma and COPD**

Given the differences between asthma and COPD, the goals of asthma treatment are driven by the need to suppress chronic inflammation, whereas the drivers for COPD treatment are the reduction in symptoms (Buist, 2003). The first line of treatment in both cases is to promote airway dilation and reduce airway inflammation. Current British Thoracic Society (BTS) guidelines on asthma treatment and National Institute for Health and Clinical Excellence (NICE) indicate first-line treatment with bronchodilators (short and long acting) and anti-inflammatory therapy, following which a stepwise approach is taken.

#### **1.1.5.1 Bronchodilators**

Often termed *reliever medicines*, short-acting beta<sub>2</sub> agonists (SABAs) are used to acutely treat the symptoms of asthma or can be administered just before exercise. These agents act on the β<sub>2</sub> adrenoceptors found on the smooth muscles of the airways causing relaxation and bronchodilation. SABAs such as salbutamol and terbutaline, have an onset of action within five minutes and a peak effect within four to six hours (Buist, 2003).

Bronchodilators also include long-acting beta<sub>2</sub> agonists (LABAs) such as salmeterol xinafoate (SX) and formoterol fumarate dihydrate (FFD) are indicated for the chronic treatment of moderate asthma and COPD. Similarly to SABAs, these drugs have a rapid onset of action (between five to twenty minutes) and their effects can last for more than twelve hours. LABAs however, should only be used in combination with an appropriate inhaled corticosteroid (ICS) and discontinued in the absence of benefit due to LABA associated deaths in a small group of individuals (Nelson et al., 2006).

Anticholinergic agents, such as ipratropium bromide (IB) and tiotropium bromide (TIO) also produce bronchodilation. These act by blocking vagal nerve stimulation on bronchial smooth muscles as a result of blocking muscarinic

cholinergic receptors (Brown et al., 1984). These drugs are less effective as reliever medicines in asthma and not recommended for the long-term management of this disease. In contrast, both drugs are indicated for the treatment of COPD with the newer and longer acting TIO having once daily dosing, compared to the shorter-acting IB (Vincken et al., 2002).

#### **1.1.5.2 Anti-Inflammatory Drugs**

Inhaled corticosteroids (ICSs) such as the glucocorticoids budesonide (BUD), fluticasone propionate (FP) and mometasone furoate are the most effective drugs used in controlling persistent asthma in adults and children (Murphy, 2010) and additionally offer mainstay therapy for COPD patients. Increase in airway calibre is achieved by modifying airway inflammation response through a wide variety of pathways including the suppression of circulating cytokines and spasmogens known to cause inflammation (Rang, 2003). The full effect of ICS therapy is achieved after several days of therapy (Rang, 2003) (Neal, 2002) and when discontinued, deterioration of clinical control follows within weeks to months of most patients (Murphy, 2010). For patients with COPD, especially current or recent smokers, the full benefit of ICS treatment is less likely to be seen. Recently, it has been proposed that failure to suppress inflammation by ICS therapy in these patients may be related to decreased histone deacetylase 2 (HDAC2) expression in the peripheral regions of their lungs (Barnes, 2008).

#### **1.1.5.3 Combined Inhaled Therapy**

A wide range of inflammatory mediators are involved in the persistence of asthma and COPD. Clinical studies identifying the benefits of multi-drug therapy in chronic respiratory disease have influenced current treatment guidelines and established best practice in this area.

The addition of a LABA to ICS therapy has been shown to achieve better asthma control than ICS therapy alone (Matz et al., 2001) and has been demonstrated with the combination of SX and FP (Nelson et al., 2003). For patients with severe COPD, the combination of BUD and FFD has shown to improve exacerbation rates when compared to  $\beta_2$ -agonists alone (Szafranski et

al., 2003) and improved 3-year survival rates for COPD patients receiving a combination of FP and SX (Calverley et al., 2003).

Inhaled formulations containing ICS and LABA are available including the combination of FP with SX in *Advair*® (USA) and *Seretide*® (Europe) marketed by GlaxoSmithKline and BUD combined with FFD in *Symbicort*®, marketed by AstraZeneca.

## **1.2 Pulmonary Drug Delivery**

The delivery of medication via the inhaled route enables the direct access to drug targets for the treatment of patients with asthma and COPD, avoiding degradation within the gastrointestinal tract or first-pass effects (Byron and Patton, 1994). Moreover, the reduced dose required, when compared to oral administration, minimise side effects and provides rapid and predictable onset of action (Timsina et al., 1994a). Since the pulmonary epithelium provides a large surface area for deposition and slow mucociliary clearance, pulmonary delivery of therapeutic agents by inhalation has become established as the preferred method of treatment for respiratory conditions.

### **1.2.1 Particle Deposition in the Lungs**

For a therapeutic effect to take place, inhaled drug particles must deposit on the site of action (Byron and Patton, 1994). Depending on the condition being treated, the target area will vary (Brain, 1985). Understanding the mechanisms in which particles deposit from air streams and the relationship between these properties and the physiological considerations of the lung, help determine the requirements for successful pulmonary drug delivery. While control of aerodynamic particle size is crucial, deposition by inertial impaction, sedimentation and diffusion (shown with reference to airway generation in Figure 1.2) highly influence lung deposition (Loalor, 1996) (Zeng, 2001). Additional mechanisms that contribute to the complex nature of respiratory drug

delivery include interception and electrostatic precipitation. These are all described below.

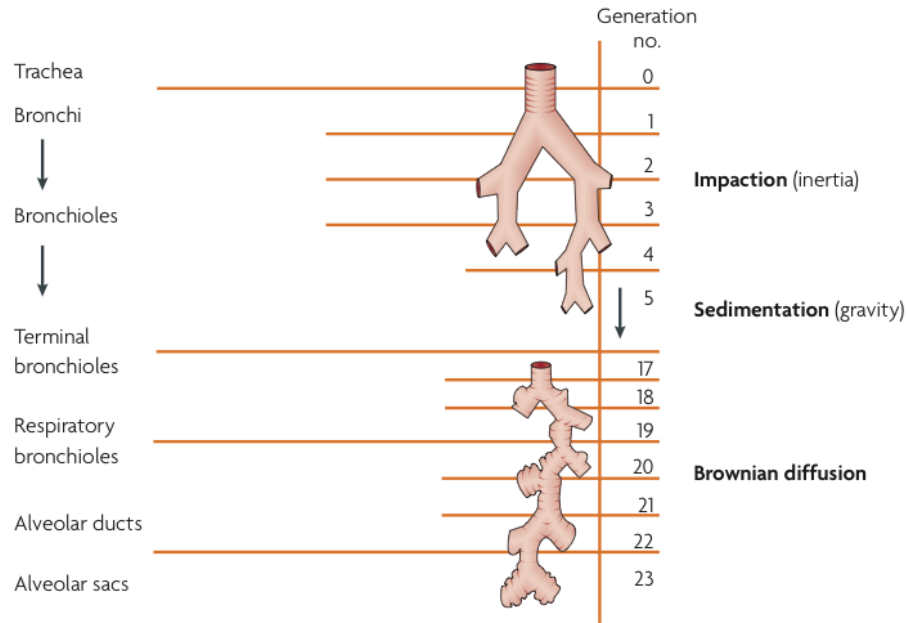


**Figure 1.2 The deposition profile of inhaled particles as a function of airway generation (Reproduced from Patton and Byron, 2007)**

### 1.2.2 Inertial Impaction

The principle mode of deposition for larger particles in the upper airways of the lungs relies on inertial impaction (Hinds, 1982). For particles entrained in an air stream, inability to respond to the rapid changes in airflow directions associated with the bifurcations of the respiratory airways leads to impaction of the particle on to the respirable surface. This form of deposition is dependent on physical attributes of the suspended particle, notably size and density which is mathematically described by Stokes' number ( $Stk$ ), a dimensionless parameter relating to the probability of impaction and defined by the following equation:

$$Stk = \frac{\rho_p d^2 V}{18\eta R}$$

**Equation 1.1**

where  $\rho_p$  is the particle density,  $d$  is the particle diameter,  $V$  is the air velocity,  $\eta$  is the air viscosity and  $R$  is the airway radius. The greater a particle's Stokes' number, the more likely it is to deposit by impaction (Crowder et al., 2002).



Increased density, particle diameter and air velocity will result in a greater impaction rate while reduced airway radius will also contribute to impaction.

### 1.2.3 Sedimentation

Sedimentation of particles within the respiratory tract occurs as a function of gravitational forces exerted on suspended particles (Brain, 1985). Stokes' Law describes the terminal velocity ( $V_t$ ) at which particles between 1 and 40  $\mu\text{m}$  settle from a laminar airstream:

$$V_t = \frac{(\rho_p - \rho_a)d^2g}{18\eta}$$

Equation 1.2

where  $\rho_a$  is the density of air and  $g$  is the acceleration due to gravity. This process is also time dependent, since particles must be given sufficient residence time and therefore, dominates in the smaller airways of the lungs and alveoli where lower airflow velocities are found (Patton and Byron, 2007).

### 1.2.4 Brownian Diffusion

For particles of diameter less than 1  $\mu\text{m}$ , the effect of gravity decreases and the influence of Brownian motion caused by the random bombardment of gas particles increases (Brain, 1985). Since the efficiency of this process is influenced by residence time, the diffusion and displacement of sub-micron sized particles can be greatly increased by breath-holding techniques when administering these materials to patients (Zeng, 2001).

### 1.2.5 Interception

If a particle is elongated, the centre of gravity may be some distance from one of the distal ends (Crowder et al., 2002). Interception is classed when a collision between an exposed area of a particle and an obstacle occurs, while that given particle maintains the centre of gravity within the air stream. It is most notable

for longer, needle shaped particles in the smaller airways and alveoli (Johnson, 1994).

### **1.2.6 Electrostatic Precipitation**

For particles that enter the airways charged, they may influence deposition by altering or inducing polarity to the airway walls. Though significance of this form of particle deposition is yet to be fully understood, ongoing research in this field has received interest (Young et al., 2007b) (Hickey et al., 2007b).

## **1.3 Respiratory Drug Delivery Devices**

There are three main inhaler devices readily available for patient use in the pulmonary drug delivery market. These are nebulisers, pressurised metered dose inhalers (pMDIs) and dry powder inhalers (DPIs) (Daniher and Zhu, 2008) (Chow et al., 2007). All three can be used for the treatment of respiratory disorders such as asthma and COPD.

### **1.3.1 Nebulisers**

Nebulisers generate an aerosol by converting aqueous solutions or aqueous suspensions into a respirable cloud through the use of compressed air or piezoelectric transducer (Mitchell and Nagel, 1997). Patients do not require the coordination between device and breathing to obtain therapeutic doses making nebulising systems suitable for all ages (Loffert et al., 1994). Limitations from these devices arise from the prolonged duration of administration, high operating costs and restricted portability of devices (Garcia-Contreras and Hickey, 2003). Though some of these restrictions are being overcome through newer technological developments, nebulisers are often reserved for geriatric, paediatric and hospitalised patients and administration of new chemical entities (NCE) in animal and man (Dalby and Suman, 2003).

### **1.3.2 Pressurised Metered Dose Inhalers (pMDIs)**

The first pressurised metered dose inhalers (pMDIs) appeared in the pharmaceutical drug delivery market in 1956 and has been established as the most prescribed inhaler device worldwide (Virchow et al., 2008). In comparison to other delivery modes, pMDIs are cheap, portable and easy to use for most patients (Mitchell and Nagel, 1997).

These devices consist of an API in solution or suspended fine particles within a liquefied gas propellant, sealed into a canister. Connected to the canister is a metering valve which when actuated, releases a metered volume of solution or suspension through a narrow orifice, driven by high vapour pressures of the propellant, resulting in the emergence of a high velocity plume (Mitchell and Nagel, 1997). This process of liquid atomisation, combined with the evaporation of propellant, results in the creation of an aerosol of drug particles suitable for respiration and deposition within the respiratory tract.

Traditional propellants in pMDIs were chlorofluorocarbon (CFC), though implementation of the 1987 Montreal Protocols phased out these ozone-depleting gases for more environmentally friendly products. Hydrofluoroalkanes (HFAs) were selected by the pharmaceutical industry to serve this purpose, however complexities in reformulation and long term issues related to the future of HFA-based propellants have in part, restricted the development of these formulations (Atkins, 2006). Moreover, addition of formulation excipients such as surfactants and co-solvents that improve solubility or reduce particle aggregation, increase the complexity of the resulting formulations (Traini et al., 2007).

Despite pMDIs being the most popular form of prescribed inhaled product, limitations on the efficacy of these devices are routinely attributed to poor or improper inhaler technique (Dalby and Suman, 2003) (Virchow et al., 2008). Coordination of actuation and patient inspiration, due to the high velocity of the emitted plume, often limits the efficiency of these devices and though spacer/chamber devices have been used to prevent these issues, pMDIs often

deliver less than one third of the emitted dose to lungs in the most trained of patients (Virchow et al., 2008).

### **1.3.3 Dry Powder Inhalers (DPIs)**

The inconveniences associated with nebuliser use and the concerns related to pMDI drug delivery have spurred increasing interest in dry powder systems for inhalation (Son and McConville, 2008). Dry powder inhalers (DPIs) allow a metered dose of drug to be delivered to the airways as a dry powder aerosol without the need of propellant (Timsina et al., 1994a). Since the generation of a respirable aerosol is produced from a patient's inspiration from DPIs, there is no longer an issue of coordination with the device (Hickey, 2004). Moreover, the slower velocities of the particles emitted from the device, compared to pMDI delivery, potentially avoids the excessive drug losses due to throat and upper airway impaction (Pauwels et al., 1997).

Drug particles employed in DPI formulations have a mass median aerodynamic diameter (MMAD) less than 5  $\mu\text{m}$  which enable deposition within the lung (Timsina et al., 1994a) (Prime et al., 1997) (Daniher and Zhu, 2008). To achieve this size, APIs formulated for DPI delivery are often comminuted by energy intensive processes such as air jet milling (Islam and Gladki, 2008) though other particle engineering techniques such as spray drying and supercritical fluid technologies exist (Telko and Hickey, 2005) (Chow et al., 2007). These respirable sized particles are intrinsically cohesive as a result of large surface areas and high surface energy, leading to particle aggregation, poor flow and entrainment complexities (Feeley et al., 1998).

Metering and aerosolisation of respirable materials is therefore, a difficult process and is commonly overcome by blending these fine respirable particles with a larger, coarser inert excipient, notably lactose monohydrate (Bell et al., 1971). This excipient, known traditionally as the carrier, has a particle size range of between 20 – 200  $\mu\text{m}$  and is blended with the API to produce an ordered mixture (Ganderton, 1992) (Telko and Hickey, 2005). As a patient inspires, turbulent airflow generated within a device disperses and fluidises the formulation with sufficient force to deaggregate the drug particles from the

carrier particles (Malcolmson and Embleton, 1998) (Shur et al., 2008). These drug particles are then entrained within the inspired airstream and delivered to the lungs while the carrier particles are deposited within the oropharyngeal regions of the patient. The integration of turbulent airflow within a DPI device leads to inhaler resistance that will therefore require a patient to provide greater inspiratory force to achieve a desired air flow (Islam and Gladki, 2008). Consequentially, a balance between device resistance and optimum flow rates for drug delivery needs to be engineered within a device (Timsina et al., 1994a).

There are three different types of DPI available on the market; single dose, multidose and reservoir based inhalers (Prime et al., 1997) (Islam and Gladki, 2008) (Daniher and Zhu, 2008). Illustrations of these approaches are shown in Figure 1.3. The early devices approved by regulatory bodies employed the delivery of medicament through individually metered hard gelatin capsules that required individual loading and triggering from the inhaler device (Prime et al., 1997) (Dalby and Suman, 2003). Examples of which include the Spinhaler® and Rotahaler®, and even though these have been superseded by multi-dose and reservoir DPIs, both have gained increasing popularity in emerging economies due to robustness, ease of use and access to individual unit doses (Bhome, 2009).

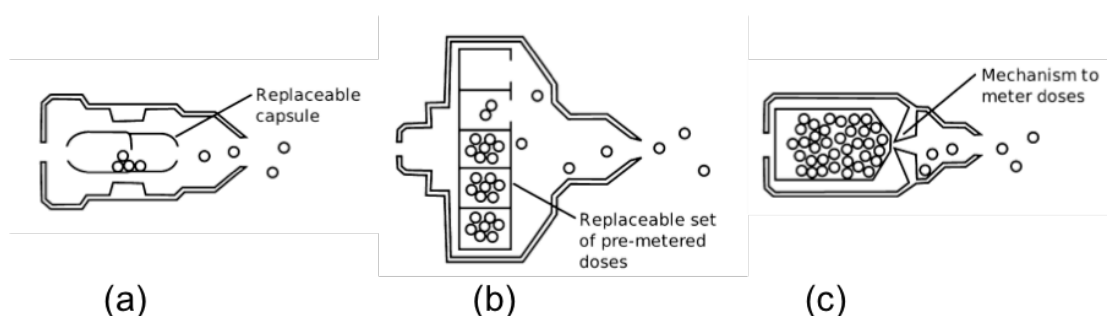


**Figure 1.3 The three different types of unit dosing mechanisms employed in commonly used DPI devices; a – single unit-dose, b – multiple unit-dose, c – reservoir metered (Adapted from Daniher and Zhu, 2008)**

Pre-metered multidose inhalers include the successful GlaxoSmithKline Diskhaler® and Discus® devices. In the former, a pre-metered drug formulation is contained within a foil blister on a circular disk containing four or eight blisters. The device requires the patient to pierce through a foil blister, with an

in-built punch, prior to actuation. Upon forced inspiration, the contained formulation is dispersed within that airstream and a fraction of the active ingredient contained in the inspired formulation is delivered to the lungs. Re-priming of the device allows for rotation of the blister disk, exposing the piercing punch to the next blister (Newman and Busse, 2002). The Discus® (Accuhaler®) utilises a foil strip upon which formulation containing blisters are pre-filled. These devices follow the same principles of the Diskhaler® but due to the sophisticated coiling and blistering techniques employed, they contain 60 individual doses within each device (Newman and Busse, 2002), improving the practical implications of using the inhaler.

Reservoir DPIs dispense a single dose from a bulk reservoir contained within the device via an in-built metering chamber. The first device containing this mechanism was the Turbuhaler® (AstraZeneca), which employs a rotating base with a number of cavities of defined dimensions, permitting unit dosing of the formulation. Since the entire bulk is exposed to some extent to the surrounding atmosphere, a desiccant is required to maintain a dry powder throughout the shelf-life of the product (Prime et al., 1997). To achieve high powder dispersion efficiencies, the Turbuhaler® device relies on high resistance and helical airstreams to create the necessary turbulent airflow for particle delivery. More recent reservoir inhalers such as the Easyhaler® (Ranbaxy Ltd., UK) and Clickhaler® (Vectura Plc., UK) improve fine particle delivery by the use of changing airflow paths and by impaction plates, respectively (Son and McConville, 2008).

It is well documented that for DPIs delivery efficiency is largely governed by the inspirational profile of the recipient patient (Timsina et al., 1994a) (Islam and Gladki, 2008). DPIs, therefore, must provide adequate internal resistance in order to deaggregate and fluidise the formulation, while considering the limitations and variability of inspiratory force a patient with respiratory conditions can achieve when using the device (Malcolmson and Embleton, 1998).

### **1.3.4 Summary of the Various Drug Delivery Options to the Lungs**

A brief overview on current forms of respiratory drug delivery has been described above. Though each form has significant advantages and disadvantages in the treatment of respiratory conditions, the delivery of therapeutic agents through a simple device that is independent to patient coordination or inspiration profiles appears to be the most favourable mechanism (Islam and Gladki, 2008). Developments within the DPI field in terms of device design and investigations into dry powder formulation strategies demonstrate the focus on optimising existing DPIs. Moreover, the exploration of novel approaches to this area demonstrates the relative merits of further investigation within this field. The rest of this chapter will concentrate on the pharmaceutical considerations of DPI formulations. Emphasis is placed on the crystallisation process, as the first process over which pharmaceutical formulators have any control. Consequently, this work will highlight how the crystallisation process may lead to materials that define future processability and functionality.

## **1.4 Pharmaceutical Considerations in the Formulation of DPI Powders**

As discussed, DPI devices rely on the delivery of a unit dose of medication to a patient in one of three ways; single unit-dose, multiple unit-dose or reservoir metered dose. Traditional techniques in producing these formulations rely on blending the active pharmaceutical ingredients with an inert carrier, though other sophisticated formulation approaches are under investigation within the pharmaceutical industry.

As shown in Figure 1.4, the production of most DPI formulations relies on a number of unit operations in order to produce a DPI formulation suitable for patient use. Key to this process is the isolation of active ingredients by the process of crystallisation whereby large crystals are produced and subsequently milled, following a 'top-down' approach in order to produce fine particle with a median geometric diameter between 1 - 5  $\mu\text{m}$  (Telko and Hickey,

2005). Blending of these particles with large carrier particles improves handling, dosing and fluidisation (Malcolmson and Embleton, 1998), yet the strong interparticulate forces between the active ingredients and carrier particles results in typical delivery efficiencies of only 10-30% (Timsina et al., 1994a). The balance of attractive and cohesive forces experienced between these formulation components therefore, greatly influences the entrainment and deposition profile of the active ingredients within DPI formulations (Begat et al., 2004c) (Jones et al., 2008) in addition to influencing the blending dynamics (Pilcer and Amighi, 2010). Variability in the process history of these materials, such as changes in the crystallisation or micronisation operations, may consequentially lead to differences in formulation performance. Understanding and controlling the interfacial properties between APIs and excipient carrier particles, enables the formulation of DPI drug products of defined quality and functionality (Edge et al., 2008). Moreover, integration of appropriate analytical processes during the formulation process could reduce the reliance of QC and QA evaluation in the validation of DPI formulations. This section aims to introduce the concepts and complexity behind powder blending, the forces experienced between particles in the powder bulk and the issues resulting from micronised materials, in relation to DPI formulations.



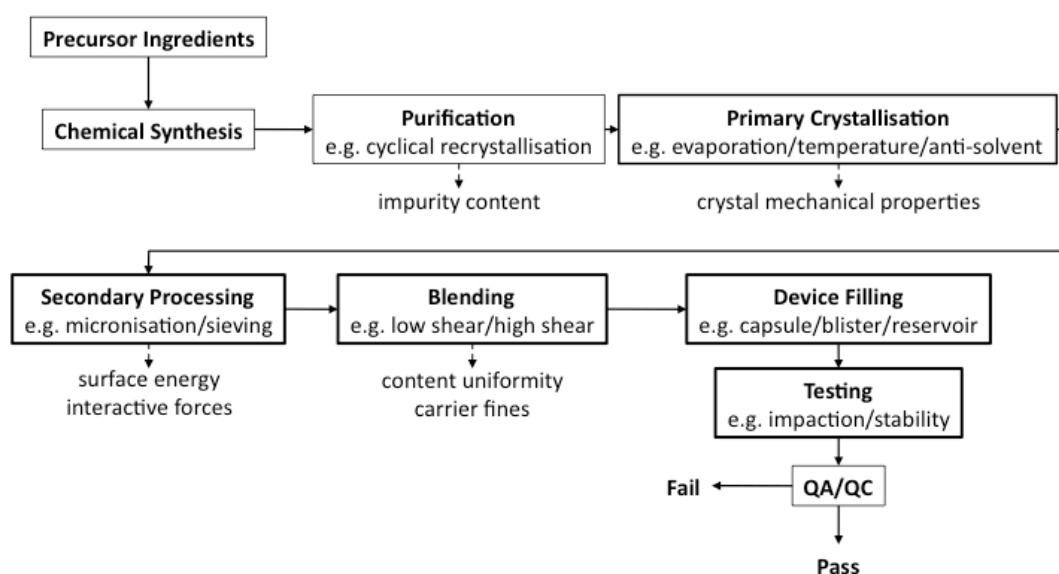


**Figure 1.4** An overview of the various steps required in producing a formulated dry-powder inhalation device and the possible implications of each process

### **1.4.1 Types of DPI formulations**

Carrier free formulations could comprise of engineered particles specifically produced for respirable drug delivery, which can be produced using techniques such as spray drying (Steckel and Brandes, 2004), supercritical fluid processing (Schiavone et al., 2004) and ultrasonically assisted crystallisation (Dhumal et al., 2009). The use of pelletised drug only formulations in AstraZeneca's Turbuhaler® comprise of softly aggregated particles which are then deaggregated in a turbulent airflow, highlighting the balance between device resistance and the tailoring of the interparticle forces of the formulation.

In addition to drug only formulations, modifications of the forces between drug particles by the addition of an additive has been successfully shown to change the flow and aerosolisation behaviour of micron-sized particles. Coating of particles by mechanical means (Yokoyama et al., 1987) (Begat et al., 2008) or by the spray-drying a mixture of drug and additive (Seville et al., 2007) are two common examples. Modification of the interparticle forces, by the use of force-controlling agents, has been proven to improve aerosolisation and formulation performance (Begat et al., 2008). Coatings such as magnesium stearate, which is commonly used as a die and punch lubricant in solid oral dosage forms, has been a subject of much interest within the inhalation field as a way of significantly improving the behaviour of DPI formulations and their aerosolisation efficiency (Beilmann et al., 2007) (Jones et al., 2008) (Shur et al., 2008).

The use of carrier based formulations remain the most popular method for DPI formulation preparation, where the forces generated within a device from a patient's forced inspiration may detach fine drug particles from coarse carriers (Telko and Hickey, 2005) (Islam and Gladki, 2008). In order to produce a successful formulation, formulators require knowledge relating the mixing properties of multi-component mixtures, the interparticle forces that are involved in this process and the various factors that can modify the resulting performance. The following sections of this chapter aim to explore this area further.

### **1.4.2 Blending**

In order to improve the non-pharmacological attributes of a DPI formulation, a drug carrier is often blended with the active ingredient. This facilitates handling, dosing and metering of the drug (Timsina et al., 1994a) (Telko and Hickey, 2005).

Traditionally, a coarse fraction of lactose monohydrate is introduced to the formulation to act as a bulking agent and mixed with the API. With reference to early work in this field, many formulations include a size fraction of lactose of 63 – 90  $\mu\text{m}$  (Bell et al., 1971). In order to optimise the delivery of these formulations, selection of appropriate carrier attributes such as particle size, shape and surface topography requires a multifaceted approach. These include bulk physical, rheological and chemical characterisation techniques combined with knowledge of blending techniques and delivery device attributes (Jones et al., 2008).

Processing history of the carrier can alter the blending efficiency and performance of DPI formulations (Chow et al., 2007). Milling and sieving of lactose monohydrate has been shown to affect the fine particle fraction of delivered drug and has been in part, attributed to the generation of fine lactose materials in the energy intensive processes altering the carrier surface (Steckel et al., 2006). The influence of fine excipient materials, such as added milled lactose or those intrinsically produced, has also been shown to modify the performance of DPI formulations (Zeng et al., 2001) (Shur et al., 2008).

Successful blending of two or more components requires the use of blending equipment to produce an ordered, homogenous mixture. The use of mixing equipment such as co-shifting, convective turbula mixing and high sheer blending can however, lead to changes in bulk powder properties and has been investigated in the context of DPI performance (Dickhoff et al., 2005) (Bridson et al., 2007) (Shur et al., 2008). Predicting the required energy input to create ordered blends and the effect of these processes on the functionality of the resulting blends is however, poorly understood.

### 1.4.3 Interparticulate Forces

The long-range interparticulate interactions experienced between particles of binding energies less than  $40 \text{ kJ.mol}^{-1}$  are considerably weaker than shorter-range interactions, such as ionic and covalent bonding (Johnson, 1996). These forces can either be cohesive, between particles of the same chemical structure, or adhesive, between particles and materials of different physical and chemical properties (Johnson et al., 1971). As the size of particles becomes smaller, the effect of gravity on these materials becomes increasingly negligible, especially for particles of size less than  $10 \text{ }\mu\text{m}$  (Deryaguin et al., 1978)

Interactions between particles, such as those found in DPI formulations, are produced from a range of different mechanisms and forces and are therefore, important to understand and characterise. These include van der Waals, capillary and electrostatic interactions (Johnson et al., 1971) (Young et al., 2003). Furthermore environmental conditions (temperature and relative humidity) and particle morphology may directly influence these particle interactions and resulting forces (Fuller and Tabor, 1975) (Zeng, 2001) (Hooton et al., 2004).

#### 1.4.3.1 Lifshitz - van der Waals Interactions

The Lifshitz – van der Waals interactive forces are composed of three separate interactive forces known as Debye-induction force, Keesom-orientation force and dispersion force (Lifshitz, 1955). These forces arise from the formation of dipole moments in surrounding electron clouds as particles become close. Debye-induction forces relate to the interaction forces between permanent and induced dipoles, while Keesom orientation forces represent the forces between two permanent dipoles (Lifshitz, 1955). Dispersion forces, also termed London dispersion force, result from the interaction between two induced dipoles, and are generally of greater magnitude than induction or orientation forces (Li et al., 2006).

The van der Waals forces ( $F_{VDW}$ ) between two ideally smooth spheres in a vacuum is described by Hamaker (Hamaker, 1937) :

$$F_{VDW} = \frac{H}{12s^2} \left( \frac{d_1 d_2}{d_1 + d_2} \right)$$

**Equation 1.3**

where  $H$  is the Hamaker constant (Equation 1.4),  $s$  is the separation distance between the spheres and  $d_1$  and  $d_2$  are the diameters of the two spheres. The Hamaker constant is given by:

$$H = \pi^2 v_1 v_2 \lambda_{1,2}^d$$

**Equation 1.4**

where  $v_1$  and  $v_2$  are the number of atoms per unit volumes of particle 1 and 2 and  $\lambda_{1,2}^d$  is the constant of dispersion:

$$\lambda_{1,2}^d = -\frac{3}{4} h F a^2$$

**Equation 1.5**

where  $h$  is Planck's constant,  $F$  is the vibration frequency of the interacting electronic oscillators and  $a$  is the polarisability of the molecules.

The adhesive force between a sphere (diameter  $d_1$ ) and a plane composed of the same material and separated by distance  $s$  is described by:

$$F_{VDW} = \frac{H_{11} d_1}{6s^2}$$

**Equation 1.6**

whereas the adhesion between a sphere (diameter  $d_1$ ) and a plane composed of different materials and separated by distance  $s$  is expressed by:

$$F_{VDW} = \frac{\sqrt{H_{11}H_{22}}}{6s^2} d_1$$

**Equation 1.7**

where  $H_{11}$  and  $H_{22}$  are the Hamaker constant for the particle and the plane surface, respectively.

From the equations above the importance of the bulk separation distance,  $s$ , for interacting bodies is critical in determining the van der Waals forces between two solid objects. The short-acting van der Waals forces retards rapidly as separation distance is increased. Therefore, van der Waals forces exert their influence only over a range of approximately 10 nm (Hamaker, 1937).

#### **1.4.3.2 Capillary Forces**

The attractive force related to the environmental effect of moisture on powders is termed capillary force and is related to the physico-chemical properties of the contacting materials (Hiestand, 1966). Capillary forces arise from the partial water vapour pressure in the atmosphere, which may condense into the spaces between contiguous surfaces forming a meniscus at the point of contact (Fuller and Tabor, 1975). Its influence is related to the material properties such as gap geometry, surface free energy, wettability and surface roughness (Fuller and Tabor, 1975) and can have detrimental effects on powder flow and fluidisation (Hiestand, 1966) (Bérard et al., 2002) (Son and McConville, 2008).

The magnitude of this capillary force ( $F_c$ ) between two identical smooth spheres (radius  $r$ ) can be calculated as:

$$F_c = 2\pi\gamma_w r \cos \alpha$$

**Equation 1.8**

where  $\gamma_w$  is a surface tension of water and  $\alpha$  is a contact angle between water and the spheres. For a sphere (radius  $r$ ) adhering to a surface, the capillary

force resulting from the condensation of water between this interface can be calculated as:

$$F_c = 2\pi\gamma_w r(\cos \alpha + \cos \beta)$$

**Equation 1.9**

where  $\alpha$  and  $\beta$  are the contact angles of the water with the surface and particle, respectively.

For particles of the respirable size, control over the environmental relative humidity (RH) is therefore, essential throughout the formulation and storage period. As the RH exceeds 50%, it becomes the dominating force over other adhesional forces (Hiestand, 1966) and is known to effect particle interactions within DPI formulations (Bérard et al., 2002) (Zeng et al., 2007) (Young et al., 2007b) introducing performance variability within the end drug-product.

#### **1.4.3.3 Electrostatic Forces**

Electrostatic forces are exemplified in daily life by dust attracted to various surfaces. During powder handling, particles can be charged by contact or friction with other particles or surfaces. This is termed triboelectrification (Staniforth and Rees, 1982) (Hickey et al., 2007b).

When two charged particles are brought to close proximity, they will experience a net attractive or repulsive force, related to the charged state of each particle. This force can be described by Coulomb's law:

$$F_{EL} = \frac{q_1 q_2}{4\pi\epsilon s^2}$$

**Equation 1.10**

where  $F_{EL}$  is the electrostatic force,  $q_1$  and  $q_2$  are the electrical charges on the two particles,  $\epsilon$  is the permittivity and  $s$  is the separation distance between the particles.

An uncharged particle may become charged if an image charge is induced upon it by the approach of a charged particle (Onsager and Samaras, 1934). The resultant electrostatic force may be shown by:

$$F_{EL} = \frac{q^2 \left( 1 - \frac{2}{\sqrt{r^2 + s^2}} \right)}{16\pi\epsilon s^2}$$

**Equation 1.11**

where  $s$  the separation distance between charged and uncharged particles. This equation may be modified to describe the adhesion of a charged particle to a flat, earthed conducting surface via the formation of an image charge by making the assumption that  $r \rightarrow \infty$ :

$$F_{EL} = \frac{q^2}{16\pi\epsilon s^2}$$

**Equation 1.12**

Contact between two uncharged particles with different work functions will appear in the flow of electrons from the particle with the lower work function to the particle with the higher work function until an equilibrium is established (Tabor, 1976). The resultant force of attraction ( $F_w$ ) can be described as:

$$F_w = \pi\epsilon r \frac{(\Delta U)^2}{s}$$

**Equation 1.13**

where  $r$  is the radius of the particles and  $\Delta U$  is the potential difference arising from the difference in work functions.

These equations suggest that electrostatic forces are firstly dependent on the electrical properties of the particles involved and secondly, separation distance between these particles (Tabor, 1976). This leads to the dominance of van der



Waals forces, which are subsequently responsible to a greater extent, for the strength of the adhesional force, especially if the influence of electrostatic forces and capillary forces are low (Johnson, 1996).

#### **1.4.4 Factors Influencing the Degree of Interparticulate Forces**

In addition to the composite of interparticle forces outlined above, the physical nature of individual particles, the surfaces and surrounding environment they are exposed to can influence the magnitude of forces experienced. The most important of these factors are outlined below.

##### **1.4.4.1 Surface Free Energy**

For solid materials, the surface free energy represents the total energy from a solid surface in equivalence to the surface tension of a liquid (Johnson et al., 1971) (Planinsek et al., 2001). However, unlike liquids, the molecules of a solid are unable to move, leading to an inhomogeneous distribution of energy over the solid surface. The levels and distribution of these energy changes are dependent in part, on the history of the material (Johnson, 1998) (Young et al., 2007a). The quantity of work required to separate two surfaces is called the work of adhesion ( $W_a$ ) and is related to the surface free energy of the surfaces by the following equation:

$$W_a = A_s(\gamma^C + \gamma^D - \gamma^{CD})$$

**Equation 1.14**

where  $A_s$  is the area of surface produced by the separation,  $\gamma^C$  and  $\gamma^D$  are the free energies per unit surface area of solids C and D in air, respectively; and  $\gamma^{CD}$  is the free energy of the C-D interface per unit area. In addition, according to the geometric mean equation, the interfacial free energy between any two surfaces C and D can be expressed in its dispersion and polar components by:

$$\gamma_{CD} = \gamma_C + \gamma_D - 2(\gamma_C^{LW} \cdot \gamma_D^{LW})^{1/2} - 2(\gamma_C^p \cdot \gamma_D^p)^{1/2}$$

**Equation 1.15**

where  $\gamma_C^p$  and  $\gamma_D^p$  are the polar contributions to the surface energy for solid C and D, respectively. Therefore, the work of cohesion ( $W_c$ ) (i.e. the work required to separate two surface of the same material) is shown by:

$$W_c = 2A_s \gamma^C$$

**Equation 1.16**

As the above demonstrates, the thermodynamic work of adhesion and cohesion is directly related to the force of adhesion and cohesion. These two forces are therefore, dependent on the surface free energies of the interacting particles (Johnson et al., 1971).

In order to investigate the work of adhesion between two particles, continuum contact mechanics are employed to model the interactive forces occurring as the result of two spheres coming into contact, in the absence of significant electrostatic force. Two models derived from Hertzian mechanics (Hertz, 1881) are used in this instance, the Johnson-Kendall-Roberts model (JKR) (Johnson et al., 1971) and the Deriaguin-Müller-Toporov model (DMT) (Derjaguin et al., 1975), shown below in Equation 1.17:

$$F_{adh} = n\pi R^* W_a$$

**Equation 1.17**

Where  $F_{adh}$  is the force of adhesion,  $n$  is a predetermined constant related to the model in use (3/2 for JKR and 2 for DMT),  $R^*$  is the harmonic mean of the particle radii (contact radius) and  $W_a$  is the thermodynamic work of adhesion. The JKR model investigates the surface forces occurring within the contact region, while DMT theory models the effect of attractive forces outside the contact region. The choice of model used when investigating these forces is

dependent on the system being measured, the DMT model is found to be appropriate for small particles of low adhesion and the JKR model is suitable for larger radii particles of greater compliance (elasticity) and higher adhesional forces (Cappella and Dietler, 1999). These models are often used during colloidal probe based techniques, where the interactive forces between particles and substrate surfaces are used to quantify the adhesional forces experienced between particles and substrate surfaces. These measured pull-off forces are then used to derive the thermodynamic adhesive forces and are discussed in greater detail later in this section.

#### **1.4.4.2 Mechanical Interlocking**

The irregular nature of secondary processed drug particles for inhalation allows for greater propensity to the interlocking of particles through direct contact of asperities and microscopically rough surface topographies (Adolfsson et al., 1997). If the direct contact between two particles is over a small surface area, it can in some instances, result in the increasing yield of the material and in turn increase the mechanical locking and van der Waals interactions (Fuller and Tabor, 1975).

#### **1.4.4.3 Particle Size and Shape**

The van der Waals forces have been shown to be proportional to the particle diameter ( $d$ ), while gravitational forces are proportional to the cube of the diameter ( $d^3$ ). Consequently, as the particle size reduces, the adhesion force experienced becomes more significant (Johnson et al., 1971). For particles of size less than 10  $\mu\text{m}$ , the adhesion force dominates over forces experienced by gravity (Hiestand, 1966).

The effect of particle morphology on the forces experienced between particles can be understood when taking into account the ranges over which these forces exist. Any modification in particle size will have implication on the separation distance of particles and therefore, the electrostatic forces (influenced in the range of 10 nm) and longer ranging van der Waals forces (Johnson et al., 1971). Ability for particles to pack in an ordered manner, for example needle-

like particles, may increase adhesion forces, due to increased contact area between the surfaces (Zeng, 2001). Furthermore, processing these materials can alter packing properties, modifying the interparticle forces and thereby changing powder properties (Steckel et al., 2006).

#### **1.4.4.4 Surface Roughness**

Since the separation distance between particles can affect the adhesion forces, roughness of a particle surface or the substrate it comes into contact with will affect adhesion forces. This is due to the change in contact geometry between the adhering particle and the substrate (Fuller and Tabor, 1975). For a smooth surface, a particle adhering to this surface would have greater contact area and decreased separation distance (Fuller and Tabor, 1975) (Johnson, 1998). In contrast, for the same particle in contact with a surface with a roughness at a smaller scale than that of the particle, the separation distance will increase and contact area decrease, leading to reduced adhesion. If the contact surface has a roughness greater than that of the adhering particle, mechanical interlocking is possible, and contact area is therefore increased, increasing the adhesion force experienced by that particle (Johnson et al., 1971).

#### **1.4.4.5 Particle Deformation**

The mechanical nature of particulate materials will influence the propensity of deformation at the contact site between particles. The attractive forces experienced by particles can cause this deformation and thereby alter the contact area and magnitude of interparticle forces (Li et al., 2006). Within the context of DPI formulations however, these forces are only recognised as significant modifiers of particle re-entrainment following aerosolisation (Johnson, 1998).

#### **1.4.4.6 Relative Humidity**

Two different mechanisms related to relative humidity can influence interparticulate forces. As discussed previously, environmental RH can induce the sorption and condensation of water on the surfaces of particles and the surfaces in which they are in contact. This can cause the formation of liquid

bridges and increased capillary forces (Young et al., 2003). Additionally, the conductivity and dissipation of charge will increase for particles in a humid environment. This is of interest in the field of respiratory drug delivery, since the humidification of the airways can alter the electrostatic nature of the entrained particles (Byron et al., 1997).

#### **1.4.5 The Impact of Particle Size Reduction on the Physico-Chemical Behaviour of APIs**

The production of inhaled formulations for DPIs requires active drug particles of the respirable size. Traditional methods of crystallisation used in the large-scale production of these APIs fail to provide adequate control over particle size and engineer particles suitable for pulmonary delivery (Shekunov and York, 2000). Particle size reduction is therefore, an essential process in producing these materials, as shown in Figure 1.4, upon primary crystallisation process and prior to blending. The resulting particles from this technique are adversely affected by the high-energy input and relatively uncontrolled nature of the process and can lead to detrimental effects in formulating orally inhaled drug products (OIDPs) of defined specification (Steckel et al., 2006).

The comminution process of reducing primary drug crystals to a respirable size can be achieved by a wide variety of techniques. Commonly used processes in DPI production include ball milling, vibration milling and air jet milling (Chow et al., 2007).

Jet milling has emerged as the most popular method of particle size reduction in the context of DPI formulation (Chow et al., 2007), attributed to its simplicity and minimal contamination of processed materials (Katz and Kalman, 2007). These mills produce super and ultra-fine materials by particle impaction and attrition, using a feed gas pass through a venturi and micronisation chamber at supersonic speeds (Brodka-Pfeiffer et al., 2003). Successive collisions between particles and the walls of the micronisation system result in the fracture, chipping and overall loss of size of the feed material, which then loose inertia and pass from the circulating gas into a collecting hopper (Midoux et al., 1999). The most important parameters of these systems which can be controlled are

the feed rate, feed pressure and grinding pressure (Brodka-Pfeiffer et al., 2003) (Katz and Kalman, 2007). The extent of comminution will largely be determined by the particle size and mechanical properties of the input material (Kwan et al., 2004), including pre-existing crystal flaws and material ductility (de Vegt et al., 2008).

Since the number of collision events taking place for each individual particle is uncontrolled, output product characteristics such as shape, morphology, surface properties and electrostatic charge are largely unpredictable (Steckel et al., 2003) (de Vegt et al., 2005). Moreover, the relatively high input energies subjected to the material can induce a loss of crystallinity (Ogura and Sobue, 1970) and lead to chemical and physical changes within the product (Begat et al., 2003) (De Gusseme et al., 2008).

The micronisation process can lead to disordered, metastable regions on the crystal surface, inducing mechanical or surface activation of crystalline materials (Begat et al., 2003) (Brodka-Pfeiffer et al., 2003). These changes have been associated with agglomeration and particle size changes (Ng et al., 2008) and have been shown to lead to changes in the *in vitro* and *in vivo* performance of the formulation (Steckel et al., 2006).

## **1.5 Characterisation of Pharmaceutically Processed Materials**

From the previous sections, it is evident that the processing of active pharmaceutical ingredients and excipients by micronisation or blending can result in changes to the physical and chemical nature of these materials. With reference to Figure 1.4 we can see that the quality control and quality assurance testing is only performed once a product is formulated. After this process, the product is either rejected or accepted against pre-determined parameters (Tougas et al., 2009). To date, *in vitro* cascade impaction testing is the only QC tool used in relating pharmaceutical formulation development, production and batch release (Chow et al., 2007). However, a number of analytical techniques of bulk powders and individual particles aim to relate one

or more properties to the final performance of the DPI formulation and may provide information *a priori* relating the functionality of the final product prior to formulation. This section aims to review some of the commonly employed methods in evaluating the differences found in the crystallinity, interfacial energy and interactive forces of particulate systems in order to relate those findings to DPI performance.

### **1.5.1 Crystallinity**

The stresses placed on crystalline materials during processing can lead to disorders and defects within the crystal lattice and may lead to thermodynamic changes to the crystalline form in addition to stability and performance modifications to formulated products. The use of appropriate analytical methods in detecting these changes is evident in regulatory interest in controlling and defining acceptable limits of these changes throughout the development and manufacturing process (Yu, 2008). This section highlights some of the key analytical approaches in detecting the changes in crystallinity of bulk pharmaceutical samples.

#### **1.5.1.1 Thermal Analysis**

The thermal analysis of materials using techniques such as differential scanning calorimetry (DSC) are most often used as a tool in evaluating a material's response to heat and can be used to accurately quantify enthalpic transitions of small quantities of material (Clas et al., 1999), including those used within DPI formulations. DSC is often used to investigate the physico-chemical changes that result as a function of processing, for example the loss of crystallinity by milling (Wildfong et al., 2006). While studies have aimed to investigate the correlation between measurements of amorphous content via thermal analysis and aerosolisation performance (Velaga et al., 2004), the relative insensitivity in detecting non-crystalline domains of bulk samples lower than 5% (Lappalainen and Karppinen, 2010), limits the use of DSC for the quantification of discrete changes to a material (Saunders et al., 2004).

Isothermal microcalorimetry is another such technique used to investigate formulation components. The continual monitoring of thermal events occurring within a sample held under constant temperature can be used to assess enthalpic transitions with greater sensitivity compared to DSC (Dilworth et al., 2004). A thermal activity monitor was used to perform analysis on salbutamol sulphate samples micronised at different grinding pressures (Brodka-Pfeiffer et al., 2003). The group found that increasing pressures resulted in detection of a greater amount of non-crystallinity and that after 6 bar, increasing the pressure resulted in non-crystalline response, with no change in particle size.

### ***1.5.1.2 Dynamic Vapour Sorption (DVS)***

Highlighted previously in this section, the external environment, namely the relative humidity that a DPI formulation is exposed to, can alter the interparticulate forces within a blend and has previously been shown to affect aerosolisation efficiency of binary formulations (Das et al., 2009). Dynamic vapour sorption enables the accurate measurement of the tendency of solids to take up water vapour from the atmosphere at a constant temperature during changes in relative humidity (RH) (Newman et al., 2008). This uptake of water, termed hygroscopicity, is often investigated during the preformulation process in order to assess physical and chemical stability of materials, including those that have been processed (Newman et al., 2008). The change in mass associated with water sorption can be characteristic of a recrystallisation process for crystalline materials with a degree of disorder, often as a result of processing or the crystallisation process. Dynamic vapour sorption is therefore, often used in the detection of non-crystallinity (amorphous content) within bulk samples and has been shown to resolve levels down to 0.5 % in lactose samples (Steckel et al., 2006). In the context of the DPI formulation process, investigation into lactose blending highlighted differences in moisture uptake of blends directly after processing and after storage (Bridson et al., 2007) indicating that the power input associated with shear blending can result in functional changes to the formulation. Additionally, detection of recrystallisation of salbutamol sulphate after milling revealed process-induced disorder of this API by DVS analysis, indicating that stresses placed onto the material during micronisation



had resulted in measurable disruption to the crystallinity of the subsequent material (Brodka-Pfeiffer et al., 2003).

#### **1.5.1.3 X-Ray Powder Diffraction**

Identification of the crystal structure of APIs produced by different crystallisation process is vital in identification of the physical structure of the crystal lattice. Inclusion of solvates, hydrates or the crystallisation of different polymorphs require detection as these changes can lead to physico-chemical differences in the material (Datta and Grant, 2004). This technique has been shown to identify differences in the diffraction profiles of a non-steroidal anti-inflammatory crystallised using different organic solvents (Di Martino et al., 2007) and the identification of different polymorphic forms of API (Jarring et al., 2006) (Perkins et al., 2009). Additionally, XRPD has been used to identify the presence of two APIs in crystals engineered for inhaled delivery (Westmeier and Steckel, 2008) (Pitchayajittipong et al., 2009). The effect of milling on APIs has also been investigated using XRPD to identify the polymorphic transition of fananserine during the mechanical process (De Gusseme et al., 2008). The use of this technique however, is not sensitive enough to quantify the relative changes in crystallinity.

### **1.5.2 Methods of Surface Energy Determination**

The detection of changes in material crystallinity provides information relating to the impact of processing operations in the changes to thermodynamic properties of materials but does not directly assess the impact on interparticle forces. Therefore, techniques that quantify the interactive forces of processed materials may offer additional understanding on how these materials may behave in a DPI formulation, where the interparticle forces underpin the aerosolisation and efficiency of drug delivery.

#### **1.5.2.1 Contact Angle Measurement**

This technique encompasses the measurement of contact angles between liquids and solid surfaces. In many cases, the compaction of a powder sample is used as the investigational material and the measurement of the resulting

droplet angle for several liquids of known polar and dispersive components is performed (Planinsek et al., 2001). Using the method of Good and van Oss, three different liquids of known nonpolar, acid (electron acceptor) and base (electron donor) components are measured to quantify surface free energy as a function of Lifshitz-van der Waals (nonpolar) and acid-base (polar) components (Van Oss et al., 1988). The use of such a technique has been shown to be beneficial in the general physico-chemical assessment of material wettability (Good, 1992) and differences in material free energy, for relation to adhesion against various surfaces (Podczek et al., 1996). Limitations on the value of bulk compact measurements arise from the deformative stress placed on the specimens during compaction and the resulting changes in roughness and porosity of material as a result (Duncan-Hewitt and Nisman, 1993) and therefore, examples of use of this technique alone in the pharmaceutical literature are sparse.

#### **1.5.2.2 Inverse Gas Chromatography (IGC)**

A commonly employed approach in determining the interfacial properties of pharmaceutically relevant materials is the use of inverse gas chromatography (IGC). In this technique, the material of interest is packed into a column and the time required for a gas probe to pass through is determined. By measuring the retention times of a series of probes of different polarity, the surface free energy as well as other parameters can be qualitatively determined (Grimsey et al., 2002).

IGC has routinely been used to investigate differences in interfacial properties of milled materials and supercritically engineered particles (Tong et al., 2002) (Schiavone et al., 2004), where stable samples produced supercritically were found to have a lower surface energy than those that were crystallised and then milled. More recently, work by Das et al. investigated the effect of humidity on the surface free energy of coarse lactose and milled salmeterol xinafoate. They found an increase of surface energy related directly to increases of relative humidity, leading to increases in capillary forces. Furthermore, these change also led to increases in the emitted fraction of powder formulations from a DPI device, attributing the agglomerative nature of capillary forces on powders, to

better flow properties and therefore improved device emptying (Das et al., 2009). A combined approach of atomic force microscopy (AFM) and IGC measurements have highlighted the different surface free energies of different forms of carbamazepine (Perkins et al., 2009), while investigations into bovine serum albumin spray-dried into two forms showed no difference in IGC, the use of AFM imaging has revealed differences in surface roughness leading to differences in DPI performance (Adi et al., 2008).

### **1.5.3 Measuring particle removal efficiency**

Key to the delivery of active ingredients by DPI formulations is the effective removal of drug particles from the carrier surface. Approaches that enable the measurement of particle forces against other surfaces are routinely used to evaluate the particle removal efficiency. This section addresses the use of these methodologies in developing tools to predict the entrainment and delivery profile of DPI products.

#### **1.5.3.1 Centrifugal Techniques**

Though classed as a bulk technique, the use of centrifuge measurements enables the investigation of adhesional forces between particles and investigational surfaces (Podczek et al., 1996). Briefly, samples are placed onto a disk located on a centrifuge and a given load (press-on force) is applied to the particles by rotating the disk facing inwards. Subsequently, particles are counted and then mounted facing away from the centre and samples are rotated in a series of progressively increasing speeds, recording the number of particles remaining after each speed. While this process is relatively cheap and requires low quantities of sample, single particle measurements cannot be performed and generation of data relating to particle-particle interactions is limited.

### **1.5.4 Single Particle Investigations of Interfacial Forces**

Bulk measurement techniques of pharmaceutical materials provide a useful means of investigating a broad population of particles. However, results are

often limited in providing in-depth understanding, due to the heterogeneous nature of the materials under investigation. Single particle investigations therefore, enable the measurement of properties independently from the influences of the bulk and are useful in quantifying interfacial properties of materials by the use of multiple measurements of different individual particles.

#### **1.5.4.1 Colloidal Probe Atomic Force Microscopy**

The atomic force microscope enables the investigation of interactive forces between a cantilever based probe and interacting surface at a nano-Newton resolution (Cappella and Dietler, 1999). By replacing the cantilever tip with a colloidal probe, interactions between a substrate sample and micrometer sized particles can be investigated. Unsurprisingly, this form of measurement has had significant implications to the field of DPI formulation, as the interactive forces between inter-particle components play a critical role in the behaviour of these mixtures (Roberts, 2005). Initial work in this area was limited, due to the irregular nature of particles attached leading to significant variations in contact area between the probe and substrate surface. Two refined approaches have overcome this issue by either quantifying the contact area directly or interacting the same colloidal probes with smooth surfaces of interest.

Using a test grating containing a uniform series of sharp spikes of defined size and geometry, a raster-scanned image of an interacting probe can be reverse imaged and deconvoluted to quantify a 3D image of the tip (Hubner et al., 2003) (Clifford and Seah, 2005a). These data can then be used to determine tip sharpness parameters and effective contact areas for particles attached to modified cantilevers. Once these parameters have been determined, interactive forces can be calculated between these particles and investigational materials by interactive measurements between the two materials. Using JKR theory, which accounts for surface forces occurring within the contact area only (Johnson et al., 1971), or DMT theory whereby adhesion forces are deemed to occur outside the contact area (Deryaguin et al., 1978), this technique can quantify surface energies and work of adhesion. Work by Hooton et al. using this approach has demonstrated the possibility of normalising particle adhesion data from different particles by calculating force per unit area in order to show

differences of adhesional forces for salbutamol sulphate prepared in two very different manners (Hooton et al., 2004). Further work demonstrated the use of this approach alongside bulk IGC measurements for milled and unmilled budesonide (Davies et al., 2005). The group found variability in values obtained from AFM measurements, attributing these to orientational differences between the different particles fixed onto the cantilevers, drawing attention to the limitations and complexity arising from individual particle measurements. The values obtained for IGC measurements of micronised materials, though different to AFM measurement, did highlight the complimentary nature of each technique in understanding the physico-chemical interactions between materials of DPI formulation interest.

Another approach using colloidal AFM is to interact individual particles of interest to two smooth surfaces of substrate crystals, one of the same material and another of the excipient. Without the need of quantifying the true contact area of the investigational probe, AFM measurements of interparticle forces using this methodology provides a ratio of the thermodynamic work of cohesion to adhesion. From these measurements, the force of cohesion (drug-drug) and force of adhesion (drug-excipient) can be obtained and by dividing the cohesive force over the adhesive force, a cohesive-adhesive balance (CAB) value is calculated and expressed by Equation 1.18 and illustrated in Figure 1.5,

$$\frac{F_{coh}}{F_{adh}} = \frac{n\pi R^* W_{coh}}{n\pi R^* W_{adh}}$$

**Equation 1.18**

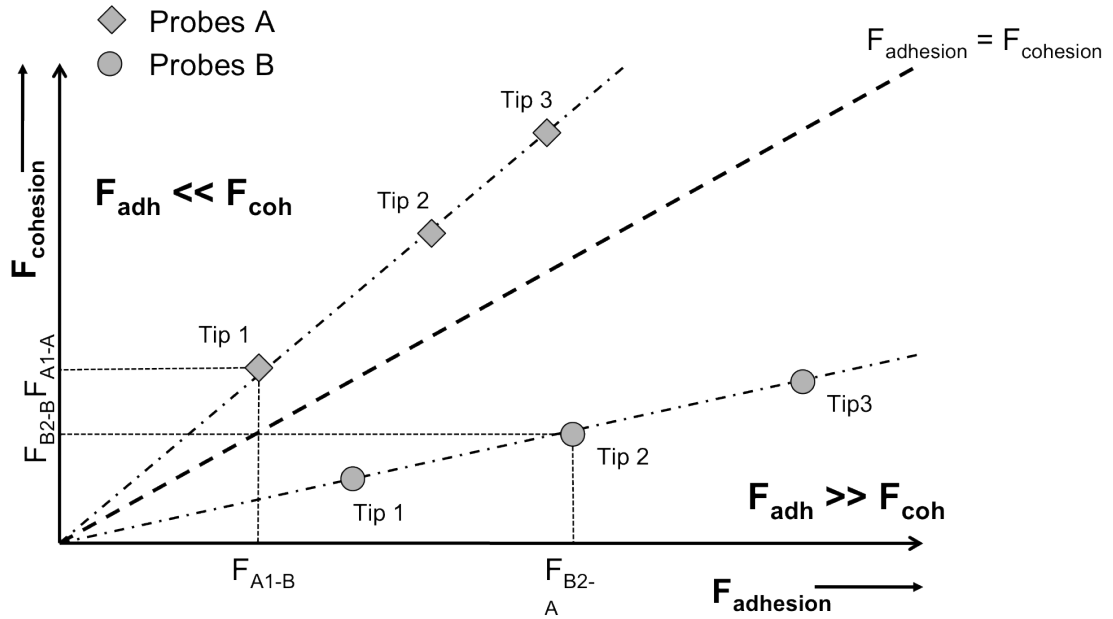


**Figure 1.5 A representative graphical description of a CAB-graph for a binary system (Adapted from Begat et al., 2004)**

where  $F_{coh}$  and  $F_{adh}$  are the cohesive and adhesive forces measured by AFM, and  $W_{coh}$  and  $W_{adh}$  are the thermodynamic work of cohesion and adhesion, respectively (Traini et al., 2005). The use of multiple colloidal probes in this approach negates the need to quantify the spring-constant for each cantilever, as the thermodynamic ratio of the work of cohesion and adhesion interactions extrapolated from surface interaction measurement are assumed to follow the same theoretical model of contact mechanics.

The CAB approach has been demonstrated to observe differences in interactive forces with lactose for salbutamol sulphate and budesonide (Begat et al., 2004b) and the interactions of salbutamol sulphate with different sugar excipient crystals (Hooton et al., 2006). Moreover the technique has shown applications within a liquid environment, investigating interactions within model liquid propellants (Traini et al., 2005) and shown to relate to dry powder inhalation delivery (Begat et al., 2004c); whereby micronised budesonide was found to be cohesively led in comparison to the adhesively led salbutamol sulphate, affecting both the mixing and fluidisation behaviour of each material. Additionally, further work found that fluticasone propionate has an adhesion to lactose monohydrate 4.55 times greater than the force of cohesion (Jones et

al., 2008) and that the performance of these carrier-based formulations could be altered by the inclusion of fine particles of tertiary excipient materials.

## **1.6 Primary Crystallisation of APIs**

The process of crystallisation is fundamental to the isolation and purification active pharmaceutical ingredients and excipients (Fujiwara et al., 2005) and therefore receives significant attention in order to produce a product of defined quality standards (Variankaval et al., 2008). As a consequence, this is often the final process that determines the physico-chemical nature of primary materials for secondary processing. From Figure 1.4 we can see how this step may have significant downstream implications in the handling, processing and functionality of these materials (Shekunov and York, 2000) (Datta and Grant, 2004). By understanding the crystallisation process and its possible impact on the physical properties of the resultant crystals, the effects of micronisation and subsequent performance of DPI formulations may be better understood.

### **1.6.1 Background Theory of Crystallisation**

A crystalline solid is defined as being comprised of a rigid lattice of molecules, atoms or ions, in a thermodynamically stable order, characteristic of the substance (Mullin, 2001). This repeating pattern extends in three dimensions, defining internal crystal structure and external crystal morphology for organic molecular crystals, which retain this structure by a combination of forces including van der Waals, hydrogen bonding, ionic and electrostatic interactions (Sheth and Grant, 2005). These can be attractive or repulsive in nature, ranging from 0.5 – 150 kJ.mol<sup>-1</sup> depending on the type of intermolecular interaction, though in the case of most organic crystals, van der Waals and hydrogen bond interactions dominate (Datta and Grant, 2004). In many cases the molecules being crystallised can be prepared by the careful selection and control of crystallisation conditions. In turn, the product can be recovered as native free bases (or acids), they can be hydrated, anhydrous or solvated. Each will have differences on the pharmaceutical and pharmacokinetic properties of the

resulting material and therefore, this process must be optimised to produce material of the greatest quality (Variankaval et al., 2008).

#### **1.6.1.1 Nucleation**

The driving force for the nucleation involves the creation of a supersaturated solution or the supercooling of a solid melt (Mullin, 2001) (Fujiwara et al., 2005). For a solution, this can be created by cooling, evaporation and/or addition of an antisolvent, including the addition of an acid or base to change the pH (Rodriguez-Hornedo and Murphy, 1999). Supersaturation is referred to as a state in which the concentration of a substance in a solvent at a certain temperature and pressure, is greater than the saturated solubility of that substance under controlled conditions (Myerson, 1993) and is routinely defined by Equation 1.19:

$$\sigma = (c - s) / s$$

**Equation 1.19**

where  $\sigma$  is the relative supersaturation,  $c$  is the concentration of the crystallising substance in the supersaturated solution and  $s$  is the solubility (Rodriguez-Hornedo and Murphy, 1999).

At the point of supersaturation, the solution is not in equilibrium and nucleation can occur if a sufficient level of supersaturation can be generated. Prior to the point of nucleation the solution is termed metastable, wherein a metastable zone exists whereby crystals can grow without nucleation (Myerson, 1993). The formation of nuclei from solution, which act as a growth centres for crystals can occur in two ways. Primary crystallisation occurs in the absence of crystalline surfaces and can be homogeneous, whereby local concentration fluctuations give rise to regions of ordered or clustered molecules forming nuclei that grow. Primary heterogeneous nucleation occurs where foreign materials in the solution or equipment, reduce energy barriers for nucleation, and therefore require lower levels of supersaturation for nucleation and crystal growth (Mullin,



2001). The nucleation process can be further induced by agitation, changes in pressure and ultrasound radiation (Myerson, 1993) (Ruecroft et al., 2005).

The thermodynamic investigations of homogeneous nucleation are based on work by Gibbs (Gibbs, 1948) and Volmer (Volmer, 1939), describing the overall Gibbs free energy for an aggregate undergoing a phase transition ( $\Delta G$ ) as

$$\Delta G = \Delta G_v + \Delta G_s$$

**Equation 1.20**

where  $\Delta G_v$  is the volume free energy (negative value) and  $\Delta G_s$  is the surface free energy associated with the with the formation of an aggregate (positive value) (Rodriguez-Hornedo and Murphy, 1999). This can be further expressed as

$$\Delta G = 4\pi r^2 \gamma + \pi r^3 \Delta G_v$$

**Equation 1.21**

when modelling for spherical nuclei of radius  $r$  and  $\gamma$  denotes surface tension. As the value of  $\Delta G_s$  is dependent on  $r^2$  and  $\Delta G_v$  increases proportionally to  $r^3$ , upon reaching a critical radius ( $r_{crit}$ ),  $\Delta G_v$  increases faster than  $\Delta G_s$  enabling the growth of the nucleus thermodynamically more favourable than re-dissolution (Myerson, 1993). At this point, nucleation is replaced by crystal growth and can be described by Equation 1.22:

$$r_{crit} = \frac{-2\gamma}{\Delta G_v}$$

**Equation 1.22**

The rate of nucleus formation is given by the Arrhenius expression

$$B_0 = A.e^{\left(\frac{-\Delta G_{crit}}{kT}\right)}$$

**Equation 1.23**

where  $A$  is a pre-exponential factor ( $10^{30}$  nuclei.cm<sup>-3</sup>.s<sup>-1</sup>) and  $k$  is the Boltzmann constant (Myerson, 1993). Using the Gibbs-Thompson equation to relate solubility  $S$  to particle size  $r$  using the molecular volume  $V_m$  gives:

$$\ln S = \frac{2\gamma V_m}{kTr}$$

**Equation 1.24**

By combining Equation 1.22, Equation 1.23 and Equation 1.24, the rate of nucleation can be described as

$$B_0 = A.e^{\left[\frac{-16\pi\gamma^3 V_m^2}{3k^3 T^3 (\ln S)^2}\right]}$$

**Equation 1.25**

From Equation 1.25, the rate of nucleation is seen to be dependent on the temperature, supersaturation and surface energy. Additionally, surface tension increases would lead to decrease of nucleation, promoting the formation of nuclei of the lowest possible surface free energy (Myerson, 1993) (Rodriguez-Hornedo and Murphy, 1999).

#### **1.6.1.2 Crystal Growth**

Once the barriers to nucleation are overcome, nuclei are able to grow into macroscopic crystals and this is termed crystal growth. Single molecular units are incorporated to a crystal surface over a number of steps including the transport of units from the bulk solution to the crystal surface, adsorption of the growth unit to the impingement site, diffusion from the impingement site to a growth site and incorporation of the growth unit into the crystal lattice (Rodriguez-Hornedo and Murphy, 1999).

From a thermodynamic standpoint, the attachment of units would be favourable at point where the greatest surface free energy is found on the crystal surface (Nývlt et al., 1985) and tend to be found in regions where growth units can be incorporated to the maximum number of nearest neighbours (Myerson, 1993). From Figure 1.6 it can be seen that incorporation at a kink site on a ledge will result in the formation of three-unsaturated bonds, a ledge without a kink site will result in two bonds and the attachment of a unit to a surface alone will result in only one bond (Kossel, 1934). This theory goes some way to explain the layer-by-layer nature of crystal growth but fails to incorporate in the model for the appearance of growth sites and the rates of crystal growth (Myerson, 1993).

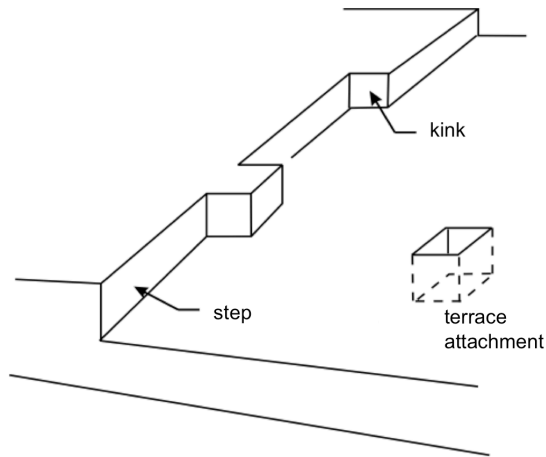


**Figure 1.6 The surface structure of a growing crystal (Adapted from Myerson, 1993)**

The growth of crystals is a process governed by internal and external factors (Rodríguez-Hornedo and Murphy, 1999). A range of growth mechanisms have been proposed in the literature (Nývlt et al., 1985) (Myerson, 1993) (Mullin, 2001), taking into account the diffusion of molecules, integration of molecules within the lattice and the formation of nucleating clusters on crystal surfaces. Discriminating between these models, which take into account supersaturation, temperature and growth faces, is often difficult in identifying the correct model responsible for growth and requires a combined approach of growth theory and topographical observations (Rodríguez-Hornedo and Murphy, 1999).

The growth rate of different crystal faces was shown by Wulff to grow at rates proportional to surface energy, leading to an observed crystal habit – the external appearance of the crystal. The crystal habit can vary, largely based on the rate of nucleation and crystal growth (Abu Bakar et al., 2009). External factors surrounding solvent environment, presence of impurities and temperature can modify the rate of growth on specific faces. This can lead to a change in the rates of growth on various faces and in turn, affect the crystal size distribution (Mullin, 2001).

### **1.6.2 Effect of Solvents and Impurities on Crystallisation**

A crystal is internally composed of a repeating series of molecules or atoms that then form the building blocks of a solid crystal. The ability of each unit molecule to pack in a different manner will result in the formation of polymorphic forms of the same compound, which in many cases can result in serious differences in the physico-chemical properties of the material (Gardner et al., 2004). Moreover, if the repeating internal structure is disrupted in any way, the imperfection can lead to displacements within the structure and strain placed on the lattice structure. These imperfections can be substitutional, whereby a foreign particle occupies the area in which the unit cell was to be incorporated, or the space between unit molecules/atoms can be occupied a foreign element and is termed interstitial impurity. Where a unit has failed to be incorporated and a void exists, it is termed a vacancy. These three imperfections are classed as point defects since they involve a single point within a lattice (Myerson, 1993). Other defects termed line dislocations and screw dislocations represent line defects, which are found in most crystals (Mullin, 2001). These arise due to miss-alignment of molecules within the lattice, resulting in spiral growth and miss matching of boundaries, producing crystals of varying physical, thermal and mechanical properties (Mullin, 2001).

The crystallisation of organic materials from solution can be greatly affected by the solvent used. Solvent-solute interactions can influence the mass transfer of solute to the crystal surface while the degree of solute solubility will determine the resulting mass (yield) of crystals obtained (Myerson, 1993). Moreover, altering the kinetics of crystal growth is known to change the crystal habit

(Garekani et al., 2001) (Banga et al., 2007) and alter the polymorph formed (Parmar et al., 2007). In the screening of solid forms, solvent selection is based on a wide range of parameters including a broad distribution of solution properties (density, viscosity, polarity), purity, solvent toxicity, chemical reactivity and environmental impact (Myerson, 1993) (Camarasu et al., 2006) (Aaltonen et al., 2009). Often, mixtures of solvents are tested, with water-solvent mixtures favoured in the screen for hydrates of desired pharmacokinetic properties (Aaltonen et al., 2009).

Impurities, either from the solvent or introduced by other means, can have a significant effect on the growth of crystals and the strength of the resulting intermolecular bonds, leading to further changes in crystal habit and consequential impact on future processing (Wood, 2001). Apart from changes in solution properties, for example metastable zone width and solubility parameters, impurities can lead to preferential adsorption of solute molecules to different faces (Mullin, 2001) (Fiebig et al., 2007). These effects can occur as a result of impurities being adsorbed to an immobile position on the crystal surface, reducing or blocking the advancement of growing crystal layers. In contrast, mobile impurities may adsorb to the surface of a growing crystal and relocate by diffusion, in two dimensions over the surface. The relative effect this type of impurity will have on the growth kinetics of a crystal will be determined by the relative mobility of the impurity. Specific studies investigating the kinetics of both types of impurities were postulated by Cabrera and Vermilyea (1958) and the reader is directed to that reference e literature for further details regarding this topic.

### **1.6.3 The Mechanical Properties of Crystalline Materials**

The crystallisation of pharmaceutical materials is known to influence a variety of processing factors that may then lead to changes in the functionality of the resultant product (Edge et al., 2008). One key process mentioned previously, is the milling of crystals into the respirable size range. Mechanical properties of these materials, processing conditions of the mill and pre-existing flaws and imperfections in the crystalline material are known to affect particle fracture (Rumpf, 1973). The size reduction efficiency therefore, is largely a function of

the material properties (material function) and the ability of loads exerted from the milling process or particle-particle collision being transformed into the propagation of fractures within the solid materials (Teipel, 2004). It has been shown that three material functions are highly influential on the breakage of solid materials; Young's modulus ( $E$ ), hardness ( $H$ ) and critical stress intensity factor ( $K_c$ ) (Ghadiri and Zhang, 2002) (Kwan et al., 2004), representing the resistance of a material to elastic deformation, plastic deformation and crack propagation, respectively.

Solid material behaviour within the mill can be described as linearly elastic, plastic or viscoelastic (Ward and Hadley, 1995) (de Vegt et al., 2006). For a linearly elastic material, stress applied to the material is proportional to the deformation that occurs and is independent of loading rate (Clifford and Seah, 2005a). This proportionality factor is a characteristic of one mechanical property of a material and is called the Young's modulus, (also known as elastic modulus) and is described by the following equation

$$\sigma = E.\varepsilon$$

**Equation 1.26**

where  $\sigma$  is the tensile stress and  $\varepsilon$  is the extensional deformation (Rowe and Roberts, 1995) (Teipel, 2004). These elastic-plastic properties determine the breaking resistance as well as the formation and propagation of cracks and therefore, define the degree of size reduction (Zugner et al., 2006). Moreover, as the particle size reduces, materials show a transition from elastic to plastic behaviour resulting in increased deformity of the material alongside reduced probability of breaking (Shekunov and York, 2000) (Teipel, 2004).

## **1.7 Methods of Measuring the Young's Modulus of Organic Materials**

The elasticity of a material has significant implications for a wide variety of pharmaceutical preparations, notably in the production of tablets (Bassam et al.,

1990) and the milling behaviour of pharmaceutical ingredients (Zugner et al., 2006). Understanding the compaction behaviour of excipients and APIs used in the production of solid oral dosage forms has relied heavily on various bulk techniques such as flexure testing (Roberts et al., 1991) and compression testing. These ideas have influenced the understanding of comminution behaviour of pharmaceutical materials, relating to the processing of inhaled formulations, though limitations of these methods have led to advances in newer techniques such as the indentation of single crystals. The use of acoustic pulse monitoring has also evolved in determining the elastic modulus of compacts (Akseli et al., 2009) but will not be discussed in this work.

### **1.7.1 Flexure Testing (Beam Bending)**

A traditional method of measuring the Young's modulus using a bulk approach involves the creation of a beam of test material within a special punch and die at different compression pressures to achieve a range of porosities (Rowe and Roberts, 1995). This rectangular beam is then subjected to a transverse load and the deflection caused by bending of the beam is measured. If the beam is supported at two points and loaded at two, it undergoes a four-point beam bending (Bassam et al., 1990), while if it supported at two points but loaded at one, it is known as three-point beam bending (Roberts et al., 1991). Initial tests using these methods required 15-20 g of material for four-point bending experiments and although modification of the three-point bending method required approximately 200 mg, this technique is often considered as expensive and time consuming (Masterson and Cao, 2008).

### **1.7.2 Compression Testing**

This method relies on applying a compressive stress onto a compact or single crystal and measuring the corresponding strain to calculate the compressive Young's modulus of elasticity (Leigh et al., 1967) (Leuenberger and Rohera, 1986). Compression testing of compacts similarly requires repeated measurements of specimens of various porosities while single crystal techniques can be influenced by crack propagation of the material (Rowe and Roberts, 1995), again limiting its use for accurate characterisation.

### 1.7.3 Nanoindentation Measurements

Indentation tests rely on applying a given load to the surface of a sample with an indenter of defined geometry, recording the penetration depth of the probe and in many cases, the material response after loading. The most common probes used in this technique are square-based pyramid (Vickers indenter), three-sided pyramid (Berkovich indenter) and spherical ball (Brinell indenter) (Meier et al., 2008). These indenters are produced from hard materials such as diamond, sapphire, steel or silicon and are chosen based on the samples being investigated and the operating parameters while taking into account the measurements required from the instrument.

As techniques of fabricating various instrumental components have developed, increasing resolution and control over loading forces and penetration depths have enabled the application of loads ranging between  $10^{-5}$  and  $10^{-2}$  N resulting in recorded penetration depths in the nanometre range (Fraxedas et al., 2002). Many instruments are now commercially available to perform nanoindentation tests using a rigid probe placed on a pendulum (Nanotester, Micromaterials, UK) or by application of a voltage over capacitive plates resulting in probe movement (Triboindenter, Hysitron Inc., USA). These approaches rely on the elastic recovery of a sample after a set load is placed at a given loading rate and then withdrawn. Marked hysteresis between the loading and unloading portion of the curves are seen (Figure 1.7) and data from such plots can be extrapolated to obtain the elastic modulus and hardness of a material (Oliver and Pharr, 1992). Moreover, if the cracks formed from the indentation can be measured, the fracture toughness ( $K_{IC}$ ) can also be determined (Ponton and Rawlings, 1989).

Work by Liao and Wiedmann (2005) used this technique to observe differences in the mechanical properties of acetaminophen (paracetamol) and potassium chloride produced by rapid (quenched) or slow recrystallisation methods. For the quenched samples, where crystallisation occurs rapidly and in a relatively uncontrolled manner, the measured Young's modulus for each sample was higher than those recrystallised slowly. These results were attributed to



differences to the dislocation propensity of each of the materials (Liao and Wiedmann, 2005). The effect of crystal face was also investigated by Ramos and Bahr on slowly grown sucrose crystals, highlighting the different elastic limits of each face (Ramos and Bahr, 2007). Additionally, work by Taylor et al., identified the use of nanoindentation in determining differences in the mechanical properties of a wide range of pharmaceutical ingredients (Taylor et al., 2004b), aiming to relate differences to milling behaviour of these materials (Taylor et al., 2004a).

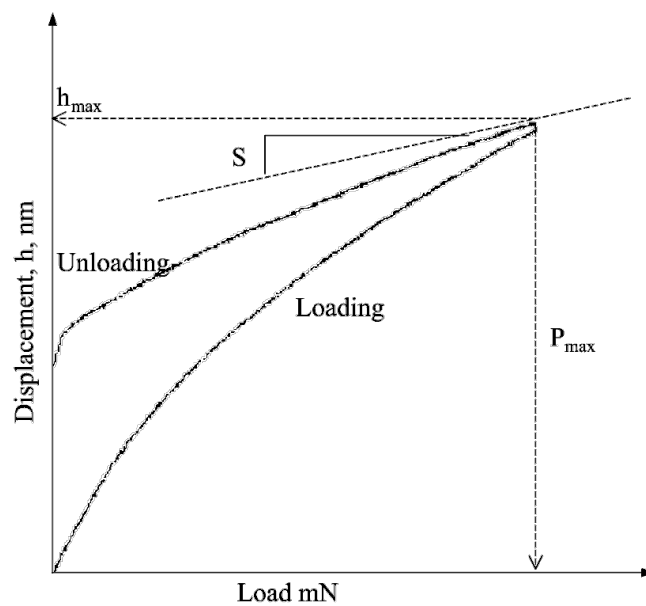


**Figure 1.7** A representational load versus displacement graph obtained from a single nanoindentation experiment (Reproduced from Taylor et al., 2004)

Atomic force microscopy has emerged as another important tool in the assessment of nanoscale properties of a wide variety of materials (Cappella and Dietler, 1999). Force-distance curves, whereby a cantilever and probe of defined stiffness and contact area can be loaded perpendicularly (z-axis) upon a sample, enable the investigation of indentation depths of single crystals. From these experiments and use of contact mechanics, various mechanical parameters, including the Young's modulus can be determined.

The Hertzian model of deformation (Hertz, 1881) takes into account the deformation of an elastic sphere on a flat surface, neglecting the surface forces

or adhesion of the tip on the sample modelled in Johnson-Kendall-Roberts theory (JKR) and Derjaguin-Müller-Toprov Theory (DMT). It can be used when indentation takes place under low loads and surface interactions are to a greater extent, negligible (Cappella and Dietler, 1999). This approach can use a hemispherical probe and models the loading curve to extrapolate the elastic modulus of a material. Work by Perkins et al. (2007) demonstrated the use of AFM nanoindentation on lactose monohydrate crystals and compared these results to previously established nanoindentation instruments, using a sharp indenter and extrapolation of the unloading curve using the Oliver and Pharr approach. The group concluded that AFM, due to its superior resolution and non-destructive approach, has significant advantages over the larger indenters used and provides a means of accurately measuring the elastic modulus of pharmaceutical materials.

## **1.8 Aim of Study**

The primary crystallisation of APIs is known to directly influence the physical and chemical nature of the resulting material. This thesis aims to investigate these differences and in addition to evaluating the effect on the mechanical properties of primary sources of APIs. Furthermore, the work aims to highlight the possible relationship of the physico-mechanical properties of APIs in relation to primary crystallisation with secondary processing of these APIs and influence on formulations for carrier-based dry powder inhalation delivery.

The outline of this thesis in relation to the aims is shown in the flow diagram in Figure 1.8 below. Chapter 3 will outline the development of an atomic force microscope approach in determining the Young's modulus of different organic materials used within the pharmaceutical formulation of orally inhaled drug products. In Chapter 4, the role of solvents in determining the elastic modulus of primary crystals of fluticasone propionate will be investigated and the effects this has on the processing of DPI formulations. Subsequently, Chapter 5 will explore the relationship between crystal habit and the mechanical nature of budesonide – specifically the affect of crystal habit on the formulation properties of a DPI formulation. The final experimental chapter, Chapter 6, assesses the implications of the crystal hydrate of ipratropium bromide compared to a relatively novel technique of producing anhydrous ipratropium bromide for DPI formulation. The general conclusions of this thesis will be presented in Chapter 7, alongside proposed further work.

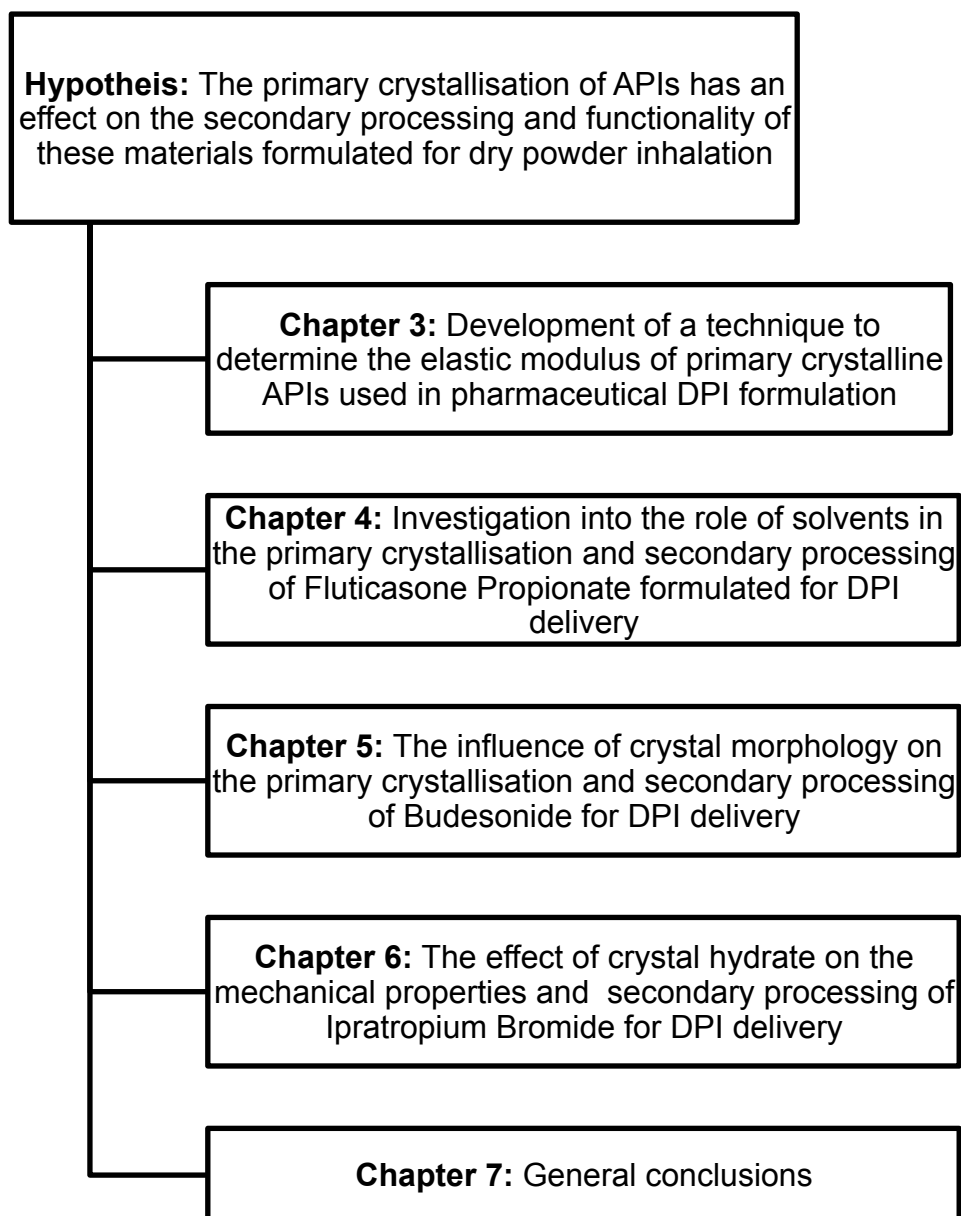


**Figure 1.8** A flow diagram illustrating the structure of this thesis in relation to the primary hypothesis.

## **Chapter 2: General Methods and Materials**

### **2.1 General Physicochemical Characterisation**

#### **2.1.1 Overview**

Dry powder inhalation formulations contain drug particles of respirable size blended with coarser carrier particles. The physical and chemical properties of these materials are known to affect the quality and performance of the resulting formulation. Characterisation of the primary crystals and processed materials is therefore, essential in developing efficient processes and effective DPI products. This section provides details relating to the specific techniques used to comprehensively test components of DPI formulations, including the topographical, morphological, thermal and crystal properties. Additionally, in order to measure the effect these variables have on the final product, the *in vitro* testing of DPI performance is also detailed.

#### **2.1.2 Scanning Electron Microscopy**

The shape and size of materials used in the formulation of inhaled products is known to influence the resulting performance (Timsina et al., 1994a). Scanning electron microscopy (SEM) provides high-resolution images from 20-100,000 times magnification enabling the visualisation of individual particles and their surfaces (Hickey et al., 2007a).

Images are produced by the use of electrons generated by an electron gun and focused on to a spot on the specimen through a series of magnetic lenses. This collimated beam of electrons is raster scanned across the sample and the secondary electrons produced on each spot are detected and amplified. These signals are then processed to produce a final image. To prevent divergence of the electron beam and because of the high acceleration voltages required, usually between 0.5 – 50 kV, SEM is carried out under vacuum. Moreover, since the surface of the sample must be conductive, a thin layer of gold is coated upon an electrically grounded specimen.

Though various image analysis software platforms exist that quantify geometric parameters of materials imaged in this manner, SEM has widely remained as a qualitative approach in pharmaceutical material size analysis. This is partly due to the large number of particles required to be measured for statistical significance, operator related bias in sampling or dispersion of materials and the complex process of distinguishing between agglomerates within a given image.

### **2.1.3 Particle Size Analysis**

The particle size of APIs and excipients used in pharmaceutical formulation is known to affect various rheological and pharmacokinetic parameters and will largely influence the safety and efficacy of formulated drug products (Shekunov et al., 2007). For DPIs, the determination of particle size distribution (PSD) is critical since any changes may result in significant variations in the blending properties, fluidisation, aerosolisation and performance of the inhaled formulation (Timsina et al., 1994a) (Shur et al., 2008). Techniques such as sieving, sedimentation, electrozone sensing, microscopy and cascade impaction can be used in obtaining the PSD of particulate material.

Laser diffraction (low angle laser light scattering (LALLS)) is routinely used in the rapid and accurate measurement of particle size for components of inhaled formulations (de Boer et al., 2002) (Zeng et al., 2007) and can be used in the wet or dry dispersion state. When particles pass through light, a diffraction pattern is scattered, with smaller particles scattering at larger angles. Furthermore, in certain materials, light is also reflected, refracted and absorbed, depending on the light source, particle size and optical properties of the material being investigated (Keck and Mueller, 2008). In the most popular LLALS systems, a monochromatic laser is scattered by particles dispersed in its path, as shown in Figure 2.1. The incidental light that has been diffracted is then focused onto a multi-element detector from which these patterns are then integrated to derive a volume-weighted distribution of volume equivalent diameters (Shekunov et al., 2007 (Keck and Mueller, 2008).

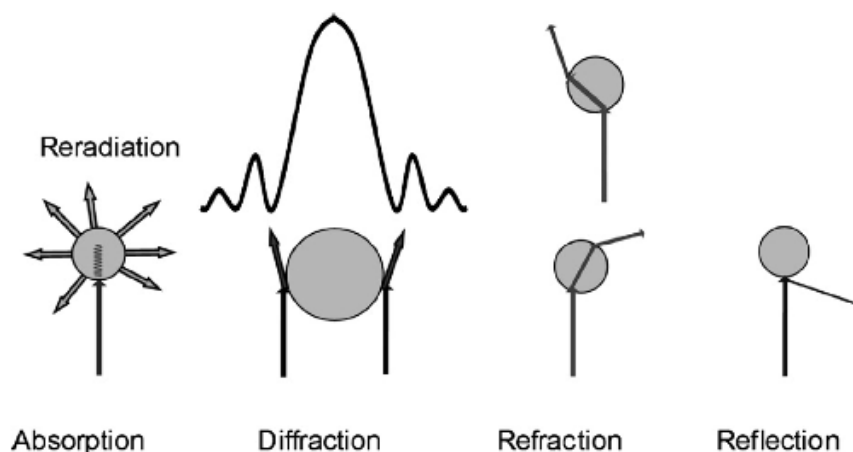


**Figure 2.1** Scattering phenomena that occur when particles are illuminated with light (Reproduced from Keck and Mueller 2008)

Two models are used in LALLS in derivation of the complex diffraction patterns of light scattering by particles, Mie theory and Fraunhofer diffraction. The first requires knowledge of the refractive index (RI) of the materials being investigated and makes the assumption that all particles are smooth spheres, calculating the particle size from the measured angle of scatter combined with the optical properties of these materials (Mie, 1908 (Keck and Mueller, 2008)). For materials of unknown RI, variable shape and particle size greater than the wavelength of the operating system, Fraunhofer approximation can be applied to the diffracted light patterns to derive particle size.

#### 2.1.4 Differential Scanning Calorimetry

Understanding the response of materials to thermal stress has been central to the characterisation of pharmaceutical materials. Routinely, differential scanning calorimetry (DSC) is employed within the pharmaceutical industry to provide detailed information to relating the physical and energetic properties of a sample that include, but are not limited to crystallisation, melting, and decomposition (Clas et al., 1999). This is achieved by measuring the heat flow required to heat and cool a reference and sample at the same rate. Differences in this energy required is charted and subsequently provides a *thermal fingerprint* of that sample, a representative example is shown in Figure 2.2. Quantitative information relating the endothermic and exothermic properties as well as the heat capacity of the sample has been used to identify different

polymorphs of the same API (Tong et al., 2001), assess the influence of mechanical activation on the physical stability of salbutamol suphate (Brodka-Pfeiffer et al., 2003) and identify thermal differences between anhydrous and solvated forms of the same API (Caira et al., 2007).

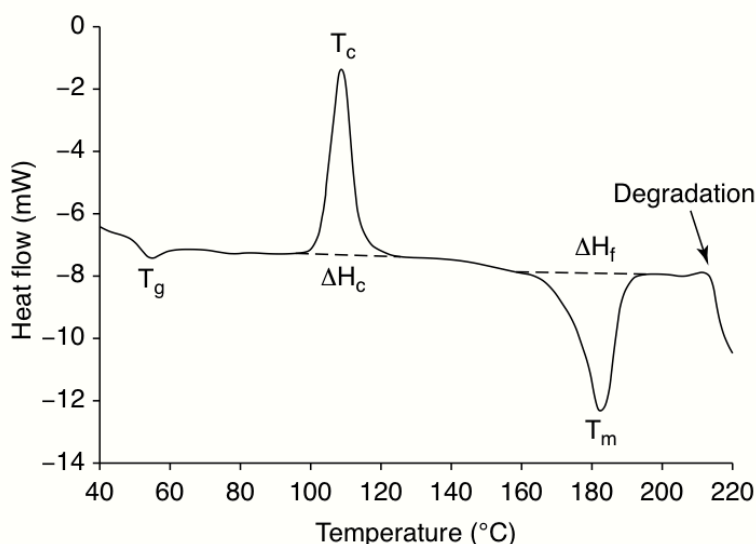


**Figure 2.2** A representative DSC trace showing the glass transition temperature ( $T_g$ ), recrystallisation exotherm temperature ( $T_c$ ) and enthalpy ( $\Delta H_c$ ), melting endotherm temperature ( $T_m$ ) and enthalpy ( $\Delta H_f$ ) and onset of degradation. Endothermic transitions are down (Reproduced from Class et al., 1999)

### 2.1.5 X-Ray Powder Diffraction

X-ray diffraction is commonly employed in the routine solid crystal form screening of organic crystalline materials (Aaltonen et al., 2009). It can be used to determine the crystal structure and in many cases, used to confirm the presence of molecular adducts such as solvates and hydrates introduced by the crystallisation process (Datta and Grant, 2004). Development of single crystal X-ray diffraction techniques led to the analysis of powder materials using X-ray powder diffraction (XRPD), enabling the evaluation of processed materials (Harris et al., 2001). Diffraction patterns are obtained by directing a monochromatic X-ray beam at a sample and measuring the scattered radiation on a detector. By changing the angle between the radiation source, and the detector plate, the intensity of detected radiation from the sample can be plotted against the angle of incidence. Since crystalline materials are composed of a regular lattice, the detected X-rays will correspond to the repeated properties of the material, while areas containing disordered regions of reduced crystallinity



will produce peaks of little or no definition. These peaks occur only when Bragg's law is satisfied:

$$n\lambda = 2d_p \sin \theta$$

**Equation 2.1**

where  $n$  is an integer (the order of reflection),  $\lambda$  is the wavelength of the X-ray,  $d_p$  is the distance between planes of the crystal and  $\theta$  is the angle between the incident X-rays and the crystal surface (Bragg, 1913).

Since the values of  $n$ ,  $\lambda$  and  $\theta$  are recorded, the crystal structure can be solved using the Bragg equation, thereby identifying different polymorphic and solvated forms of the same material (Datta and Grant, 2004).

## **2.2 Atomic Force Microscopy**

### **2.2.1 Overview**

The atomic force microscope (AFM) was developed by Binnig, Quate and Gerber in 1986 from its predecessor, the scanning tunnel microscope (STM) and has found uses in varying applications ranging from biophysics to particulate science (Cappella and Dietler, 1999). Most AFM systems comprise of a microfabricated cantilever probe upon which a laser is focused on the apex. With reference to Figure 2.3, reflected laser light is then detected onto a four-quadrant photodiode detector. A scanner containing a piezoelectric ceramic enables the precise (sub-Angstrom (Å)) positioning of samples mounted upon it by applying a known voltage against electrodes responsible for x, y and z movement resulting in a proportional expansion or contraction of the scanner. In the case of a multimode AFM (Bruker Nano AFM, Santa Barbara, CA, USA), the sample is moved relative to a stationary cantilever. To ensure that continual contact between the probe and the sample is maintained, a feedback loop controller can be integrated between the photodiode analyser and the movement controller of the piezo scanner. Continual monitoring of a defined parameter (cantilever deflection, amplitude, height, etc...) will alter the position

of the sample relative to the probe by optimising the piezo scanner position (Jalili and Laxminarayana, 2004).

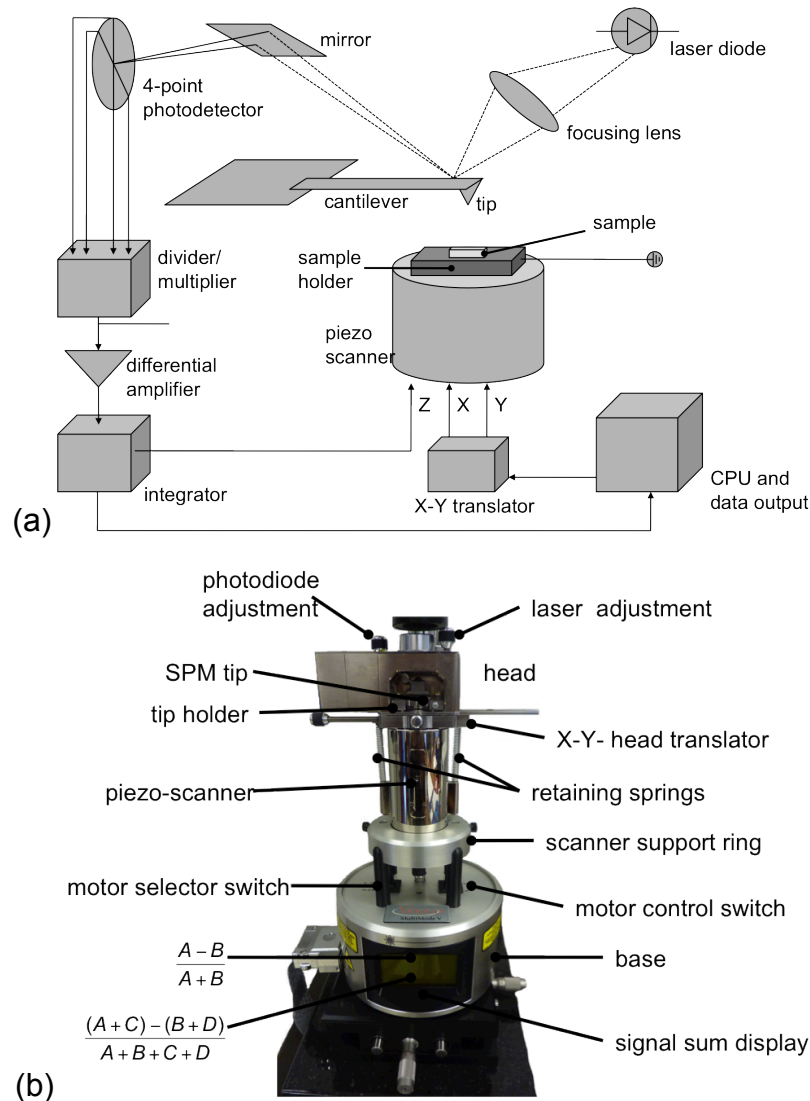


**Figure 2.3** A schematic representation of an AFM (a) and a photograph of a multimode™ AFM (b)

### 2.2.2 Topographical Surface Analysis

By raster scanning an AFM probe over a sample surface, deflection of the cantilever caused by surface irregularities such as protrusions, dislocations or other defects will be recorded on the photodiode detector. These data are then processed by dedicated software to provide a 3D image of the substrate surface that can subsequently be analysed to provide topographical detail relating to the surface parameters such as roughness. There are three

fundamental operating modes that can be used to acquire images of substrate surfaces. An illustration of each mode is provided in Figure 2.4.

Contact mode AFM was the first surface profiling method whereby an image is obtained by keeping the probe at either a constant height or force upon the sample. This method has potentially destructive implications for the tip from irregular samples or can result in possible damage to soft samples from the shear forces produced by lateral movements of the investigational probe (Jalili and Laxminarayana, 2004).

With non-contact AFM, the stiff cantilever is resonated at its resonant frequency 50-150 Å above the sample surface and topographical images are constructed by detecting changes in the oscillating frequency, amplitude or phase of the probe caused by van der Waals interactions between the probe and the substrate surface. Though this technique has been extensively used in the tribological investigation of a wide range of materials, drawbacks include loss of detail to images as a result of surface water interaction with probe tips (Jalili and Laxminarayana, 2004).

The third mode of operation is tapping mode. This technique relies on a fixed continual oscillation of the cantilever probe at the resonant frequency, allowing intermittent contact of the tip to the substrate surface. The feedback loop adjusts for and changes between the tip and the surfaces that are observed by the photodiode detector and a topographic image is then constructed from this processed data. Tapping mode overcomes the limitations of both non-contact and contact modes of AFM imaging and has been developed into a useful tool in not only obtaining topographical images, but also mapping the different physico-mechanical properties of crystal substrates (Begat et al., 2003).

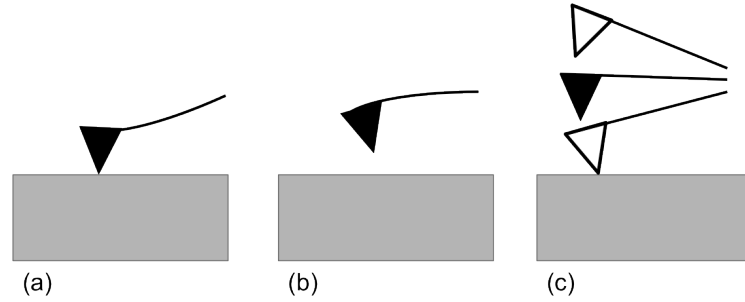


**Figure 2.4** An illustration of different imaging modes with tip and deflection showing contact (a), non-contact (b) and tapping-mode (c) tip interactions with a substrate

## 2.3 Force Interaction Microscopy

### 2.3.1 Overview

Alongside the development of imaging modes, AFM has enabled the investigation of cantilever probe and substrate interactions at a given X,Y coordinate. If the stiffness of the cantilever is known, the deflection of the cantilever can be derived into the force acting on the tip using Hooke's law:

$$F = -kx$$

#### Equation 2.2

where  $F$  is the force acting on the cantilever tip (N),  $k$  is the spring constant of the cantilever ( $\text{N.m}^{-1}$ ) and  $x$  is the cantilever deflection (Colton, 2004). For reliable force measurements, the accurate determination of the spring constant should be obtained for each individual probe. While this value is often quoted by the manufacturer, this nominal value can be up to a factor of two or more in error (Clifford and Seah, 2005b) and therefore, true determination of individual spring constants are crucial for quantitative analysis. Furthermore, converting the deflection signal and the piezo displacement into force and distance values requires a conversion factor obtained from a linear fit of the constant compliance region. Additional sensitivity is also obtained by calibration of the interacting tip on a non-indenting surface such as glass, silica or mica.

A range of forces are experienced by an interacting probe as it comes into contact, then withdrawn from the substrate surface and are represented in

Figure 2.5. Initially the probe is a large distance from the sample surface and no deflection is recorded. As the substrate is brought closer to the probe, long-range electrostatic forces often provide a repulsive force against the probe, recording a cantilever deflection away from the sample. When this distance is further decreased, attractive short-ranging van der Waals interactions overcome the repulsive forces and, depending on the stiffness of the cantilever, the probe jumps to contact with the substrate surface. Once contact is made, the probe can be pressed onto the surface with a pre-determined loading force prior to withdrawal. Upon retraction of the probe, sufficient force must be given in order to overcome the adhesive forces experienced between the probe and the substrate surface. Integration of the net difference between the adhesion force at the point of pull-off and zero interaction state can then be used to determine the energy of adhesion.

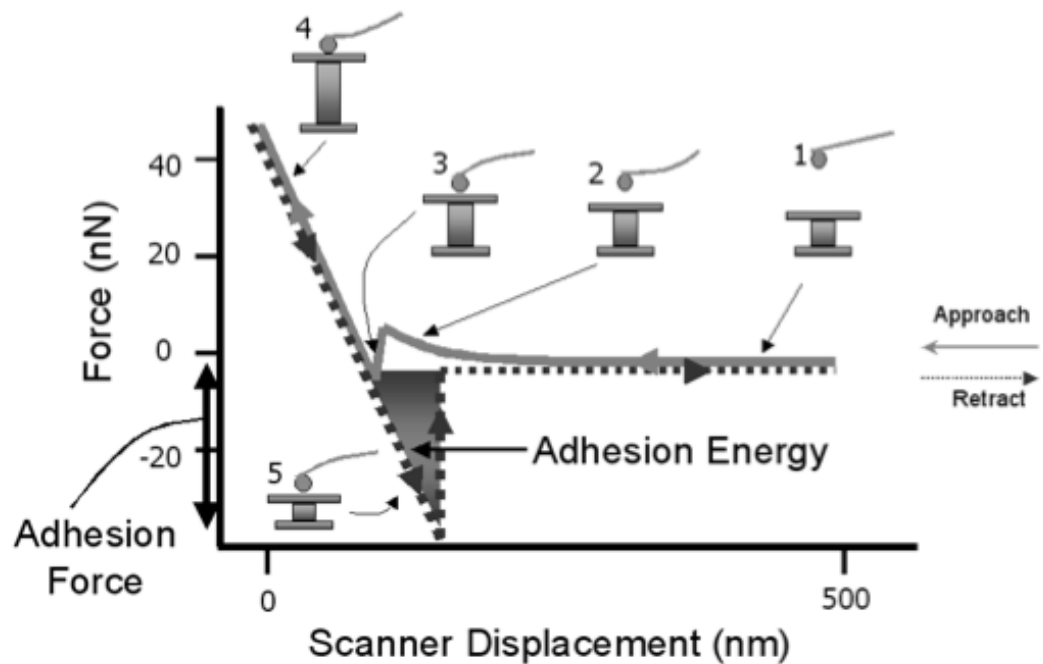


**Figure 2.5** A schematic force-distance curve obtained from AFM using a colloidal probe technique. Adapted from (Turner et al., 2007)

These measurements can be performed individually, or similarly to imaging modes, within a raster-scan across a substrate surface at a pre-defined X and Y interval, providing a force map, highlighting variations of surface adhesion over a given area. Modifications of the functional probes used at the apex of AFM

cantilevers have resulted in wide application of this technique, replacing the nominally sharp probes with materials of interest.

### 2.3.2 Colloidal Probe Microscopy

If the integrity of the colloidal probe can be maintained throughout the experiment, an approach relating to the cohesive and adhesive properties of the interacting particle can be used to provide quantitative measurements. Known as cohesive-adhesive balance (CAB) measurements, individual drug particles are interacted with the dominant face of extremely smooth crystals of the same drug and excipient, to provide relative forces of cohesion and adhesion respectively. By performing these measurements in a force-volume mode, whereby a series of measurements are performed with the same cantilever and particle over a set area of the substrate crystal, a large number of force-stance curves can be extrapolated to quantify the appropriate forces. Using JKR and DMT models of deformation, the resulting van der Waals force of adhesion between two spheres is given by Equation 2.3

$$F_{VDW} = n\pi R^* W_{ad}$$

**Equation 2.3**

where  $R^*$  is the harmonic mean of the particle radii (contact radius),  $W_{ad}$  is the thermodynamic work of adhesion ( $\text{mJ.m}^{-2}$ ) and  $n$  is a predetermined constant depending on the selected model ( $n = 3/2$  for JKR and  $n = 2$  for DMT) (Begat et al., 2004b). The cohesive-adhesive balance can be calculated by dividing the relative forces of cohesion by the relative forces of adhesion and is expressed by Equation 2.4

$$\frac{F_{coh}}{F_{adh}} = \frac{R^*_{cohesion} n\pi W_{coh}}{R^*_{adhesion} n\pi W_{adh}}$$

**Equation 2.4**

where  $F_{coh}$  and  $F_{adh}$  are the cohesive and adhesive forces measured by AFM, and  $W_{coh}$  and  $W_{adh}$  are the thermodynamic work of cohesion and adhesion, respectively. When a number of probes are plotted on a graph of cohesion versus adhesion, a linear relationship from the ratio of cohesion and adhesion by different probes forms a straight line, from which gradient is used to obtain the CAB value for that material.

### 2.3.3 AFM Nanoindentation

Indentation experiments provide information relating to the elastic, plastic and viscoelastic properties of materials (Lee, 2007). The ability of obtaining force-distance curves using AFM has enabled the investigation of every kind of surface under various environments providing high lateral (25 nm), vertical (0.1 Å) and force (1 pN) resolution (Cappella and Dietler, 1999).

For AFM indentation experiments, the Young's modulus of a material (E) can be obtained by knowledge of the indentation occurring after applying a load to a given material. If elastic conditions are maintained, Hertzian mechanics can be applied to model the loading curve and extract the elastic modulus. This process requires a non-destructive technique in which deformations are reversible. Therefore, appropriate choice of operating parameters is crucial for the accurate determination of this modulus (Perkins et al., 2007).

**As previously mentioned, the Hertz model of deformation operates within the model of an elastic sphere deforming a spherical surface (**

Equation 2.5). In context of an AFM instrument, the radius of the sphere is based on the radius of the indenting tip (R) and the loading force determined by Hooke's Law, where  $k$  is the spring constant of the indenting cantilever and  $\Delta z$  is the relative piezo displacement. The Poisson ratio of the indented material ( $\nu$ ) is taken as 0.3 and the resulting deformation is denoted by  $\delta$ .

$$E = \frac{3(1-\nu^2)k\Delta z}{4\delta^{3/2}R^{1/2}}$$

**Equation 2.5**

From this model, it can be seen that the controllable parameters are the loading force applied to the material and the radius of the indenting probe. Work by Perkins et al. (2007) demonstrated the destructive effect of a smaller radius probe on the surface of lactose, showing that Hertzian conditions were not met. Moreover, their work demonstrated that loading force, related to cantilever stiffness, must only provide enough for indentation within the elastic limits of a material. Accurate determination of the spring constant and indenter geometry are therefore, vital in quantitative measurement of the Young's modulus in this manner.

### **2.3.3.1 Data Handling**

The AFM produces a force-distance curve containing data relating to the deflection of the cantilever and piezo displacement. These data are required to be processed in order to produce two values that can then be used to calculate the Young's modulus, the force placed on the sample by the tip and indentation depth of the tip. The following method has been developed from the principles based in previously published work (Salerno and Bykov, 2006) (Perkins et al., 2007) and are outlined in detail below.

During the indentation process, the cantilever deflection is recorded on a photodetector and output as a voltage, representing deflection (A-B), which needs to be converted into a distance of deflection. This is performed by using Equation 2.6:

$$distance = \frac{(A - B)voltage \times instrument\ sensitivity \times attenuation}{detector\ sensitivity}$$

**Equation 2.6**

whereby the four-quadrant AFM detector is calibrated to obtain instrument sensitivity, attenuation is defined by the operator and detector sensitivity is measured from the gradient of deflection versus z-voltage, when in constant compliance.



The substrate is brought into contact in the z direction to the cantilever as a series of stepped movements by the piezo, this z-step size needs to be calculated using the equation:

$$z - \text{step size} = \frac{\text{scan size}}{\text{number of steps in scan}}$$

**Equation 2.7**

Both scan size and the number of steps in a scan are assigned by the operator.

The deflection of a cantilever versus the cumulative z-step are charted to produce a plot similar to Figure 2.6

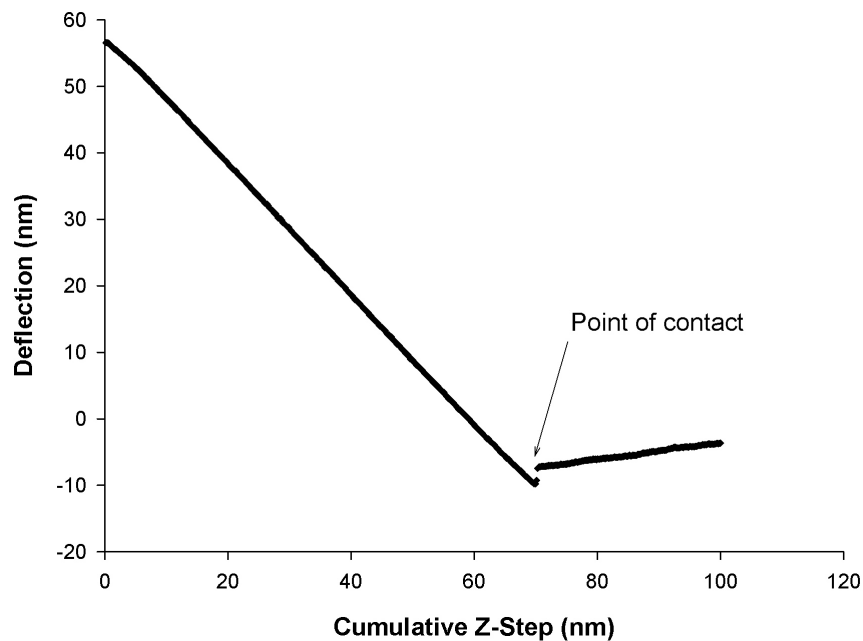


**Figure 2.6 A representative deflection versus cumulative z-step for a single nanoindentation experiment performed using AFM**

From the plot of cantilever deflection versus cumulative z-step the point of contact is determined. From here, the deflection and z-step are set as the origin and the points proceeding from contact to end of indentation are adjusted using the change in deflection and calculated z-step size from the y and x axis respectively.

The values of the zeroed z-step and deflection for the sample are compared to the indentation profile of the reference material. Since the reference (non-indenting) material provides greater elastic resistance to the probe, it should be higher, since the probe will indent the sample in situations where operating parameters are optimal. If there is no difference at this point, the measurement is discarded, as there may be false engagement of the probe, incorrect operating parameters or other irregularity.

Next, the loading force of the tip on the sample is calculated using Hooke's Law (Equation 2.2). This requires the spring constant of the cantilever, the distance travelled by the piezo (cumulative z-step) and the constant compliance value obtained from evaluating the indentation of the reference material.

$$\text{loading force (N)} = z - \text{step} \times \text{spring constant} \times \text{constant compliance}$$

**Equation 2.8**

The indentation of the probe with the sample is obtained by the difference between the deflection of the probe recorded for the reference and sample under the same load. This value is then converted to metres, raised to the power of 3/2 and plotted on the x-axis against the loading force to produce loading versus indentation<sup>3/2</sup> plot, as shown in Figure 2.7.

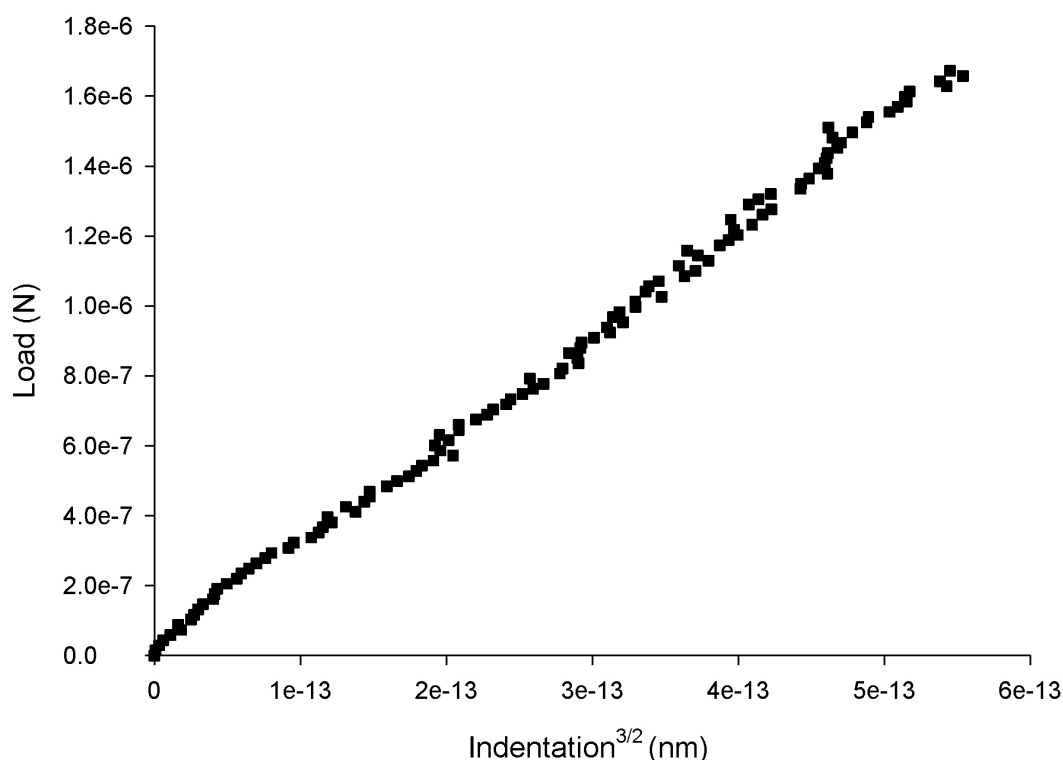


**Figure 2.7** A representative nanoindentation plot of loading force versus indentation obtained from an AFM experiment

From the plot of loading force versus indentation<sup>3/2</sup> a gradient is obtained. Alongside this value and the other parameters that include tip radius and Poisson's ratio, the Young's modulus is calculated using the Hertzian model of deformation (

Equation 2.5).

## 2.4 *In vitro* Testing of Inhaled Drug products

In order to assess the performance of inhaled drug products, *in vitro* techniques utilise the principles of particle impaction and impingement (de Boer et al., 2002). The US and European Pharmacopeia describe five different cascade impactors/impingers suitable for the characterisation of fine particles and selection of appropriate technique is based on the product being tested and the detail of particle size required from the assay. These techniques provide measurements based on the aerodynamic particle size of the materials being tested, taking into account particle shape, size density and viscosity. Moreover, they provide a means of recovering and quantifying the amount of active

pharmaceutical ingredient contained in the aerosol cloud, separate from the particle size distribution of other excipients. For these reasons, these techniques are routinely used in the development and quality control of DPIs.

#### 2.4.1 Next Generation Impactor (NGI) Testing

The principle mode of operation for cascade impactors, with respect to DPIs, relies on the aerosolisation of a unit dose that is drawn through an impactor by means of a laminar air stream. The aerosol stream passes through a series of stages within which nozzles or jets are directed towards plates of impaction. Particle deposition on each stage is dependent on its aerodynamic size and as each stage becomes progressively smaller as a function of jet/nozzle size, particle deposition becomes finer until all remaining particles are collected on a filter stage (Mitchell et al., 2007).

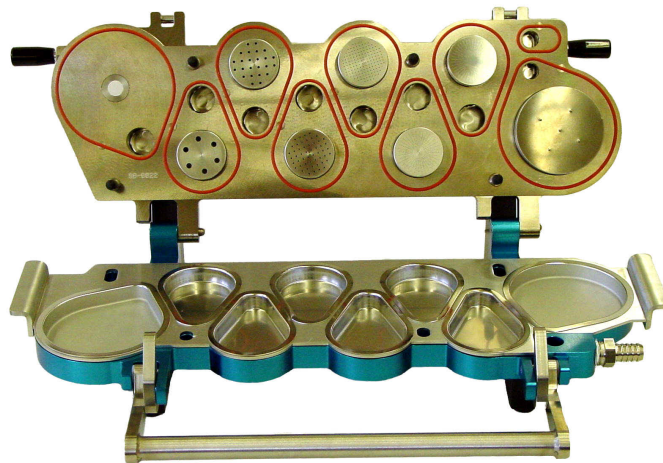


**Figure 2.8 Next Generation Impactor (NGI) (Adapted from <http://www.mspcorp.com>)**

The Next Generation Pharmaceutical Impactor (NGI), shown in Figure 2.8, was launched in 2000 as a result of developments by a group of prominent pharmaceutical companies to produce a device specific for pharmaceutical inhaler testing. It comprises of seven stages, plus a micro-orifice collector (MOC) and operates by vacuum pump at a range of 15 – 100 L.min<sup>-1</sup>. A standardised induction port containing a 90° bend is connected to the inhaler device via a mouthpiece adapter and entrance of the NGI in order to mimic the human throat. A vacuum pump is then set to a desired flow rate in order to

produce a reproducible pressure drop across the inhaler and actuated to draw a specific volume of air under sonic conditions.

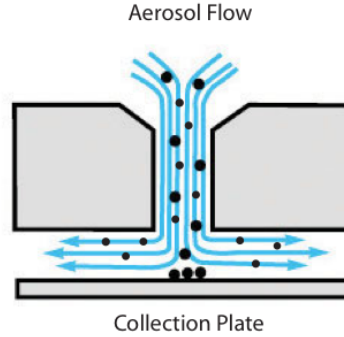


**Figure 2.9** A schematic representation of particle impactation through a NGI nozzle (Adapted from <http://www.copleyscientific.com>)

Within the NGI, particle deposition (illustrated in Figure 2.9) occurs as a result of two forces; hydrodynamic forces caused by airflow changes and particle momentum. For a set nozzle diameter and flow rate, particles will impact on a collection plate. The efficiency with which particles of varying size impact onto a given stage follows a sigmoidal function and the cut-off diameter give for each stage is described as the aerodynamic diameter for which 50% of particles impact (Marple et al., 2003). The cut-off diameter of each stage can be described using Stokes' law (Mitchell and Nagel, 2003) (Marple et al., 2003):

$$\sqrt{C_{50}d_{50}} = \sqrt{\frac{9\pi\mu n_n W^3}{4\rho_{ae}Q}} \cdot \sqrt{St_{50}}$$

**Equation 2.9**

where  $\mu$  is the air viscosity,  $n_n$  is the number of nozzles on the stage,  $\rho_{ae}$  is unit density (i.e., 1 g.cm<sup>3</sup>),  $Q$  is the total volumetric flow rate through an impactor stage and  $St_{50}$  is the Stokes number at 50% collection efficiency.

When operated at a flow rate of 60 L.min<sup>-1</sup>, the cut-off diameters of each NGI stage exhibit as follows:

- Throat and pre-separator: >12.8  $\mu\text{m}$
- Stage 1: 8.06 – 12.8  $\mu\text{m}$
- Stage 2: 4.46 – 8.06  $\mu\text{m}$
- Stage 3: 2.82 – 4.46  $\mu\text{m}$
- Stage 4: 1.66 – 2.82  $\mu\text{m}$
- Stage 5: 0.94 – 1.66  $\mu\text{m}$
- Stage 6: 0.55 – 0.94  $\mu\text{m}$
- Stage 7: 0.34 – 0.55  $\mu\text{m}$
- MOC 0.14 – 0.34  $\mu\text{m}$

The fine particle dose (FPD) can, therefore, be defined as the mass of drug deposited on stage 3 and below (<4.46  $\mu\text{m}$ ).

## **Chapter 3: Investigation of the Mechanical and Surface Interfacial Properties of Long-Acting $\beta$ 2 Agonists and Inhaled Corticosteroids**

### **3.1 INTRODUCTION**

Successful delivery of active pharmaceutical ingredients (APIs) to the lung using dry powder inhalers (DPI) requires particles to be less than 5  $\mu$ m. As a result, APIs intended for delivery to the lungs usually undergo intense processing using air-jet mills to reduce the particle size of the primary API crystals to enable delivery of the therapeutic agent to this region. These micronised particles of the API are then blended with large carrier particles of lactose monohydrate to form an adhesive mixture, which enables accurate metering of the dose and improves flow properties to aid device filling. The force generated upon the patient's inspiration then aids the fluidisation and de-aggregation of the fine API particles from the lactose.

The complex nature of the surface interfacial interactions between drug and excipient within a DPI blend governs the overall relationship between device and de-aggregation efficiency of the formulation and therefore, directly influences the functionality and therapeutic effectiveness of the drug product. Subtle variations in the processing of materials for inclusion in DPI drug products will impact the surface interfacial free energy of the components, which may affect the performance and efficacy of the final drug product. It is, therefore, important to understand the relationship between material processing and material physicochemical properties to produce DPI drug products with the desired performance and stability attributes.

Current pharmaceutical manufacturing processes of APIs for use in DPI drug products remains empirical and are not designed efficiently with the desired functionalities. The future of pharmaceutical manufacturing of APIs for DPIs,

therefore, is the generation of products with well-defined properties and functionality. This is the primary goal of pharmaceutical product engineering, which is achieved through control of the 'property function' of a product.

The 'property function' was initially defined by Rumpf and further developed by Peukert (Vogel and Peukert, 2005) as the relationship between the physicochemical properties of particulate systems (*i.e.*, particle size, morphology, surface properties) and product properties. A further consideration in producing products with well-defined properties is the 'process function', which relates specific process parameters (*e.g.* air-jet micronisation) to the physicochemical properties of the product (Vogel and Peukert, 2005). Hence, both the process and property functions must be known, understood and controlled in order to achieve products with defined functionality and properties that have been built in by design (Vogel and Peukert, 2005).

Current pharmaceutical manufacturing strategies for DPI dosage forms, generally involve the engineering of the API into specific crystalline forms. The API crystals are then processed into particles to the required particle size range using destructive 'top-down' strategies such as air-jet milling and then formulated into dosage forms. Although it is possible to control particle size of materials using such processes, the control of particle surface properties and morphology is extremely difficult. The inability to control surface properties of micronised materials is directly related to variability in the performance of the drug product, because small differences in batch-to-batch preparations can result in extreme variations in surface properties of processed materials and therefore, equivalent batches may possess varying property function (Feeley et al., 1998).

Furthermore, there is a paucity of data relating the physicochemical properties of the primary API crystals on downstream secondary processing of the materials by air-jet milling and the resultant affect on formulation structure and product functionality. Hence, to control the specific performance and stability properties of DPI dosage forms, the central product design principle in DPI manufacturing must focus on tailoring the physicochemical and mechanical



properties of the primary API crystals to enable careful control of property function of the secondary processed API particles and therefore, drug product performance and stability.

Crystallisation processes are routinely used in the isolation and purification of APIs, governing the physicochemical properties of the resulting crystalline material. APIs produced in this manner are significantly larger than those required for respiratory drug delivery and therefore, require comminution of the primary crystals in order to produce a particle size distribution (PSD) required for respiratory drug delivery. Suitable techniques such as fluid air-jet-milling rely on overcoming the material function of individual particles in order to fracture and break up larger material into smaller particles within a turbulent airflow. The high levels of stress placed on the feed materials, combined with the relative inefficiency of this unit process leads to an inhomogeneous power input throughout the bulk, often resulting in reduced crystallinity of the output material. These energy differences, often found at the surface of individual particles contribute to instability of micronised formulations over time. Characterisation of key mechanical properties of crystalline product is therefore, essential in understanding the milling behaviour of different materials, reducing the time and cost of milling studies and aiding the transferability of processes and equipment. Understanding the differences between the mechanical properties of APIs therefore, aids fundamental understanding relating to the variability of this property and possible future processing parameters of these materials.

Three key parameters have previously been reported to determine the milling efficiency of organic crystalline materials; Young's modulus ( $E$ ), Hardness ( $H$ ) and critical stress intensity factor ( $K_c$ ). The hardness of a material represents resistance to plastic deformation and has been investigated closely alongside the critical stress intensity factor and has been shown to empirically differentiate between samples, but not directly represent milling behaviour. The resistance to elastic deformation of a given material is represented by the Young's modulus and has been reported to vary significantly between different APIs and different polymorphs. Moreover, the Young's modulus of a material affects the

absorption and dissipation of energy transferred to it from a given process, such as comminution. For effective milling of these materials, formation and propagation of cracks, and therefore the reduction of particle size, will occur as a result of overcoming the elastic properties of individual particles. A low Young's modulus will represent a highly elastic material that in theory will have greater resistance to particle size reduction by milling.

Early methods of Young's modulus analysis relied on bulk testing of powder samples using three and four point beam bending where compacts of materials being investigated are produced to different porosities. Flexure measurements extrapolated to zero porosity can be used to calculate Young's modulus value but neglect the effects of work hardening during compaction and fragmentation or bonding mechanisms, often making results unusable or unreliable. This destructive process requiring large quantities of material and the time-consuming nature of these experiments led to a need to develop better techniques in determining the elastic properties of crystalline material with minimal sample preparation or product loss.

Development of micro and nano indentation techniques using single crystals enables direct investigation of individual particles selected from a powder bulk. Microindentation relies on placing loading forces onto individual crystals using sharp indenters followed by investigation of the indentation using microscopy in order to characterise mechanical properties. Limited by use of large crystals grown specifically for the test, often non-representative of the test sample, and the inability to accurately determine the elastic response of a material from unloading, specific indentation instrumentation devices were developed. These systems enable higher load sensitivity using smaller indenters – resulting in reduced loading forces and the direct testing of batch material relevant to the pharmaceutical product. In a typical experiment, a sharp tip of known geometry, is loaded and unloaded onto a sample at a controlled rate and force while constantly measuring the mechanical response of the sample. Extrapolation of the unloading curve is performed using parameters deduced by Sneddon or use of Oliver and Pharr methods (Jalili and Laxminarayana, 2004). Though these indentation methods require the use of sharp indenting probes in a small area,

the pressure placed on samples results in plastic deformation and can be seen by the dissimilar load and unloading profile recorded by these instruments. Extraction of the Young's modulus from a loading profile may not therefore, be representative of the original material.

The atomic force microscope (AFM) has emerged as a useful tool in high-resolution characterisation of micro and nano-scale interactions between cantilever probes and sample substrates. Atomic force microscopy has allowed the investigation of nanoNewton forces at nanometre indentation depth of organic crystalline material, revealing the nanomechanical properties of materials.

The aim of this study was to determine the Young's modulus of API and excipient crystals utilised in inhaled drug delivery. Furthermore, the cohesive-adhesive surface interfacial properties of the secondary processed micronised form of the APIs were determined against an inert highly orientated pyrolytic graphite (HOPG) surface.

## 3.2 METHODS AND MATERIALS

### Materials

Salmeterol xinafoate and fluticasone propionate were supplied by Merck Generics (Potters Bar, UK). The formoterol dihydrate and budesonide was supplied by (Sicor, Santhia, Italy). Lactose monohydrate was obtained from (DOMO, Borculo, Netherlands). All solvents used were supplied by Fisher Scientific UK (Loughborough, UK) and were of at least HPLC analytical grade. Where stated, water was ultra pure produced by reverse osmosis (MilliQ; Millipore, Molsheim, France).

#### 3.2.1 Crystal Substrate Crystallisation

Identifying the differences in Young's modulus of pharmaceutically relevant APIs required selection of drugs used in the field of inhaled drug delivery. Two long acting beta-2 agonists (LABAs) salmeterol xinafoate and formoterol fumarate dihydrate were chosen alongside two glucocorticosteroids, fluticasone propionate and budesonide. For comparison, a common excipient used in DPI formulations, lactose monohydrate was also included in this study (Table 3.1).

**Table 3.1 Crystalline substrates grown for AFM measurements**

Substrate	Class
Lactose monohydrate	Excipient
Salmeterol Xinafoate	LABA
Budesonide	Glucocorticosteroid
Fluticasone Propionate	Glucocorticosteroid
Formoterol Fumarate Dihydrate	LABA

In order to produce uniformly smooth crystal surfaces for reproducible mechanical measurements and suitable for cohesive-adhesive measurements, individual substrates were grown using primary nucleation on circular microscope glass coverslips (diameter 12mm, Agar Scientific, Essex, UK).

Briefly, saturated solutions of each sample were prepared in sealed glass vials using a suitable solvent and an individual drop was placed on to the glass slip by passing the solution through a 0.22  $\mu\text{m}$  PTFE membrane syringe filter (Whatman Inc., Clifton, NJ, USA). In the case of lactose and salmeterol, a second glass coverslip was placed on top of the droplet to create a “sandwich” to allow nucleation and crystal growth. Upon the presence of crystals, the two coverslips were cleaved apart to reveal substrate crystals on each side. For fluticasone, budesonide and formoterol however, the cover slip was placed onto a glass vertical post support over a crystallisation vessel that contained a miscible non-solvent. A saturated droplet of the respective drugs was then placed onto the coverslip. A glass beaker was then used to seal the system and allowed equilibration of the vapour phases ensuring controlled nucleation and crystal growth (sitting-drop method) (Begat et al., 2004a) . After a given amount of time required to complete crystallisation, the glass cover slips were removed and affixed to magnetic AFM stubs using epoxy glue (Araldite Precision; Huntsman International, UK) prior to analysis. Details of both methods are given in Table 3.2.

**Table 3.2 Details of the crystallisation solvents and methods used in producing substrate crystals for analysis**

Substrate	Solvent	Non-Solvent	Method
Lactose	Water (100°C)	n/a	1 g/mL (sandwich)
Salmeterol xinafoate	Methanol (25°C)	n/a	75% API saturation (sandwich)
Budesonide	N,N- dimethylformamide	Ethanol	(sitting-drop)
Fluticasone propionate	Acetone	Water	(sitting-drop)
Formoterol fumerate dihydrate	Methanol	25% methanol/75% acetone	(sitting-drop)

### 3.2.2 Topographical and Mechanical Analysis using Atomic Force Microscopy (AFM)

Investigation of the nanoscale properties of the crystalline substrates was performed using an atomic force microscope (Nanoscope IIIa and J-scanner (all Bruker Nano AFM, Santa Barbara, CA, USA) in force or tapping mode. Two different AFM probes were used in this study, one with large indenting spherical tip (R150-NCL, Nanosensors, Neuchatel, Switzerland) and one with smaller spherical tip (Veeco-TESP, DI, Cambridge, UK), both of similar nominal cantilever stiffness.

### 3.2.3 AFM Probe Tip Size Characterisation

For accurate extrapolation of AFM force-distance data for Young's modulus determination, the true radius of the indenting tip must be known. Though in

many cases the tip radius of these probes are provided by the supplier, high levels of uncertainty in these values, compounded by batch-to-batch variations, in certain cases 25-50%, can lead to wide ranges in modulus measurements using this number alone.

In this study, qualitative observation of the tip radius was performed using scanning electron microscopy (SEM) at the apex of each fresh probe. The probe from each manufacturer was affixed to an SEM tray using Tempfix (Agar Scientific, Essex, UK) and then coated with gold for two minutes (Edwards Sputter Coater, Crawley, UK) prior to imaging using SEM (Joel JSM6480LV, Tokyo, Japan) under an accelerating voltage of 20 kV.

Accurate determination of the tip radius was performed using a tip-characterisation grating (TGT01; NT-MDT, Moscow, Russia) in which the probe being investigated is raster scanned over the test grating composed of a uniform array of sharp spikes which in turn, reverse images the investigational tip. This image was then deconvoluted to determine tip radius using image analysis software (SPIP Image Metrology ApS, Lingby, Denmark). This process was performed before and after indentation measurements to ensure measurements had not altered tip parameters.

#### **3.2.4 Young's Modulus Determination**

Prior to indentation, suitable areas of investigation were identified using tapping mode (TM) AFM. Areas of 5 x 5  $\mu\text{m}$  with suitably smooth surfaces, as determined by measurements of surface roughness,  $R_a$  (mean surface roughness) and  $R_q$  (root mean squared surface roughness), were selected for nanoindentation measurements.

In order to calibrate the AFM nanoindentation system, a constant compliance gradient was obtained by recording a force-distance curve between the silicon AFM probe and silica (Agar Scientific, Cambridge, UK). The silica provided a suitably hard and non-elastic reference surface. The spring constant of the cantilever was measured using a thermal tuning method (Sader et al., 1995).

The same AFM probes were then used to assess the mechanical properties of each crystal using a trigger threshold of 40 nm and a scan rate of 0.5 Hz, indenting in a 3x3 grid with a distance of 1  $\mu\text{m}$  between each measurement (n=9). The force-distance curves were exported and processed using custom software to convert recorded voltage measurements into tip deflections alongside relative piezo displacements. At a predetermined loading force, by subtracting the deformation profile of the suitably hard reference surface from the sample deformation profile, the true deformation of the sample, hence the indentation depth was calculated. Plotting the loading force against indentation<sup>3/2</sup>, the gradient can be used to determine the Young's modulus for each individual indentation using the Hertzian model of deformation:

$$E = \frac{3(1 - \nu^2)k\Delta z}{4\delta^{3/2}R^{1/2}}$$

**Equation 3.1** The Hertz model of deformation

### 3.2.5 Cohesive-Adhesive Balance (CAB) Measurements

Micronised particles of each API were attached onto standard V-shaped tipless cantilevers with pre-defined spring constants (DNP-020, DI, CA, USA) using an epoxy resin glue (Araldite, Cambridge, UK), as previously described (Begat et al., 2004b). Five probes were prepared for each drug, and all probes were examined with an optical microscope (magnification 50x) to ensure the integrity of the attached particle, before allowing the thin layer of glue to dry.

The substrate was loaded on to the AFM scanner stage, which was enclosed in a custom-built environmental chamber, in which the ambient conditions were maintained at a constant temperature of 25 °C ( $\pm 1.5$  °C) and relative humidity of 35 % RH ( $\pm 3$  %). The interaction forces were measured by recording the deflection of the AFM cantilever as a function of the substrate displacement (z) by applying Hooke's Law ( $F = -kz$ ). Individual force curves (n = 1024) were conducted over a 10  $\mu\text{m}$  x 10  $\mu\text{m}$  area at a scan rate of 4 Hz and a compressive load of 40 nN. Parameters were kept constant over the study. Spring constants



of the cantilevers used employed in this study were measured using the thermal tuning method.

Due to the vast array of force data generated, custom-built software was used to extract data contained within each force-volume measurement. The collected force data was analyzed to ensure normal distribution, indicating uniform contact between the drug probe and excipient substrate. Arithmetic mean and standard deviation were obtained from force data and used to produce CAB plots for the interactions of the different substrates to HOPG.

### **3.3 RESULTS AND DISCUSSION**

#### **3.3.1 Quantification of Spring Constant and Contact Radius of AFM probes**

In order to obtain accurate values from indentation profiles and to allow direct comparison between different indenting AFM cantilever probes, the stiffness and contact radius must be determined. It is known that nominal values for both properties can vary significantly and therefore a single probe from each batch was used in this study and that same probe was subsequently characterised.

SEM investigation provided qualitative assessment of probe radius and clearly highlighted differences in probe geometry, showing the sharper tip of Veeco-TESP probes, compared to the blunter Nanosensors-R150 tip (Figure 3.1). At higher magnifications however, stress placed on cantilevers from the electron beam caused flexing of the probe and resulted in blurring of the tip. This effect, coupled with the unknown deposition thickness of gold from prior coating allowed only indicative measurements of probe radius.

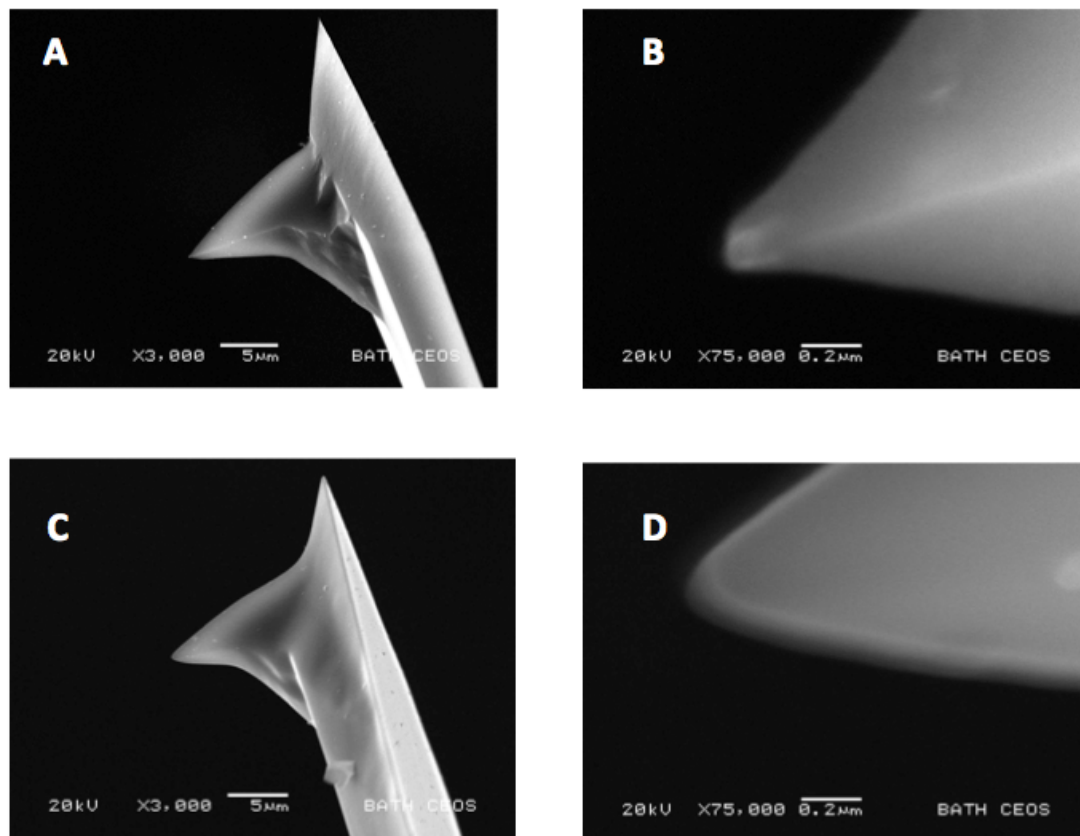


**Figure 3.1** Representative scanning electron micrograph images of the two different AFM cantilever probes used for nanoindentation in this study (A-B: Veeco TESP; C-D: Nanosensors R150-NCL) qualitatively indicating differences in probe tip-radius

A non-destructive and accurate method of determining probe radius involved use of a tip characterisation grid. Deconvolution of the image produced from this grating confirmed the SEM observations and assigned a tip radius of 55 nm and 318 nm for the Veeco and Nanosensor probes, respectively. Details of the radius and cantilever stiffness are shown in Table 3.3.

**Table 3.3** The two different AFM probes used in this study <sup>(a)</sup> measured by thermal tuning, <sup>(b)</sup> using the manufacturers quoted value)

Probe	Tip Radius (nm)	Spring Constant (N/m)
TESP	55	36.0 <sup>a</sup>
Nanosensors	318	36.5 <sup>b</sup>

### 3.3.2 Determination of Young's Modulus of Crystalline Substrates

Areas suitable for indentation were located on each crystal substrate and a 5 x 5  $\mu\text{m}$  image was taken in tapping mode to confirm nano-scale smoothness. Mean roughness ( $R_a$ ) and root mean squared roughness ( $R_q$ ) values are shown in Table 3.4. Optical microscopy revealed well-defined crystals of all samples and atomic force microscopy investigation confirmed smooth crystal substrates, suitable for mechanical and CAB analysis (Figure 3.2).

**Table 3.4 Surface roughness measurements for all substrates using TM-AFM ( $R_a$ , Mean roughness;  $R_q$ , Root mean squared roughness)**

Substrate	Image $R_a$ (nm)	Image $R_q$ (nm)
Lactose monohydrate	0.137	0.231
Salmeterol Xinafoate	0.317	0.482
Budesonide	0.484	1.051
Fluticasone Propionate	0.418	0.626
Formoterol Fumarate Dihydrate	0.556	0.898

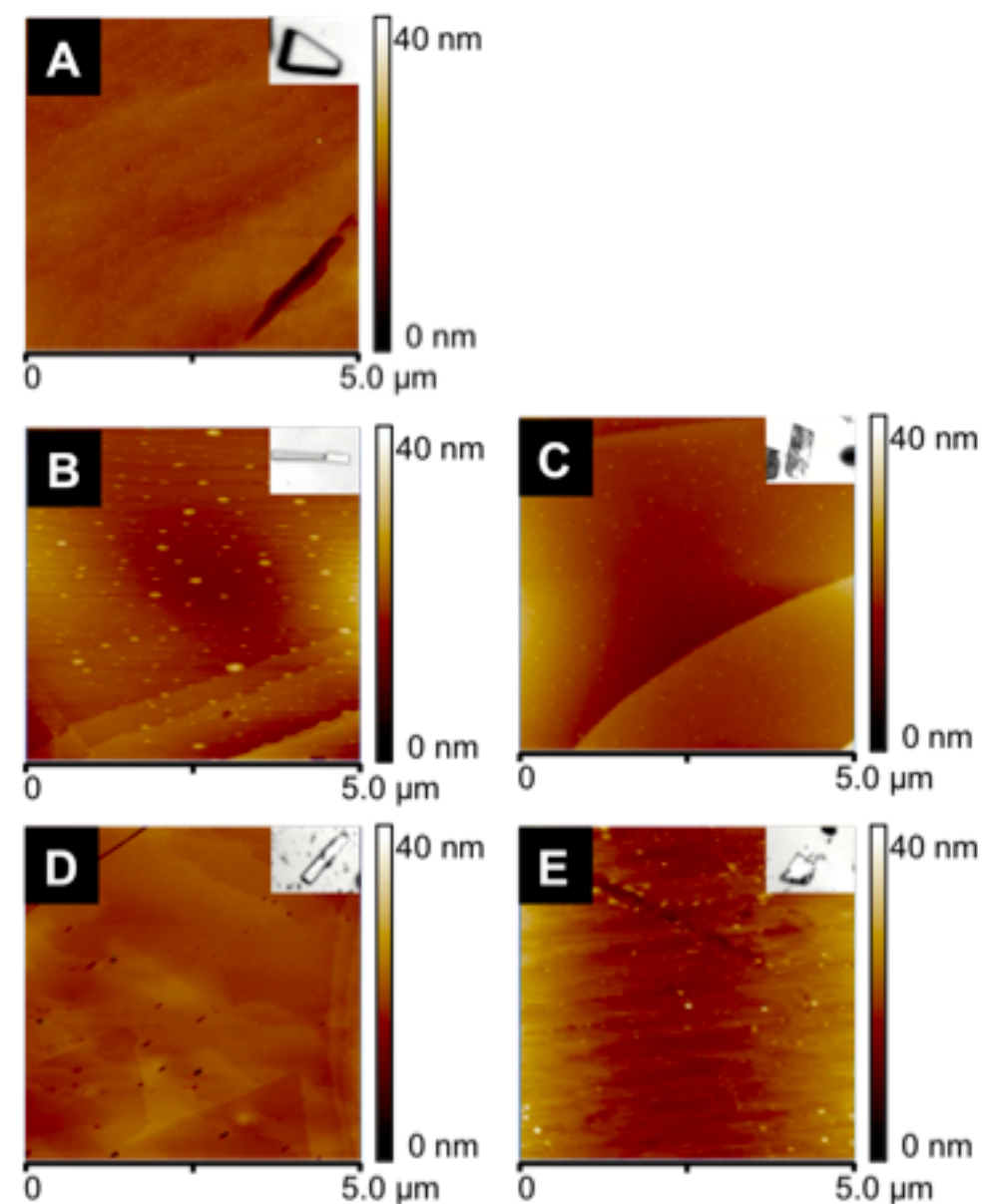


**Figure 3.2** Representative optical and AFM images of all samples prior to indentation (A) Lactose, (B) Salmeterol, (C) Budesonide, (D) Fluticasone, (E) Formoterol

Initial observations of indentation profiles suggested plastic deformation of the sharper Veeco-TESP tip into the budesonide, fluticasone and formoterol crystals, resulting in non-linear loading profiles and visual observation of crystal surface disruption after grid indentation. When repeated measurements were performed using the Nanosensor probe with a larger tip radius, and therefore, reduced loading pressure, Hertzian deformation was observed which allowed data to be modelled within the elastic region. Representative images of the crystal surfaces of a single lactose and fluticasone propionate crystal investigated using the respective AFM probes are shown in Figure 3.3.

Regardless of probe used, the sharp and forceful initial contact made with each tip was observed to cause non-elastic damage to the surface and therefore, data from such regions were not included in the measurement of crystal mechanical properties.

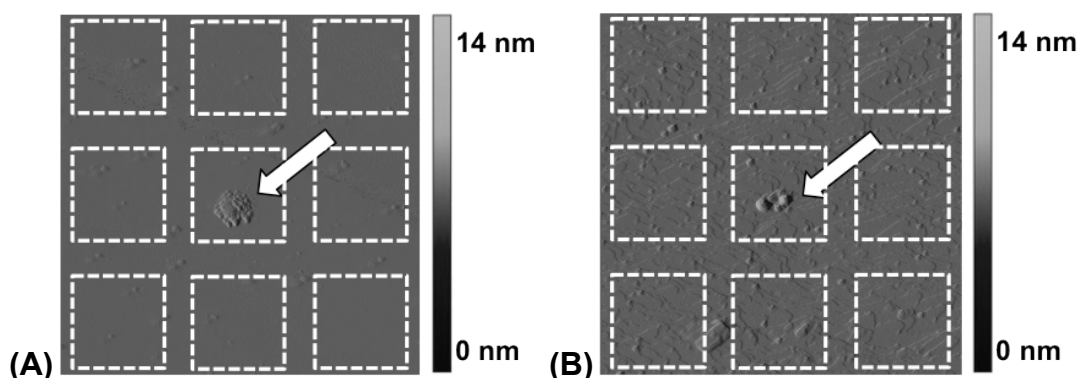


**Figure 3.3 AFM TM images of crystal surfaces after nanoindentation with the respective indenting probes (A: Lactose-TESP, B: FP-Nanosensors). The white squares indicate areas of loading and the arrows indicate initial point of probe contact which were unsuitable for Hertzian extrapolation**

Clear differences in the indentation profiles of the different crystals and indenting probes were observed as shown in Figure 3.4. Greater loading forces on the lactose crystal surface resulted in smaller indentation depths, which suggested that lactose had high resistance to elastic deformation. In comparison, low loading forces on the salmeterol xinafoate crystal resulted in large indentation depths, which suggested that the crystal had low resistance to elastic deformation.

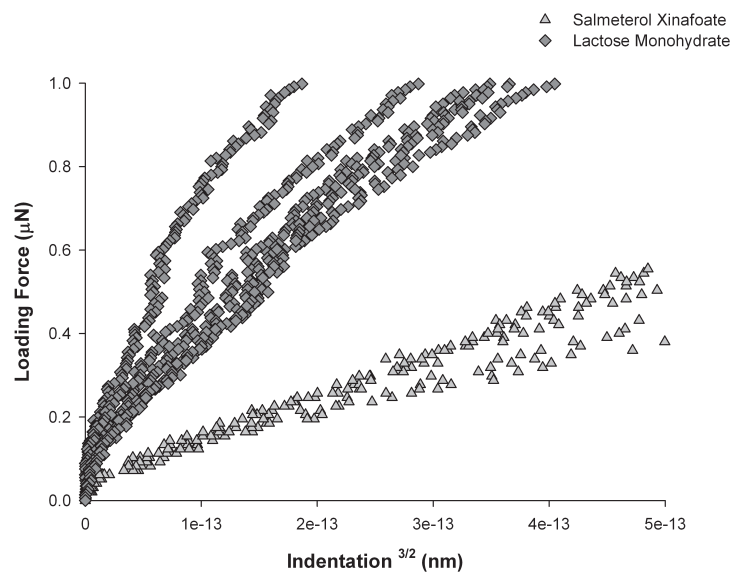


**Figure 3.4 Individual loading forces plotted against the indentation depths of salmeterol and lactose monohydrate crystals using a Veeco-TESP AFM probe**

The indentation profiles of budesonide, formoterol and fluticasone are shown in Figure 3.5. These data suggest that formoterol had the lowest resistance to elastic deformation followed by fluticasone propionate. In contrast, budesonide had a greater resistance to elastic deformation.

The gradients of the individual loading curves shown in indentation plots in Figure 3.4 and Figure 3.5, were extrapolated and fitted to the Hertzian model of deformation to produce Young's modulus values for each sample. The Young's modulus measurements of each crystal are shown in Figure 3.6 and summarised in Table 3.5.

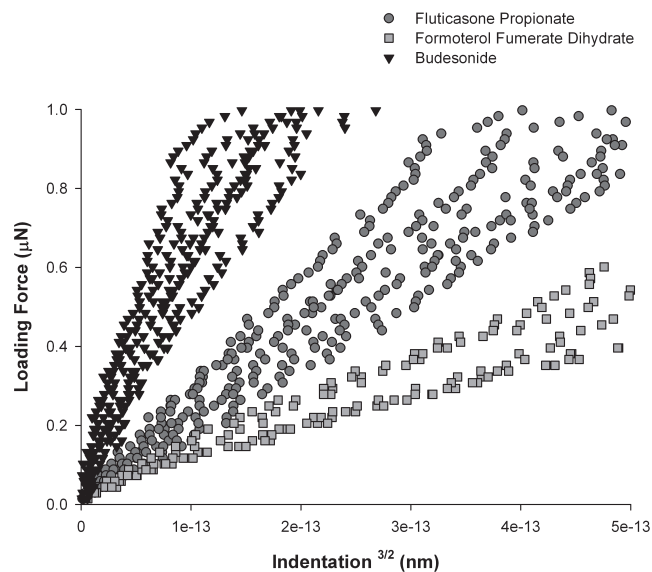


**Figure 3.5 Individual loading forces against the indentation depths of fluticasone, budesonide and formoterol crystals using a Nanosensor probe AFM probe**

These data show that the Young's modulus of each of the crystals was different and therefore exhibited different mechanical properties. The rank order of the Young's modulus measurements from those of the highest stiffness (high Young's modulus) to the lowest followed the rank order lactose > salmeterol and budesonide > fluticasone > formoterol.

The different mechanical properties of the crystals may be related to the kinetics of the specific crystallisation process for each crystal. Surrounding solvent environment and energy input all affect the external morphology of individual crystals, which in turn have their own unique physicochemical and mechanical properties. Solvent inclusion, defects and imperfections within the lattice may also play an important part in determining the mechanical parameters of the material.



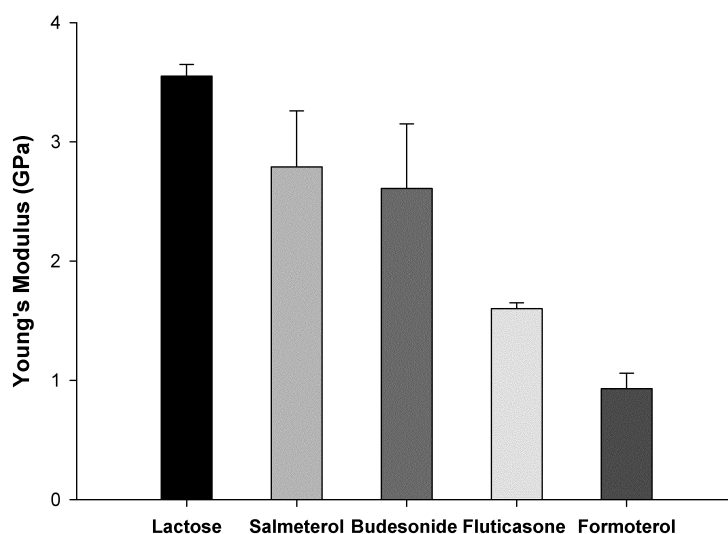


**Figure 3.6** Young's modulus measurements of different pharmaceutical crystals determined by AFM nanoindentation

**Table 3.5** Measured Young's modulus values for each crystal substrate using AFM nanoindentation

Substrate	Young's Modulus (GPa)
Lactose monohydrate	3.55 ± 0.10
Salmeterol xinafoate	2.79 ± 0.47
Budesonide	2.61 ± 0.54
Fluticasone propionate	1.60 ± 0.05
Formoterol fumerate dihydrate	0.93 ± 0.13

In addition to determining the nanomechanical properties of the primary API crystals, the physicochemical and surface interfacial properties of the secondary-processed micronised forms of the same APIs were determined.

The particle size and specific surface area are shown in Table 3.7, which indicate that the APIs were within the 1 – 5  $\mu\text{m}$  range required for pulmonary drug delivery. Analysis of the specific surface area of the APIs suggests that micronised budesonide had the largest surface area, which was then followed by micronised salmeterol xinafoate and micronised formoterol fumerate

dihydrate, respectively. In contrast, the specific surface area of fluticasone propionate was the smallest of all the samples analysed. The surface interfacial properties of the APIs were measured with respect to highly ordered pyrolytic graphite (HOPG) using the CAB approach to colloidal probe AFM. The CAB plots and summary of CAB ratio of the APIs are shown in Figure 3.7 and Table 3.7, respectively. The measured CAB ratio of sample fluticasone propionate (FP) with respect to HOPG was 1.13, which suggests that cohesive FP-FP interactions were 1.13 times greater than the FP-HOPG. The interactions of formoterol fumerate dihydrate produced a CAB ratio of 0.86, which suggests that adhesive interactions of formoterol to HOPG were 1.16 times greater than the cohesive interactions of formoterol. Similarly, the CAB ratio of salmeterol was 0.73 with respect to HOPG, which suggests that the adhesive interaction of salmeterol to HOPG were 1.37 times greater than the cohesive interactions of salmeterol. The CAB ratio of budesonide suggested that the adhesive affinity of budesonide to HOPG was 1.54 times greater than the cohesive budesonide-budesonide interactions. These data suggest that budesonide had the highest adhesive tendency to HOPG.

These CAB ratio data alone do not provide any quantitative discrimination of the cohesive strengths of these APIs in relation to their adhesion to HOPG. Since the dispersive surface energy of HOPG has been determined as 71 mJ.m<sup>-2</sup> and the dispersive surface energy of the micronised drug material is available from reference data shown in Table 3.6, the cohesive strength of each API may be estimated using equations Equation 1.15, Equation 1.16 and Equation 1.18 shown in chapter 1, and using the following derived equations:

$$F_{Drug-Substrate} = 3\pi R^* \cdot \sqrt{(\gamma_1\gamma_2)^{LW} + (\gamma_1\gamma_2)^P}$$

Equation 3.2

$$F_{Drug-HOPG} = 3\pi R^* \cdot \sqrt{(\gamma_1\gamma_3)}$$

Equation 3.3

where  $\gamma$  is the dispersive surface energy of HOPG. Since the CAB ratio is calculated from the ratio of the force of cohesion to the force of adhesion, and HOPG is known to not have a polar contribution, the cohesive strength of the API samples interacted with this substrate can be calculated using the following equation:

$$\sqrt{(\gamma_1\gamma_2)^{LW}} + \sqrt{(\gamma_1\gamma_2)^P} = CAB \cdot \sqrt{(\gamma_1\gamma_3)^{LW}}$$

**Equation 3.4**

Calculated values for the cohesive strength for each investigated API can be seen in Table 3.6. These data suggest the following rank order of the cohesive strength of the APIs;

$$FP > FFD > SX > BUD$$

**Table 3.6** Calculated cohesive strength values of API samples interacted with HOPG using AFM colloidal probe microscopy. IGC reference values were provided from a previous study (Jones et al., 2008)

Drug Substrate	IGC Reference Value (mJ.m <sup>-2</sup> )	Calculated Cohesive Strength (mJ.m <sup>-2</sup> )
FP	60.8	74.3
BUD	60.2	42.5
SX	47.9	42.6
FFD	57.5	54.3

The calculated cohesive strength is a combination of the dispersive and polar components of the surface energies of the micronised and crystalline drug substrates. These data indicate the polar van der Waals interactions may have an influence on these drug-drug cohesive interactions.

The nano-mechanical analysis of the APIs suggested significant differences in their respective crystalline Young's moduli. These data suggest that the efficiency of further processing of the crystals by air-jet micronisation may be

different. For example, the lower Young's modulus of FP indicates that the material may undergo elastic deformation more readily upon milling than SX or lactose, which have a higher Young's modulus and therefore, less likely to undergo elastic deformation.

Similarly, differences in the material surface interfacial properties of the micronised APIs in this study, with respect to HOPG highlighted the different cohesive strengths of the API. Since the interfacial properties of micronised materials play an important role in the formation of homogenous powder blends for inhalers and their subsequent disaggregation efficiency, robust characterisation of the API is necessary. The different cohesive strengths of the APIs are therefore expected to affect their functionality in DPI formulations.

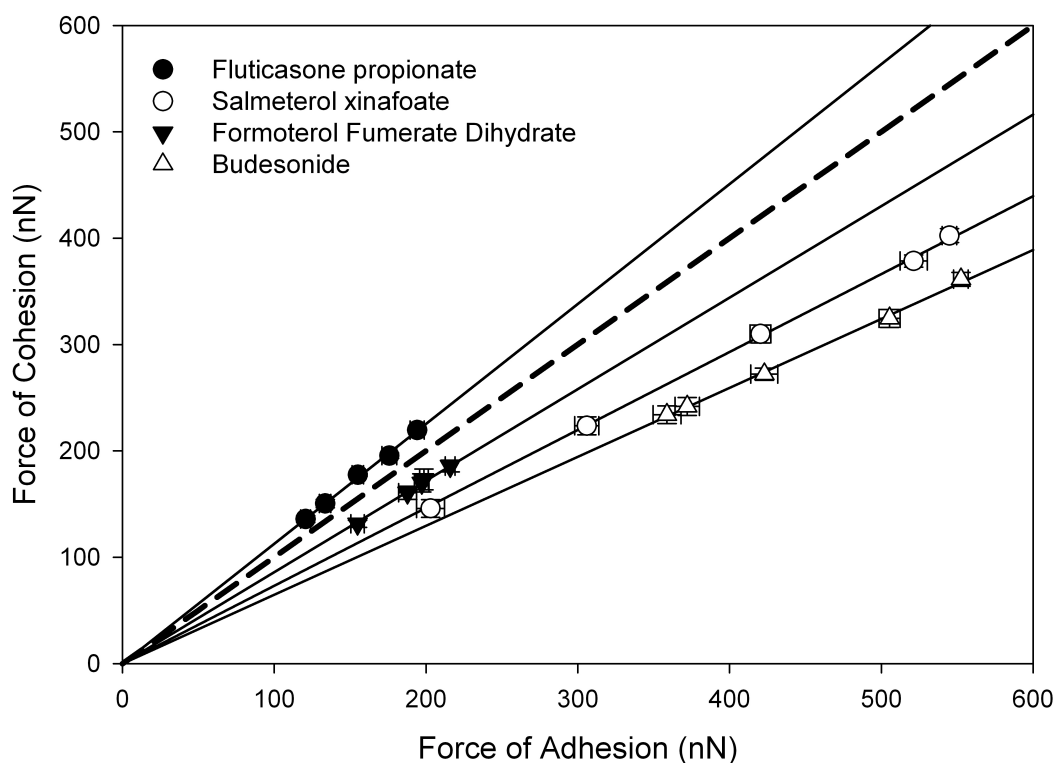


**Figure 3.7 Cohesive-adhesive balance of the different inhaled APIs with respect to Highly Ordered Pyrolytic Graphite (HOPG) where the dashed line represents a CAB ratio of 1.0**

**Table 3.7 Summary of the physicochemical properties and CAB ratios of the micronised form of the different APIs**

Substrate	Particle size ( $\mu\text{m}$ )			Specific Surface Area ( $\text{m}^2/\text{g}$ )	CAB Ratio $\pm$ S.D.	$R^2$
	$d_{10}$	$d_{50}$	$d_{90}$			
Salmeterol xinafoate	1.10	2.34	4.39	7.22	$0.73 \pm 0.01$	0.9966
Budesonide	1.11	2.49	4.41	8.92	$0.65 \pm 0.02$	0.9978
Fluticasone propionate	0.98	2.34	4.24	6.05	$1.13 \pm 0.01$	0.9966
Formoterol fumerate dihydrate	1.27	2.55	4.67	6.21	$0.86 \pm 0.02$	0.9940

### **3.4 CONCLUSIONS**

The atomic force microscope has been shown to be suitable for differentiating the differences in elastic response of pharmaceutically relevant crystals and will aid understanding of the processing behaviour of these materials. Additionally, this study has demonstrated that evaluation of the indentation profiles and topography of the resultant measurements is critical to selecting suitable indentation parameters in order to stay within the elastic constraints of the investigated material. The interfacial properties of these materials have also been seen to have differing properties and provide a further parameter upon which the functionality of micronised APIs may alter the performance of these materials when included within a DPI formulation.

## **Chapter 4: Investigation into the influence of primary crystallisation conditions on the mechanical properties and secondary processing behaviour of fluticasone propionate**

### **4.1 INTRODUCTION**

Carrier-based dry powder inhalers (DPI) are complex dosage forms, which are comprised of micronised drug particles (less than 5  $\mu\text{m}$ ) that are blended with coarse lactose monohydrate carrier particles. The fluidisation and entrainment of the formulation in the device is driven by the patient's inspirational force, which together with the resistance of the device, provide the de-aggregation energy to overcome the surface interfacial forces within a DPI blend to disperse the fine drug particles.

Conventional methods of producing drug for inclusion in DPI formulations begin with batch crystallisation processes, which routinely use an anti-solvent to precipitate or crystallise the drug. The use of an anti-solvent alongside mechanical agitation during crystallisation can lead to poor mixing and local levels of high supersaturation resulting in heterogeneous particle growth. This in turn can lead to variability in particle size and morphology of the crystalline material (Dhumal et al., 2009). The isolated primary crystals then undergo micronisation to reduce the overall drug particle size. The mechanical stresses created within the micronisation process, coupled with the relative inefficiency of this unit operation, highlight the importance of understanding the critical properties of the primary crystalline feed material, in order to produce materials for inclusion in the final drug product with defined specification and functionality.

The bulk crystallisation step of the API is primarily utilised to isolate and purify APIs. However, the possible influence of the physico-chemical properties of the primary API crystals on downstream secondary processing (e.g. micronisation)

and its resultant effect on formulation structure and product functionality is not well understood. The crystallisation process, however, is known to influence the mechanical properties of primary crystals (Liao and Wiedmann, 2005) and has been reported to have a strong influence on the micronisation behaviour of solids (Zugner et al., 2006).

The mechanical (elastic–plastic) properties of the crystalline API to be micronised play a fundamental role in determining the resistance to fracture. For the low variation in the hardness of organic materials, this property may define the degree of particle size reduction of the primary crystals. The Young's modulus represents a material's resistance to elastic deformation and has been reported to have a strong influence on the micronisation efficiency of pharmaceutical solids (Zugner et al., 2006). Materials with low Young's modulus tend to have low resistance to elastic deformation and therefore are difficult to micronise, whereas materials with a high Young's modulus micronise more efficiently owing to their greater resistance to elastic deformation. Materials that exhibit a low Young's modulus may therefore pose significant challenges during development of DPI drug products, as they tend to require multiple milling cycles to achieve the desired particle size specification. The process of multiple milling cycles may significantly impact the surface interfacial properties of the drug particles, which could result in formulations that are variable. Hence, determination and characterisation of the mechanical properties of primary drug crystals may help improve the efficiency of secondary micronisation processing of primary drug crystals, and therefore, provide drug particles with the desired properties for inclusion in the final drug product.

Use of commercially available nano-indenting platforms that apply a load via a sharp indenter and measure the elastic response, have been shown to measure differences in the elastic modulus of different pharmaceutical ingredients (Taylor et al., 2004b) and detect differences in this property as a function of crystallisation conditions (Liao and Wiedmann, 2005). The atomic force microscope (AFM) has emerged as an alternative tool in the assessment of nanoscale properties of pharmaceutical materials and has enabled the measurement of the Young's modulus by placing a load force on an



investigational material through an AFM cantilever of defined stiffness and possessing a probe tip of defined contact area (Fraxedas et al., 2002) (Perkins et al., 2007). The AFM based approach has been compared to an established nano-indenting instrument in order to determine the Young's modulus of lactose monohydrate crystals (Perkins et al., 2007). The work highlighted the advantages of this non-destructive AFM technique as a means of accurately obtaining the elastic modulus of pharmaceutically relevant materials. Furthermore, It appears that in most single particle loading situations, plastic flow occurs on the impacted surface, depending upon the relative mechanical strength at the contact region and this is then followed by cracking and fragmentation. In some studies, the processes of impact attrition of brittle crystalline particles have been likened to those occurring during the indentation cracking of such materials. This seems quite reasonable, as the fragmentation processes are a consequence of localised loading with stress conditions, which are fairly similar to those existing during the loading on a flat surface by a hard indenter. Therefore, nanoindentation studies by AFM may be a suitable approach to assess the mechanical properties of pharmaceutical solids. AFM nanoindentation has been used to quantify the elastic modulus of many pharmaceutical APIs. For example carbamazepine revealed differences in the Young's modulus for different polymorphs of the API, ranging from 2.69 to 5.18 GPa and suggested this parameter influenced the milling behaviour and the resulting interfacial properties of the micronised materials for each polymorph (Perkins et al., 2009).

Comminution of crystalline drugs can lead to significant changes in the physico-chemical nature on the surfaces of drugs (Buckton, 1997) (Brittain, 2002). The atomic force microscope enables the investigation of these changes through the use of a colloidal particle technique, interacting a cantilever based probe with nanometer and nanoNewton resolution (Cappella and Dietler, 1999). Using a tipless AFM cantilever and attaching a colloidal probe, interactions between a substrate sample and single micrometer sized particles, such as micronised APIs, can be investigated. This form of measurement has had significant implications to the field of DPI formulation, as the interactive forces between inter-particle components play a critical role in the behaviour of these mixtures

(Roberts, 2005). Two approaches are commonly used to assess these interfacial properties, quantifying the contact area of the attached colloidal particle (Hooton et al., 2003) or interacting the same colloidal probes with smooth surfaces of interest (Begat et al., 2004a).

The cohesive-adhesive balance (CAB) approach enables the evaluation of the cohesive and adhesive forces resulting on micronised materials for inclusion within DPI formulations against another component of the formulation (Begat et al., 2004c) and has been investigated alongside *in vitro* performance of DPI formulations (Hooton et al., 2006) (Jones et al., 2008). This assessment of APIs that have been secondary processed is routinely performed prior to formulation of the final product, yet the influence of the primary crystallisation process on these materials is not fully recognised.

The aim of this study was to assess the influence of different anti-solvent crystallisation processes on the mechanical properties of the resulting fluticasone propionate crystals and the effect these properties had on the micronisation and performance in both binary and combination based DPI formulations.

## 4.2 MATERIALS AND METHODS

### 4.2.1 Materials

Crystalline fluticasone propionate was supplied by Sterling (Perugia, Italy). All solvents used were of HPLC grade (Fisher Chemicals, Loughborough, UK). Ultra pure water was produced by reverse osmosis (MilliQ, Millipore, Molsheim, France). Inhalation grade of lactose monohydrate (SV003, Vehgel, Netherlands) was purchased from DMV-Fonterra.

### 4.2.2 Methods

#### ***Methodology for the crystallisation of fluticasone propionate***

Saturated solutions of fluticasone propionate were prepared in acetone at 21°C under continual stirring. The solutions were then filtered in heated labware using a 0.45 µm nylon membrane filter (Whatman, Brentford, UK) and introduced to a sealed glass crystallisation vessel continually stirred by an overhead stainless steel three blade stirrer with a water-jacket temperature control maintained at 21°C (K20; Haake, Karlsruhe, Germany). For the control sample (**A**), the drug was crystallised by controlled evaporation of the solution at 21°C. For the other samples, an excess of 3 different anti-solvents were added to the saturated solutions (**B, C and D**) at a rate of 50 ml/min followed by a reduction of jacket temperature of all samples to 5°C. Crystals were collected by vacuum filtration and allowed to dry under ambient conditions until a stable weight was achieved. The resulting materials were stored at 19°C over silica gel.

#### ***Particle Size Analysis***

Particle size distributions of all samples were measured in the wet state using a Sympatec HELOS and CUVETTE (Sympatec GmbH, Clausthal-Zellerfeld,

Germany) laser diffraction system using an R3 lens (0.5-175  $\mu\text{m}$ ). Approximately 20 mg of powder was suspended in HPLC grade cyclohexane containing 0.5% Lecithin (Lot: A0204330001, Acros Organics, Geel, Belgium) using sonication for 5 minutes and immediately transferred into a 50 ml cuvette to produce an appropriate optical concentration (10-25%). Each measurement was performed in triplicate and particle size analysis was performed using WINDOX 5.0 software CUVETTE (Sympatec GmbH, Clausthal-Zellerfeld, Germany).

### ***Scanning Electron Microscopy***

Particle morphology of all fluticasone propionate samples was investigated using scanning electron microscopy (SEM). Sample aliquots were fixed onto sticky carbon tabs (Agar Scientific, Cambridge, UK) followed by removal of excess powder using pressurised air. Samples were subsequently sputter coated with gold (Edwards Sputter Coater S150B, Edwards High Vacuum, Sussex, UK) to achieve a thickness of approximately 20 nm. Imaging was performed using a scanning electron microscope (JEOL JSM6480LV, Tokyo, Japan) using 15 kV accelerating voltage.

### ***X-ray powder diffraction (XRPD) analysis of crystalline fluticasone propionate samples***

To determine the X-ray powder diffraction (XRPD) pattern of the FP samples, all samples were analysed on a Bruker Powder Diffractometer (D8; Bruker AXS Inc., Madison, USA) using  $\text{CuK}\alpha$  radiation ( $\lambda = 1.54 \text{ \AA}$ ). The data were collected over a single  $2\theta$  sweep with range  $2\theta = 5 - 30^\circ$  and step size of  $0.025^\circ/\text{step}$  and step time of 1.5 seconds.

### ***Young's Modulus measurements of fluticasone propionate samples***

FP samples were mounted on to a freshly cleaved mica surface using an appropriate adhesive (Microstik, Agar Scientific, Stansted, UK), ensuring

particles were held immobile with the dominant crystal face exposed. Mica was pre-fixed to an AFM stub using an epoxy resin glue (Araldite Precision, Bostik Ltd, Leicester, UK). To calibrate the AFM nanoindentation system (Nanoscope IIIa and J-scanner (all Bruker Nano AFM, Santa Barbara, CA, USA), a constant compliance gradient was obtained by interacting a silicon probe AFM probe, with a tip radius of 318 nm and a spring constant of  $k = 36 \text{ N/m}$ , with a silica substrate, which has a suitably hard and non-elastic surface ( $E = 75 \text{ GPa}$ ). The spring constant was measured by the manufacturer using the Sader method (Clifford and Seah, 2005b), (R150-NCL, Nanosensors, Neuchatel, Switzerland).

The same AFM probe was then used to assess the mechanical properties of single crystal samples using a loading force of ( $2 \mu\text{N}$ ) and a scan rate of 0.5 Hz. Repeated force-distance measurements were performed on virgin areas of each crystal, orientated so that the dominant face with respect to the indenter was indented. The force-distance curves were exported and processed using custom-built software to determine the Young's modulus for each individual indentation.

For accurate extrapolation of AFM force-distance data to a Young's modulus value, the true radius of the indenting tip must be known. Tip radius determination was performed using a tip-characterisation grating (TGT01; NT-MDT, Moscow, Russia) in which the probe being investigated is raster scanned over the test grating composed of a uniform array of sharp spikes which in turn, produces a reverse image of the probing tip. This image was deconvoluted to determine tip radius, using a well-established technique using image analysis software (SPIP Image Metrology ApS, Lingby, Denmark) (Hutter and Bechhoefer, 1993) (Clifford and Seah, 2005a) (Hooton et al., 2004). This measurement was performed before and after indentation measurements to ensure indenting probe integrity was maintained. In this study, the hemispherical probe radius was determined to be 318 nm.

Quantification of the probe cantilever nominal spring constant was performed using a dynamic method of thermal noise analysis (Hutter and Bechhoefer, 1993). A spring constant of  $36.2 \pm 0.2 \text{ N/m}$  was recorded using this approach

and agreed with the manufacturer's quoted value measured using the Sader method (Sader et al., 1995).

Force-distance measurements were performed on different areas of a single crystal so that the dominant face with respect to the indenter was indented. The cantilever deflection and piezo displacement were derived into a Young's modulus value using the Hertzian model of deformation shown in Equation 4.1 (Hertz, 1881) (Plassard et al., 2004)

$$E = \frac{3(1-\nu^2)k\Delta z}{4\delta^{3/2}R^{1/2}}$$

**Equation 4.1** The Hertz model of deformation ( $E$ : Young's modulus,  $k$ : spring constant of the indenting cantilever,  $\Delta z$ : relative piezo displacement,  $\delta$ : indentation depth,  $R$ : radius of indenter,  $\nu$ : Poisson ratio of the indenting probe)

#### **4.2.3 Micronisation of crystalline samples of fluticasone propionate by air-jet milling**

Particle size reduction of selected FP samples was performed using air jet milling (McOne, Jetpharma, Balerna, Switzerland) under nitrogen at an operating venturi and ring pressure of 7 bar and 5 bar, respectively. Samples were micronised to a  $d_{90}$  size of less than 4.50  $\mu\text{m}$  for formulation use. Samples not meeting this specification were re-processed in the mill until the required particle size was obtained. Approximately 1 g of sample was introduced to the venturi over a milling time of 2 minutes. All samples were collected and stored at 19°C over silica gel.

#### **4.2.4 Methodology of the cohesive-adhesive balance (CAB) approach to colloidal probe atomic force microscopy (AFM)**

##### ***Crystallisation of Substrates***

In order to perform quantitative binary and combination AFM-CAB analysis of secondary processed FP samples, smooth single crystal surfaces of fluticasone propionate, salmeterol xinafoate and lactose monohydrate were produced. Briefly, saturated solutions of FP in 2 ml of acetone were prepared and sonicated prior to filtration *via* a 0.22- $\mu\text{m}$  PTFE membrane filter (Whatman Inc., Clifton, NJ, USA). FP was crystallised using water as the anti-solvent. Briefly, a microscope cover slip (12 mm x 12 mm) was supported on a vertical post in a crystallisation dish that contained the anti-solvent. A droplet of the saturated solution of the drug was then placed on the coverslip using a syringe attached to the 0.22- $\mu\text{m}$ -membrane filter. The system was sealed by inverting a glass lid in the crystallisation dish to allow vapour phases of the miscible solvents to come into equilibrium resulting in heterogeneous nucleation and crystal growth within the droplet. The glass cover slip was then attached to a magnetic AFM stub.

Atomically smooth lactose crystals were generated in a similar process that is described elsewhere (Begat et al., 2004b). Briefly, a solution of lactose ( $1\text{ g.m}^{-1}$ ) in double-distilled water was heated to  $100\text{ }^{\circ}\text{C}$  with constant stirring and, then filtered through a  $0.2\text{ }\mu\text{m}$  PTFE membrane filter (Whatman Inc, Clifton, NJ, USA). A single saturated drop of the lactose solution was administered on to the centre of a glass cover slip (Agar Scientific, Stansted, UK) and a second cover slip was placed on top to form a sandwich. The sandwich was then allowed to cool resulting in the production of large atomically smooth crystals of lactose. The process of crystallisation was monitored by optical microscopy and the cover slips carefully separated once all the solvent had evaporated, resulting in the growth of crystals over the surface of both cover slips. A similar process was followed for salmeterol, whereby a 75% solution of API was made in methanol at  $25\text{ }^{\circ}\text{C}$ , filtered as above and sandwiched with a coverslip to produce crystals on both surfaces.

### **4.2.5 Atomic Force Microscopy – Colloidal Probe Force Measurements**

Prior to force measurements, individual particles from each sample of FP were attached onto standard V-shaped tipless cantilevers with pre-defined spring

constants (DNP-020, DI, CA, USA) using an epoxy resin glue (Araldite, Cambridge, UK), as previously described (Begat et al., 2004b). Five probes were prepared for each batch of FP, and all probes were examined with an optical microscope (magnification 50x) to ensure the integrity of the attached particle, before allowing the thin layer of glue to dry.

The single crystal substrate was loaded onto an AFM scanner stage, which was enclosed in a custom-built environmental chamber, in which the ambient conditions were maintained at a constant temperature of 25 °C ( $\pm 1.5$  °C) and relative humidity of 35 % RH ( $\pm 3$  %). The interaction forces were measured by recording the deflection of the AFM cantilever as a function of the substrate displacement ( $z$ ) by applying Hooke's Law ( $F = -kz$ ). Individual force curves ( $n = 1024$ ) were performed over a 10  $\mu\text{m}$  x 10  $\mu\text{m}$  area at a scan rate of 4 Hz and a compressive load of 40 nN. All parameters were kept constant over the study.

### ***Data Processing***

Due to the vast array of force data generated, custom-built software was used to extract the information contained within each force-volume measurement. The collected force data was analyzed to ensure normal distribution, indicating uniform contact area between the drug probe and the smooth substrate surfaces. Arithmetic mean and standard deviation were obtained from force data and used to produce CAB plots for the interactions of the different batches of fluticasone propionate to lactose monohydrate.

#### **4.2.6 Preparation of Powder Formulations**

Binary formulation blends (0.8 % w/w) FP samples A and C were produced with a coarse grade of lactose monohydrate (Respitose, SV003, DMV-Fonterra Excipients, Vehgel. Netherlands). Briefly, coarse lactose was added geometrically to the drug, and mixed with a Whirlimixer (Fisons Scientific Apparatus, Ipswich, UK) for 30s between each addition. Sufficient amount of the carrier material was added to produce 200  $\mu\text{g}$  doses of respective batches



of FP per 25 mg of blend. Following the complete addition of the carrier, the formulation was further mixed in a Turbula for 40 min (Type T2F, Bachofen AG, Basel) at an operating rate of 46 rpm.

Similarly, combination DPI blends containing FP samples A and C, salmeterol xinafoate (SX) and lactose monohydrate were prepared using the same protocol. Combination DPI blends were prepared contained 0.8 % w/w of each drug in each respective combination preparation with lactose.

#### **4.2.7 HPLC Analysis of Fluticasone Propionate and Salmeterol Xinafoate**

Determination of drug content and analysis of NGI measurements was carried out using HPLC methodology. Briefly, the HPLC consisted of a pump (Jasco PU-980, Jasco Corp., Japan) coupled to a UV detector (Jasco UV-975) set at 228nm for parallel detection of both APIs ( $t_r$  for salmeterol 3.4 min;  $t_r$  for fluticasone propionate 6.7 min). The pump flow rate was set to 1 ml.min<sup>-1</sup> through a RP-8 column (LiChroChart 125-4, LiChroSpher 100, 5 mm, Merck, Germany) with a pre column (LiChroChart 4-4, LiChroSpher 100, 5 mm, Merck, Germany) was used as stationary phase, which was conditioned to 40 °C in a column oven. Quantification was carried out by an external standard method. Linearity was checked between 1 and 100 mg/mL for each individual API.

#### **4.2.8 Content Uniformity Measurements**

Following blending and subsequent storage for 24 hours in 44%RH, ten random samples of  $25 \pm 1$  mg, from different areas of the powder bed were weighed and dissolved in 50 ml of mobile phase. The amount of drug in each sample was obtained from HPLC assay and the content uniformity expressed as percentage relative standard deviation (RSD).

#### **4.2.9 *In vitro* Aerosolisation Studies**

Following content uniformity testing,  $25 \pm 1$  mg of each blend was loaded into size 3 hydroxypropylmethyl cellulose (HPMC, Shionogi Qualicaps SA, Basingstoke, UK) capsules. The capsules were stored at 44 % RH for 24 h prior to *in vitro* testing. This was done to ensure the dissipation of any electrostatic charges introduced during processing. Testing was performed using a Next Generation Impactor (NGI, Copley Scientific, Nottingham, UK) with pre-separator, which was connected to a vacuum pump (GE Motors). The pre-separator contained 15 ml of mobile phase. The NGI cups were coated with 1 %  $v/v$  silicone oil in hexane to eliminate any particle bounce. For each experiment, ten individual 25 mg capsules of the same blend were discharged into the NGI at  $90 \text{ L}\cdot\text{min}^{-1}$  for 2.7 s, equivalent to a total volume of 4L, from a Cyclohaler<sup>®</sup> DPI device (TEVA, Haarlem, Netherlands). Before beginning each test, the flow rate was verified with a flow meter (DFM 2000, Copley Scientific, Nottingham, UK). The amount of drug deposited on each part of the NGI was determined by the HPLC method used for determining content uniformity. This protocol was repeated three times for each blend, in order to calculate the mass median aerodynamic diameter (MMAD), geometric standard deviation (GSD), fine particle dose (FPD) that reaches stages 3 and below within the NGI and fine particle fraction (FPF), which is the percentage that is delivered to the lower stages of the NGI as a function of either the emitted dose or recovered dose.

### **Statistical Analysis**

Linear regression analysis was used for the assessment of HPLC calibration. Statistical analysis between different populations was carried out using one-way analysis of variance. Comparison of the mean values was performed by Tukey's multiple comparison. All statistical analyses were performed using GraphPad Prism software (GraphPad Software Inc, California, USA). Error bars in graphical representations of data show  $\pm 1$  standard deviation in all cases.

### **4.3 RESULTS AND DISCUSSION**

The complex nature of the interfacial interactions between drug and excipient governs the overall relationship between device and de-aggregation efficiency of the formulation and therefore directly influences the functionality and therapeutic effectiveness of the drug product. Subtle variations in the processing of materials for inclusion in DPI drug products will impact the surface interfacial free energy of the components, which may directly affect the performance and efficacy of the final drug product. Hence, it is important to understand the relationship between material processing and material physicochemical properties to produce DPI drug products with the desired performance and stability attributes.

#### **4.3.1 Characterisation of the physicochemical properties of crystals of fluticasone propionate produced using different anti-solvents**

The particle shape and morphology of crystals of FP produced using different anti-solvents were analysed by SEM and the crystal faces identified via crystal modelling. As shown in Figure 4.1, the addition of different anti-solvents resulted in different crystal morphologies, although the dominant crystal face for all samples was the (010) face. Sample B and Sample D possessed a needle like morphology, whilst Sample A and Sample C exhibited a defined plate like shape. The difference in the crystalline habits of samples A – C and B – D can be related to the different rates of crystal growth of the crystal faces, which is a direct function of the crystallisation process by which each batch was produced.

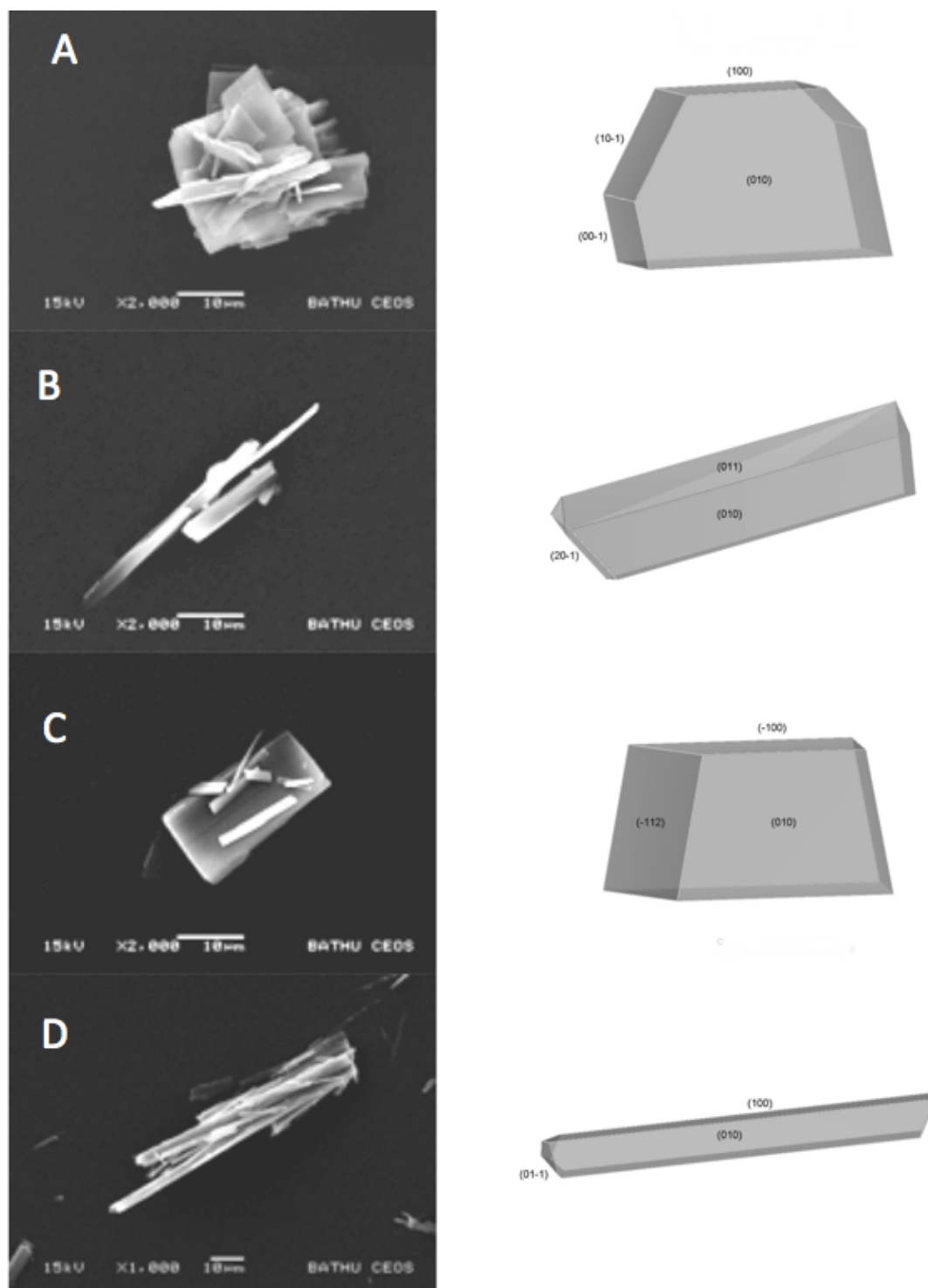


**Figure 4.1** Representative SEM images and corresponding simulated morphologies of crystals of fluticasone propionate produced using different anti-solvents.

The particle size distributions of all the batches of unmicronised FP are shown in Figure 4.2 and are summarised by the 10 %, 50 % and 90 % undersize particle size measurements in Table 4.1. The particle size distribution (PSD) of all the crystalline samples of FP was broad, where particles ranged from 1 – 60

$\mu\text{m}$ . In addition, the particle size of samples B and D are smaller than samples A and C, which maybe related to the needle shape of crystals of samples B and D.

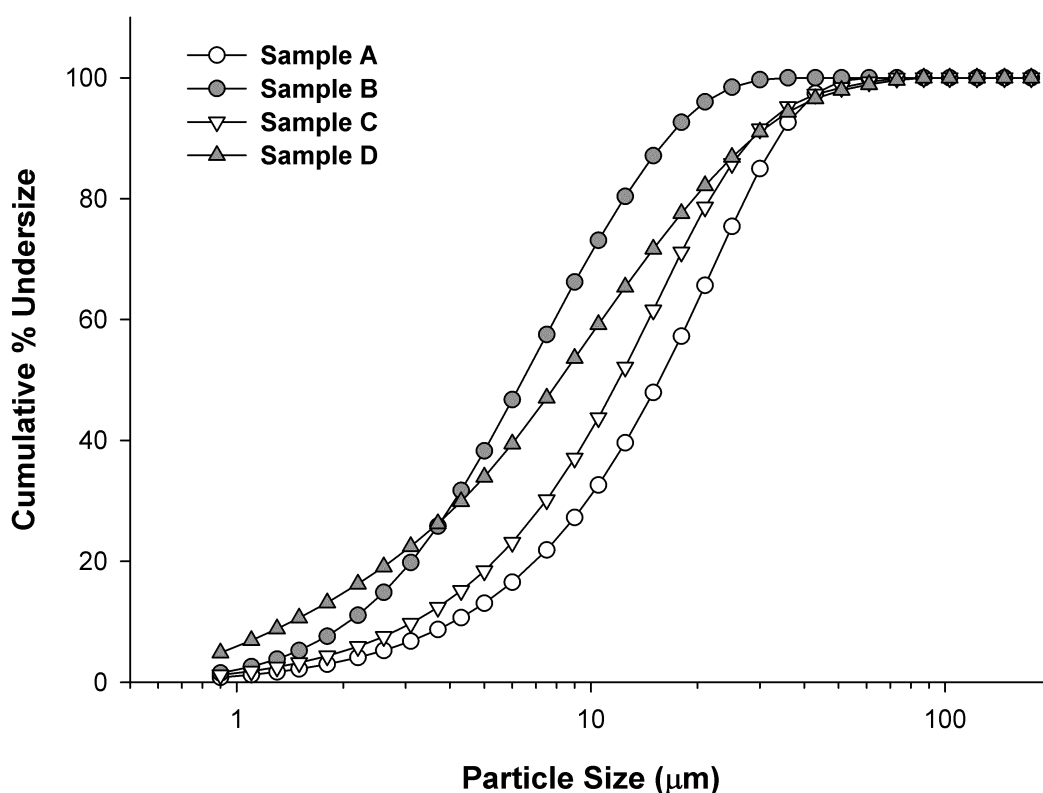


Figure 4.2 Cumulative particle size distribution of crystals of fluticasone propionate produced using different anti-solvents.

Table 4.1 Particle size distribution (PSD) and Young's modulus of crystals of fluticasone propionate using different solvents.

Sample	$d_{10}$ ( $\mu\text{m}$ )	$d_{50}$ ( $\mu\text{m}$ )	$d_{90}$ ( $\mu\text{m}$ )	Young's modulus (GPa $\pm$ S.D.)
A	$5.54 \pm 0.05$	$26.56 \pm 0.21$	$64.82 \pm 0.36$	$0.61 \pm 0.07$
B	$2.08 \pm 0.04$	$6.45 \pm 0.08$	$16.57 \pm 0.15$	$2.42 \pm 0.53$
C	$5.37 \pm 0.02$	$26.61 \pm 0.05$	$54.26 \pm 0.27$	$12.44 \pm 2.48$
D	$1.43 \pm 0.01$	$8.18 \pm 0.04$	$28.75 \pm 0.17$	$1.49 \pm 1.16$

The X-ray powder diffractograms (XRPD) of each of the FP samples are shown in Figure 4.3. The presence of distinct peaks in the XRPD diffractogram between  $10^{\circ}$ - $40^{\circ}$  at angle  $2\theta$  of all batches of FP was present, which suggests that the materials were of the same polymorphic form and therefore, the use of different ant-solvents did not change the polymorphic form of the different samples.

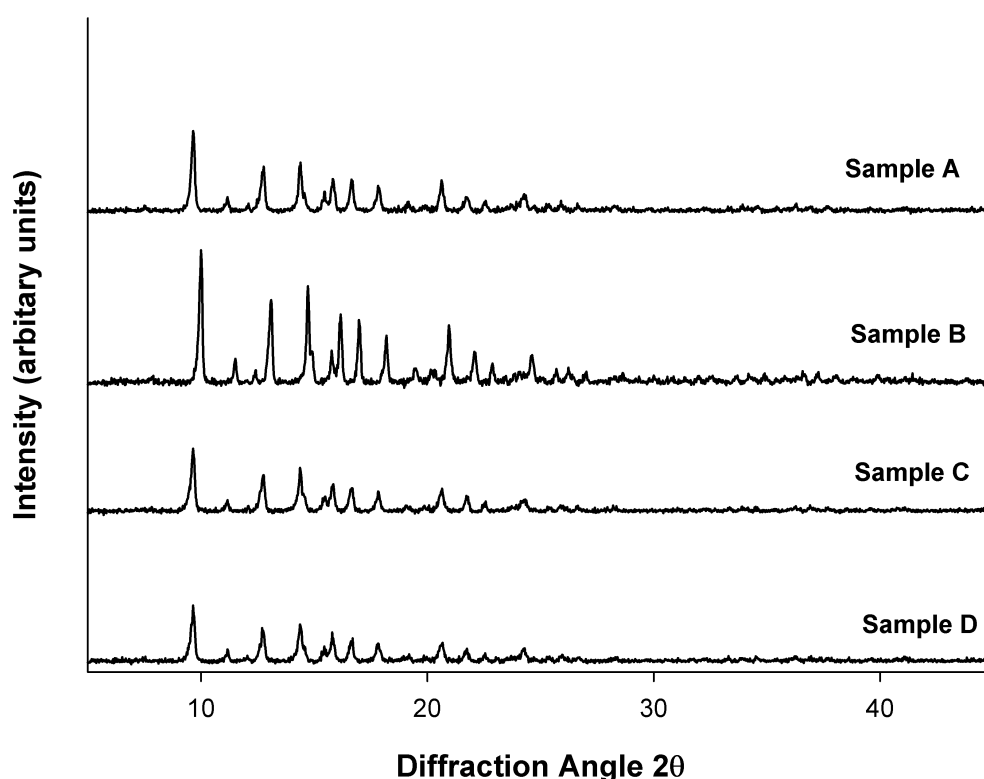
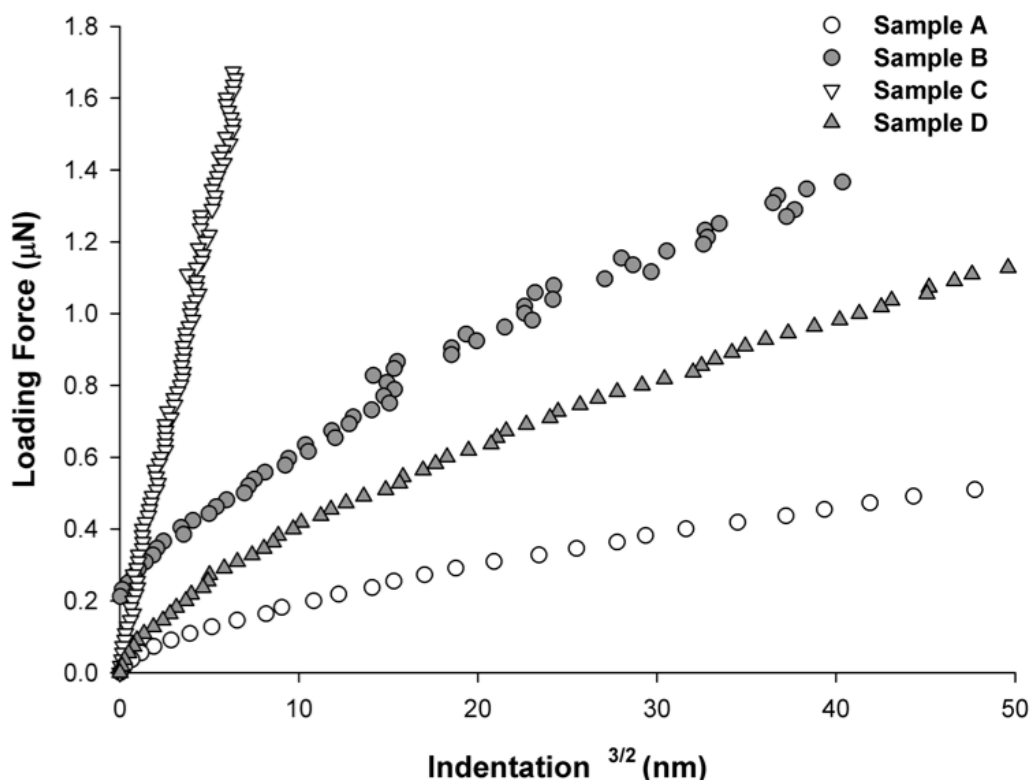


Figure 4.3 X-ray powder diffractograms of the different samples of fluticasone propionate.

#### 4.3.2 Nanomechanical measurements of the Young's modulus of FP samples

The AFM was used to indent individual crystals of fluticasone propionate from each batch of crystallised material. The loading force against the measured indentation depth of each of the samples was directly compared and a representative measurement from each batch is shown in Figure 4.4. These data suggest that with an increasing loading force sample A indented the most,

followed by samples D and B. However, sample C required loading forces greater than  $1.6 \mu\text{N}$  to create an indentation depth of approximately  $10 \text{ nm}^{3/2}$  into crystal. Extrapolating the data into a Hertzian model of deformation, the Young's modulus of FP crystals produced using different solvent/anti-solvent conditions were calculated using Equation 4.1.



**Figure 4.4** The measured loading force against indentation depth<sup>(3/2)</sup> for each sample of crystalline fluticasone propionate.

The Young's modulus of all the samples ranged from 0.61 – 12.44 GPa. Sample A had the lowest Young's modulus  $E = 0.61 \pm 0.07 \text{ GPa}$ , whilst the Young's modulus of sample C was  $E = 12.44 \pm 2.48 \text{ GPa}$ . The Young's modulus of samples B and D were  $2.42 \pm 0.53 \text{ GPa}$  and  $1.49 \pm 1.15 \text{ GPa}$ , respectively. These data suggest that FP crystals of sample C had a significantly ( $p < 0.05$ ) greater resistance to elastic deformation than the other samples, whilst sample A was likely to undergo elastic deformation. The Young's modulus of FP crystals of sample C suggests that these primary crystals may exhibit greater degree of stiffness and therefore more likely to fracture more efficiently upon air-jet milling than the other samples (Zugner et

al., 2006). Hence, the use of different anti-solvents to crystallise FP yielded crystals with different mechanical properties, which may directly influence secondary processing behaviour, which, in turn, may directly influence the physicochemical and interfacial properties of the API.

In order to investigate the relationship between the mechanical properties and their micronisation efficiency, primary crystals of samples A and C were chosen for secondary processing by air-jet milling. The physicochemical and surface interfacial properties of the resultant secondary processed samples were also determined and related to their performance in binary and combination DPI formulations.

#### **4.3.3 Physicochemical and surface interfacial properties of secondary processed crystals of sample A and C**

The possible relationship between mechanical properties of primary crystals of FP and the micronised API product, the micronisation behaviour, particle size reduction properties, interfacial properties and *in vitro* performance of binary formulations of FP and combination formulations with SX was investigated.

In order to obtain the required specification in the  $d_{90\%}$  of the particle size distribution ( $d_{90\%} < 4.5 \text{ } \mu\text{m}$ ) of the micronised FP for formulation, Sample A needed multiple cycles in the air-jet mill. Sample A had to be passed through the air jet mill a total of four times. Meanwhile, primary crystals of sample C, which exhibited a similar PSD and morphology to sample A, only required a single cycle in the mill. The PSD of the micronised samples that matched the required PSD specification, alongside their particle size reduction ratios with respect to the primary crystals and total number of milling cycles are shown in Table 4.2. These data suggest that the Young's modulus of the primary crystals may influence micronisation efficiency, where materials with a low Young's modulus (greater elasticity) require intensive re-processing to achieve particle size reduction.



**Table 4.2** An overview of the number of milling cycles required to obtain the defined particle size requirements and the final particle size distributions of the micronised fluticasone propionate.

Sample	Number of Milling Cycles	Final Micronised $d_{10}$ ( $\mu\text{m}$ )	Final Micronised $d_{50}$ ( $\mu\text{m}$ )	Final Micronised $d_{90}$ ( $\mu\text{m}$ )
<b>A</b>	4	$1.01 \pm 0.01$	$2.31 \pm 0.01$	$4.25 \pm 0.01$
<b>C</b>	1	$0.93 \pm 0.01$	$2.23 \pm 0.01$	$4.31 \pm 0.01$

Thermal analysis of the micronised samples A and C indicated that both materials had an onset of melting at approximately 295 °C, which was related to the melting of form I of FP (Pitchayajittipong et al., 2009).

In order to determine the effect of the mechanical properties of the primary crystals and the possible influence of multiple micronisation cycles on the surface interfacial properties of the process micronised materials, the cohesive-adhesive balance (CAB) of the micronised FP after each cycle was measured with respect to crystal substrates of fluticasone propionate, lactose monohydrate and salmeterol xinafoate (SX).

The CAB plots and summary of the CAB ratios of sample A following each micronisation cycle are shown in Figure 4.5 and Table 4.3. The CAB value of sample A FP following the 1<sup>st</sup> milling cycle with respect to lactose and SX was  $1.35 \pm 0.01$  and  $1.21 \pm 0.02$ , respectively. These data suggest that for equivalent contact geometry, the cohesive FP-FP interactions were 1.35 and 1.21 times greater than the FP-Lactose and FP-SX interactions, respectively.

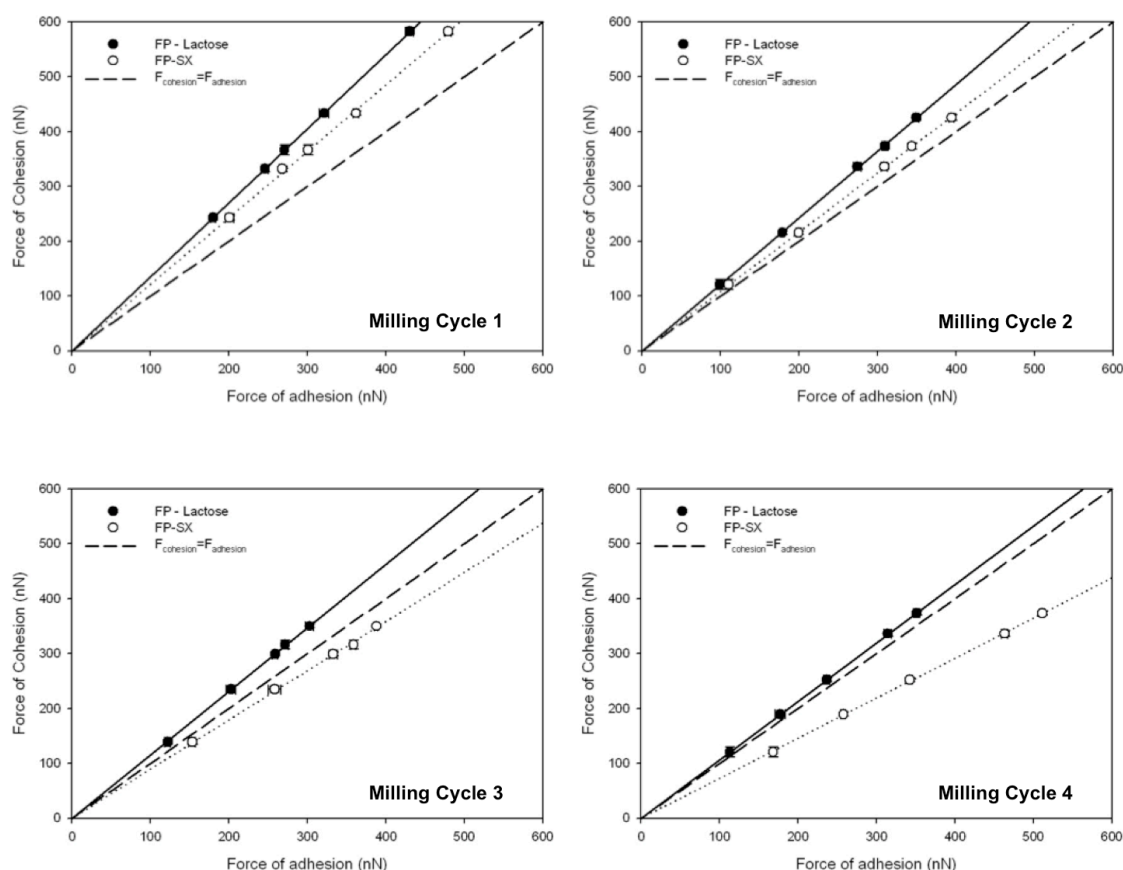


**Figure 4.5 Comparison of the force of cohesion, force of adhesion and CAB ratio of fluticasone propionate – lactose systems (FP-Lactose) and fluticasone propionate – salmeterol xinafoate systems (FP-SX) produced following re-pass air-jet milling of sample A crystals of fluticasone propionate over four cycles.**

**Table 4.3 Comparison of the force of cohesion, force of adhesion and CAB ratio of fluticasone propionate – lactose systems (FP-Lactose) and fluticasone propionate – salmeterol xinafoate systems (FP-SX) produced following re-pass air-jet milling of sample A crystals of fluticasone propionate over four cycles.**

Number of Milling Cycles	FP-Lactose CAB Ratio ( $\pm$ SD)	FP-SX CAB Ratio ( $\pm$ S.D.)
Milling Cycle 1	1.35 $\pm$ 0.01	1.21 $\pm$ 0.02
Milling Cycle 2	1.21 $\pm$ 0.02	1.08 $\pm$ 0.01
Milling Cycle 3	1.15 $\pm$ 0.01	0.90 $\pm$ 0.02
Milling Cycle 4	1.06 $\pm$ 0.01	0.73 $\pm$ 0.02

The CAB ratio of sample A with respect to lactose decreased to 1.21 after the second pass, processing of the material for a third time resulted in a CAB ratio of 1.15 and after the final milling cycle the CAB ratio of sample A was 1.06. These data suggest that that each milling cycle of sample A significantly

increased the adhesive tendency of the FP to the lactose, although the cohesive FP-FP interaction of sample A still remained dominant force of interaction.

The CAB ratio of sample A FP with respect to SX decreased from 1.21 following the 1<sup>st</sup> milling cycle to 0.73 after the fourth milling cycle. Interestingly, multiple milling cycles of the FP shifted the force balance of the FP-SX interactions from an initial cohesive (FP-FP) led system to an adhesive (FP-SX) led system. For a combination based product, this shift in the overall balance of forces may significantly affect the blending dynamics and formulation structure of a carrier based DPI formulations.

The CAB ratios of the material used to formulate both binary and combination based formulations of sample A with respect to lactose and SX were  $1.06 \pm 0.01$  and  $0.73 \pm 0.02$ , respectively.

The CAB plots and summary of the CAB ratios of sample C following each micronisation cycle are shown in Figure 4.6 and Table 4.4. The CAB ratios of this higher Young's modulus FP following micronisation with respect to lactose and SX were  $1.01 \pm 0.01$  and  $0.95 \pm 0.02$ , respectively. These data suggest that for equivalent contact geometry, the FP-FP interactions exhibited a similar force of interaction as the adhesion of the FP to lactose, while the FP-SX force of adhesion was approximately 5% greater.

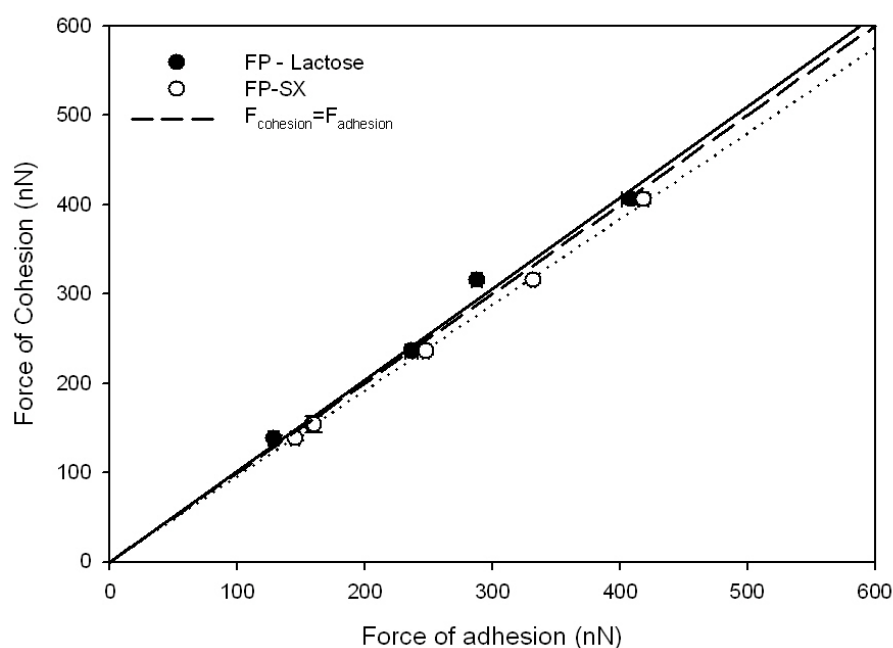


**Figure 4.6** Comparison of the force of cohesion, force of adhesion and CAB ratio of fluticasone propionate – lactose systems (FP-Lactose) and fluticasone propionate – salmeterol xinafoate systems (FP-SX) produced following air-jet milling of sample C crystals of fluticasone propionate.

**Table 4.4** Comparison of the force of cohesion, force of adhesion and CAB ratio of fluticasone propionate – lactose systems (FP-Lactose) and fluticasone propionate – salmeterol xinafoate systems (FP-SX) produced following air-jet milling of sample C crystals of fluticasone propionate.

Number of Milling Cycles	FP-Lactose CAB Ratio ( $\pm$ SD)	FP-SX CAB Ratio ( $\pm$ S.D.)
Milling Cycle 1	1.01 $\pm$ 0.01	0.95 $\pm$ 0.02

Interestingly, the FP-lactose interactions of sample A following the 4<sup>th</sup> micronisation cycle and sample C after one-pass of the microniser were similar. However, the adhesive FP-SX interactions of sample A after four-passes of the microniser were significantly ( $p < 0.05$ ) greater than that of sample C. This may result in variations in the delivery of SX from a combination DPI formulation if formulated with sample A FP.

These data suggest that the use of different anti-solvents can change the Young's modulus of the primary crystalline FP samples. Our study has indicated that the particle reduction efficiency of the micronised product is directly

affected by the Young's modulus of the FP and as a result may directly influence the physico-chemical and interfacial properties of the secondary processed API.

#### **4.3.4 *In vitro* inhalation performance of binary and combination DPI formulations containing secondary processed FP from samples A and C**

The aerosolisation performance of binary DPI formulations containing secondary processed sample A and C FP was evaluated. In addition both batches of micronised FP were also formulated with SX to enable evaluation of combination DPI formulations of FP and SX. Of particular interest was to determine the influence of primary and secondary processing on the physicochemical and surface interfacial properties of FP and the resultant effect on DPI formulation performance and stability.

The relationship between drug concentration (0.2, 0.5, 1, 5, 10 and 50  $\mu\text{g}.\text{ml}^{-1}$ ) and peak area for each drug was found to be linear, with linear regression analysis yielding a coefficient of determination ( $R^2$ ) of 1.000 and is shown in Figure 4.7.

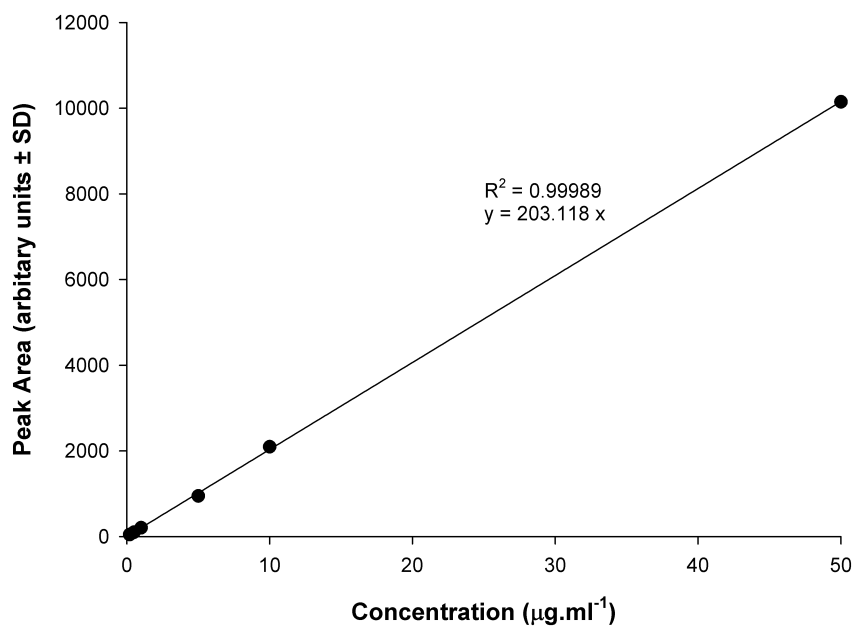


**Figure 4.7 Representative HPLC calibration curve obtained for FP**

A representative HPLC trace for a calibration sample of FP 10 µg.ml<sup>-1</sup> is shown in Figure 4.8.

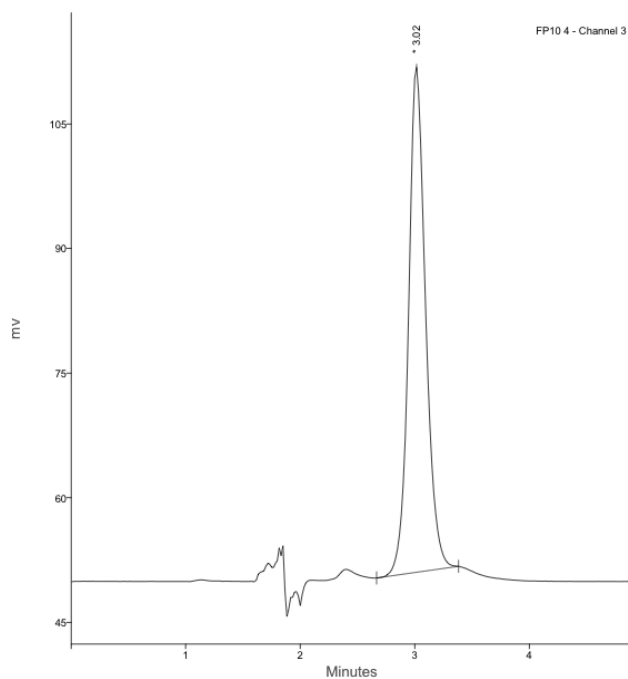


**Figure 4.8 A Representative HPLC trace for FP**

**Drug content uniformity**

The relative standard deviation (%RSD) of the drug content of two binary DPI formulations containing either micronised sample A or C is shown in Table 4.5. The %RSD was less than 5% indicating that homogenous binary blends were produced with both batches of FP. In addition, the %RSD of FP and SX of two combination DPI formulations containing micronised sample A or C are shown in Table 4.6 and Table 4.7, respectively. The %RSD of the actives in either formulation was less than 5 %, which suggests a homogeneous distribution in the formulated blend.

**Table 4.5 *In vitro* formulation performance (emitted dose (ED), fine particle dose (FPD), fine particle fraction of the emitted dose (FPF<sub>ED</sub>) and mass median aerodynamic diameter (MMAD) and geometric standard deviation (GSD)) from aerosolisation of binary DPI formulations of fluticasone propionate into the NGI (n = 3).**

Formulations Batch	Mean ED ( $\mu\text{g} \pm \text{S.D.}$ )	Mean FPD ( $\mu\text{g} \pm \text{S.D.}$ )	Mean FPF <sub>ED</sub> ( $\% \pm \text{S.D.}$ )	MMAD ( $\mu\text{m} \pm \text{GSD.}$ )	%RSD
A	166.9 $\pm$ 4.2	17.5 $\pm$ 1.8	10.5 $\pm$ 0.9	3.0 $\pm$ 1.5	4.6
C	161.3 $\pm$ 6.0	13.4 $\pm$ 1.1	8.3 $\pm$ 0.8	3.3 $\pm$ 1.5	3.7

**Table 4.6 *In vitro* formulation performance (emitted dose (ED), fine particle dose (FPD), fine particle fraction of the emitted dose (FPF<sub>ED</sub>) and mass median aerodynamic diameter (MMAD) and geometric standard deviation (GSD)) from aerosolisation of combination DPI formulations containing micronised fluticasone propionate (FP) sample A and salmeterol xinafoate (SX) into the NGI (n = 3).**

Formulations Batch	Mean ED ( $\mu\text{g} \pm \text{S.D.}$ )	Mean FPD ( $\mu\text{g} \pm \text{S.D.}$ )	Mean FPF <sub>ED</sub> ( $\% \pm \text{S.D.}$ )	MMAD ( $\mu\text{m} \pm \text{GSD.}$ )	%RSD
FP	165.4 $\pm$ 4.7	16.5 $\pm$ 1.0	10.0 $\pm$ 0.6	3.3 $\pm$ 1.4	4.7
SX	142.5 $\pm$ 9.1	32.2 $\pm$ 1.9	21.0 $\pm$ 3.4	2.5 $\pm$ 1.3	4.2

**Table 4.7 *In vitro* formulation performance (emitted dose (ED), fine particle dose (FPD), fine particle fraction of the emitted dose (FPF<sub>ED</sub>) and mass median aerodynamic diameter (MMAD) and geometric standard deviation (GSD) from aerosolisation of combination DPI**

formulations containing micronised fluticasone propionate (FP) sample C and salmeterol xinafoate (SX) into the NGI (n = 3).

Formulations Batch	Mean ED ( $\mu\text{g} \pm \text{S.D.}$ )	Mean FPD ( $\mu\text{g} \pm \text{S.D.}$ )	Mean FPF <sub>ED</sub> (% $\pm$ S.D.)	MMAD ( $\mu\text{m} \pm \text{GSD.}$ )	% RSD
FP	153.8 $\pm$ 6.8	20.0 $\pm$ 1.7	13.0 $\pm$ 1.5	3.1 $\pm$ 1.5	4.3
SX	141.0 $\pm$ 5.9	18.2 $\pm$ 0.6	12.9 $\pm$ 0.7	2.8 $\pm$ 1.5	3.5

#### 4.3.5 *In vitro* aerosolisation performance of binary DPI formulations containing micronised samples A and C

The FPD of sample A micronised FP was  $17.5 \pm 1.8 \mu\text{g}$  whereas the FPD of sample C micronised FP was  $13.4 \pm 1.1 \mu\text{g}$ . However, as shown in Table 4.5 the emitted doses of the formulations were different. Upon normalization of the FPD by the emitted dose and expressed as the percentage fine particle fraction of the emitted dose (%FPF<sub>ED</sub>), the %FPF<sub>ED</sub> of the sample A was  $10.5 \pm 0.9$  and sample C was  $8.3 \pm 0.8$ , which suggests that performance of the formulations were similar. These data are supported by the stage-by-stage data for both formulations, which are shown in Figure 4.9. These data corroborate well with the force balance measurements of the FP samples, with both materials having similar adhesive affinity to the carrier lactose, as suggested by CAB measurements, and therefore similar deaggregation efficiency.



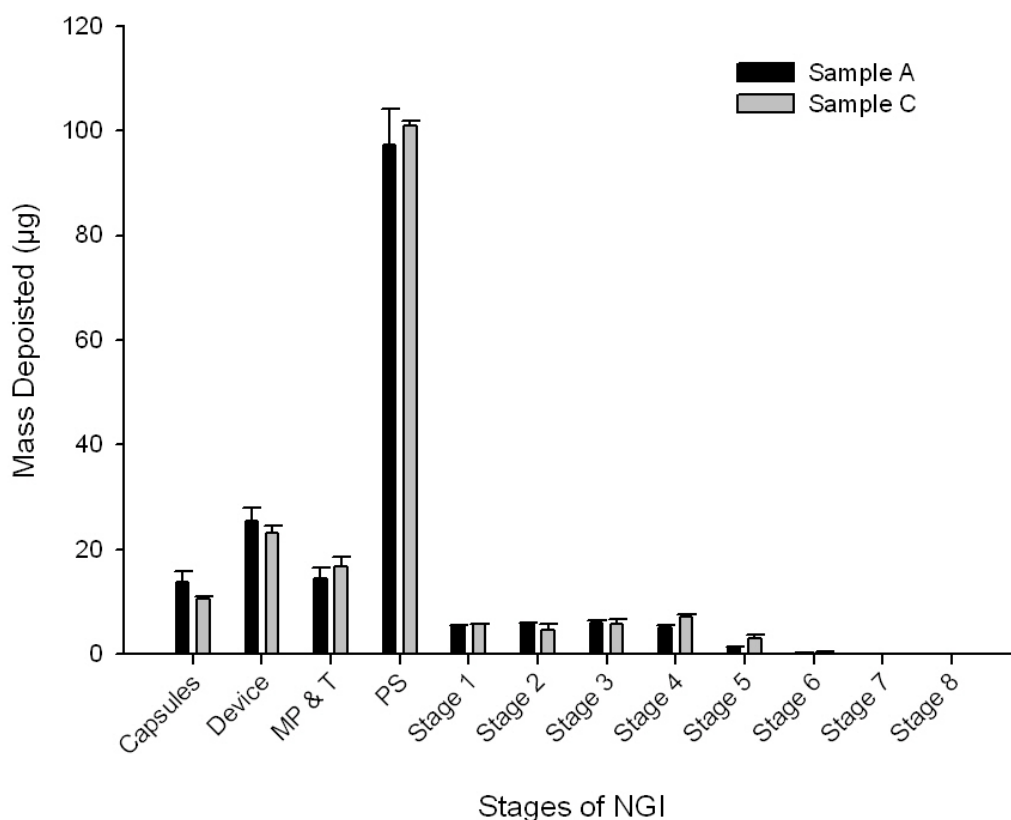


**Figure 4.9** *In vitro* stage-by-stage deposition of fluticasone propionate following aerosolisation of binary DPI formulations containing samples A and C of micronised fluticasone propionate.

#### **4.3.6 *In vitro* aerosolisation performance of combination DPI formulations of FP and SX containing micronised FP from samples A and C**

The *in vitro* stage-by-stage deposition of combination DPI formulations of SX and FP, prepared with samples A and C are shown in Figure 4.10 and Figure 4.11, respectively. Furthermore, the mean emitted dose, fine particle dose (FPD) and the percentage fine particle fraction of the emitted dose (%FPF<sub>ED</sub>) along with the mass median aerodynamic diameter (MMAD) and geometric standard deviation (GSD) of SX and FP samples A and C following aerosolisation of the formulations are shown in Table 4.6 and Table 4.7, respectively.

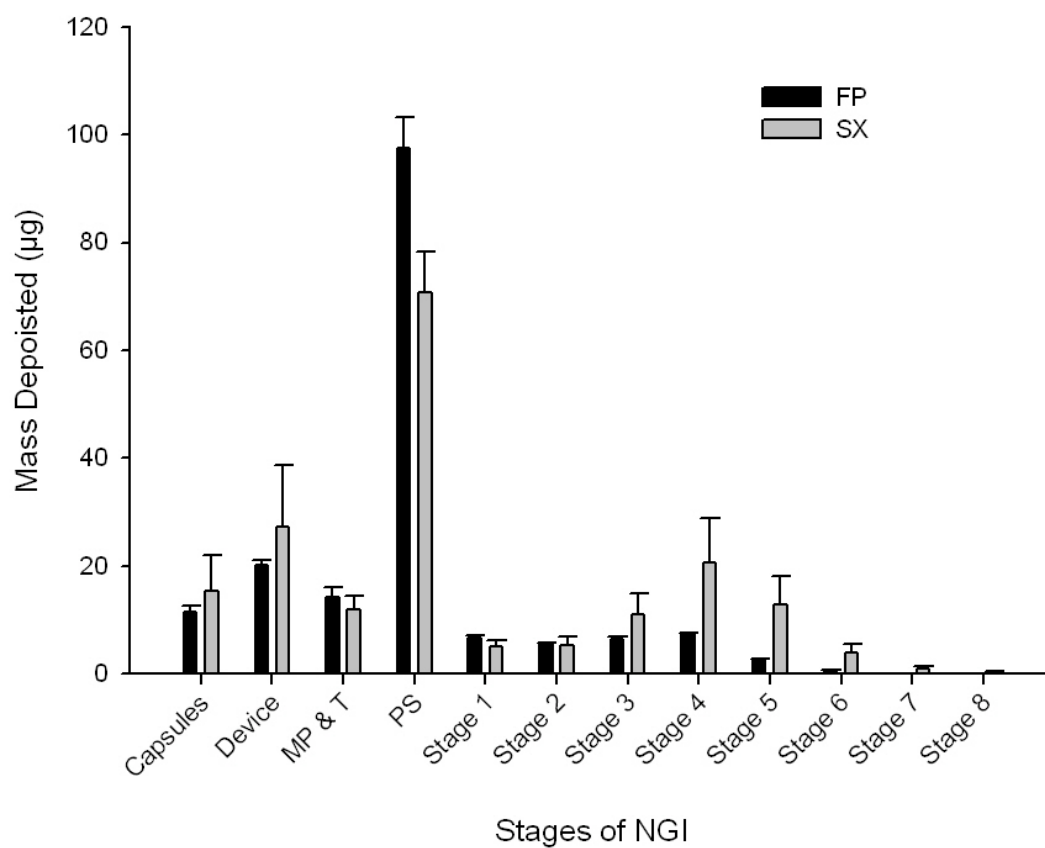


**Figure 4.10** *In vitro* stage-by-stage deposition of fluticasone propionate and salmeterol xinafoate following aerosolisation of combination DPI formulations containing micronised fluticasone propionate sample A.

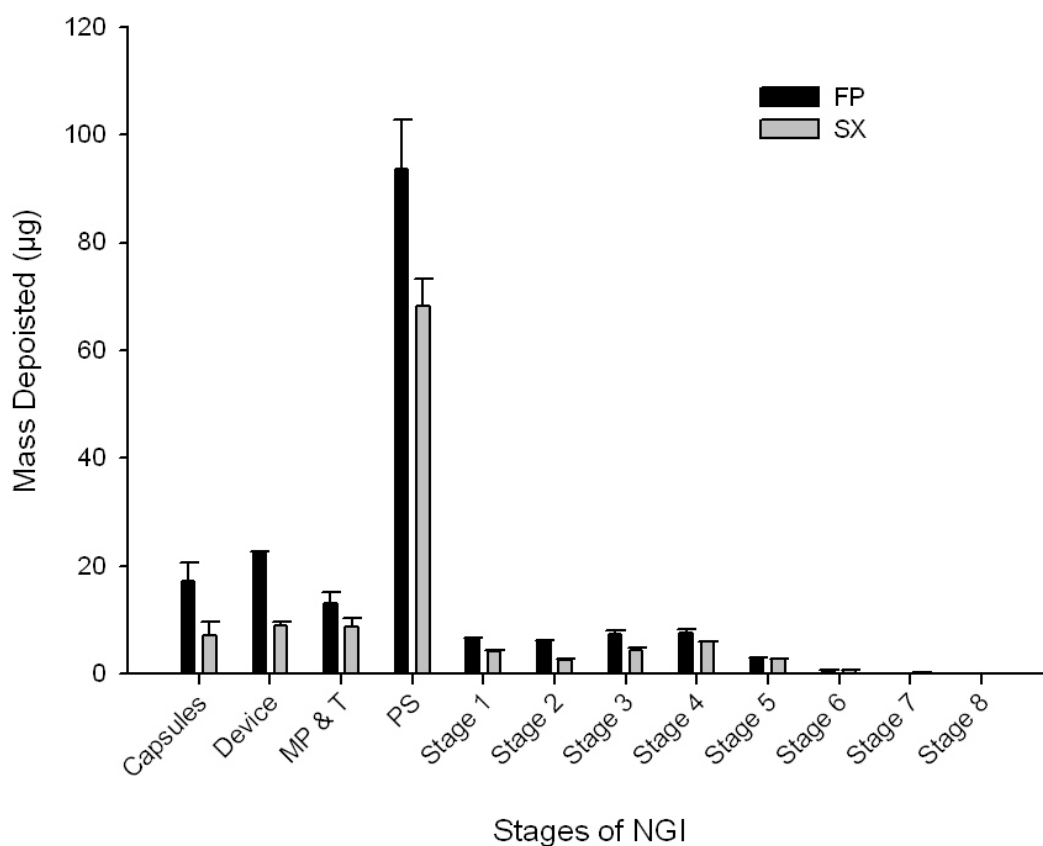


**Figure 4.11** *In vitro* stage-by-stage deposition of fluticasone propionate and salmeterol xinafoate following aerosolisation of combination DPI formulations containing micronised fluticasone propionate sample C.

The emitted dose of the combination FP/SX formulation containing sample A was determined as  $165.4 \pm 4.7 \mu\text{g}$  for FP and  $142.5 \pm 9.1 \mu\text{g}$  for SX (Table 4). The FPD and % FPF<sub>ED</sub> of FP and SX upon aerosolisation of this formulation was  $16.5 \pm 1.0 \mu\text{g}$  and  $32.2 \pm 1.9 \mu\text{g}$  and  $10.0 \pm 0.6 \%$  and  $21.0 \pm 3.4 \%$ , respectively. These data suggest that the performance of SX was significantly better than that of FP ( $p < 0.05$ ). These measurements are supported by the stage-by-stage deposition data shown in Figure 4.10, which shows greater deposition of SX on to the lower stages of the impactor.

No significant changes were seen in the performance of FP in combination with SX when compared to the binary formulation, suggesting the addition of SX had little effect on the formulatory properties between sample A FP and lactose.

In comparison, the emitted dose of the combination FP/SX formulation containing sample C micronised FP was determined as  $153.8 \pm 6.8 \mu\text{g}$  for FP and  $141.0 \pm 5.9 \mu\text{g}$  for SX (Table 5). The FPD and % FPF<sub>ED</sub> of FP and SX upon aerosolisation of this formulation was  $20.0 \pm 1.7$  and  $18.2 \pm 0.6 \mu\text{g}$  and  $13.0 \pm 1.5$  and  $12.9 \pm 0.7 \%$ , respectively. These data suggest that there was an improvement in the performance of the FP in the combination DPI formulation containing FP sample C and SX.

Whilst the CAB ratios of the two micronised FP samples with respect to lactose monohydrate are similar, these *in vitro* data suggest that the difference in the adhesive interactions between FP and SX of sample C may influence the performance of FP within the combination formulation.

Evaluation of the performance of SX in combination with FP sample A and sample C show significant differences between the two formulations. In combination with FP sample A, a significantly higher FPD and FPF is seen for the SX dose. For FP sample C in combination with SX, the SX performance falls by almost 40%, suggesting the differences in the interactive nature of the micronised FP with SX may influence the *in vitro* performance of these two samples. The CAB value for FP with respect to lactose for both samples was similar. However, differences for the FP samples with respect to SX were measured, indicating that of the increase in adhesive tendency for sample A FP to SX had resulted in significant improvement of the delivery of SX with respect to sample C.

#### **4.4 CONCLUSIONS**

This study has demonstrated the use of a modern technique to detect subtle modifications in the mechanical properties of crystalline fluticasone propionate particles produced using different anti solvents and standard processing methods. The choice of primary crystallisation conditions was found to be critical in determining the physico-chemical properties of the secondary processed material. These variations were highlighted by the range of Young's modulus measured for different crystallisation conditions of FP. These variations in the mechanical properties of FP also directly influenced the particle size reduction efficiencies upon micronisation. Low Young's modulus FP samples required additional milling cycles to sufficiently reduce the particle size distribution to a respirable size range. These variations in mechanical properties and different energy requirements, via multiple micronisation cycles, for particle size reduction were also shown to influence the cohesive-adhesive properties of the FP samples with respect to lactose monohydrate and in combination with SX. These changes in the balance of interfacial forces may ultimately lead to variability in formulation performance of the DPI formulations, as indicated by the aerosolisation performance of these samples when formulated in combination with SX and suggested that variations in the interactive forces significantly affected the fine particle delivery performance of a DPI formulation. By gaining an understanding of how the primary crystallisation process affects secondary processing, interfacial forces and the functionality of a DPI formulation, greater quality control in the formation of these complex products may be achieved.

## **Chapter 5: Influence of primary crystallisation conditions on the mechanical and interfacial properties of micronised budesonide for dry powder inhalation**

### **5.1 INTRODUCTION**

To achieve therapeutic delivery of an active pharmaceutical ingredient (API) to the lung via dry powder inhalers (DPI), the aerodynamic particle of the API needs to be less than 5  $\mu\text{m}$  (Timsina et al., 1994b). However, the cohesive behaviour of particles less than 20  $\mu\text{m}$  precludes efficient handling and accurate metering of into a DPI device. As a result, API particles need to be blended under relatively high shear with a coarse excipient, such as lactose monohydrate, to form an ordered mixture (Bell et al., 1971). The overall performance of these ordered mixtures is highly dependent on the interfacial forces of the API and the relative magnitude of the cohesive (drug-drug) and adhesive (drug-excipient) interactions. This balance of these forces is dominated by the physico-chemical properties of the API, which is directly influenced by the process history of the material. An understanding of the processing and its influence on API properties needs to be defined and controlled in order to produce a stable and robust DPI formulation.

The common approach of processing API's for lung delivery is based on a "top-down" strategy, where large, primary crystals from a bulk crystalliser are secondary processed using energetic comminution techniques (e.g. micronisation) to reduce the particle size of the API to meet set specifications (Chow et al., 2007). The particle size reduction operation is energy intensive and exerts high stresses on the input crystalline API material during particle-particle collisions. The result of these stresses is the generation of undesirable product properties such as the formation of defects and dislocations within the crystalline lattice and possible generation of amorphous disorder. This surface

disorder may adversely impact the stability of the final drug product and interfacial properties of the API which may directly influence inter-particle interactions and concomitantly the mixing dynamics and performance of the final product (Krycer and Hersey, 1981) (Buckton, 1997) (Begat et al., 2003).

The bulk crystallisation step of the API is primarily utilised to isolate and purify APIs. However, the possible influence of the physico-chemical properties of the primary API crystals on downstream secondary processing (e.g. micronisation) and its resultant affect on formulation structure and product functionality is not well understood. The crystallisation process, however, is known to influence the mechanical properties of primary crystals (Liao and Wiedmann, 2005) and has been reported to have a strong influence on the micronisation behaviour of solids (Zugner et al., 2006).

The mechanical properties of crystalline solids are characterised by the hardness and Young's modulus of a solid. For organic crystals, the hardness is generally low and its range small. The Young's modulus of a material represents it's resistance to elastic deformation and has been reported to have a strong influence on the micronisation behaviour of solids (Zugner et al., 2006) and provides a meaningful parameter to characterise possible variations in mechanical behaviour. Use of commercially available nano-indenting platforms that apply a load via a sharp indenter and measure the elastic response, have been shown to observe differences in the elastic modulus of different pharmaceutical ingredients (Taylor et al., 2004b) and detect differences in this property as a function of crystallisation conditions (Liao and Wiedmann, 2005).

The atomic force microscope (AFM) has emerged as an alternative tool in the assessment of nanoscale properties of pharmaceutical materials and enables the measurement of the Young's modulus by placing a load force on an investigational material through an AFM cantilever of defined stiffness possessing a probe tip of defined contact area (Fraxedas et al., 2002) (Perkins et al., 2007). The AFM based approach has been compared to an established nano-indenting instrument to determine the Young's modulus of lactose monohydrate crystals (Perkins et al., 2007). The work highlighted the

advantages of this non-destructive AFM technique as a means of accurately obtaining the elastic modulus of pharmaceutically relevant materials. Additionally, AFM nanoindentation has been used to quantify the elastic modulus of pharmaceutical APIs including budesonide, whereby a Young's modulus of approximately 10 GPa was found (Davies et al., 2005). A further study into carbamazepine revealed differences in the Young's modulus for different polymorphs of the API, ranging from 2.69 to 5.18 GPa and suggested this parameter influenced the milling behaviour and the resulting interfacial properties of the micronised materials for each polymorph (Perkins et al., 2009).

Comminution of crystalline APIs can lead to significant changes in the physico-chemical nature of the surfaces of APIs (Buckton, 1997) (Brittain, 2002). The atomic force microscope enables the investigation of these changes through the use of a colloidal particle technique, interacting a cantilever based probe with nanometer and nanoNewton resolution (Cappella and Dietler, 1999). Using a tipless AFM cantilever and attaching a colloidal probe, interactions between a substrate sample and single micrometer sized particles, such as micronised APIs, can be investigated. This form of measurement has had significant implications to the field of DPI formulation, as the interactive forces between inter-particle components play a critical role in the behaviour of these mixtures (Roberts, 2005). Two approaches are commonly used to assess these interfacial properties, quantifying the contact area of the attached colloidal particle (Hooton et al., 2003) or interacting the same colloidal probes with smooth surfaces of interest (Begat et al., 2004a).

The cohesive-adhesive balance (CAB) approach enables evaluation of the cohesive and adhesive forces on micronised materials for inclusion within DPI formulations against another component of the formulation (Begat et al., 2004c) and has been investigated alongside *in vitro* performance of DPI formulations (Hooton et al., 2006) (Jones et al., 2008). This assessment of APIs that have been secondary processed is routinely performed prior to formulation of the final product, yet the influence of the primary crystallisation process on these materials is not fully recognised.



Optimising the crystallisation conditions to engineer crystalline APIs of desired quality is an approach used by pharmaceutical manufacturers to produce crystalline material suitable for the processing and manufacturing of DPI products (Chow et al., 2008). Current practices include controlling impurity levels (Wood, 2001), particle size (Beach et al., 1999) (Hu et al., 2008) (Murnane et al., 2009) and crystal habit of the primary API (Murnane et al., 2008) (Abu Bakar et al., 2009). Changes to the crystal morphology of the harvested crystals are known to lead to changes in the processing behaviour of APIs, for example the compaction behaviour (Garekani et al., 2001) (Banga et al., 2007). Investigation into the milling of two different habits of succinic acid suggested that crystal morphology influenced the milling behaviour of this material (Chikhalia et al., 2006), further influencing the functionality of the processed material.

Additionally, changes in the crystal habit have been shown to modify the interfacial properties (e.g., surface free energy) of the crystal due to modifications in the relative proportions of different chemical groups exposed on the respective growth faces. Muster and Prestidge have demonstrated the influence of molecule orientation at crystal faces on the surface free energy and interfacial interactions of model hydrophobic silica particles (Muster and Prestidge, 2002). Furthermore, two different budesonide habits were shown to have dissimilar cohesive-adhesive balance values on the {102} and {002} faces against different sugars (Hooton et al., 2008), highlighting the importance of crystal face specific properties and their possible implications on processing, formulation and delivery of APIs.

While it is understood that modification of the crystal habit can affect the milling properties of organic materials, the relationship between the physico-mechanical nature of primary crystals, including elastic modulus and the resulting physico-chemical attributes of the micronised materials in the context of DPI formulations is poorly understood.

The aim of the present study was to investigate the influence of crystal morphology on the mechanical properties of unprocessed API and the effect on

the physicochemical and interfacial interactions of the secondary processed material including the downstream effect on carrier-based DPI formulation performance. In this study, budesonide, a hydrophobic corticosteroid, was crystallised using two different solvents. The Young's modulus of the primary crystals on the same crystal faces was determined by AFM nanoindentation and related to the secondary processing of the materials. The interfacial properties of the secondary processed samples produced from the two different crystalline habits were determined using the cohesive-adhesive balance (CAB) method to colloidal-probe AFM with respect to lactose monohydrate. Furthermore, *in vitro* performance of the two samples was investigated in a carrier-based DPI formulation.

## 5.2 METHODS AND MATERIALS

### 5.2.1 Materials

Crystalline budesonide was supplied by Sicor (Santhia, Italy). Acetone, N,N-dimethylformamide and heptane were supplied by Fisher Scientific UK (Loughborough, UK) and were 99.9% pure. Ultra pure water was prepared by MilliQ using reverse osmosis (Millipore, Molsheim, France).

### 5.2.2 Crystallisation of Budesonide

Crystalline particles of budesonide were produced in a water-jacketed glass crystallisation vessel using conventional solvent/anti-solvent crystallisation. Two different organic solvents were selected and water was used as the anti-solvent. Saturated solutions of budesonide were made using acetone (**Sample A**) and N,N-dimethylformamide (**Sample B**) at 25°C followed by filtration using heated glass lab-ware and a 0.45 µm nylon membrane filter (Whatman, Brentford, UK). Exactly 60 mL of these solutions were rapidly introduced to a sealed glass crystallisation vessel continually stirred using a magnetic stirrer at 700 RPM with water-jacket maintaining the vessel temperature at 25±0.01°C (K20; Haake, Karlsruhe, Germany).

Ultra pure water was added to the vessel at a rate of 600 mL/hr to obtain a ratio of 1:7 saturated budesonide solution to anti-solvent, using a computer controlled syringe driver (Harvard PHD2000 Infusion Pump, Harvard Apparatus, Massachusetts, USA) connected to a hypodermic needle (21G, BD, New Jersey, USA). The resulting crystalline materials were extracted using vacuum filtration and washed using 100 mL cold water then dried under vacuum at 40°C until a steady weight was achieved. Samples of these materials were then stored at 19°C over silica gel.

### 5.2.3 Particle Size Reduction

Particle size reduction of the manufactured crystals of budesonide was performed using an air jet mill (McOne, Jetpharma, Balerna, Switzerland) with a

feed rate of approximately 0.5 g/min using dry nitrogen gas at operating venturi and ring pressures of 6 and 3 bar, respectively.

## 5.2.4 Physico-Chemical Characterisation

### 5.2.4.1 Particle Morphology and Size Analysis

All samples were characterised to determine their morphology using scanning electron microscopy (Joel, Japan) at 20 kV. Particles were attached to a carbon sticky tab and sputter coated with gold for 5 minutes (Edwards Sputter Coater, Crawley, UK) prior to imaging, producing a thickness of approximately 20 nm.

The particle size distribution of primary crystals and micronised samples of budesonide was measured using laser diffraction (HELOS, Sympatec, Clausthal-Zellerfeld, Germany) using a wet dispersion system (CUVETTE, Sympatec, Clausthal-Zellerfeld, Germany). Approximately 5 mg of sample was suspended in 5 mL of dispersion media, composed of heptane (HPLC grade) and 0.1% w/w lecithin. The suspension was sonicated for 180 s following prior investigation to ensure no sample dissolution or destruction, before addition to a glass cuvette containing 50 mL of dispersant and a magnetic stirring bar rotating at 1000 rpm. Sizing was performed (a series of 5 repeats) when the optical concentration was equal to or greater than 10%, over a duration of 20 s. Particle size analysis was performed using Windox 5.0 software (Sympatec, Clausthal-Zellerfeld, Germany) following Fraunhofer diffraction theory to calculate the cumulative undersize particle parameters  $d_{10}$ ,  $d_{50}$  and  $d_{90}$ , the volume median diameter (VMD) and the sample span (Equation 5.1).

$$Span = \frac{d_{90} - d_{10}}{d_{50}}$$

Equation 5.1

### 5.2.4.2 Crystal Modelling

Computational molecular dynamic modelling was used to predict the physical crystal habit of the budesonide samples (MS Modelling, Accelrys Software Inc., Cambridge, UK). Crystallographic data for budesonide were obtained from the

Cambridge Structural Database and based on single crystal diffraction data (Albertsson et al., 1978). With reference to the SEM images of each sample, the Miller indices of the crystal faces produced from each solvent were identified.

#### **5.2.4.3 X-Ray Powder Diffraction (XRPD)**

To determine the X-ray powder diffraction (XRPD) pattern of crystalline budesonide, samples were analysed on a Bruker Powder Diffractometer (D8 Advance AXS; Bruker Inc., Madison, USA). Samples were filled into 0.7 mm glass capillaries and mounted on a goniometer head. The data were collected using CuK $\alpha$  radiation ( $\lambda=1.5418$  Å) over a single  $2\theta$  sweep with range  $2\theta = 5 - 50^\circ$  and step size of  $0.025^\circ/\text{step}$  and step time of 1.5 seconds. The monochromator slit was set to 2 mm and the detector was Si(Li).

#### **5.2.4.4 Differential Scanning Calorimetry (DSC)**

A differential scanning calorimeter (DSC, 2190, TA Instruments, Surrey, UK) was used to perform thermal analysis on all crystalline samples of budesonide after previous calibration using indium. Powder samples ( $n=3$ ) of approximately 3.0 mg were accurately weighed into aluminium pans, ensuring a total covering of the base by pressing down the samples and then hermetically sealed. The temperature was equilibrated to  $50^\circ\text{C}$  before heating at a rate of  $10^\circ\text{C}/\text{min}$  to  $350^\circ\text{C}$  under dry nitrogen purge (0.30 L/min).

#### **5.2.4.5 AFM Nanoindentation measurements**

An atomic force microscope (AFM) was used to indent ( $n=9$ ) individual crystals ( $n=3$ ) using a Nanoscope IIIa and J-scanner (all DI, Santa Barbara, CA, USA). The indenting probe was hemispherical in shape and possessed a nominally high spring constant (R150-NCL, Nanosensors, Neuchatel, Switzerland).

For accurate extrapolation of AFM force-distance data to a Young's modulus value, the true radius of the indenting tip must be known. Tip radius determination was performed using a tip-characterisation grating (TGT01; NT-MDT, Moscow, Russia) in which the probe being investigated is raster scanned over the test grating composed of a uniform array of sharp spikes which in turn,

produces a reverse image of the probing tip. This image was deconvoluted to determine tip radius, using a well-established technique using image analysis software (SPIP Image Metrology ApS, Lingby, Denmark) (Hutter and Bechhoefer, 1993) (Clifford and Seah, 2005a) (Hooton et al., 2004). This measurement was performed before and after indentation measurements to ensure indenting probe integrity was maintained. In this study, the hemispherical probe radius was determined to be 318 nm.

Quantification of the probe cantilever nominal spring constant was performed using a dynamic method of thermal noise analysis (Hutter and Bechhoefer, 1993). A spring constant of  $36.2 \pm 0.2$  N/m was recorded using this approach and agreed with the manufacturer's quoted value measured using the Sader method (Sader et al., 1995).

Force-distance measurements were performed on different areas of a single crystal so that the dominant face with respect to the indenter was indented. The cantilever deflection and piezo displacement were derived into a Young's modulus value using Hertzian model of deformation shown in Equation 5.2 (Hertz, 1881) (Plassard et al., 2004)

$$E = \frac{3(1-\nu^2)k\Delta z}{4\delta^{3/2}R^{1/2}}$$

**Equation 5.2** The Hertz model of deformation ( $E$ : Young's modulus,  $k$ : spring constant of the indenting cantilever,  $\Delta z$ : relative piezo displacement,  $\delta$ : indentation depth,  $R$ : radius of indenter,  $\nu$ : Poisson ratio of the indenting probe)

## **5.2.5 Cohesive-Adhesive Balance**

### **5.2.5.1 Atomic Force Microscopy – Topography analysis of substrate surfaces**

The surface topography and roughness measurements of budesonide and lactose crystals were investigated using a Nanoscope IIIa controller, a Multimode AFM and a J-type scanner (all (Bruker Nano AFM, Santa Barbara, CA, USA). All AFM surface topography images were recorded in Tapping Mode

operation, in which, imaging was conducted using TESP Olympus tips (DI, Cambridge, UK) at a scan rate of 1 Hz. Surface roughness measurements were analysed over a 10  $\mu\text{m}$  X 10  $\mu\text{m}$  area. To quantify the variations in the surface properties of the crystal surfaces, the root-mean-squared surface roughness measurement ( $R_q$ ) and the mean surface roughness ( $R_a$ ) of the height deviations of the surface asperities were computed using Nanoscope software (v 4.23r4, (Bruker Nano AFM, Santa Barbara, CA, USA)).

#### **5.2.5.2 Atomic Force Microscopy – Interaction Force Measurements**

Prior to force measurements, particles from each batch of budesonide were attached onto standard V-shaped tipless cantilevers with pre-defined spring constants (DNP-020, DI, CA, USA) using an epoxy resin glue (Araldite, Cambridge, UK), using a previously described method (Begat et al., 2004a). Five tips were prepared for each of the batches of budesonide, and all probes were examined with an optical microscope (magnification 50x) to ensure the integrity of the attached particle, before allowing the thin layer of glue to dry.

A single crystal of lactose monohydrate with well-defined habit and appropriate smoothness ( $<1\text{ nm } R_a$  and  $R_q$ ) was carefully grown to provide a uniform surface for force of adhesion measurements while an unmicronised crystal of similar surface smoothness on the (002) face was selected from each primary source of budesonide samples for the force of cohesion measurements.

The substrate was loaded on to the AFM scanner stage, which was enclosed in a custom-built environmental chamber, in which the ambient conditions were maintained at a constant temperature of 25  $^{\circ}\text{C}$  ( $\pm 1.5\text{ }^{\circ}\text{C}$ ) and relative humidity of 35 % RH ( $\pm 3\text{ }%$ ). The interaction forces between lactose and budesonide substrates were measured by recording the deflection of the AFM cantilever as a function of the substrate displacement ( $z$ ) by applying Hooke's Law ( $F = -kz$ ). Individual force curves ( $n = 1024$ ) were performed over a 10  $\mu\text{m}$  x 10  $\mu\text{m}$  area at a scan rate of 4 Hz and a compressive load of 40 nN. The instruments other operating parameters, including the laser position were kept constant over the study. To quantify AFM force measurements it is imperative to measure the spring constants of the cantilevers used. However, as described by Begat *et al*

(2004), the CAB technique compares adhesion and cohesion with an individual colloid probe, which eliminates the need to accurately determine the spring constant.

#### **5.2.5.3 Data Processing**

With the vast array of data generated during force volume measurements, custom-built software was used to extract data. The collected force data were analysed to ensure normal distribution, indicating uniform contact between the drug probe and excipient substrate. Arithmetic mean and standard deviation were obtained from force data and used to produce CAB plots for the interactions of the different batches of budesonide to lactose monohydrate.

#### **5.2.6 HPLC Analysis of Budesonide**

Quantification of budesonide utilised HPLC coupled with UV detection. The system comprised a high pressure pump (Jasco PU-980, Jasco Corp., Japan) flowing at 1.5 mL/min through a 5 µm ODS HPLC column (Hypersil, Jones Chromatography Ltd., Hengoed, UK) fixed within a temperature controlling column oven (Jasco CO-965, Jasco Corp., Japan) at 40°C and a UV detector (HP-1050, Agilent Technologies UK Ltd., Wokingham, UK) set to 235 nm. The mobile phase consisted of HPLC grade methanol (45%), acetonitrile (35%) and 20% ultra pure water.

#### **5.2.7 Preparation of DPI formulation**

Binary formulations containing 200 µg micronised budesonide and lactose monohydrate (Respitose, SV003, DMV-Fonterra Excipients, Vehgel. Netherlands) per 25 mg shot weight were prepared to evaluate aerosolisation performance. Each 4 g of formulation contained 0.0320 g API and 3.968 g of lactose monohydrate.

Blends were prepared in glass vials using a geometric blending sequence. Briefly, the weighed drug was placed between two layers of lactose of approximately the same volume and mixed for 60 s (Whirlimixer, Fisons, Loughborough, UK). Subsequent additions of lactose were added



geometrically, with a further 60 s of mixing after each addition. The vial was transferred into a Turbula mixer (Turbula T2F, Willy A Bachofen AG, Basel, Switzerland) and subsequently mixed for a further 45 minutes. The samples were then stored at 44 % RH for 24 hours prior to content uniformity determination.

#### **5.2.8 Content Uniformity**

Following blending, ten random samples of  $25 \pm 1$  mg, from different areas of the powder bed were weighed and dissolved in 50 mL of mobile phase. The amount of drug in each sample was obtained from HPLC assay and the content uniformity was expressed as percentage relative standard deviation (%RSD).

#### **5.2.9 *In Vitro* Aerosol Deposition Studies**

Prepared blends of each material was accurately filled into HPMC capsules ( $25 \pm 1$  mg, QualiV, Qualicaps, bn. E0701921, Madrid, Spain) and stored at 44% RH for 24 hours prior to testing. The *in vitro* performance of each formulation was evaluated using a Next Generation Impactor (NGI, Copley Scientific, Nottingham, UK) with pre-separator. The pre-separator was charged with 15 mL mobile phase. Each of the individual stages were coated with 1% silicon oil (Agros Organics, Geel, Belgium) in hexane solution and allowed to air dry. The flow rate of through the impactor was set to  $90 \text{ L.min}^{-1}$  using a digital flow meter (DFM2000, Copley Scientific, Nottingham, UK). The formulations were aerosolised from a Cyclohaler (TEVA, Netherlands) over a duration of 2.7 s at  $90 \text{ L.min}^{-1}$ . For each repeat ( $n=3$ ), two capsules were actuated after which the whole system was individually washed down with mobile phase. The capsules, device, mouthpiece and throat were individually washed into 50 mL volumetric flasks. The pre-separator was removed from the NGI and filled with 85 mL of mobile phase, sealed and then shaken for 1 minute. An aliquot was then taken from all samples for HPLC analysis. For each of the stages within the NGI, mobile phase was pipetted directly onto each stage. Stages 1 – 5 were allocated 20 mL, stages 6 and 7 received 10 mL and stage 8 had 10 mL. The stages were then shaken on a bench-top laboratory shaker (IKA Vibramax VXR, Staufen, Germany) for five minutes before removing aliquots of each for

HPLC analysis. The HPLC assay was the same as above, using the drug content analysis by HPLC process outlined above.

## 5.3 RESULTS AND DISCUSSION

### 5.3.1 Physicochemical Characterisation of Primary Budesonide Crystals

The particle size distributions (PSD) of the primary sources of the two budesonide samples are shown in Table 5.1. The volume mean diameter of samples A and B were similar, although the span of the PSD was wider for sample B with the presence of a greater number of coarser crystals. Scanning electron micrographs and crystal modelling of the dominant crystal faces of samples A and B are shown in Figure 5.1. SEM images of samples supported the particle size analysis data with the suggestion of a wider distribution in particle size of sample B. Two distinctive crystal morphologies were evident for the 2 samples, in which the crystals produced from acetone (sample A) possessed a diamond like habit, while budesonide crystallised from DMF (sample B) conformed to a more tabular morphology. Together with the modelling of the crystal habit, these images suggest that the different solvents used in the primary solvent/anti-solvent crystallisation affected the growth kinetics of the different faces of the crystalline samples, although there was no evidence that a new crystalline face was formed. For sample B, the slow growing {002} faces dominated, while the addition of anti-solvent to the acetone solution (sample A), under otherwise identical crystallisation conditions, suggested that the {011} and {101} faces grew at a much lower slower rate than {002}. Previous work investigating the surface chemistry of different budesonide faces modelled *in silico*, identified differences in the polarity of the {002} and {101} faces of budesonide (Hooton et al., 2008). It was found that the {002} face was capable of apolar interaction only and by altering the relative dominance of this face through habit modification, the potential for surface interactions was changed.

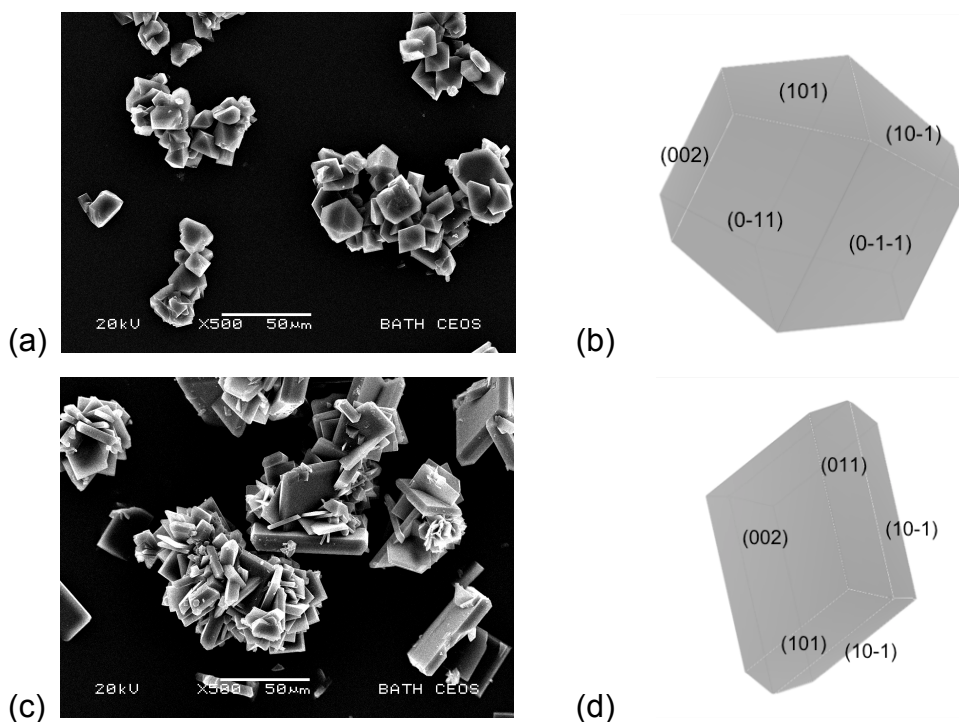


**Figure 5.1** Scanning electron micrographs and computer models of the crystal habits of Sample A (a,b) and Sample B (c, d)

**Table 5.1** Particle size distribution of crystalline budesonide samples A and B.

<b>SAMPLE</b>	<b>D<sub>10%</sub></b> <b>(<math>\mu\text{m} \pm \text{SD}</math>)</b>	<b>D<sub>50%</sub></b> <b>(<math>\mu\text{m} \pm \text{SD}</math>)</b>	<b>D<sub>90%</sub></b> <b>(<math>\mu\text{m} \pm \text{SD}</math>)</b>	<b>Span</b>	<b>VMD</b> <b>(<math>\mu\text{m} \pm \text{SD}</math>)</b>
Sample A	17.79 $\pm$ 0.04	40.13 $\pm$ 0.07	62.84 $\pm$ 0.20	1.12 $\pm$ 0.01	40.40 $\pm$ 0.58
Sample B	16.96 $\pm$ 0.25	58.72 $\pm$ 0.55	95.20 $\pm$ 0.90	1.33 $\pm$ 0.01	57.87 $\pm$ 0.54

Representative DSC thermograms of samples A and B are shown in Figure 5.2. For both samples, an endothermic peak was observed at  $\sim 260^\circ\text{C}$ , consistent with the previously reported melting point of crystalline budesonide (Velaga et al., 2002) (Bandi et al., 2004) (Tajber et al., 2009). There is however, a suggestion in the DSC thermograms that the melting endotherm for sample B is broader and the onset temperature of melting was observed to be approximately 3 degrees lower than sample A. The melting point of sample A was approximately  $263^\circ\text{C}$  and for sample B was approximately  $260^\circ\text{C}$ . This

lowering in the onset and peak melting temperatures may suggest greater levels of impurities or greater levels of disorder in the primary crystals of sample B (Clas et al., 1999). Endothermic events occurring below 100°C were observed in both samples and may be indicative of the presence of residual solvents or the presence of crystal disorder.

The XRPD diffractograms of the two samples are shown in Figure 5.3. The representative diffractograms for the two samples displayed similar sharp diffraction peaks at the same two-theta angles, which suggested that the samples were crystalline and exhibited the same polymorphic form.

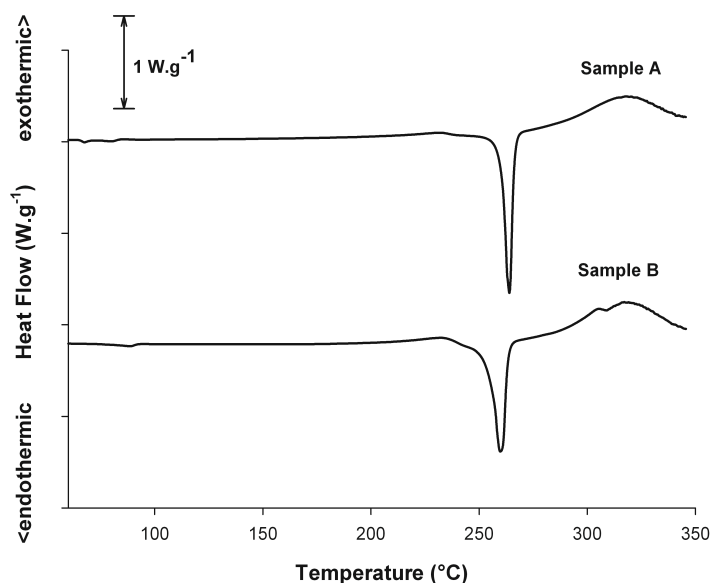


Figure 5.2 Representative thermograms of budesonide samples A and B.

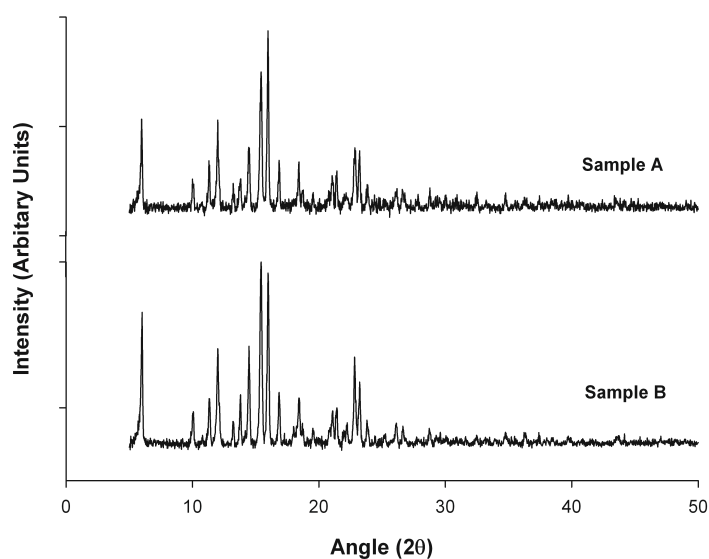


Figure 5.3 The X-ray powder diffraction profiles of the primary budesonide crystals of samples A and B.

### 5.3.2 Mechanical measurements of the primary budesonide crystals

All mechanical measurements were performed on the  $\{002\}$  faces, particularly as it provided the most accessible face for probe-substrate interaction during force loading experiments, and allowed direct comparison of the influence of crystallisation conditions on the Young's modulus. With the use of a hemispherical probe with a large radius and a stiff cantilever, the press-on forces were controlled to maintain Hertzian deformation during mechanical

loading and unloading of the crystal substrates. Topographical imaging of the crystal surfaces were recorded before and after each indentation cycle to ensure the suitability of the crystal surface for indentation and to ensure that no plastic deformation had occurred upon loading and unloading.

Representative surface topography images of the {002} faces of samples A and B before and upon indentation are shown in Figure 5.4. The arrows in Fig. 5.4B and D indicate the regions where the probe made initial contact with the substrate during tip-substrate engagement. This is the point at which high loading stresses being placed on the crystal surface during engagement led to plastic deformation. The additional loading and unloading measurements on the substrate surfaces show no sign of plastic deformation.

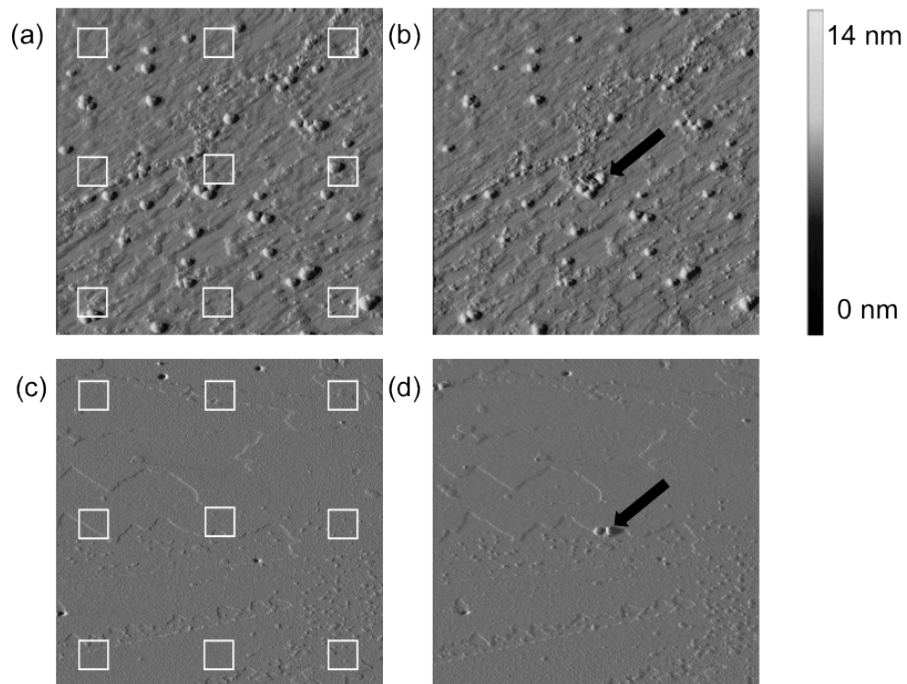


**Figure 5.4** Atomic force microscope images ( $3 \times 3 \mu\text{m}$ ) of Sample A before indentation (a), Sample A post indentation (b) and Sample B prior to indentation (c) and Sample B after indentation. The boxes ( $\square$ ) indicate areas where mechanical measurements were undertaken. The black arrows indicate the point of initial contact upon tip-substrate engagement, where high loading has resulted in plastic deformation.

Representative indentation<sup>3/2</sup> versus loading force plots of samples A and B are shown in Figure 5.5. These data indicate that the indentation of sample A was significantly greater than that of sample B, suggesting that sample B exhibited a greater resistance to elastic deformation.

The gradients of the individual loading versus indentation<sup>3/2</sup> curves were calculated and used to measure the Young's modulus values via the Hertzian model of deformation (Equation 5.2). The Young's modulus measurements for samples A and B are summarised in Table 5.2. The Young's modulus of sample B was significantly higher than sample A (ANOVA,  $p < 0.01$ ), indicating that changing the solvent environment during primary crystallisation may directly impact the mechanical properties of these materials.

These observed variations in Young's modulus and the possible influence of primary crystallisation conditions are further supported by AFM nanoindentation measurements on the (002) face of budesonide by Davies et al. (2005), who recorded an E value of 10GPa for unmicronised budesonide. These range of values obtained in this study and that of Davies, suggest that primary crystallisation conditions, which directly influence nucleation kinetics and crystal growth, may directly influence the material's resistance to deformation. A similar range of Young's modulus measurements were measured for the dominant {010} crystal face of fluticasone propionate, in which the addition of different anti-solvents to a solution of fluticasone propionate (FP) in acetone significantly altered the mechanical properties of the resulting crystals (Kubavat et al., 2009). Moreover, the study by Kubavat et al. demonstrated the need for repeated micronisation cycles of FP with a low Young's modulus, suggesting the influence of elastic modulus on this material's resulting secondary processing behaviour.



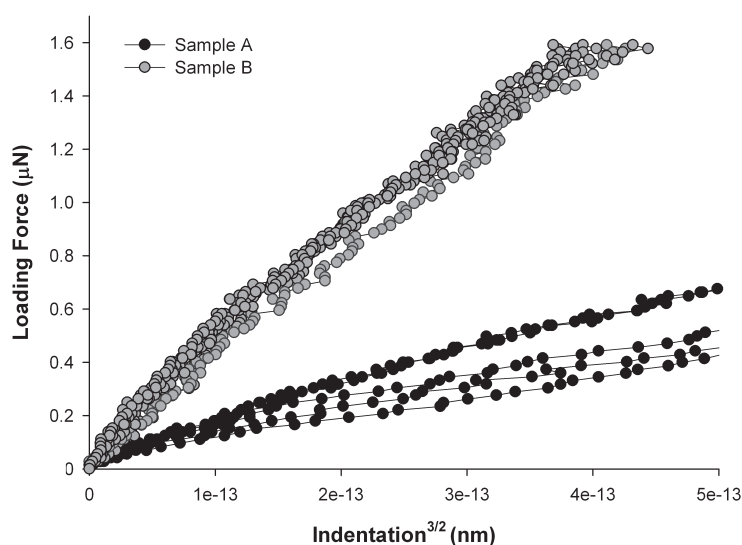


**Figure 5.5** Individual loading force against indentation<sup>3/2</sup> for the contact of a hemispherical probe on the {002} faces of a number of different crystals of samples A and B.

**Table 5.2** The Young's modulus values obtained on the {002} face of different crystals of samples A and B using AFM nanoindentation. At total of 8 nanoindentation measurements were undertaken on three different crystals of each sample (n=24).

<b>SAMPLE</b>	<b>Young's Modulus (GPa ± SD)</b>
Sample A	0.95 ± 0.50
Sample B	4.04 ± 1.35

### 5.3.3 Effect of crystal habit and mechanical properties of primary budesonide crystals on secondary processing and DPI formulation performance

An air-jet microniser was employed to reduce the crystalline particles to a respirable size range (less than 5 μm). The micronised batches were investigated for differences in their interfacial interactions using the CAB approach to colloidal probe AFM, and *in vitro* deposition performance upon being blended with a coarse grade of lactose monohydrate.

The particle size distribution (PSD) of the unmicronised and micronised budesonide samples A and B are shown in Figure 5.6 and PSD analysis of the micronised material is provided in Table 5.3. Although the volume median diameter and span of the primary crystals of sample A was smaller than sample B, the particle size reduction ratios and span of the respective micronised PSDs were not conserved. The VMD reduction of sample A was 88.7%, which was smaller than that of sample B that had a VMD reduction of 93.8%. The increase in the span of the PSD for sample A suggests that the efficiency of particle size reduction for sample A was not as efficient as sample B. This observation in the milling behaviour could be related to a change in the crystal morphology, as highlighted by the study of adipic acid (Chikhalia et al., 2006) whereby the milling was altered by differing crystal habits. This chapter's work suggest that exposed crystalline faces can be fractured more effectively, or that the increase in the Young's modulus of sample B may have a contributing factor to the efficiency of particle size reduction, as previously shown for fluticasone propionate (Kubavat et al., 2009).

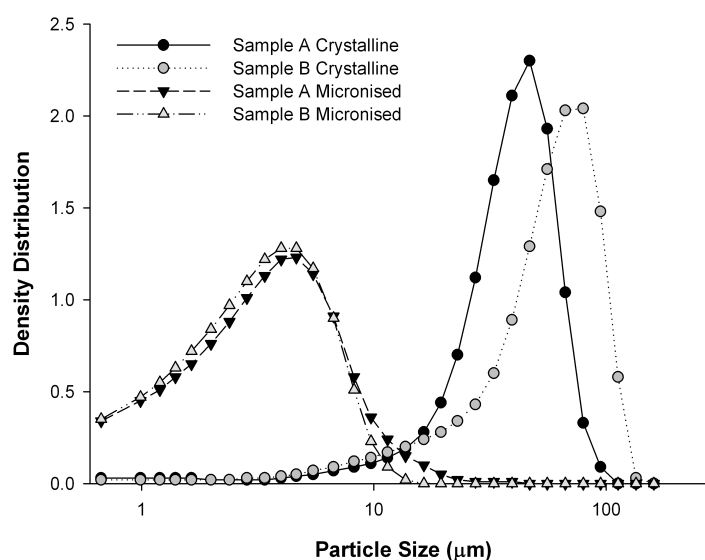


**Figure 5.6** The particle size distribution of the unmicronised (primary) and micronised (secondary) samples of budesonide.

**Table 5.3 Particle size distribution analysis of micronised budesonide samples A and B.**

<b>SAMPLE</b>	<b>D<sub>10</sub> (<math>\mu\text{m} \pm \text{SD}</math>)</b>	<b>D<sub>50</sub> (<math>\mu\text{m} \pm \text{SD}</math>)</b>	<b>D<sub>90</sub> (<math>\mu\text{m} \pm \text{SD}</math>)</b>	<b>Span (<math>\pm \text{SD}</math>)</b>	<b>VMD (<math>\mu\text{m} \pm \text{SD}</math>)</b>
Sample A	0.96 $\pm$	3.38 $\pm$	8.02 $\pm$	2.11 $\pm$ 0.05	4.18 $\pm$
	0.02	0.06	0.01		0.09
Sample B	0.95 $\pm$	3.14 $\pm$	6.90 $\pm$	1.90 $\pm$ 0.03	3.59 $\pm$
	0.02	0.05	0.03		0.04

The surface interfacial properties of each of the micronised materials were investigated using AFM-CAB with respect to surfaces of lactose monohydrate.

The CAB data of the two micronised budesonide samples with respect to their interactions with the {002} faces of their respective unm micronised forms and lactose monohydrate are shown plotted in Figure 5.7. The CAB measurements of the micronised particles were 0.728 ( $R^2 = 0.9970$ ) and 0.578 ( $R^2 = 0.9980$ ) for samples A and B, respectively. The CAB value of sample B was similar to previously reported measurements of commercially supplied micronised budesonide of 0.543 with respect to lactose monohydrate (Hooton et al., 2008). These data suggest that the force of adhesion of micronised budesonide samples to lactose was greater than the corresponding force of cohesion. Further analysis suggests that for a equivalent force of cohesion the adhesion of the micronised particles from sample B to lactose was approximately 22 % greater than particles from sample A. These data suggest that a greater deaggregation energy may therefore be required to elutriate the respirable sized particles of sample B from a lactose monohydrate surface.

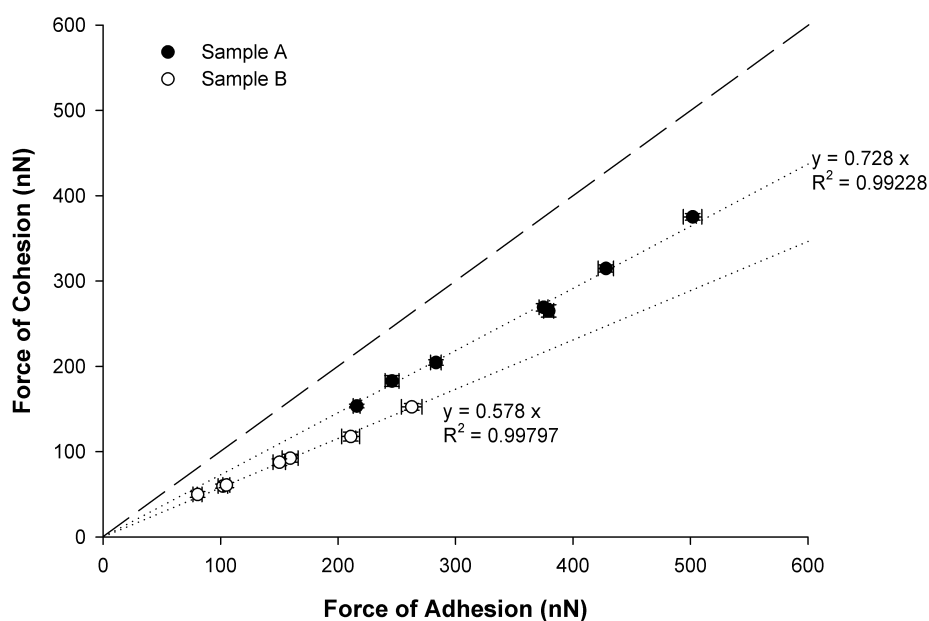


**Figure 5.7 CAB plots for micronised samples A and B of budesonide with respect to lactose**

To enable accurate quantification of API during *in vitro* testing, HPLC analysis was performed. The relationship between budesonide drug concentration (0.5, 1, 5, 10 and 50  $\mu\text{g}.\text{mL}^{-1}$ ) and peak area for each drug was found to be linear, with linear regression analysis yielding a  $R^2$  value of 0.99999 and is shown in Figure 5.8.

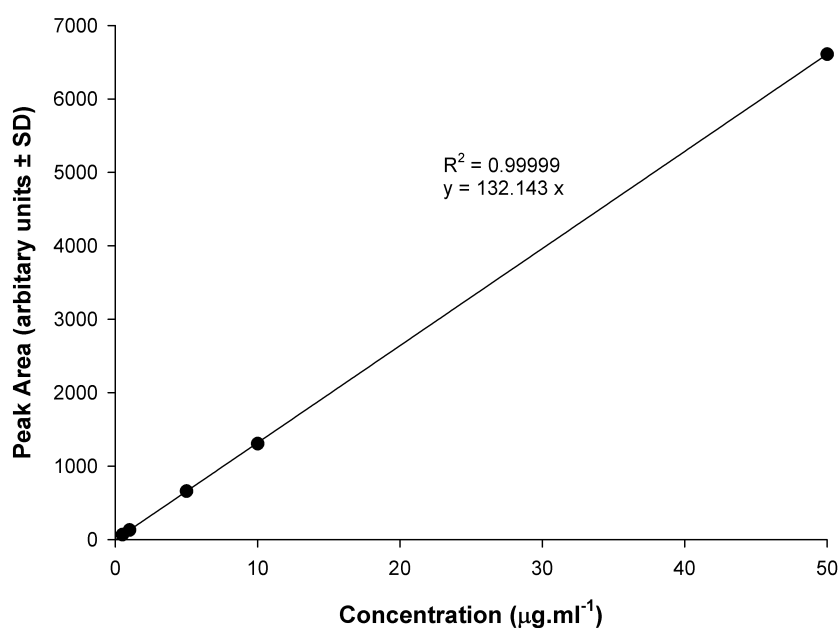


**Figure 5.8 Representative HPLC calibration curve obtained for budesonide**

A representative HPLC trace for a calibration sample of budesonide  $1 \mu\text{g}.\text{mL}^{-1}$  is shown in Figure 5.9.

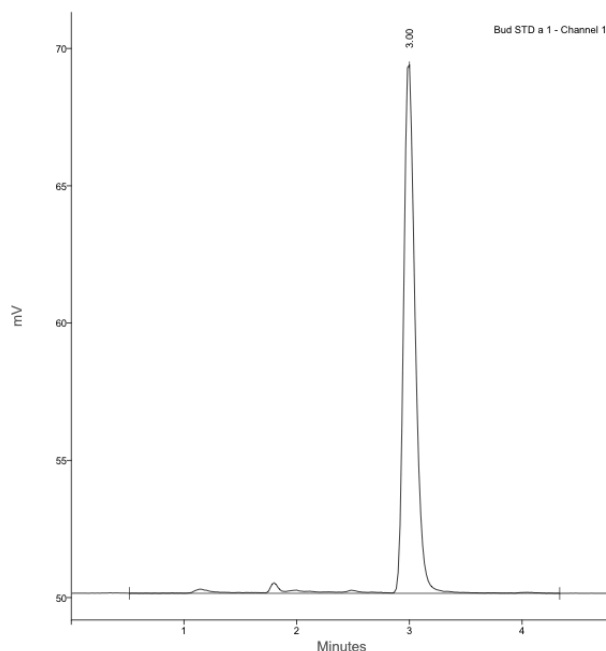


**Figure 5.9 A representative HPLC trace for budesonide**

The content uniformity of each formulation was evaluated prior to impaction testing and is expressed as a percentage relative standard deviation (%RSD).

These were determined to be 1.72 % and 1.03 % for samples A and B, respectively, suggesting homogeneous distribution of the API throughout the formulation blend. Given that these values were lower than 5 %, both formulations were deemed suitable for *in vitro* impaction testing.

The *in vitro* aerosolisation performance of carrier based DPI formulations containing samples A and B was assessed using a next generation impactor (NGI). The drug deposition profiles of both formulations are shown in Figure 5.10 and the emitted dose (ED), fine particle dose (FPD) and fine particle fraction (FPF) data are summarised in Table 5.4.

The stage-by-stage deposition profiles of samples A and B upon aerosolisation from the Cyclohaler device were similar. However, there was a significantly greater mass of drug deposited on stages 2 – 8 of the impactor upon aerosolisation of sample A (ANOVA,  $P < 0.05$ ) as indicated by the significant increase in fine particle dose (Table 5.4). The fine particle dose (FPD) of sample A was  $15.9 \pm 0.37 \mu\text{g}$ , whereas the FPD of sample B was  $11.7 \pm 0.29 \mu\text{g}$ . These data indicate that the deaggregation efficacy of sample A was greater than that of sample B. In addition, there were no significant differences between the emitted dose of each formulation containing either sample A or sample B.

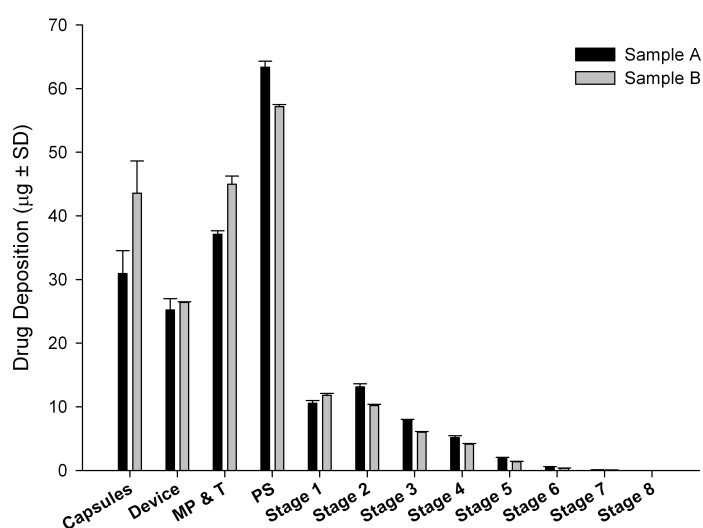


**Figure 5.10 NGI stage-by-stage deposition profile of budesonide samples A and B**

**Table 5.4** *In vitro* performance characteristics of the two samples of budesonide using NGI testing (FPF<sub>RD</sub> – fine particle fraction of the recovered dose, FPF<sub>ED</sub> – fine particle fraction of the emitted dose)

	Sample A	Sample B
Emitted Dose ( $\mu\text{g} \pm \text{SD}$ )	164.1 (1.44)	161.8 (1.64)
Fine Particle Dose ( $\mu\text{g} \pm \text{SD}$ )	15.9 (0.37)	11.7 (0.29)
FPF <sub>RD</sub> (% $\pm$ SD)	8.15 (0.23)	5.27 (0.11)
FPF <sub>ED</sub> (% $\pm$ SD)	9.68 (0.28)	7.24 (0.11)
MMAD $\pm$ GSD ( $\mu\text{m}$ )	4.38 $\pm$ 2.43	5.20 $\pm$ 2.54

The aerosolisation performances of carrier-based formulations are influenced by the interfacial forces of interaction between the API and carrier lactose. CAB analysis of budesonide samples A and B indicated that the adhesive tendency of budesonide sample B to lactose was greater than that of sample A. Hence, the higher aerosolisation efficiency of sample A may be related to its lower adhesive affinity to lactose which may have resulted in greater deaggregation efficiency in comparison to sample B. These data suggest that the use of different crystallisation conditions may lead to significant differences in the mechanical properties of the primary crystalline material, which may affect the surface interfacial force balance of secondary processed micronised materials. The impact of these changes to the surface properties of the micronised materials may affect the final drug product performance.

## **5.4 CONCLUSIONS**

This study has demonstrated the importance of understanding the implications of modifying the crystal habit for budesonide included in carrier-based DPI formulations. The use of different crystallisation conditions has led to significant differences in the mechanical properties of the primary crystalline material and altered the CAB value of the micronised materials. In turn, these differences are suggested to influence the *in vitro* performance of DPI formulations. This work highlighted the effect and implications resulting from changes in the primary crystallisation of APIs and advocates careful consideration when developing crystallisation processes for these materials.



## **Chapter 6: The Influence of Crystal Form on the Primary Crystallisation and Secondary Processing of Ipratropium Bromide for Dry Powder Inhalation**

### **6.1 INTRODUCTION**

For therapeutic delivery of active pharmaceutical ingredients (APIs) to the lungs via a dry powder inhaler (DPI), the particle size range of the API needs to be between 1 – 5  $\mu\text{m}$  (Timsina et al., 1994a). For these particles, gravitational and inertial forces are weak and van der Waals, capillary and electrostatic forces dominate. The dominance of the physical forces versus body mass results in sub-10  $\mu\text{m}$  particles being highly cohesive.

The cohesive behaviour of micron-sized API particles prevents accurate metering and handling of the material for inclusion in the final DPI drug product. To circumvent this problem, API particles are generally blended with large inert carrier particles of lactose monohydrate (Bell et al., 1971), which enables metering of the dose and filling of the formulation into the device (Malcolmson and Embleton, 1998). The aerosolisation efficiency of this interactive mixture is dependent on the balance of cohesive (drug-drug) and adhesive (drug-lactose) interparticulate forces. This force balance within a DPI formulation is dependent on the process history of the API, which will affect the surface interfacial properties of the API particles and, therefore, their cohesive and adhesive interactions (Begat et al., 2004a).

The dominant approach in producing API particles for DPI drug products centres on destructive top-down strategies, where primary API crystals are secondary processed by micronisation using high-energy air-jet mills (Shekunov and York, 2000). The primary crystallisation process of APIs is a key step in the production of pharmaceutical products, and any variability in the properties of

the primary crystals may directly influence variability down-stream upon secondary processing of the material. Thus, control of material properties during primary crystallisation is required in developing drug products within a well-defined design space (Yu, 2008) (Variankaval et al., 2008). Key to this process is the selection of appropriate solvents and operating conditions in order to produce primary crystals with defined crystal habit, crystal form and particle size in enabling safe and effective handling upon secondary processing.

Traditional methods of reducing the particle size of APIs to the respirable size range have included various comminution techniques such as ball, hammer and air-jet milling. The industrial standard for producing these materials however, is air-jet milling (Chow et al., 2007). This process requires feeding of primary crystals into a turbulent centrifugal airflow under high pressure. The resulting attrition is created by particle-particle and particle-wall collisions, which cause fracturing, chipping and overall particle size reduction of the coarser particles. Larger particles are held within the centrifuge for further size reduction whilst finer materials, due to the loss of inertia, enable cyclonic collection of the micronised product and subsequent filtration of the micronised materials (Midoux et al., 1999). Though the feed rate of input material and the operating pressures of the air-jet mill can be specified, the degree of particle size reduction in this process is relatively uncontrolled and often results in a non-uniform distribution of micronised materials (Parrot, 1990). If the process has failed to deliver products of a defined specification, the materials are generally reprocessed through the microniser until the required particle size distribution (PSD) is obtained.

Crystal properties such as physical form, pre-existing imperfections and flaws within the crystalline lattice influence the mechanical properties of these materials and, are attributed therefore, to the milling efficiency of organic crystals (Zugner et al., 2006). One property that represents a material's resistance to plastic deformation is the Young's modulus. The degree of elasticity has been previously shown to affect the size reduction operation (Zugner et al., 2006) and is increasingly investigated at the micro and nano-Newton range using atomic force microscopy (AFM) (Perkins et al., 2007).

The selection of appropriate salts or hydrates of APIs has been well established for many marketed products and is investigated to provide a crystal form of optimum stability, solubility and pharmacokinetic properties (Datta and Grant, 2004) (Gardner et al., 2004). Physicochemical properties of materials are known to be affected by the inclusion of water in the crystal lattice in the form of pharmaceutical hydrates (Khankari and Grant, 1995) (Agbada and York, 1994) and have been shown to alter their tableting behaviour (Di Martino et al., 2007). The influence of the effects of crystal form selection on the mechanical properties and subsequent processing behaviour of these materials is not well understood, although recent work has investigated the modification of nanomechanical properties by different polymorphic forms (Perkins et al., 2009).

The purpose of this study was to investigate the mechanical and processing differences between anhydrous and monohydrate forms of ipratropium bromide. The aerosolisation efficiency of these materials from DPI formulations was measured to determine the effect of crystal form on the functionality of the two samples. Ipratropium bromide (8-isopropyl-nor-atropine-methylbromide) is an anti-cholinergic agent used as a bronchodilator in patients with chronic obstructive pulmonary disease (COPD), in the maintenance of normal respiratory function and treatment of associated bronchospasms. It is marketed as a carrier-based DPI drug product *Atrovent*<sup>®</sup>, which utilises glucose as the carrier particles.

## 6.2 MATERIALS AND METHODS

### Materials

Crystalline ipratropium bromide (IB) was supplied by Amplachem Inc. (Indiana, USA). Lactose monohydrate (Respitose, SV003) was obtained from DMV-Fonterra Excipients (Vehgel, Netherlands). All solvents used were supplied by Fisher Scientific UK (Loughborough, UK) and were 99.9% pure. Ultra pure water was produced by MilliQ from reverse osmosis (Millipore, Molsheim, France).

#### 6.2.1 Determination of IB Solubility

The solubility of ipratropium bromide was determined in ethanol and ultra pure MilliQ water over a range of temperatures (5-40°C for H<sub>2</sub>O and 20-40°C for ethanol). An excess of IB was placed into a 100 ml conical flask and approximately 75 ml of solvent was added. Flasks containing drug and solvent were sealed using a glass Quickfit glass stopper and tightly sealed with Parafilm (Pechiney Plastic Packaging, Chicago, USA) prior to being placed into an agitating water bath (Grant SS40D, Grant Instruments, Chelmsford, UK) with additional cooling unit (Grant C1G, Grant Instruments, Chelmsford, UK). Samples of approximately 1.0 ml were taken after 48 hours of shaking at a set temperature, using an extended steel needle and glass syringe stored at the appropriate temperature prior to filtration via a 0.22 µm membrane syringe filter (Whatman Inc., Clifton, NJ, USA). From the filtered solution, 100 µL samples (n=3) were taken using a Gilson pipette and placed into volumetric flasks and made up to the appropriate volume using 0.1mM HCl. Solubility of IB was calculated by comparison of AUC for samples and calibration curves performed at the same time using the same HPLC protocol outlined below.

### 6.2.2 Crystallisation of IB

Ipratropium bromide monohydrate crystals were produced using a seeding crystallisation approach. Crystal seeds were first produced from a saturated solution of IB in water. An excess of IB was added to 50ml ultra pure water and was continuously stirred by a magnetic stirring bar over 2 hours whilst the temperature was maintained at 25°C. This solution was then filtered using a 0.45 µm nylon filter (Whatman International Ltd., Maidstone, UK) fitted within heated glassware. The resulting solution was then stirred at 500 RPM by a PTFE coated octahedral magnetic stirrer bar (25 x 5 mm) and cooled to 5°C, at a rate of 0.2°C.min<sup>-1</sup>. After 24 hours, crystals were isolated using vacuum filtration (Whatman International Ltd., Maidstone, UK) and dried at 30°C under vacuum. Once a stable weight was achieved, the seed crystals were passed through a stainless steel 500 µm sieve (Endecotts Ltd., London, UK). An aliquot of 500 mg was used as the seeding material.

The IB seeds were then placed into another 50ml saturated solution of IB at 25°C, prepared as before, and stirred at 500 RPM by a magnetic stirrer (25 x 5 mm) for 5 minutes after which the temperature was reduced to 21.5°C at a rate of 0.2°C.min<sup>-1</sup>. Crystals were harvested 24 hours later using vacuum filtration through a 0.45 µm nylon filter and rinsed once with 50 ml cold acetone before being placed into vacuum oven at 30°C. Once a steady weight of IB was achieved, these materials were removed from the oven and stored at 19°C under ambient RH (30 – 40% RH).

In an effort to produce anhydrous ipratropium bromide, crystals were prepared using supercritical carbon dioxide (SCO<sub>2</sub>) to remove solvent from a solution of IB in ethanol. This anti-solvent crystallisation approach is often nominally termed GAS (gas anti-solvent) or SAS (supercritical anti-solvent) (Jung and Perrut, 2001) (Fages et al., 2004) (Shoyele and Cawthorne, 2006) .

A schematic diagram of the process is shown in Figure 6.1. A saturated solution of IB in 50 ml ethanol at 25°C was made using the previous method and placed into a 150 ml fritted glass extraction vessel with a 0.2 µm porous

membrane.  $\text{SCO}_2$  was passed through the ethanolic solution by pumping liquid  $\text{CO}_2$  through a high-pressure pump connected to a heat exchanger (P-500, Thar Technologies Inc., Pittsburgh, PA, USA) at a flow rate of  $10 \text{ g}\cdot\text{min}^{-1}$ . The temperature of the rig was maintained at  $40^\circ\text{C}$  by an air heated oven (Thar Inc.), minimizing secondary crystallisation prior to solvent extraction. During operation, a constant working pressure of 100 bar was maintained using an automated backpressure regulator (BP-1580-81, Thar Inc.) and effluent  $\text{CO}_2$  was expelled through a custom HEPA filtration system. The process was performed for a total of 3 hours after which depressurisation at a rate of  $2 \text{ bar}\cdot\text{min}^{-1}$  followed. Resulting crystals were subsequently removed from the extraction vessel and stored at  $19^\circ\text{C}$  under ambient RH (30 – 40% RH).

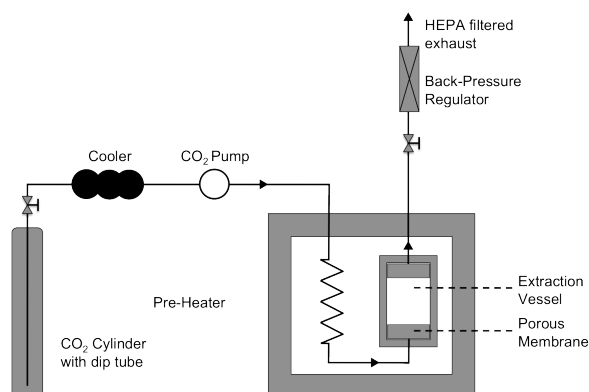


**Figure 6.1** A schematic representation of the supercritical fluid extraction rig used to produce anhydrous IB.

## Particle Size Reduction

Particle size reduction of crystalline IB was performed using an air jet mill (McOne, Jetpharma, Balerna, Switzerland) with a feed rate of approximately  $0.25 \text{ g}\cdot\text{min}^{-1}$  using dry nitrogen with operating venturi and ring pressures of 5 and 3 bar, respectively. Micronised materials were immediately recovered and placed into storage at  $19^\circ\text{C}$  and 44% RH for 7 days prior to further investigation.

### 6.2.3 Physicochemical Properties Analysis

#### 6.2.3.1 *Particle Morphology and Size Analysis*

Particle morphology was investigated using scanning electron microscopy (SEM). Primary crystalline and micronised samples were placed onto carbon sticky tabs affixed to aluminium SEM trays. Excess material was removed from the tab using compressed air and immediately after, sputter coated with gold (Edwards Sputter Coater S150B, Edwards High Vacuum, Sussex, UK) for 5 minutes to produce a thickness of 20 nm. SEM imaging was performed using a JEOL microscope (JSM6180LV, Tokyo, Japan) under an accelerating voltage of 15 kV.

The particle size distribution of primary crystals and micronised samples of IB were measured using laser diffraction (HELOS, Sympatec, Clausthal-Zellerfeld, Germany) using a wet dispersion system (CUVETTE, Sympatec, Clausthal-Zellerfeld, Germany). Approximately 5 mg of sample was suspended in 5 ml of dispersion media, comprising of hexane (HPLC grade) and 0.1% w/w lethicin. The suspension was sonicated for 180 s following prior investigation ensuring no sample dissolution or destruction, before addition to a glass cuvette containing 50 ml of dispersant and a magnetic stirring bar rotating at 1000 rpm. Sizing was performed by laser diffraction over a series of 5 repeats when the optical concentration was equal to or greater than 10%, over a duration of 20 s. Particle size analysis was performed using Windox 5.0 software (Sympatec, Clausthal-Zellerfeld, Germany) following Fraunhofer diffraction theory in order to calculate the cumulative undersize particle parameters  $d_{10}$ ,  $d_{50}$  and  $d_{90}$ , the volume median diameter (VMD) and the sample span (Equation 5.1).

$$Span = \frac{d_{90} - d_{10}}{d_{50}}$$

Equation 6.1

### **6.2.3.2 Topographical Atomic Force Microscope Imaging**

The surface topography of IB crystals was investigated using tapping mode<sup>TM</sup> imaging using a Nanoscope IIIa and J-scanner (all DI, Santa Barbara, CA, USA). Samples were immobilized on steel AFM stubs using carbon adhesive tape (Agar Scientific, Cambridge, UK). The surface morphology was investigated using TESP Olympus tips (Di, Cambridge UK)) at a scan rate of 0.5 Hz.

### **6.2.3.3 Nanoindentation Measurements performed using Atomic Force Microscopy**

An atomic force microscope (AFM) was used to indent (n=10) individual crystals (n=3) using a Nanoscope IIIa and J-scanner (all DI, Santa Barbara, CA, USA). The indenting probe (R150-NCL, Nanosensors, Neuchatel, Switzerland), possessed a hemispherical tip radius of 318 nm, measured by reverse image of the probing tip against a tip-characterisation grating (TGT01; NT-MDT, Moscow, Russia) and deconvolution of the image using analysis software (SPIP Image Metrology ApS, Lingby, Denmark) (Hutter and Bechhoefer, 1993) (Clifford and Seah, 2005a) (Hooton et al., 2004). The spring constant was measured using a dynamic method of thermal noise analysis (Hutter and Bechhoefer, 1993) and was recorded to be  $36.2 \pm 0.2$  N/m in agreement with the manufacturers quoted value which was obtained using the Sader method (Sader et al., 1995).

Force-distance measurements were performed on different areas of a single crystal so that the dominant face with respect to the indenter was indented such that a 1µm space was provided between measurements. The cantilever deflection and piezo displacement were derived into a Young's modulus value using Hertzian model of deformation, shown in Equation 6.2 (Hertz, 1881) (Plassard et al., 2004).



$$E = \frac{3(1-\nu^2)k\Delta z}{4\delta^{3/2}R^{1/2}}$$

**Equation 6.2** The Hertz model of deformation ( $E$ : Young's modulus,  $k$ : spring constant of the indenting cantilever,  $\Delta z$ : relative piezo displacement,  $\delta$ : indentation depth,  $R$ : radius of indenter,  $\nu$ : Poisson ratio of the indenting probe)

#### 6.2.3.4 Differential Scanning Calorimetry

A differential scanning calorimeter (DSC, 2190, TA Instruments, Surry, UK) was used to perform thermal analysis on all crystalline samples of IB after calibration using indium. Samples of approximately 3.0 mg were accurately weighed in aluminium pans, ensuring a total covering of the base by pressing down the material and subsequently covered with an aluminium pan lid, which were not hermetically sealed. The temperature was equilibrated to 50°C before heating at a rate of 10°C.min<sup>-1</sup> to 350°C under dry nitrogen purge (0.30 L/min).

#### 6.2.3.5 X-Ray Powder Diffraction (XRPD)

The X-ray powder diffraction (XRPD) pattern of the IB samples were analysed on a Bruker Powder Diffractometer (D8 Advance AXS; Bruker Inc., Madison, USA). Samples were filled into 0.7 mm glass capillaries and mounted onto a goniometer. The data were collected using CuK $\alpha$  radiation ( $\lambda$ =1.5418 Å) over a single 2 $\theta$  sweep with range 2 $\theta$  = 5 - 50° and step size of 0.025°/step and step time of 1.5 seconds. The monochromator slit was set to 2 mm and the detector was Si(Li).

### 6.2.4 Atomic Force Microscopy – Interactive Force Measurements

A single crystal of lactose monohydrate with well-defined habit and appropriate smoothness (<1 nm R<sub>a</sub> and R<sub>q</sub>) was carefully grown to provide a uniform surface for force of adhesion measurements and is described in detail elsewhere (Hooton et al., 2006).

Prior to force measurements, individual micronised particles of each IB sample were attached onto standard V-shaped tipless cantilevers with pre-defined

spring constants (DNP-020, DI, CA, USA) using an epoxy resin glue (Araldite, Cambridge, UK) (Begat et al., 2004a). Seven probes were prepared for each of the batches of IB and all probes were examined with an optical microscope (magnification 50x) to ensure the integrity of the attached particle, before allowing the thin layer of glue to dry.

The substrate was loaded on to the AFM scanner stage, which was enclosed in a custom-built environmental chamber, in which the ambient conditions were maintained at a constant temperature of 25 °C ( $\pm$  1.5 °C) and relative humidity of 35 % RH ( $\pm$  3 %). The interaction forces were measured by recording the deflection of the AFM cantilever as a function of the substrate displacement ( $z$ ) by applying Hooke's Law ( $F = -kz$ ). Individual force curves ( $n = 1024$ ) were conducted over a 10  $\mu$ m x 10  $\mu$ m area at a scan rate of 4 Hz and a compressive load of 40 nN. Parameters were kept constant over the study. In order to quantify AFM force measurements it is imperative to measure the spring constants of the cantilevers used. However, as described by Begat et al. (2004b), the CAB technique compares adhesion and cohesion with an individual colloid probe, which eliminates the need to accurately determine the spring constant.

#### **6.2.4.1 Data Processing**

Due to the vast array of force data generated, custom-built software was used to extract data contained within each force-volume measurement. The collected force data was analysed to ensure normal distribution, indicating uniform contact between the drug probe and excipient substrate. Arithmetic mean and standard deviation were obtained from force data and used to produce CAB plots for the interactions of the different batches of IB to lactose monohydrate.

#### **6.2.5 HPLC Analysis of Ipratropium Bromide**

Quantification of IB utilised HPLC coupled with UV detection (Agilent 1200 HPLC system, London, UK). The HPLC consisted of a binary pump,

autosampler injecting 100  $\mu\text{L}$  per sample, temperature controlled column oven. The HPLC method was modified from a previous approach and utilised a gradient HPLC approach (Simms et al., 1998). The mobile phase consisted of a mixture of an ion-pair buffer and acetonitrile. The buffer consisted of 100mM  $\text{KH}_2\text{PO}_4$  in which the pH was adjusted to 4.0 using dilute phosphoric acid ( $\text{H}_3\text{PO}_4$ ). Mobile phase A was produced by the addition of 800 ml buffer to 200 ml acetonitrile and mobile phase B was produced by the addition of 550 ml buffer to 450 ml acetonitrile. Both mobile phases were thoroughly mixed and degassed prior to use in analysis. The gradient was established over approximately 20 mins, which is described in Table 6.1.

A Hypersil BDS C18 column (Fisher, Loughborough, 5  $\mu\text{m}$ , 250 x 4.6 mm i.d.) was used for high-throughput analysis of samples and the multi-wavelength detector set to 210 nm. IB had a retention time of approximately 7 minutes and was quantified to a level of 0.25  $\mu\text{g}.\text{ml}^{-1}$  with reproducible linearity over standard concentrations up to 50  $\mu\text{g}.\text{ml}^{-1}$  ( $R^2 > 0.999$ ).

**Table 6.1 Binary pump settings for the gradient mixing of two different buffer compositions used in the detection of IB.**

Time (minutes)	% Mobile Phase B	Flow Rate (ml.min <sup>-1</sup> )
0	0	1.0
4.99	0	1.0
8.00	100	1.0
12.99	100	1.0
14.00	0	2.0
19.00	0	2.0
19.80	0	1.0

### 6.2.6 Preparation of carried-based DPI formulations

Binary formulations containing lactose monohydrate (Respitose, SV003, DMV-Fonterra Excipients, Vehgel, Netherlands) and 200 µg micronised IB per 25 mg shot weight were prepared in order to evaluate aerosolisation performance. Since 41.7 µg IB monohydrate is equivalent to 40 µg of anhydrous IB, each 4 g formulations were prepared with 0.0320 g anhydrous ipratropium bromide or 0.0336g ipratropium bromide monohydrate in addition to the corresponding amount of lactose monohydrate (3.96800 g and 3.96664 g respectively).

Blends were prepared in glass vials using a geometric blending sequence. The API was placed in-between two layers of lactose of approximately the same volume and mixed for 60 s (Whirlimixer, Fisons, Loughborough, UK). Subsequent additions of lactose were added geometrically, with a further 60 s of mixing after each addition. The vial was transferred into a Turbula mixer (Turbula T2F, Willy A Bachofen AG, Basel, Switzerland) and mixed for a further 45 minutes. The samples were then stored at 44 % RH for 24 hours prior to content uniformity determination.

### 6.2.7 Content Uniformity

Following blending, ten random samples of  $25 \pm 1$  mg, from different areas of the powder bed were weighed and dissolved in 50 ml of 0.1mM HCl. The amount of drug in each sample was obtained from HPLC assay and the content uniformity expressed as percentage relative standard deviation (RSD).

### 6.2.8 *In Vitro* Aerosol Deposition Studies

Prepared blends of each material was accurately filled into HPMC capsules ( $25 \pm 1$  mg, QualiV, Qualicaps, bn. E0701921, Madrid, Spain) and stored at 44% RH for 24 hours prior to testing. The *in vitro* performance of each formulation was evaluated using a Next Generation Impactor (NGI, Copley Scientific, Nottingham, UK) with a pre-separator. The pre-separator was charged with 15 ml mobile phase. Each of the individual stages were coated in 1% silicon oil (Agros Organics, Geel, Belgium) in hexane solution and allowed to air dry. The flow rate of through the impactor was set to  $90 \text{ L}\cdot\text{min}^{-1}$  using a digital flow meter (DFM2000, Copley Scientific, Nottingham, UK). The formulations were aerosolised from a Cyclohaler (TEVA, Netherlands) for a duration of 2.7 s at  $90 \text{ L}\cdot\text{min}^{-1}$ , equivalent to a total inhaled volume of 4 L. For each repeat ( $n=3$ ), two capsules were actuated after which the whole system was individually washed down with mobile phase. The capsules, device, mouthpiece and throat were individually washed into 50 ml volumetric flasks. The pre-separator was removed from the NGI and filled with 85 ml of mobile phase, sealed and then shaken for 1.0 minute. An aliquot was then taken from all samples for HPLC analysis. For each of the stages within the NGI, mobile phase was pipetted directly onto each stage. Stages 1 – 5 were allocated 20 ml, stages 6 and 7 received 10 ml and stage 8 was delivered 10 ml. The stages were then shaken on a bench-top laboratory shaker (IKA Vibramax VXR, Staufen, Germany) for five minutes before removing aliquots of each for HPLC analysis. The HPLC assay was the same as above, using the drug content analysis by HPLC process outlined above.

## 6.3 RESULTS AND DISCUSSION

### 6.3.1 Solubility of IB in Experimental Solvents

The solubility of IB in ethanol and ultra pure MilliQ water was investigated over a range of operating temperatures in accordance to the crystallisation approach utilised in each study and is shown in Figure 6.2. IB demonstrated high aqueous solubility in comparison to ethanol at higher temperatures and therefore, required a significantly greater amount of material to saturate solvent solutions used in the crystallisation of IB.

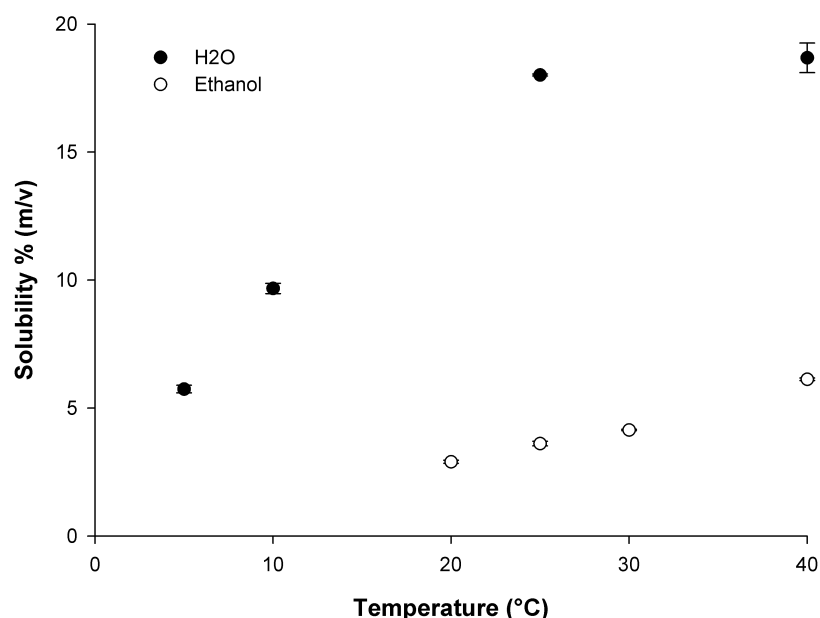


Figure 6.2 The determined solubility of IB in ethanol and H<sub>2</sub>O

### 6.3.2 Physicochemical Characterisation of primary IB crystals

In order to characterise the materials produced from the primary crystallisation process, the thermal properties of each sample were assessed using differential scanning calorimetry (DSC) and the crystallinity was investigated using powder X-ray diffraction. Scanning electron microscopy was used to assess the morphological differences and laser diffraction was employed to determine

particle size information. In addition, the Young's modulus of the dominant face of each crystal was determined by AFM nanoindentation.

### 6.3.2.1 Differential Scanning Calorimetry of primary IB crystals

Thermal analysis of the primary crystals aided the characterisation of the crystalline nature and hydrated state of ipratropium bromide. Representative thermograms of the IB samples grown from seeded crystallisation in aqueous solution and  $\text{SCO}_2$  anti-solvent crystallisation are shown in Figure 6.3. Both samples exhibited a melting point followed by degradation at  $240^\circ\text{C}$ , consistent with the pharmacopeia literature. The overlapping endothermic peaks starting at approximately  $90^\circ\text{C}$  for the monohydrate sample reveal the loss of water from the crystalline lattice (Corrigan et al., 2006), while the absence of this event for crystals formed by  $\text{SCO}_2$  anti-solvent crystallisation confirmed the presence of the anhydrous form of IB.

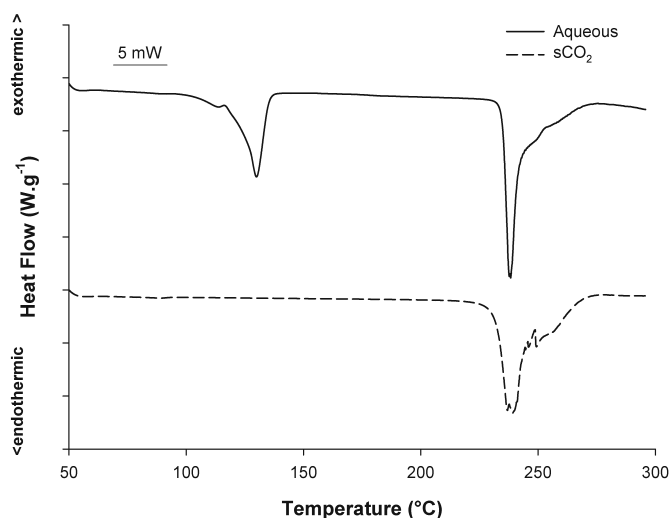


**Figure 6.3** Differential scanning calorimetry thermograms of two crystalline ipratropium bromide samples produced using a seeded aqueous and supercritical approach.

### 6.3.2.2 X-Ray Powder Diffraction of primary IB crystals

Investigation into the crystal nature of each sample was performed using powder X-ray diffraction. The resulting diffraction profiles, shown in Figure 6.4, indicate differences between the two samples, which may be due to the

presence of water within the crystalline lattice. The inclusion of water within the crystal lattice is known to change the shape, symmetry and number of molecules within the unit cell (Khankari and Grant, 1995), which will directly influence the diffraction behaviour. The sharp diffraction peak observed in the anhydrous sample at approximately 18 degrees is in keeping with previously published data, whereby a relative intensity of 76.76% for a peak was observed at 18.908 degrees (Florey, 2003), whilst the diffraction pattern observed for the monohydrate sample in this study appears similar to another investigation into IB monohydrate (Xu et al., 2010).

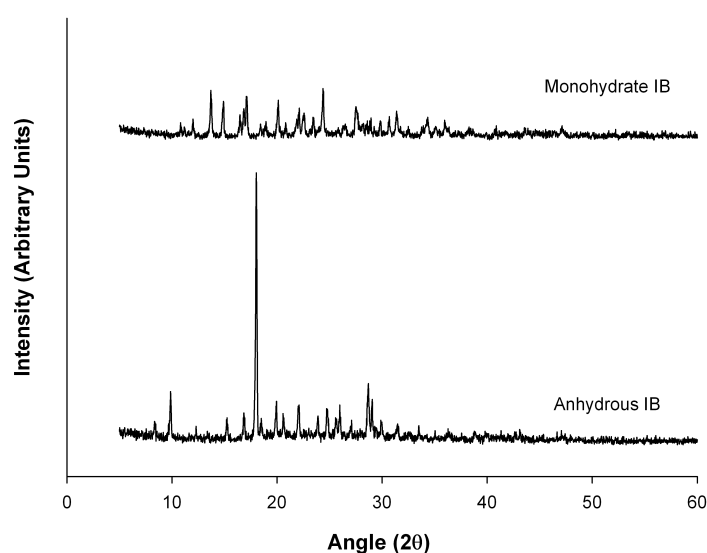


**Figure 6.4** The X-ray powder diffraction profiles for the primary crystals of ipratropium bromide anhydrous and monohydrate.

In keeping with the findings from XRPD and DSC analysis, the samples obtained by seeded aqueous crystallisation and  $\text{SCO}_2$  anti-solvent crystallisation will be referred to in the rest of this study as the monohydrate and anhydrous samples of IB, respectively.

### **6.3.2.3 Scanning Electron Microscopy of Monohydrate and Anhydrous IB crystals**

Particle morphology of the crystallised materials was investigated using scanning electron microscopy. As shown in Figure 6.5(A,B), the monohydrate IB crystals grown from seeds displayed an irregular acicular nature with no



defined habit. This may be due to the irregular nature of the IB seed material introduced during the aqueous crystallisation process. In contrast, the anhydrous form of IB prepared using supercritical fluid carbon dioxide anti-solvent crystallisation was more regular and plate-like in nature.

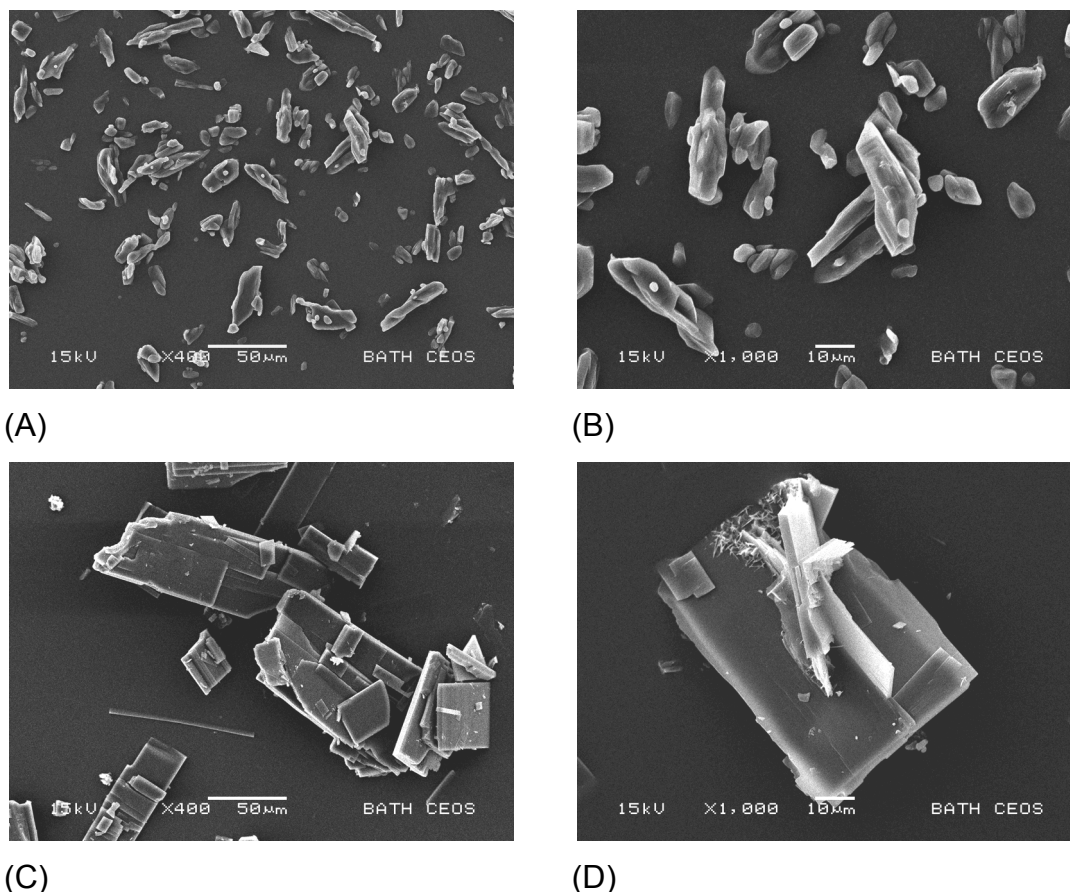


**Figure 6.5** Scanning electron micrographs of the crystalline monohydrate (A-B) and anhydrous (C-D) forms of ipratropium bromide.

Particle size analyses of the primary IB crystals are shown in Table 6.2. The PSD of both crystals were similar and, enabled comparison therefore, of the preceding processing of these materials.

**Table 6.2 Particle size distribution (PSD) of the crystalline samples obtained using laser diffraction (VMD – Volume median-mass diameter).**

<b>SAMPLE</b>	<b>D<sub>10%</sub></b> <b>(<math>\mu\text{m} \pm \text{SD}</math>)</b>	<b>D<sub>50%</sub></b> <b>(<math>\mu\text{m} \pm \text{SD}</math>)</b>	<b>D<sub>90%</sub></b> <b>(<math>\mu\text{m} \pm \text{SD}</math>)</b>	<b>Span</b> <b>(<math>\pm \text{SD}</math>)</b>	<b>VMD</b> <b>(<math>\mu\text{m} \pm \text{SD}</math>)</b>
Monohydrate	2.33 (0.01)	11.56 (0.01)	24.71 (0.03)	1.94 (0.02)	12.89 (0.01)
Anhydrous	4.93 (0.01)	14.90 (0.01)	29.10 (0.04)	1.62 (0.03)	16.23 (0.02)

### 6.3.3 Nanomechanical Analysis of Monohydrate and Anhydrous IB crystals

The dominant growth faces of the monohydrate and anhydrous IB crystals were nanomechanically indented, while maintaining Hertzian deformation. The force-distance loading curves were then extrapolated to derive the Young's modulus for these materials. Representative force-indentation curves for individual crystal faces of the monohydrate IB and anhydrous crystals are shown in Figure 6.6. The AFM was also used before and after each indentation cycle, in topographical mode, to image the crystal surface, ensuring suitability of the area for indentation and to observe evidence of plastic deformation. Areas that had undergone plastic deformation were removed from subsequent analysis.

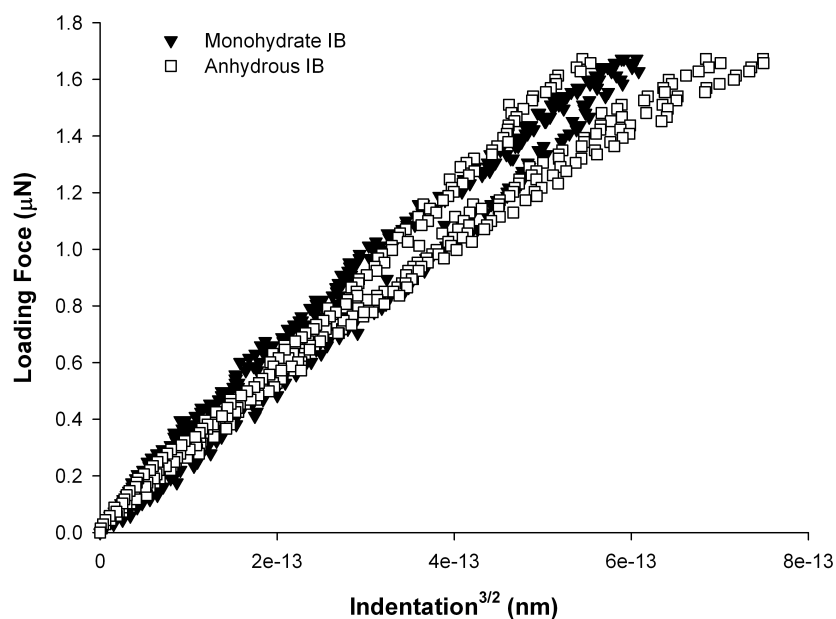


**Figure 6.6 Representative force-indentation curves for both samples of IB investigated using AFM nanoindentation**

As shown in Figure 6.7, repeated mechanical measurements revealed no significant differences between the anhydrous and monohydrate form of IB ( $P > 0.05$ ). Both forms had an average elastic modulus of  $3.68 \pm 0.73$  and  $3.20 \pm 0.50$  GPa for the monohydrate and anhydrous samples, respectively. A previous study has shown that the physical effect of crystal hydrates directly affected tableting properties and the pharmacokinetic profile of pharmaceutical materials (Khankari and Grant, 1995). Moreover, an investigation into the physical properties of anhydrous and monohydrate lactose crystals revealed significant differences in the Young's modulus of the individual crystals (Wong et al., 1988). These data highlight the anisotropic nature of the monohydrate form of lactose, showing variability of elasticity on different crystal faces.

Interestingly, the Young's modulus of the two different forms of IB suggest no differences between the nanomechanical properties of these materials. While the physico-mechanical properties are known to influence the functionality of processed APIs, these findings imply that neither form directly influences the secondary processing efficiency of IB.

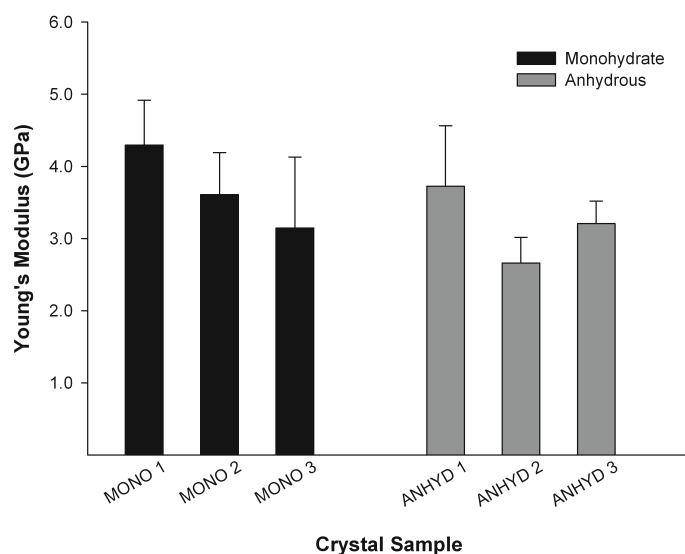


**Figure 6.7** Young's modulus measurements for three different crystals from each IB sample.

#### **6.3.4 Physicochemical Characterisation of secondary processed monohydrate and anhydrous IB**

In order to compare the *in vitro* formulation behaviour of the two samples, air-jet milling was employed to reduce the crystalline particles to a respirable size range. The physico-chemical micronised samples of monohydrate and anhydrous IB were characterised by SEM, and then investigated for differences in their interfacial interactions using the CAB approach to colloidal probe AFM.

A fluid air-jet mill was utilised to comminute each of the monohydrate and anhydrous IB samples to the respirable particle size range. Though it has been suggested that multiple milling cycles were required for IB in a previous study (Xu et al., 2010), both samples produced in this study only required a single pass. Representative SEM micrographs of the micronised samples of monohydrate IB and anhydrous IB are shown in Figure 6.8.

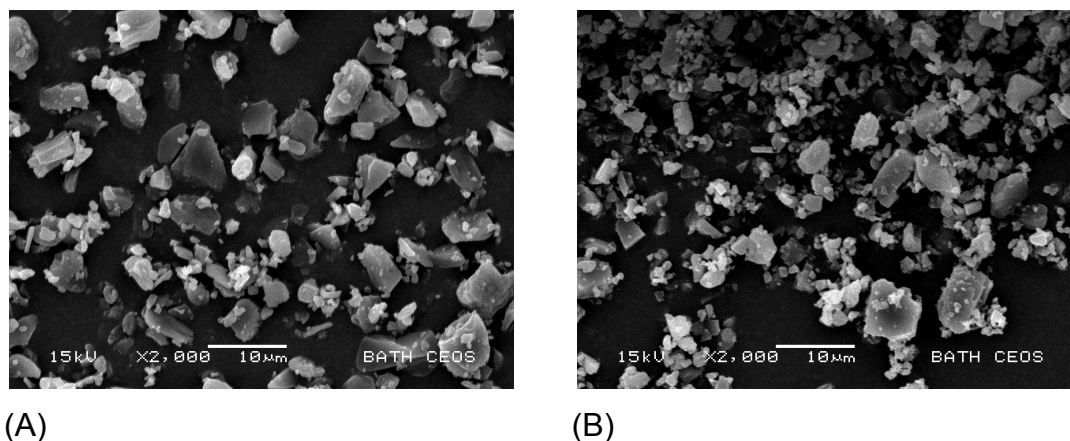


**Figure 6.8 Scanning electron micrographs of the micronised monohydrate (A) and anhydrous.**

Particle size distributions of the micronised materials produced from the monohydrate and anhydrous crystals are shown in Figure 6.9, together with their unmicronised form. The particle size distributions of the secondary processed materials were similar (Table 6.3), highlighted by Span values of 1.62 and 1.69  $\mu\text{m}$  and volume median-mass diameters of 3.34 and 3.36  $\mu\text{m}$ , for the monohydrate and anhydrous form, respectively. These data suggest that the micronisation efficiency of the monohydrate and anhydrous crystals of IB were similar. Particle size analyses of these distributions are shown in Table 6.3, and were shown to be reduced sufficiently for dry powder inhaler formulation preparations.

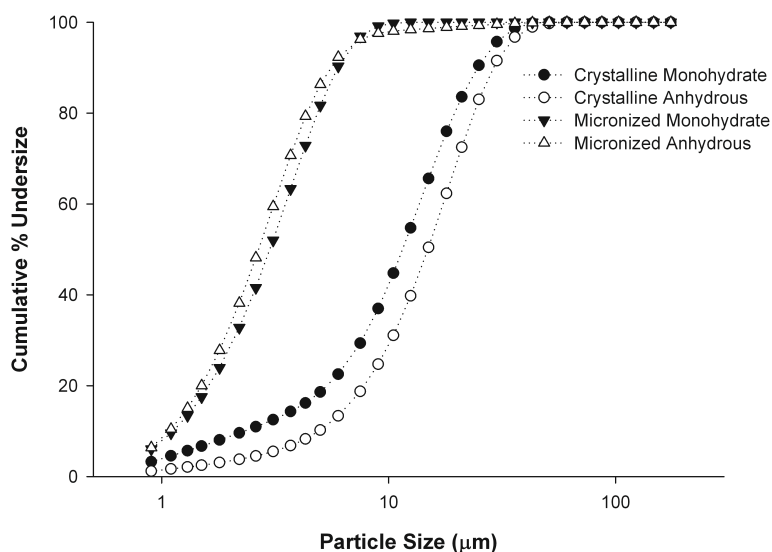


**Figure 6.9** Cumulative particle size distribution of the crystalline and micronised samples of anhydrous and monohydrate forms of ipratropium bromide.

It was noted that the anhydrous form was reduced in size to a greater extent than the monohydrate sample (Table 6.3) despite possessing a greater unprocessed PSD. Though differences in Young's modulus were not seen in previous measurements (Figure 6.7) these results may be attributed to the physical form of the crystalline materials, such as particle size or shape, resulting an altered flow and fracture behaviour within the mill.

**Table 6.3** Particle size distribution of the micronised materials determined by laser diffraction (VMD – Volume median-mass diameter).

<b>SAMPLE</b>	<b>D<sub>10%</sub></b> <b>(μm ± SD)</b>	<b>D<sub>50%</sub></b> <b>(μm ± SD)</b>	<b>D<sub>90%</sub></b> <b>(μm ± SD)</b>	<b>Span</b> <b>(± SD)</b>	<b>VMD</b> <b>(μm ± SD)</b>
Monohydrate	1.12 (0.01)	3.00 (0.01)	5.97 (0.01)	1.62 (0.01)	3.34 (0.01)
Anhydrous	1.08 (0.01)	2.68 (0.01)	5.61 (0.04)	1.69 (0.01)	3.36 (0.11)

### **6.3.5 Investigation into the Interfacial properties of Micronised anhydrous and monohydrate IB using Cohesive-Adhesive Balance (CAB) Measurements**

The surface interfacial interactions of the micronised materials were investigated using AFM-CAB with respect to surfaces of lactose monohydrate. A substrate crystal of lactose monohydrate with defined habit and appropriate smoothness ( $<1$  nm  $R_a$  and  $R_q$ ) was carefully grown to provide a uniform surface for adhesion measurements while an unmicronised crystal of similar smoothness on the dominant face was selected from the monohydrate and anhydrous IB crystals for the cohesion measurements.

The CAB plots of the micronised IB samples produced upon micronisation with respect to their monohydrate and anhydrous forms and lactose monohydrate are shown in Figure 6.10 and Figure 6.11, respectively.

The CAB measurements of the micronised particles produced from primary crystals of monohydrate or anhydrous forms of IB with respect to lactose monohydrate were 0.701 ( $R^2 = 0.9984$ ) and 0.770 ( $R^2 = 0.999$ ), respectively. These data suggest that both samples had a greater tendency to adhere to lactose with respect to their respective forms of IB and that the monohydrate and anhydrous forms of IB have little or no direct influence on the interfacial behaviour.

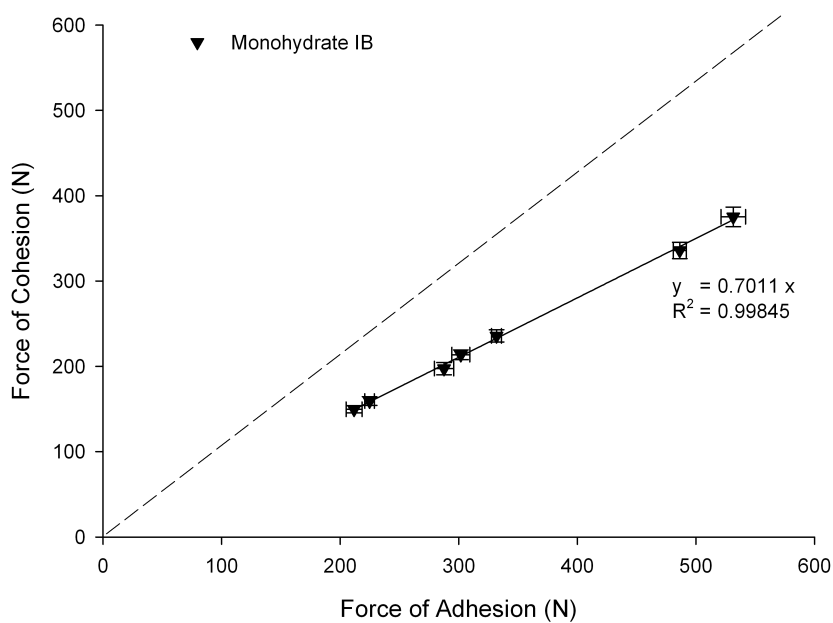


**Figure 6.10 CAB plot of monohydrate IB with respect to lactose. (The dashed line represents where  $F_{COH} = F_{ADH} = 1.0$ )**

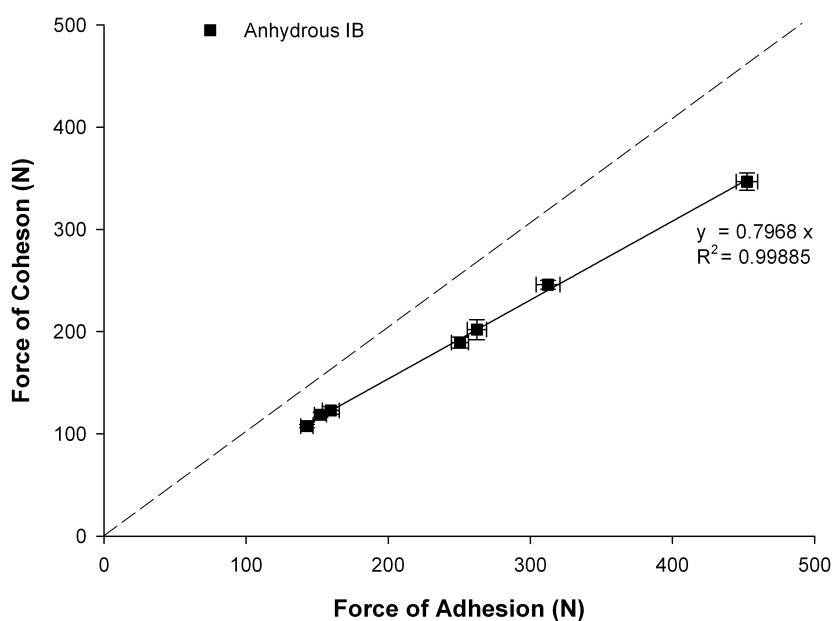


**Figure 6.11 CAB plot of anhydrous IB with respect to lactose (The dashed line represents where  $F_{COH} = F_{ADH} = 1.0$ ).**



### 6.3.6 *In Vitro* Aerosolisation Performance of Carrier-Based DPI formulations

Each micronised sample of IB was formulated with coarse lactose to produce a DPI formulation suitable for the investigation of fluidisation and delivery efficiency by inertial impaction. Formulations containing the equivalent of 200 $\mu\text{g}$  IB per shot were actuated into a Next Generation Impactor (NGI) and evaluated by HPLC once formulations were assessed for blend uniformity.

Quantification of IB was achieved using HPLC. The relationship between drug concentration (0.5, 1, 5, 10 and 50  $\mu\text{g}.\text{ml}^{-1}$ ) and peak area for each drug was found to be linear, with linear regression analysis yielding a coefficient of determination ( $R^2$ ) of 0.99964 and is shown in Figure 6.12.

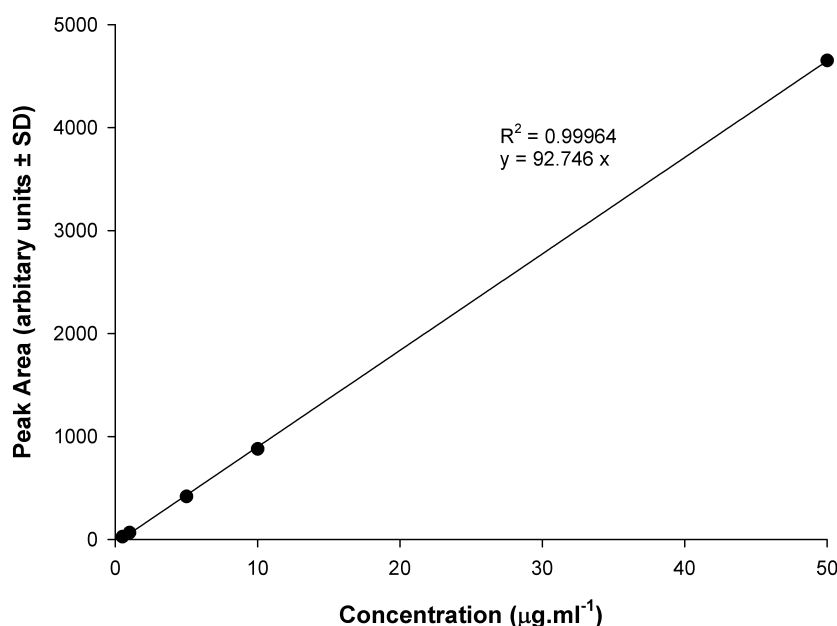
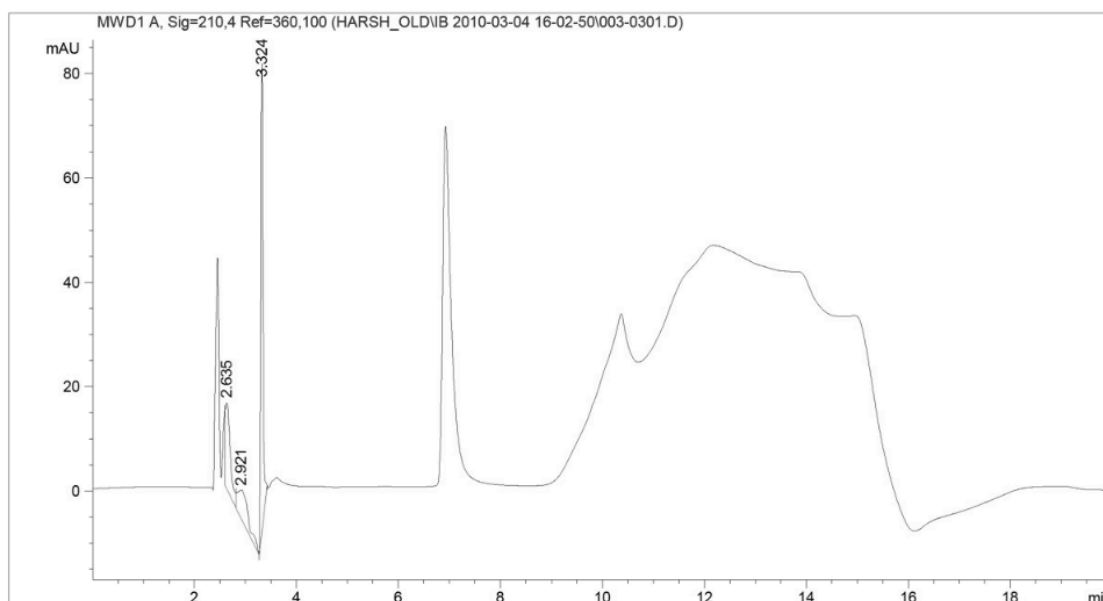


Figure 6.12 Representative HPLC calibration curve obtained for IB

A representative HPLC trace for a calibration sample of IB 10  $\mu\text{g}.\text{ml}^{-1}$  is shown in Figure 6.13, with a retention time of approximately 7.2 minutes.



**Figure 6.13 A Representative HPLC trace for IB**

The content uniformity of each formulation was evaluated and is expressed as a percentage relative standard deviation (%RSD). These were determined to be 1.95 % and 2.17 % for the monohydrate and anhydrous IB samples, respectively, suggesting a homogeneous distribution of the API throughout the formulation blend. Given that these values were lower than 5 %, both formulations were deemed suitable for *in vitro* impaction testing.

The stage-by-stage deposition profile of the formulations using inertial impaction in the NGI are shown in Figure 6.14 and *in vitro* deposition analyses are summarised in Table 6.4. Although differences in fine particle dose (FPD) were observed between the monohydrate and anhydrous IB formulations,  $201.70 \pm 18.33$  and  $228.58 \pm 4.31$   $\mu\text{g}$  respectively, when normalised as a function of emitted dose, the fine particle fraction showed no significant difference. These data suggest that there was no significant impact on performance by the crystallisation of the anhydrous form of IB, supporting the nanomechanical and CAB measurements for the interfacial properties of these samples.

**Table 6.4** *In vitro* aerosolisation properties of DPI formulations produced from the monohydrate and anhydrous crystal form of ipratropium bromide (ED: emitted dose, FPD: fine-particle dose, MMAD: mass median aerodynamic diameter, GSD: geometric standard diameter FPF<sub>ED</sub>: fine-particle fraction of the emitted dose).

	Monohydrate ( $\pm$ SD)	Anhydrous ( $\pm$ SD)
ED ( $\mu$ g)	201.70 $\pm$ 18.33	228.58 $\pm$ 4.31
FPD ( $\mu$ g)	45.71 $\pm$ 5.99	53.28 $\pm$ 2.64
MMAD ( $\mu$ m)	3.83	3.33
GSD ( $\mu$ m)	2.02	1.99
FPF <sub>ED</sub> (%)	22.62 $\pm$ 1.32	23.30 $\pm$ 0.81

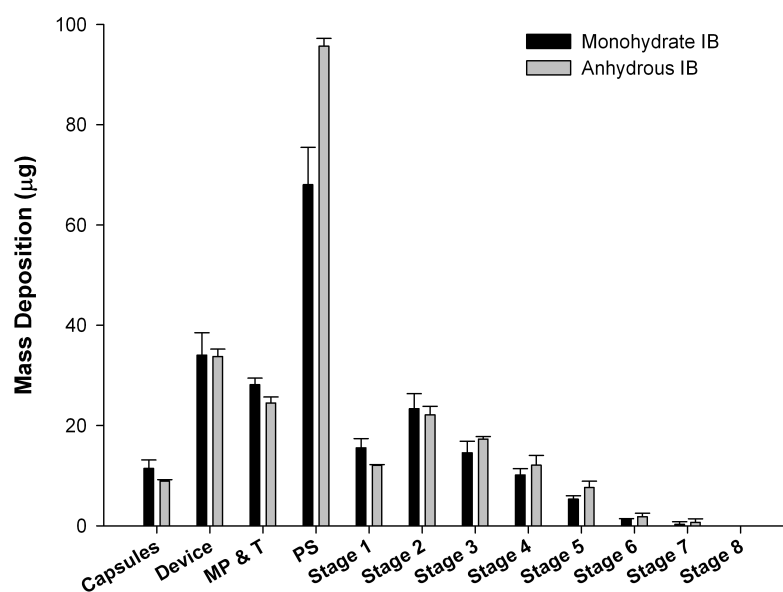


**Figure 6.14** Mean mass deposition profiles for monohydrate and anhydrous carrier-based DPI formulations.

## **6.4 CONCLUSIONS**

This study has demonstrated the use of supercritical fluid technology in producing an anhydrous form of ipratropium bromide suitable for inclusion in a carrier-based DPI formulation when compared to the monohydrate form. Investigation into the mechanical nature of the primary crystalline material by atomic force nanoindentation suggested no differences in the elastic modulus of these materials. Subsequent micronisation and assessment of interfacial properties by the CAB approach also indicated no observable differences. A better understanding of the influence of crystallisation conditions on the physico-mechanical properties of APIs produced with conventional and novel techniques may therefore lead to materials of superior quality and functionality.

## **Chapter 7: General Conclusions and Further Work**

### **7.1 Introduction**

The process of crystallisation is a fundamental step in the isolation and purification of active pharmaceutical ingredients. Defining the physical and chemical characteristics of the resulting material, this process traditionally has been tailored to produce materials of suitable handling characteristics, such as ease of filtration and powder flow. Due to the complexity of many drug delivery approaches, for example dry powder inhaler formulations, further processing of these primary crystals is required to produce suitable material for incorporation into these products.

Described in the opening section of this body of work, the micronisation of pharmaceutical materials by jet-milling is often implicated in significant and detrimental changes in material behaviour. For DPI formulations containing these micronised materials and larger coarse carrier particles, this can often be seen as a source of variability in their performance and is associated with the input of high energies and the relatively uncontrolled nature of the process. In response, studies have investigated the role of crystallisation in determining the mechanical properties of model drugs, such as acetaminophen (Liao and Wiedmann, 2005), and compared the mechanical properties of a wide variety of APIs (Taylor et al., 2004b).

Research into the relationship between mechanical properties of APIs and micronisation performance has highlighted the Young's modulus as an important characteristic in influencing the milling behaviour (Zugner et al., 2006) (Meier et al., 2008) and this property has been demonstrated to be readily measured using an atomic force microscope based approach (Perkins et al., 2007) (James et al., 2009). There remained however, a lack of understanding as to whether the crystallisation process alters the Young's modulus of the resulting primary crystals significantly enough to translate into specific

differences in the processing or performance of these materials intended for DPI delivery.

## 7.2 Summary

The development and understanding of an AFM based nanoindentation technique enabled the investigation of the nanomechanical properties of the primary crystals of various APIs that were produced using differing crystallisation techniques. This enabled investigation of the Young's modulus of APIs specifically used in the therapeutic treatment of asthma and COPD, prior to the processing of these materials in order to assess their performance when included within a DPI formulation. Alongside other established characterisation techniques to characterise the primary crystals and resulting micronised materials, the Young's modulus was shown to influence the milling behaviour and resulting interparticle forces which corroborated with observed *in vitro* impaction testing. The resulting chapters presented in this thesis highlight the range of the measured Young's modulus for different APIs when solvent composition, crystal habit and crystal form are altered during the crystallisation.

In the first experimental section, chapter 3, a series of different APIs were grown under controlled conditions in order to determine a reference technique suitable for assessment of primary crystalline samples produced on a small scale. Moreover, the observed indentation profile of two samples, lactose monohydrate and salmeterol xinafoate, indicated that these crystals presented significantly greater resistance to deformation from a relatively large radius AFM probe. These findings led to investigation of a wide range of probes that were suitable in stiffness and contact area to produce deformation within the elastic limit and supported early work by Perkins et al. (2007) suggesting that true Young's modulus measurements using the Hertzian model of deformation required the appropriate selection of operating parameters. This led to the quantification of the elastic modulus of lactose ( $3.55 \pm 0.10$  GPa), salmeterol xinafoate ( $2.79 \pm 0.47$  GPa), Budesonide ( $2.61 \pm 0.54$  GPa), fluticasone propionate ( $1.60 \pm 0.05$  GPa) and formoterol fumarate dihydrate ( $0.93 \pm 0.13$

GPa). As a secondary study within this chapter, the interactive nature of the secondary processed micronised forms of each material was investigated against HOPG, a well characterised reference surface. From these AFM based interactive force measurements and knowledge of the dispersive surface energy of HOPG, the cohesive nature of each sample was estimated and suggested that the relative differences between these forces for each API could result in differences in DPI formulation performance and functionality.

The investigation into the crystallisation of fluticasone propionate by changing the solvent composition enabled investigation of the nanomechanical properties of the resulting primary crystals. As shown in chapter 4, this study indicated that a wide range of Young's modulus was obtained, depending on the solvents used. Furthermore, these differences were observed in two samples whereby the material with the highest elasticity, sample A ( $0.61 \pm 0.07$  GPa) required a further three micronisation cycles to reduce the primary crystal size similar to another sample with significantly higher stiffness, sample C ( $12.44 \pm 2.48$  GPa) that only required one milling cycle. This result highlighted the importance of solvent selection as a precursor to determining physico-mechanical behaviour. Investigation of the CAB of the micronised materials after each cycle of milling indicated that successive cycles caused the material to have an increasing tendency to adhere to lactose. Interestingly, the sample that required only one milling cycle showed a similar affinity to adhere to lactose and these findings were supported by *in vitro* assessment of DPI formulations of binary FP formulations for each sample. For FP samples A and C in combination with SX, the SX performance was decreased by approximately 40% when combined with FP sample C. This indicated disturbance of the intricate balance of forces within the tertiary formulation and suggested that the inclusion of a processed form of FP had resulted in the modification of DPI function and performance *in vitro*.

The changes in crystallisation solvents can also lead to differences in the crystal habit. This area was explored by the use of acetone and N-N-dimethylformamide as solvents in the crystallisation of budesonide in chapter 5. Significant differences in the Young's modulus of the resulting crystals were evident, alongside changes to the physical appearance of the resulting primary

crystals. These findings supported the size reduction data of the micronised materials and resulted in the material of greatest elasticity, having greater adhesive tendency towards lactose when investigated with AFM-CAB. The possible loss of crystallinity of the budesonide sample measured by DSC, with highest elastic modulus suggests that the inclusion of crystal defects or residual solvents has lead to a material of greater stiffness. This supports the findings of Liao and Wiedmann (2005), who observed changes to the mechanical nature of acetaminophen and KCl as a function of the crystallisation rate and inclusion of crystal defects. Our work in this chapter highlights the importance of the physical nature of the primary crystals alongside the nanomechanical properties of these materials in relation to the milling behaviour of APIs and the subsequent variations in *in vitro* performance within a DPI formulation.

In the final experimental section, chapter 6, the role of crystal form for ipratropium bromide was investigated. The monohydrate form was produced using a temperature drop, seeded crystallisation method whilst the anhydrous form was produced from an organic solution of ipratropium and supercritical CO<sub>2</sub> using a GAS process. The findings in this study revealed no significant differences in the mechanical nature of the primary crystals and although the physical appearances of the crystalline material were different, the milling behaviour of these samples were conserved. Moreover, the CAB values of each material and their *in vitro* performance showed no distinction between each form. Whilst the crystal form of each sample was different, these data suggested that the elastic modulus of each sample was sufficiently high to overcome the barriers of micronisation and therefore process these materials into a suitable DPI formulation. In keeping with chapter 4 and chapter 5, this study indicates that material with a greater Young's modulus may result in a finer end product and that the Young's modulus can influence the milling behaviour in addition to the crystal habit.

### 7.3 General Conclusions



The main body of the experimental work contained in this thesis suggests that the crystallisation process alters the elastic nature of organic crystalline materials. This may be due to loss of crystallinity, by the creation of dislocations and defects within the crystal lattice, or by inclusion of residual solvents. In the case of FP, this is demonstrated to a greater extent when the solvent composition has been altered, and as a result has been shown to influence the milling behaviour and interparticulate forces that occur. Consequentially, these data indicate that with the appropriate selection of solvents and crystallisation processes, output material may be tailored to meet specific criteria for future processing. These findings are not limited to just DPI formulations but to any API that is subsequently processed in a similar fashion, including poorly soluble drugs and liquid-suspension formulations. Moreover, using this approach, variability as a result of sourcing a material from various suppliers may be reduced, as the characterisation of the Young's modulus provides insight into the possible micronisation behaviour of certain materials. This is of significant benefit to those obtaining drug materials from an array of sources, or those wishing to match competitor products, such as those within the pharmaceutical generics market.

The elastic modulus is therefore not an individual measurement that surpasses any previous technique, rather an additional tool in the characterisation of primary crystals, alongside established and validated approaches that characterise physico-chemical attributes. Understanding and controlling the variability of individual components of complex formulations may, therefore, produce products of defined specification and quality.

### **7.4 Future Work**

The crystallisation process has many different contributing elements that determine the properties of the end-product. These include operating conditions, solvent/anti-solvents and addition rates, for example. Any differences within this unit operation will often lead to changes in the material output. Advanced, in-line monitoring processes that enable the real-time

investigation of the crystallisation process provide important tools in understanding the rates (kinetics) of crystal growth. Investigating how these properties influence the Young's modulus of the resulting materials and how this property can be modified by the use of appropriate solvent conditions may lead to less empirical efforts in the development of crystallisation techniques.

Whilst this body of work has investigated the effect of traditional crystallisation techniques on the mechanical nature of the resulting material, greater interest has been placed on new approaches to the crystallisation process, such as ultrasound-assisted nucleation and microfluidic generated crystalline material. Understanding whether these processes lead to materials of greater quality or functionality is vital for the successful application of these techniques within the pharmaceutical arena and therefore, the characterisation of processability would be beneficial using a AFM nanoindentation approach.

Ultimately, this project concludes that the milling and processing of primary crystal APIs is deeply rooted in the pharmaceutical processing of DPI formulations. Though novel approaches in producing primary material of the inhalable size range do exist, limits to scale up, cost and complexity of these methods has led to a reliance on "top-down" culture in DPI formulation design. Successfully incorporating a technique, such as AFM nano-indentation, alongside other tools may lead to a better understanding of the processability of APIs incorporated in these formulations and thereby reduce variability in the final product.

## References

- Aaltonen, J., Alleso, M., Mirza, S., Koradia, V., Gordon, K. C. & Rantanen, J., (2009). Solid Form Screening - a Review. *European Journal of Pharmaceutics and Biopharmaceutics*. **71**, 23-37.
- Abu Bakar, M. R., Nagy, Z. K., Saleemi, A. N. & Rielly, C. D., (2009). The Impact of Direct Nucleation Control on Crystal Size Distribution in Pharmaceutical Crystallization Processes. *Crystal Growth and Design*. **9**, 1378-1384.
- Adi, H., Traini, D., Chan, H.-K. & Young, P. M., (2008). The Influence of Drug Morphology on the Aerosolisation Efficiency of Dry Powder Inhaler Formulations. *Journal of Pharmaceutical Sciences*. **97**, 2780-2788.
- Adolfsson, A., Olsson, H. & Nystrom, C., (1997). Effect of Particle Size and Compaction Load on Interparticulate Bonding Structure for Some Pharmaceutical Materials Studied by Compaction and Strength Characterisation in Butanol. *European Journal of Pharmaceutics and Biopharmaceutics*. **44**, 243-251.
- Agbada, C. & York, P., (1994). Dehydration of Theophylline Monohydrate Powder - Effects of Particle-Size and Sample Weight. *International Journal of Pharmaceutics*. **106**, 33-40.
- Akseli, I., Hancock, B. C. & Cetinkaya, C., (2009). Non-Destructive Determination of Anisotropic Mechanical Properties of Pharmaceutical Solid Dosage Forms. *International Journal of Pharmaceutics*. **377**, 35-44.
- Albertsson, J., Oskarsson, A. & Svensson, C., (1978). X-Ray Study of Budesonide: Molecular Structure and Solid Solutions of the (22s) and (22r) Epimers of 11 Beta, 21-Dihydroxy-16alpha-Propylmethylenedioxy-1,4-Preg- Nadiene-3,20-Dione. *Acta Crystallographica Section B*. **34**, 3027-3036.
- Atkins, P. (2006) Transition to Hfa Mdis: How Did We Get Here and Where Are We Going? IN DALBY, R. (Ed. *Respiratory Drug Delivery*. Boca Raton, Florida, Davis International Publishing.
- Bandi, N., Wei, W., Roberts, C., Kotra, L. & Kompella, U., (2004). Preparation of Budesonide- and Indomethacin-Hydroxypropyl-Beta-Cyclodextrin (Hpbcd) Complexes Using a Single-Step, Organic-Solvent-Free Supercritical Fluid Process. *European Journal of Pharmaceutical Sciences*. **23**, 159-168.
- Banga, S., Chawla, G., Varandani, D., Mehta, B. R. & Bansal, A. K., (2007). Modification of the Crystal Habit of Celecoxib for Improved Processability. *Journal of Pharmacy and Pharmacology*. **59**, 29-39.
- Barnes, P., (2004a). New Drugs for Asthma. *Nature Reviews Drug Discovery*. **3**, 831-844.

## References

---

Barnes, P. J., (2004b). Mediators of Chronic Obstructive Pulmonary Disease. *Pharmacology Reviews*. **56**, 515-548.

Barnes, P. J., (2008). Immunology of Asthma and Chronic Obstructive Pulmonary Disease. *Nature Reviews Immunology*. **8**, 183-192.

Bassam, F., York, P., Rowe, R. & Roberts, R., (1990). Young Modulus of Powders Used as Pharmaceutical Excipients. *International Journal of Pharmaceutics*. **64**, 55-60.

Beach, S., Latham, D., Sidgwick, C., Hanna, M. & York, P., (1999). Control of the Physical Form of Salmeterol Xinafoate. *Organic Process Research & Development*. **3**, 370-376.

Begat, P., Morton, D., Shur, J., Kippax, P., Staniforth, J. N. & Price, R., (2008). The Role of Force Control Agents in High-Dose Dry Powder Inhaler Formulations. *Journal of Pharmaceutical Sciences*.

Begat, P., Morton, D., Staniforth, J. & Price, R., (2004a). The Cohesive-Adhesive Balances in Dry Powder Inhaler Formulations I: Direct Quantification by Atomic Force Microscopy. *Pharmaceutical Research*. **21**, 1591-1597.

Begat, P., Morton, D., Staniforth, J. N. & Price, R., (2004b). The Cohesive-Adhesive Balances in Dry Powder Inhaler Formulations I: Direct Quantification by Atomic Force Microscopy. *Pharmaceutical Research*. **21**, 1591-1597.

Begat, P., Morton, D. A. V., Staniforth, J. N. & Price, R., (2004c). The Cohesive-Adhesive Balances in Dry Powder Inhaler Formulations II: Influence on Fine Particle Delivery Characteristics. *Pharmaceutical Research*. **21**, 1826-1833.

Begat, P., Young, P. M., Edge, S., Kaerger, J. S. & Price, R., (2003). The Effect of Mechanical Processing on Surface Stability of Pharmaceutical Powders: Visualization by Atomic Force Microscopy. *Journal of Pharmaceutical Sciences*. **92**, 611-620.

Beilmann, B., Kubiak, R., Grab, P., Häusler, H. & Langguth, P., (2007). Effect of Interactive Ternary Mixtures on Dispersion Characteristics of Ipratropium Bromide in Dry Powder Inhaler Formulations. *AAPS Pharmaceutical Science and Technology*. **8**, Article 31.

Bell, J., Hartley, P. & Cox, J., (1971). Dry Powder Aerosols I: A New Powder Inhalation Device. *Journal of Pharmaceutical Sciences*. **60**, 1559-1564.

Bérard, V., Lesniewska, E., Andrčs, C. & Pertuy, D., (2002). Dry Powder Inhaler: Influence of Humidity on Topology and Adhesion Studied by Afm. *International Journal of Pharmaceutics*.

Bhome, A. (2009) Drug Delivery Systems and Consumer Perceptions: An Indian Viewpoint. *Drug Delivery to the Lungs 20*. Edinburgh

## References

- Bragg, W. L., (1913). Diffraction of Short Electromagnetic Waves by a Crystal. *Proceedings of the Cambridge Philosophical Society*. **17**, 43-57.
- Brain, J. D., Valberg, P., A., Sneddon, S. (1985) Mechanisms of Aerosol Deposition and Clearance IN NEWHOUSE, M. F., DOLOVICH, M. B (Ed.) *Aerosols in Medicine: Principles, Diagnosis and Therapy*. New York, Elsevier.
- Bridson, R. H., Robbins, P. T., Chen, Y., Westerman, D., Gillham, C. R., Roche, T. C. & Seville, J. P. K., (2007). The Effects of High Shear Blending on Alpha-Lactose Monohydrate. *International Journal of Pharmaceutics*. **339**, 84-90.
- Brittain, H., (2002). Effects of Mechanical Processing on Phase Composition. *Journal of Pharmaceutical Sciences*. **91**, 1573-1580.
- Brodka-Pfeiffer, K., Langguth, P., Grass, P. & Hausler, H., (2003). Influence of Mechanical Activation on the Physical Stability of Salbutamol Sulphate. *European Journal of Pharmaceutics and Biopharmaceutics*. **56**, 393-400.
- Brown, I. G., Chan, C. S., Kelly, C. A., Dent, A. G. & Zimmerman, P. V., (1984). Assessment of the Clinical Usefulness of Nebulised Ipratropium Bromide in Patients with Chronic Airflow Limitation. *Thorax*. **39**, 272-276.
- Buckton, G., (1997). Characterisation of Small Changes in the Physical Properties of Powders of Significance for Dry Powder Inhaler Formulations. *Advanced Drug Delivery Reviews*. **26**, 17-27.
- Buist, A., (2003). Similarities and Differences between Asthma and Chronic Obstructive Pulmonary Disease: Treatment and Early Outcomes. *European Respiratory Journal*. **21**, 30S-35S.
- Byron, P. & Patton, J., (1994). Drug-Delivery Via the Respiratory Tract. *Journal of Aerosol Medicine*. **7**, 49-75.
- Byron, P., Peart, J. & Staniforth, J., (1997). Aerosol Electrostatics .1. Properties of Fine Powders before and after Aerosolization by Dry Powder Inhalers. *Pharmaceutical Research*. **14**, 698-705.
- Caira, M. R., Bettinetti, G., Sorrenti, M. & Catenacci, L., (2007). Relationships between Structural and Thermal Properties of Anhydrous and Solvated Crystalline Forms of Brodimoprim. *Journal of Pharmaceutical Sciences*. **96**, 996-1007.
- Calverley, P., Pauwels, R., Vestbo, J., Jones, P., Pride, N., Gulsvik, A., Anderson, J. & Maden, C., (2003). Combined Salmeterol and Fluticasone in the Treatment of Chronic Obstructive Pulmonary Disease: A Randomised Controlled Trial. *Lancet*. **361**, 449-456.
- Camarasu, C., Madichie, C. & Williams, R., (2006). Recent Progress in the Determination of Volatile Impurities in Pharmaceuticals. *Trends in Analytical Chemistry*. **25**, 768-777.

## References

---

Cappella, B. & Dietler, G., (1999). Force-Distance Curves by Atomic Force Microscopy. *Surface Science Reports*. **34**, 1-104.

Chikhalia, V., Forbes, R., Storey, R. & Ticehurst, M., (2006). The Effect of Crystal Morphology and Mill Type on Milling Induced Crystal Disorder. *European Journal of Pharmaceutical Sciences*. **27**, 19-26.

Chow, A. H. L., Tong, H. H. Y., Chattopadhyay, P. & Shekunov, B. Y., (2007). Particle Engineering for Pulmonary Drug Delivery. *Pharmaceutical Research*. **24**, 411-437.

Chow, K., Tong, H. H. Y., Lum, S. & Chow, A. H. L., (2008). Engineering of Pharmaceutical Materials: An Industrial Perspective. *Journal of Pharmaceutical Sciences*. **97**, 2855-2877.

Clas, S., Dalton, C. & Hancock, B. C., (1999). Differential Scanning Calorimetry: Applications in Drug Development. *Pharmaceutical Science and Technology Today*. **2**, 311-320.

Clifford, C. & Seah, M., (2005a). Quantification Issues in the Identification of Nanoscale Regions of Homopolymers Using Modulus Measurement Via Afm Nanoindentation. *Applied Surface Science*. **252**, 1915-1933.

Clifford, C. & Seah, M., (2005b). The Determination of Atomic Force Microscope Cantilever Spring Constants Via Dimensional Methods for Nanomechanical Analysis. *Nanotechnology*. **16**, 1666-1680.

Colton, R., (2004). Nanoscale Measurements and Manipulation. *Journal of Vacuum Science and Technogy B*. **22**, 1609-1635.

Corrigan, D. O., Corrigan, O. I. & Healy, A. M., (2006). Physicochemical and in Vitro Deposition Properties of Salbutamol Sulphate/Ipratropium Bromide and Salbutamol Sulphate/Excipient Spray Dried Mixtures for Use in Dry Powder Inhalers. *International Journal of Pharmaceutics*. **322**, 22-30.

Crowder, T., Rosati, J., Schroeter, J., Hickey, A. & Martonen, T., (2002). Fundamental Effects of Particle Morphology on Lung Delivery: Predictions of Stokes' Law and the Particular Relevance to Dry Powder Inhaler Formulation and Development. *Pharmaceutical Research*. **19**, 239-245.

Dalby, R. & Suman, J., (2003). Inhalation Therapy: Technological Milestones in Asthma Treatment. *Advanced Drug Delivery Reviews*. **55**, 779-791.

Daniher, D. I. & Zhu, J., (2008). Dry Powder Platform for Pulmonary Drug Delivery. *Particuology*. **6**, 225-238.

Das, S., Larson, I., Young, P. M. & Stewart, P., (2009). Surface Energy Changes and Their Relationship with the Dispersibility of Salmeterol Xinafoate Powders for Inhalation after Storage at High Rh. *European Journal of Pharmaceutical Sciences*. **38**, 347-354.

## References

- Datta, S. & Grant, D., (2004). Crystal Structures of Drugs: Advances in Determination, Prediction and Engineering. *Nature Reviews Drug Discovery*. **3**, 42-57.
- Davies, M., Brindley, A., Chen, X., Marlow, M., Doughty, S. W., Shrubb, I. & Roberts, C. J., (2005). Characterization of Drug Particle Surface Energetics and Young's Modulus by Atomic Force Microscopy and Inverse Gas Chromatography. *Pharmaceutical Research*. **22**, 1158-1166.
- De Boer, A., Gjaltema, D., Hagedoorn, P. & Frijlink, H., (2002). Characterization of Inhalation Aerosols: A Critical Evaluation of Cascade Impactor Analysis and Laser Diffraction Technique. *International Journal of Pharmaceutics*. **249**, 219-231.
- De Gusseme, A., Neves, C., Willart, J. F., Rameau, A. & Descamps, M., (2008). Ordering and Disordering of Molecular Solids Upon Mechanical Milling: The Case of Fananserine. *Journal of Pharmaceutical Sciences*. **97**, 5000-5012.
- De Vegt, O., Vromans, H., Den Toonder, J. & Van Der Voort Maarschalk, K., (2008). Influence of Flaws and Crystal Properties on Particle Fracture in a Jet Mill. *Powder Technology*. **191**, 72-77.
- De Vegt, O., Vromans, H., Faassen, F. & Maarschalk, K., (2005). Milling of Organic Solids in a Jet Mill. Part 1: Determination of the Selection Function and Related Mechanical Material Properties. *Particle and Particle Systems Characterization*. **22**, 133-140.
- De Vegt, O., Vromans, H., Pries, W. & Van Der Voort Maarschalk, K., (2006). The Effect of Crystal Imperfections on Particle Fracture Behaviour. *International Journal of Pharmaceutics*. **317**, 47-53.
- Derjaguin, V., Muller, V. & Toporov, Y., (1975). Effect of Contact Deformations on the Adhesion of Particles. *Journal of Colloid and Interface Science*. **53**, 314-326.
- Deryaguin, B. V., Krotova, N. A. & Similga, V. P. (1978) *Adhesion of Solids*, New York, Consultants Bureau.
- Dhumal, R. S., Biradar, S. V., Paradkar, A. R. & York, P., (2009). Particle Engineering Using Sonocrystallization: Salbutamol Sulphate for Pulmonary Delivery. *International Journal of Pharmaceutics*. **368**, 129-137.
- Di Martino, P., Censi, R., Barthelemy, C., Gobetto, R., Joiris, E., Masic, A., Odou, P. & Martelli, S., (2007). Characterization and Compaction Behaviour of Nimesulide Crystal Forms. *International Journal of Pharmaceutics*. **342**, 137-144.
- Dickhoff, B., De Boer, A., Lambregts, D. & Frijlink, H., (2005). The Interaction between Carrier Rugosity and Carrier Payload, and Its Effect on Drug Particle Redispersion from Adhesive Mixtures During Inhalation. *European Journal of Pharmaceutics and Biopharmaceutics*. **59**, 197-205.

Dilworth, S., Buckton, G., Gaisford, S. & Ramos, R., (2004). Approaches to Determine the Enthalpy of Crystallisation, and Amorphous Content, of Lactose from Isothermal Calorimetric Data. *International Journal of Pharmaceutics*. **284**, 83-94.

Duncan-Hewitt, W. & Nisman, R., (1993). Investigation of the Surface Free-Energy of Pharmaceutical Materials from Contact-Angle, Sedimentation, and Adhesion Measurements. *Journal of Adhesion Science and Technology*. **7**, 263-283.

Edge, S., Mueller, S., Price, R. & Shur, J., (2008). Factors Affecting Defining the Quality and Functionality of Excipients Used in the Manufacture of Dry Powder Inhaler Products. *Drug Development and Industrial Pharmacy*. **34**, 966-973.

Fages, J., Lochard, H., Letourneau, J., Sauceau, M. & Rodier, E., (2004). Particle Generation for Pharmaceutical Applications Using Supercritical Fluid Technology. *Powder Technology*. **141**, 219-226.

Feeley, J., York, P., Sumbly, B. & Dicks, H., (1998). Determination of Surface Properties and How Characteristics of Salbutamol Sulphate, before and after Micronisation. *International Journal of Pharmaceutics*. **172**, 89-96.

Fiebig, A., Jones, M. D. & Ulrich, J., (2007). Predicting the Effect of Impurity Adsorption on Crystal Morphology. *Crystal Growth and Design*. **7**, 1623-1627.

Florey, K. (2003) *Profiles of Drug Substances, Excipients and Related Methodology* New York, Elsevier Inc.

Fraxedas, J., Garcia-Manyes, S., Gorostiza, P. & Sanz, F., (2002). Nanoindentation: Toward the Sensing of Atomic Interactions. *Proceedings of the National Academy of Sciences*. **99**, 5228-5232.

Fujiwara, M., Nagy, Z., Chew, J. & Braatz, R., (2005). First-Principles and Direct Design Approaches for the Control of Pharmaceutical Crystallization. *Journal of Process Control*. **15**, 493-504.

Fuller, K. N. G. & Tabor, D., (1975). Effect of Surface Roughness on Adhesion of Elastic Solids. *Proceedings of the Royal Society of London. Series A, Mathematical and Physical and Engineering Sciences*. **345**, 327-342.

Ganderton, D., (1992). The Generation of Respirable Cloud from Coarse Powder Aggregates. *Journal of Biopharmaceutical Sciences*. **3**, 101-105.

Garcia-Contreras, L. & Hickey, A., (2003). Aerosol Treatment of Cystic Fibrosis. *Critical reviews in therapeutic drug carrier systems*. **20**, 317-356.

Gardner, C., Walsh, C. & Almarsson, O., (2004). Drugs as Materials: Valuing Physical Form in Drug Discovery. *Nature Reviews Drug Discovery*. **3**, 926-934.



## References

- Garekani, H., Sadeghi, F., Badiie, A., Mostafa, S. & Rajabi-Siahboomi, A., (2001). Crystal Habit Modifications of Ibuprofen and Their Physicomechanical Characteristics. *Drug Development and Industrial Pharmacy*. **27**, 803-809.
- Ghadiri, M. & Zhang, Z., (2002). Impact Attrition of Particulate Solids. Part 1: A Theoretical Model of Chipping. *Chemical Engineering Science*. **57**, 3659-3669.
- Gibbs, J. (1948) *Collected Works*, New Haven, Yale University Press.
- Good, R., (1992). Contact-Angle, Wetting and Adhesion - a Critical Review. *Journal of Adhesion Science and Technology*. **6**, 1269-1302.
- Griesenbach, U., Geddes, D. & Alton, E., (2004). Gene Therapy for Cystic Fibrosis: An Example for Lung Gene Therapy. *Gene Therapy*. **11**, S43-S50.
- Grimsey, I., Feeley, J. & York, P., (2002). Analysis of the Surface Energy of Pharmaceutical Powders by Inverse Gas Chromatography. *Journal of Pharmaceutical Sciences*. **91**, 571-583.
- Hamaker, H. C., (1937). London-Van Der Waals Forces Attraction between Spherical Particles. *Physica (Utrecht)*. **4**, 1058-1072.
- Hansel, T. T. & Barnes, P. J., (2009). New Drugs for Exacerbations of Chronic Obstructive Pulmonary Disease. *Lancet*. **374**, 744-755.
- Harris, K., Tremayne, M. & Kariuki, B., (2001). Contemporary Advances in the Use of Powder X-Ray Diffraction for Structure Determination. *Angew Chem Int Edit*. **40**, 1626-1651.
- Hertz, H., (1881). Contact of Elastic Solids. *Journal für die reine und angewandte Mathematik*. **92**, 156-171.
- Hickey, A. (2004) *Pharmaceutical Inhalation Aerosol Technology*, New York, Marcel Dekker.
- Hickey, A. J., Mansour, H. M., Telko, M. J., Xu, Z., Smyth, H. D. C., Mulder, T., Mclean, R., Langridge, J. & Papadopoulos, D., (2007a). Physical Characterization of Component Particles Included in Dry Powder Inhalers. I. Strategy Review and Static Characteristics. *Journal of Pharmaceutical Sciences*. **96**, 1282-1301.
- Hickey, A. J., Mansour, H. M., Telko, M. J., Xu, Z., Smyth, H. D. C., Mulder, T., Mclean, R., Langridge, J. & Papadopoulos, D., (2007b). Physical Characterization of Component Particles Included in Dry Powder Inhalers. II. Dynamic Characteristics. *Journal of Pharmaceutical Sciences*. **96**, 1302-1319.
- Hiestand, E. E., (1966). Powders: Particle-Particle Interactions. *Journal of Pharmaceutical Sciences*. **55**, 1325-1344.
- Hinds, W. C. (1982) *Aerosol Technology*, New York, Wiley Interscience.

## References

- Hooton, J. C., German, C., Allen, S., Davies, M. C., Roberts, C. J., Tendler, S. & Williams, P., (2004). An Atomic Force Microscopy Study of the Effect of Nanoscale Contact Geometry and Surface Chemistry on the Adhesion of Pharmaceutical Particles. *Pharmaceutical Research*. **21**, 953-961.
- Hooton, J. C., German, C. S., Allen, S., Davies, M. C., Roberts, C. J., Tendler, S. J. B. & Williams, P., (2003). Characterization of Particle-Interactions by Atomic Force Microscopy: Effect of Contact Area. *Pharmaceutical Research*. **20**, 508-514.
- Hooton, J. C., Jones, M. D., Harris, H., Shur, J. & Price, R., (2008). The Influence of Crystal Habit on the Prediction of Dry Powder Inhalation Formulation Performance Using the Cohesive-Adhesive Force Balance Approach. *Drug Development and Industrial Pharmacy*. **34**, 974-983.
- Hooton, J. C., Jones, M. D. & Price, R., (2006). Predicting the Behavior of Novel Sugar Carriers for Dry Powder Inhaler Formulations Via the Use of a Cohesive-Adhesive Force Balance Approach. *Journal of Pharmaceutical Sciences*. **95**, 1288-1297.
- Hu, T., Chiou, H., Chan, H.-K., Chen, J.-F. & Yun, J., (2008). Preparation of Inhalable Salbutamol Sulphate Using Reactive High Gravity Controlled Precipitation. *Journal of Pharmaceutical Sciences*. **97**, 944-949.
- Hubner, U., Morgenroth, W., Meyer, H., Sulzbach, T., Brendel, B. & Mirande, W., (2003). Downwards to Metrology in Nanoscale: Determination of the Afm Tip Shape with Well-Known Sharp-Edged Calibration Structures. *Applied Physics A-Materials Science & Processing*. **76**, 913-917.
- Hutter, J. L. & Bechhoefer, J., (1993). Calibration of Atomic-Force Microscope Tips. *Review of Scientific Instruments*. **64**, 1868-1873.
- Islam, N. & Gladki, E., (2008). Dry Powder Inhalers (Dpis) - a Review of Device Reliability and Innovation. *International Journal of Pharmaceutics*. **360**, 1-11.
- Jalili, N. & Laxminarayana, K., (2004). A Review of Atomic Force Microscopy Imaging Systems: Application to Molecular Metrology and Biological Sciences. *Mechatronics*. **14**, 907-945.
- James, J., Davies, M. C., Toon, R., Jinks, P. & Roberts, C. J., (2009). Particulate Drug Interactions with Polymeric and Elastomeric Valve Components in Suspension Formulations for Metered Dose Inhalers. *International Journal of Pharmaceutics*. **366**, 124-132.
- Jarring, K., Larsson, T., Stensland, B. & Ymen, I., (2006). Thermodynamic Stability and Crystal Structures for Polymorphs and Solvates of Formoterol Fumarate. *Journal of Pharmaceutical Sciences*. **95**, 1144-1161.
- Johnson, D. L. A. M., T. B., (1994). Behaviour of Inhaled Fibers - Potential Applications to Medicinal Aerosols *Particulate Science and Technology*. **12**, 161-173.

- Johnson, K. L., (1996). Continuum Mechanics Modelling of Adhesion and Friction. *Langmuir*. **12**, 4510-4513.
- Johnson, K. L., (1998). Mechanics of Adhesion. *Tribology International*. **31**, 413-418.
- Johnson, K. L., Kendall, K. & Roberts, A. D., (1971). Surface Energy and the Contact of Elastic Solids. *Proceedings of the Royal Society of London. Series A, Mathematical and Physical Sciences*. **324**, 301-313.
- Jones, M. D., Hooton, J. C., Dawson, M. L., Ferrie, A. R. & Price, R., (2008). An Investigation into the Dispersion Mechanisms of Ternary Dry Powder Inhaler Formulations by the Quantification of Interparticulate Forces. *Pharmaceutical Research*. **25**, 337-348.
- Jung, J. & Perrut, M., (2001). Particle Design Using Supercritical Fluids: Literature and Patent Survey. *Journal of Supercritical Fluids*. **20**, 179-219.
- Katz, A. & Kalman, H., (2007). Preliminary Experimental Analysis of a Spiral Jet Mill Performance. *Particle and Particle Systems Characterization*. **24**, 332-338.
- Keck, C. M. & Mueller, R. H., (2008). Size Analysis of Submicron Particles by Laser Diffractometry-90% of the Published Measurements Are False. *International Journal of Pharmaceutics*. **355**, 150-163.
- Khankari, R. & Grant, D., (1995). Pharmaceutical Hydrates. *Thermochim Acta*. **248**, 61-79.
- Kossel, W., (1934). Zur Energetik Von Oberflächenvorgängen. *Annalen der Physik*. **21**, 457-480.
- Krycer, I. & Hersey, J., (1981). Grinding and Granulation in a Vibratory Ball Mill. *Powder Technology*. **28**, 91-95.
- Kubavat, H., Shur, J. & Price, R. (2009) An Investigation into the Influence of Primary Crystallisation Conditions on the Mechanical Properties and Secondary Processing Behaviour of Fluticasone Propionate. *Proceedings of Drug Delivery to the Lungs XX*. Edinburgh, UK.
- Kumar, P., Clark, M. (2002) *Clinical Medicine*, Edinburgh, WB Saunders.
- Kwan, C., Chena, Y., Ding, Y., Papadopoulos, D., Benthall, A. & Ghadiri, M., (2004). Development of a Novel Approach Towards Predicting the Milling Behaviour of Pharmaceutical Powders. *European Journal of Pharmaceutical Sciences*. **23**, 327-336.
- Lappalainen, M. & Karppinen, M., (2010). Techniques of Differential Scanning Calorimetry for Quantification of Low Contents of Amorphous Phases. *Journal of Thermal Analysis and Calorimetry*. **102**, 171-180.

## References

- 
- Lee, J., (2007). Structural Hetrogenity of Pharmaceutical Compacts Probed by Micro-Indentation. *Journal of Material Science*. **19**, 1981-1990.
- Leigh, S., Carless, J. E. & Burt, B. W., (1967). Compression Characteristics of Some Pharmaceutical Materials. *Journal of Pharmaceutical Sciences*. **56**, 888-892.
- Leuenberger, H. & Rohera, D., (1986). Fundamentals of Powder Compression .1. The Compactibility and Compressibility of Pharmaceutical Powders. *Pharmaceutical Research*. **3**, 12-22.
- Li, Q., Rudolph, V. & Peukert, W., (2006). London-Van Der Waals Adhesiveness of Rough Particles. *Powder Technology*. **161**, 248-255.
- Liao, X. & Wiedmann, T., (2005). Measurement of Process-Dependent Material Properties of Pharmaceutical Solids by Nanoindentation. *Journal of Pharmaceutical Sciences*. **94**, 79-92.
- Lifshitz, E. M., (1955). Teorija Moleculyarnych Sil Pritasheniya Meshdu Tverdymi Telam. *Journal of Experimental Theoretical Physics*. **29**, 94-110.
- Loalor, C. B. A. H., A. J. (1996) *Pharmaceutical Aerosols for the Delivery of Drugs to the Lungs*, London, Blackie Academic and Professionals.
- Loffert, D., Ikle, D. & Nelson, H., (1994). A Comparison of Commercial Jet Nebulizers. *Chest*. **106**, 1788-1792.
- Malcolmson, R. & Embleton, J., (1998). Dry Powder Formulations for Pulmonary Delivery. *Pharmaceutical Science and Technology Today*. **1**, 394-398.
- Marple, V., Roberts, D., Romay, F., Miller, N., Truman, K., Holroyd, M., Mitchell, J. P. & Hochrainer, D., (2003). Next Generation Pharmaceutical Impactor (a New Impactor for Pharmaceutical Inhaler Testing). Part I: Design. *Journal of Aerosol Medicine*. **16**, 283-299.
- Masterson, V. M. & Cao, X., (2008). Evaluating Particle Hardness of Pharmaceutical Solids Using Afm Nanoindentation. *International Journal of Pharmaceutics*. **362**, 163-171.
- Matz, J., Emmett, A., Rickard, K. & Kalberg, C., (2001). Addition of Salmeterol to Low-Dose Fluticasone Versus Higher-Dose Fluticasone: An Analysis of Asthma Exacerbations. *Journal of Allergy and Clinical Immunology*. **107**, 783-789.
- Meier, M., John, E., Wieckhusen, D., Wirth, W. & Peukert, W., (2008). Influence of Mechanical Properties on Impact Fracture: Prediction of the Milling Behaviour of Pharmaceutical Powders by Nanoindentation. *Powder Technology*. **188**, 301-313.

## References

- Midoux, N., Hosek, P., Pailleres, L. & Authelin, J., (1999). Micronization of Pharmaceutical Substances in a Spiral Jet Mill. *Powder Technology*. **104**, 113-120.
- Mie, G., (1908). Contributions to the Optics of Diffuse Media. *Annals of Physics*. **25**, 377-445.
- Mitchell, J. & Nagel, M., (1997). Medical Aerosols: Techniques for Particle Size Evaluation. *Particulate Science and Technology*. **15**, 217-241.
- Mitchell, J., Newman, S. & Chan, H.-K., (2007). In Vitro and in Vivo Aspects of Cascade Impactor Tests and Inhaler Performance: A Review. *AAPS Pharmaceutical Science and Technology*. **8**, 110.
- Mitchell, J. P. & Nagel, M., (2003). Cascade Impactors for the Size Characterization of Aerosols from Medical Inhalers: Their Uses and Limitations. *Journal of Aerosol Medicine*. **16**, 341-377.
- Mullin, J. (2001) *Crystallization*, Oxford, UK, Elsevier Butterworth-Heinemann.
- Murnane, D., Marriott, C. & Martin, G. P., (2008). Crystallization and Crystallinity of Fluticasone Propionate. *Crystal Growth and Design*. **8**, 2753-2764.
- Murnane, D., Martin, G. P. & Marriott, C., (2009). Dry Powder Formulations for Inhalation of Fluticasone Propionate and Salmeterol Xinafoate Microcrystals. *Journal of Pharmaceutical Sciences*. **98**, 503-515.
- Murphy, A., (2010). Asthma the Condition and Its Diagnosis. *Clinical Pharmacist*. **2**, 203-207.
- Muster, T. & Prestidge, C., (2002). Face Specific Surface Properties of Pharmaceutical Crystals. *Journal of Pharmaceutical Sciences*. **91**, 1432-1444.
- Myerson, A. S. (1993) *Handbook of Industrial Crystallization*, Oxford, UK, Butterworth-Heinemann.
- Neal, M. J. (2002) *Medical Pharmacology at a Glance* London, Blackwell Science.
- Nelson, H., Chapman, K., Pyke, S., Johnson, M. & Pritchard, J., (2003). Enhanced Synergy between Fluticasone Propionate and Salmeterol Inhaled from a Single Inhaler Versus Separate Inhalers. *Journal of Allergy and Clinical Immunology*. **112**, 29-36.
- Nelson, H., Weiss, S. & Bleeker, E., (2006). The Salmeterol Multicenter Asthma Research Trial. *Chest*. **129**, 15-26.
- Newman, A. W., Reutzel-Edens, S. M. & Zografi, G., (2008). Characterization of The "Hygroscopic" Properties of Active Pharmaceutical Ingredients. *Journal of Pharmaceutical Sciences*. **97**, 1047-1059.

## References

- 
- Newman, S. & Busse, W., (2002). Evolution of Dry Powder Inhaler Design, Formulation, and Performance. *Respiratory Medicine*. **96**, 293-304.
- Ng, W. K., Kwek, J. W. & Tan, R. B. H., (2008). Anomalous Particle Size Shift During Post-Milling Storage. *Pharmaceutical Research*. **25**, 1175-1185.
- Nyvt, J., Sohnel, O., Matcuchova, M. & Broul, M. (1985) *The Kinetics of Industrial Crystallization*, Amsterdam, Elsevier.
- Ogura, K. & Sobue, H., (1970). Changes in Morphology with Milling of the Commercial Microcrystalline Cellulose. *Journal of Applied Polymer Science*. **14**, 1390-1393.
- Ohri, C. M. & Steiner, M. C., (2004). Copd - the Disease and Non-Drug Treatment. *Hospital Pharmacist*. **11**, 359-364.
- Oliver, W. & Pharr, G., (1992). An Improved Technique for Determining Hardness and Elastic Modulus Using Load and Displacement Sensing Indentation Experiments. *Journal of Material Research*. **7**, 1564-1583.
- Parmar, M. M., Khan, O., Seton, L. & Ford, J. L., (2007). Polymorph Selection with Morphology Control Using Solvents. *Crystal Growth and Design*. **7**, 1635-1642.
- Parrot, E. L. (1990) Comminution. IN SWARBRICK, J. & BOYLAN, J. (Eds.) *Encyclopedia of Pharmaceutical Technology*. New York, Marcel Dekker.
- Patton, J. S. & Byron, P. R., (2007). Inhaling Medicines: Delivering Drugs to the Body through the Lungs. *Nature Reviews Drug Discovery*. **6**, 67-74.
- Pauwels, R., Newman, S. & Borgstrom, L., (1997). Airway Deposition and Airway Effects of Antiasthma Drugs Delivered from Metered-Dose Inhalers. *European Respiratory Journal*. **10**, 2127-2138.
- Perkins, M., Bunker, M., James, J., Rigby-Singleton, S., Ledru, J., Madden-Smith, C., Luk, S., Patel, N. & Roberts, C. J., (2009). Towards the Understanding and Prediction of Material Changes During Micronisation Using Atomic Force Microscopy. *European Journal of Pharmaceutical Sciences*. **38**, 1-8.
- Perkins, M., Ebbens, S. J., Hayes, S., Roberts, C. J., Madden, C. E., Luk, S. Y. & Patel, N., (2007). Elastic Modulus Measurements from Individual Lactose Particles Using Atomic Force Microscopy. *International Journal of Pharmaceutics*. **332**, 168-175.
- Pilcer, G. & Amighi, K., (2010). Formulation Strategy and Use of Excipients in Pulmonary Drug Delivery. *International Journal of Pharmaceutics*. **392**, 1-19.
- Pitchayajittipong, C., Shur, J. & Price, R., (2009). Engineering of Crystalline Combination Inhalation Particles of a Long-Acting Beta(2)-Agonist and a Corticosteroid. *Pharmaceutical Research*.

Planinsek, O., Trojak, A. & Srcic, S., (2001). The Dispersive Component of the Surface Free Energy of Powders Assessed Using Inverse Gas Chromatography and Contact Angle Measurements. *International Journal of Pharmaceutics*. **221**, 211-217.

Plassard, C., Lesniewska, E., Pochard, I. & Nonat, A., (2004). Investigation of the Surface Structure and Elastic Properties of Calcium Silicate Hydrates at the Nanoscale. *Ultramicroscopy*. **100**, 331-338.

Podczeck, F., Newton, J. & James, M., (1996). The Adhesion Force of Micronized Salmeterol Xinafoate Particles to Pharmaceutically Relevant Surface Materials. *Journal of Physics D - Applied Physics*. **29**, 1878-1884.

Ponton, C. & Rawlings, R., (1989). Vickers Indentation Fracture Toughness Test Part 1: Review of Literature and Formulation of Standardised Indentation Toughness Equations. *Material Science and Technology*. **5**, 865-872.

Prime, D., Atkins, P., Slater, A. & Sumby, B., (1997). Review of Dry Powder Inhalers. *Advanced Drug Delivery Reviews*. **26**, 51-58.

Ramos, K. J. & Bahr, D. F., (2007). Mechanical Behavior Assessment of Sucrose Using Nanoindentation. *Journal of Material Research*. **22**, 2037-2045.

Rang, H. P., Dale, M. M., Ritter, J. M. And Moore, P. K. (2003) *Pharmacology*, London, Churchill Livingstone.

Roberts, C. J., (2005). What Can We Learn from Atomic Force Microscopy Adhesion Measurements with Single Drug Particles? *European Journal of Pharmaceutical Sciences*. **24**, 153-157.

Roberts, R., Rowe, R. & York, P., (1991). The Relationship between Young Modulus of Elasticity of Organic-Solids and Their Molecular-Structure. *Powder Technology*. **65**, 139-146.

Rodriguez-Hornedo, N. & Murphy, D., (1999). Significance of Controlling Crystallization Mechanisms and Kinetics in Pharmaceutical Systems. *Journal of Pharmaceutical Sciences*. **88**, 651-660.

Rowe, R. & Roberts, R. (1995) *The Mechanical Properties of Powders*, London, Academic Press.

Ruecroft, G., Hipkiss, D., Ly, T., Maxted, N. & Cains, P., (2005). Sonocrystallization: The Use of Ultrasound for Improved Industrial Crystallization. *Organic Process Research & Development*. **9**, 923-932.

Rumpf, H., (1973). Physical Aspects of Comminution and New Formulations of a Law of Comminution. *Powder Technology*. **7**, 145-159.

## References

- Sader, J., Larson, I. & Mulvaney, P., (1995). Methods for the Calibration of Atomic Force Microscope Cantilevers. *Review of Scientific Instruments*. **66**, 3789-3798.
- Salerno, M. & Bykov, I., (2006). Tutorial: Mapping Adhesion Forces and Calculating Elasticity in Contact-Mode Afm. *Microscopy and Analysis*. **20**, S5-S8.
- Saunders, M., Podlusi, K., Shergill, S., Buckton, G. & Royall, P., (2004). The Potential of High Speed Dsc (Hyper-Dsc) for the Detection and Quantification of Small Amounts of Amorphous Content in Predominantly Crystalline Samples. *International Journal of Pharmaceutics*. **274**, 35-40.
- Schiavone, H., Palakodaty, S., Clark, A., York, P. & Tzannis, S., (2004). Evaluation of Scf-Engineered Particle-Based Lactose Blends in Passive Dry Powder Inhalers. *International Journal of Pharmaceutics*. **281**, 55-66.
- Seville, P. C., Learoyd, T. P., Li, H.-Y., Williamson, I. J. & Birchall, J. C., (2007). Amino Acid-Modified Spray-Dried Powders with Enhanced Aerosolisation Properties for Pulmonary Drug Delivery. *Powder Technology*. **178**, 40-50.
- Shekunov, B. Y., Chattopadhyay, P., Tong, H. H. Y. & Chow, A. H. L., (2007). Particle Size Analysis in Pharmaceutics: Principles, Methods and Applications. *Pharmaceutical Research*. **24**, 203-227.
- Shekunov, B. Y. & York, P., (2000). Crystallization Processes in Pharmaceutical Technology and Drug Delivery Design. *Journal of Crystal Growth*. **211**, 122-136.
- Sheth, A. R. & Grant, D., (2005). Relationship between the Structure and Properties of Pharmaceutical Crystals. *KONA*. 36-48.
- Shoyele, S. A. & Cawthorne, S., (2006). Particle Engineering Techniques for Inhaled Biopharmaceuticals. *Advanced Drug Delivery Reviews*. **58**, 1009-1029.
- Shur, J., Harris, H., Jones, M. D., Kaerger, J. S. & Price, R., (2008). The Role of Fines in the Modification of the Fluidization and Dispersion Mechanism within Dry Powder Inhaler Formulations. *Pharmaceutical Research*. **25**, 1931-1940.
- Simms, P., Towne, R., Gross, C. & Miller, R., (1998). The Separation of Ipratropium Bromide and Its Related Compounds. *Journal of Pharmaceutical and Biomedical Analysis*. **17**, 841-849.
- Son, Y.-J. & Mcconville, J. T., (2008). Advancements in Dry Powder Delivery to the Lung. *Drug Development and Industrial Pharmacy*. **34**, 948-959.
- Staniforth, J. & Rees, J. E., (1982). Electrostatic Charge Interactions in Ordered Powder Mixes. *Journal of Pharmacy and Pharmaceutical Sciences*. **34**, 69-76.



## References

- Steckel, H. & Brandes, H., (2004). A Novel Spray-Drying Technique to Produce Low Density Particles for Pulmonary Delivery. *International Journal of Pharmaceutics*. **278**, 187-195.
- Steckel, H., Markefka, P., Tewierik, H. & Kammelar, R., (2006). Effect of Milling and Sieving on Functionality of Dry Powder Inhalation Products. *International Journal of Pharmaceutics*. **309**, 51-59.
- Steckel, H., Rasenack, N., Villax, P. & Muller, B., (2003). In Vitro Characterization of Jet-Milled and in-Situ-Micronized Fluticasone-17-Propionate. *International Journal of Pharmaceutics*. **258**, 65-75.
- Szafranski, W., Cukier, A., Ramirez, A., Menga, G., Sansores, R., Nahabedian, S., Peterson, S. & Olsson, H., (2003). Efficacy and Safety of Budesonide/Formoterol in the Management of Chronic Obstructive Pulmonary Disease. *European Respiratory Journal*. **21**, 74-81.
- Tajber, L., Corrigan, D. O., Corrigan, O. I. & Healy, A. M., (2009). Spray Drying of Budesonide, Formoterol Fumarate and Their Composites--I. Physicochemical Characterisation. *International Journal of Pharmaceutics*. **367**, 79-85.
- Tattersfield, A., Knox, A., Britton, J. & Hall, I., (2002). Asthma. *Lancet*. **360**, 1313-1322.
- Taylor, L., Papadopoulos, D., Dunn, P., Bentham, A., Dawson, N., Mitchell, J. & Snowden, M., (2004a). Predictive Milling of Pharmaceutical Materials Using Nanoindentation of Single Crystals. *Organic Process Research & Development*. **8**, 674-679.
- Taylor, L., Papadopoulos, D., Dunn, P., Bentham, A., Mitchell, J. & Snowden, M., (2004b). Mechanical Characterisation of Powders Using Nanoindentation. *Powder Technology*. **143**, 179-185.
- Teipel, U. (2004) *Energetic Materials*, Weinheim, Wiley-VCH.
- Telko, M. J. & Hickey, A. J., (2005). Dry Powder Inhaler Formulation. *Respiratory care*. **50**, 1209-1227.
- Timsina, M., Martin, G., Marriott, C., Ganderton, D. & Yianneskis, M., (1994a). Drug-Delivery to the Respiratory-Tract Using Dry Powder Inhalers. *International Journal of Pharmaceutics*. **101**, 1-13.
- Timsina, M., Martin, G. P., Marriott, C., Ganderton, D. & Yianneskis, M., (1994b). Drug-Delivery to the Respiratory-Tract Using Dry Powder Inhalers. *International Journal of Pharmaceutics*. **101**, 1-13.
- Tong, H. H. Y., Shekunov, B. Y., York, P. & Chow, A. H. L., (2001). Characterization of Two Polymorphs of Salmeterol Xinafoate Crystallized from Supercritical Fluids. *Pharmaceutical Research*. **18**, 852-858.

## References

- Tong, H. H. Y., Shekunov, B. Y., York, P. & Chow, A. H. L., (2002). Influence of Polymorphism on the Surface Energetics of Salmeterol Xinafoate Crystallized from Supercritical Fluids. *Pharmaceutical Research*. **19**, 640-648.
- Tougas, T. P., Christopher, D., Mitchell, J. P., Strickland, H., Wyka, B., Van Oort, M. & Lyapustina, S., (2009). Improved Quality Control Metrics for Cascade Impaction Measurements of Orally Inhaled Drug Products (Oips). *AAPS Pharmaceutical Science and Technology*. **10**, 1276-1285.
- Traini, D., Rogueda, P., Young, P. M. & Price, R., (2005). Surface Energy and Interparticle Force Correlation in Model. *Pharmaceutical Research*. **22**, 816-825.
- Traini, D., Young, P. M., Rogueda, P. & Price, R., (2007). In Vitro Investigation of Drug Particulates Interactions and Aerosol Performance of Pressurised Metered Dose Inhalers. *Pharmaceutical Research*. **24**, 125-135.
- Turner, Y. T. A., Roberts, C. J. & Davies, M. C., (2007). Scanning Probe Microscopy in the Field of Drug Delivery. *Advanced Drug Delivery Reviews*. **59**, 1453-1473.
- Van Oss, C., Good, R. & Chaudhury, M., (1988). Additive and Nonadditive Surface Tension Components and Interpretation of Contact Angles *Langmuir*. **4**, 884-891.
- Variankaval, N., Cote, A. S. & Doherty, M. F., (2008). From Form to Function: Crystallization of Active Pharmaceutical Ingredients. *American Institute of Chemical Engineers Journal*. **54**, 1682-1688.
- Velaga, S., Berger, R. & Carlfors, J., (2002). Supercritical Fluids Crystallization of Budesonide and Flunisolide. *Pharmaceutical Research*. **19**, 1564-1571.
- Velaga, S., Bergh, S. & Carlfors, J., (2004). Stability and Aerodynamic Behaviour of Glucocorticoid Particles Prepared by a Supercritical Fluids Process. *European Journal of Pharmaceutical Sciences*. **21**, 501-509.
- Vincken, W., Van Noord, J., Greefhorst, A., Bantje, T., Kesten, S., Korducki, L. & Cornelissen, P., (2002). Improved Health Outcomes in Patients with Copd During 1 Yr's Treatment with Tiotropium. *European Respiratory Journal*. **19**, 209-216.
- Virchow, J. C., Crompton, G. K., Dal Negro, R., Pedersen, S., Magnan, A., Seidenbergf, J. & Barnes, P. J., (2008). Importance of Inhaler Devices in the Management of Airway Disease. *Respiratory Medicine*. **102**, 10-19.
- Vogel, L. & Peukert, W., (2005). From Single Particle Impact Behaviour to Modelling of Impact Mills. *Chemical Engineering Science*. **60**, 5164-5176.
- Volmer, M. (1939) *Kinetic Der Phasenbildung*, Leipzig, Steinkopff.

## References

Ward, I. & Hadley, D. (1995) *An Introduction to the Mechanical Properties of Solid Polymers*, New Jersey, USA, John Wiley and Sons.

Westmeier, R. & Steckel, H., (2008). Combination Particles Containing Salmeterol Xinafoate and Fluticasone Propionate: Formulation and Aerodynamic Assessment. *Journal of Pharmaceutical Sciences*. **97**, 2299-2310.

Wildfong, P. L. D., Hancock, B. C., Moore, M. D. & Morris, K. R., (2006). Towards an Understanding of the Structurally Based Potential for Mechanically Activated Disordering of Small Molecule Organic Crystals. *Journal of Pharmaceutical Sciences*. **95**, 2645-2656.

Wong, D., Wright, P. & Auton, M., (1988). The Deformation of Alpha-Lactose Monohydrate and Anhydrous Alpha-Lactose Monocrystals. *Drug Development and Industrial Pharmacy*. **14**, 2109-2126.

Wood, W., (2001). A Bad (Crystal) Habit - and How It Was Overcome. *Powder Technology*. **121**, 53-59.

Xu, Z., Mansour, H. M., Mulder, T., Mclean, R., Langridge, J. & Hickey, A. J., (2010). Dry Powder Aerosols Generated by Standardized Entrainment Tubes from Drug Blends with Lactose Monohydrate: 2. Ipratropium Bromide Monohydrate and Fluticasone Propionate. *Journal of Pharmaceutical Sciences*. **99**, 3415-3429.

Yokoyama, T., Urayama, K., Naito, M., Kato, M. & Yokoyama, T., (1987). The Angmill Mechanofusion System and Its Applications. *KONA*. **5**, 59-68.

Young, P. M., Chan, H.-K., Chiou, H., Edge, S., Tee, T. H. S. & Traini, D., (2007a). The Influence of Mechanical Processing of Dry Powder Inhaler Carriers on Drug Aerosolization Performance. *Journal of Pharmaceutical Sciences*. **96**, 1331-1341.

Young, P. M., Price, R., Tobyn, M., Buttrum, M. & Dey, F., (2003). Investigation into the Effect of Humidity on Drug-Drug Interactions Using the Atomic Force Microscope. *Journal of Pharmaceutical Sciences*. **92**, 815-822.

Young, P. M., Sung, A., Traini, D., Kwok, P., Chiou, H. & Chan, H.-K., (2007b). Influence of Humidity on the Electrostatic Charge and Aerosol Performance of Dry Powder Inhaler Carrier Based Systems. *Pharmaceutical Research*. **24**, 963-970.

Yu, L. X., (2008). Pharmaceutical Quality by Design: Product and Process Development, Understanding, and Control *Pharmaceutical Research*. **25**, 2463-2463.

Zeng, X.-M., Macritchie, H. B., Marriott, C. & Martin, G. P., (2007). Humidity-Induced Changes of the Aerodynamic Properties of Dry Powder Aerosol Formulations Containing Different Carriers. *International Journal of Pharmaceutics*. **333**, 45-55.

Zeng, X.-M., Martin, G. P., Marriott, C. & Pritchard, J., (2001). Lactose as a Carrier in Dry Powder Formulations: The Influence of Surface Characteristics on Drug Delivery. *Journal of Pharmaceutical Sciences*. **90**, 1424-1434.

Zeng, X. M., Martin, G. P., Marriott, C. (2001) *Particulate Interactions in Dry Powder Formulations for Inhalation*, London, Taylor and Francis.

Zugner, S., Marquardt, K. & Zimmermann, I., (2006). Influence of Nanomechanical Crystal Properties on the Comminution Process of Particulate Solids in Spiral Jet Mills. *European Journal of Pharmaceutics and Biopharmaceutics*. **62**, 194-201.

